Measuring the masses of planets around young active stars

Norbert Zicher

St. Hilda's

University of Oxford

A thesis submitted for the degree of

Doctor of Philosophy

Michaelmas 2021

Abstract

A quarter century after the famous discovery of 51 Peg b, the radial velocity (RV) method remains a key exoplanet detection and characterisation method. For transiting planets, RVs allow us to measure mean densities and draw conclusions about the planets' compositions. This is particularly valuable for young planets, which are sensitive probes of formation and evolution models. Stellar activity is the main factor limiting RV searches for both young planets and small, temperate planets around older stars. In this thesis, I developed and tested novel approaches to extract RVs from spectra using Gaussian process (GP) regression. I then used a multi-dimensional GP framework to model the impact of stellar activity on those RVs and to disentangle activity-induced and planetary signals in the data from a year-long intensive RV monitoring campaign of the bright, young M-dwarf AU Mic using the HARPS spectrograph. This enabled me and my collaborators to measure the masses of two transiting planets, which have previously been discovered by the TESS satellite, finding $M_b = 11.7 \pm 5.0\,M_\oplus$ and $M_c = 22.2 \pm 6.7\,M_\oplus$. As both planets are similar in size to Neptune, their contrasting densities represent a challenge for current planet formation models, and warrant further investigation. Finally, I also present extensions to the standard Generalised Least-squares Periodogram (GLS), which attempt to account for stellar activity explicitly. I used these to search for additional planets in the AU Mic system using both archival and new HARPS data, excluding the presence of any additional planets with RV semi-amplitudes $\geq 50\ \mathrm{m\,s^{-1}}$ and periods $20 \leq P \leq 1000\,\mathrm{days}$.

Acknowledgements

Studying at the University of Oxford as a doctoral research student has been a highly rewarding and transformative experience. It offered me the opportunity to meet fascinating people from all over the world; it brought me wonderful friends; and of course, allowed me to learn and grow a great deal.

I consider myself very lucky for having the opportunity to live and study in a place like Oxford. It was truly magical to walk around the town and its colleges, in some way feeling the vast history that is embedded within the walls.

On the academic front, I am extremely thankful to Prof. Suzanne Aigrain. Suzanne's deep knowledge and high academic standard make her a truly inspiring scientist, a real pioneer. Yet, I found that she is a humble and very caring person. Thank you, Suzanne, for everything that you taught me. Thank you for helping me when I struggled, and thank you for your patience with me. I could not have asked for a better supervisor. I also wish to thank everyone else who was involved in my academic development, I am grateful for the wonderful discussions and insights.

On an institutional level, I am very glad that to have been part of the Department of Physics at the University of Oxford. Thank you for your support and for providing a diverse and vibrant community. I wish to also thank Prof. Anne-Marie Lagrange for hosting me at Institut de Planétologie et d'Astrophysique de Grenoble (IPAG), during my research visit.

On a personal note, I am forever grateful to my family for their unconditional love and support. In particular, I wish to thank my parents for everything they do for me, for all of their sacrifices that allowed me to be where I am today. Köszönök mindent amit értem tesztek és a végtelen támogatásotokat!

And to my dear friends (you know who you are), in Oxford and everywhere in the world, thank you for all the happy memories. Thank you to the Oxford Basketball family, for making my time at Oxford more memorable.

Finally, thank you to Lisa. Thank you for your support and love. Thank you for pushing me. You inspire me every day and make me strive to be a better man. I am grateful for having met you and having you in my life!

Declaration

The work presented in this thesis is based on the research that I have carried out at the Department of Physics, University of Oxford between October 2017 and December 2021 under the supervision of Prof. Suzanne Aigrain. My research was funded by the UK Science and Technology Facilities Council (STFC) under Grant Code ST/N504233/1, studentship no. 1947725.

I declare that no part of this thesis has been submitted in support of another degree, diploma or other qualification at the University of Oxford or any other university.

Chapters 1, 2, and 3 of this thesis present the introduction, context and background material that was at the base of the work presented in this thesis. Chapters 4, 5, and 6 form the core of this thesis and are primarily my own work. Throughout the thesis I use first person singular ('I') to present work that was carried out independently, and first person plural ('We') to describe work that I did in collaboration with others.

Chapters 4 and 6 are entirely my own work and chapter 5 was done in collaboration with others.

Chapter 4 is based on the paper entitled *One year of AU Mic with HARPS: I - measuring the masses of the two transiting planets* (Zicher et al., 2022). The work presented was led by me, in collaboration with a number of co-authors. Contributions by author: Norbert Zicher: lead author, principal investigator (PI) for observations, RV analysis & modelling, and interpretation. Oscar Barragán: RV analysis, dynamical analysis, robustness testing. Baptiste Klein: flare analysis, composition and evolution interpretation. Suzanne Aigrain: principal investigator (PI) for observations, modelling recommendations and interpretation. James Owen: composition and evolution analysis and interpretation. Laurel Kaye: TTV analysis. Louise Dyregaard: data reduction with DRS. Davide Gandolfi & Luisa Serrano: data reduction with `SERVAL` and `HARPS-TERRA`.

Chapter 5 was first conceptually developed at IPAG (Institut de Planétologie et d'Astrophysique de Grenoble) between February 2019 and May 2019 when I was visiting Prof. Anne-Marie Lagrange and her group in order to collaborate on the study of young stars. This work was funded by the UK Science and Technology Facilities Council (STFC) long term attachment (LTA) grant.

Contents

List of Figures

List of Tables

List of Abbreviations & Acronyms

1-D, 2-D . . . One- or two-dimensional, referring in this thesis to spatial dimensions.

AIC . . . . . Akaike Information Criterion.

AU Mic . . . . AU Microscopii.

BIC . . . . . Bayesian Information Criterion.

Bis-span . . . Bisector-span.

BIS . . . . . Bisector-inverse-slope.

BJD . . . . . Barycentric Julian Date.

BGLS . . . . . Bayesian generalised Lomb-Scargle.

BRaVe . . . . Bayesian RAdial VElocity package.

CCF . . . . . Cross-correlation function.

DRS . . . . . (HARPS/HARPS-N/ESPRESSO) Data Reduction Software.

DTFT . . . . . Discrete-time Fourier transform.

DLW . . . . . Differential-line-width.

EPRV . . . . . Extreme precision radial velocity.

ESO . . . . . European Southern Observatory.

ESPRESSO . Echelle SPectrograph for Rocky Exoplanets and Stable Spectroscopic Observations.

EXPRES . . . EXtreme PREcision Spectrograph.

FAP . . . . . False alarm probability.

FWHM . . . . Full width at half maximum.

GLS . . . . . Generalised Lomb-Scargle.

GP . . . . . Gaussian process.

H_α . . . . . Hydrogen-alpha.

HARPS . . . . High Accuracy Radial Velocity Planet Searcher.

LACP . . . . . Linear activity-corrected periodogram.

(G)LSP . . . . (Generalised) Lomb-Scargle periodogram.

(GdG)LSP . . (Gaussian process G dG) Lomb-Scargle periodogram.

MAP . . . . . Maximum *a posteriori*.

ML . . . . . Maximum-likelihood.

MCMC . . . . Markov-chain Monte Carlo.

PI . . . . . Principal Investigator.

QP . . . . . Quasi-periodic.

RMS . . . . . Root-mean-square.

RV . . . . . Radial velocity.

SE . . . . . Squared exponential.

$S_{\rm HK}$ . . . . . Calcium H & K line emission metric.

SNR . . . . . Signal-to-noise ratio.

TESS . . . . . Transiting Exoplanet Survey Satellite.

WF . . . . . Window-function.

Units

This work uses the unit conventions described by Prša et al. (2016, Resolution B3 of the IAU general assembly of 2015).

- Solar radius, $R_\odot = 6.957 \times 10^{10}\,\mathrm{cm}$.
- Solar mass, $M_\odot = 1.988 \times 10^{33}\,\mathrm{g}$.
- Jupiter radius, $1R_\mathrm{J} = 7.1492 \times 10^{9}\,\mathrm{cm}$.
- Jupiter mass, $1M_\mathrm{J} = 1.898 \times 10^{30}\,\mathrm{g}$.
- Earth radius, $1R_\oplus = 6.3781 \times 10^{8}\,\mathrm{cm}$.
- Earth mass, $1M_\oplus = 5.971 \times 10^{27}\,\mathrm{g}$.
- Astronomical Unit, $\mathrm{AU} = 1.4960 \times 10^{13}\,\mathrm{cm}$.
- Gravitational constant, $\mathrm{G} = 6.67408 \times 10^{8}\,\mathrm{cm^3\,g^{-1}\,s^{-2}}$.

Extraordinary claims require extraordinary evidence.

— Carl Sagan

1 A personal introduction

Contents

1.1 Context and motivation

The discovery of exoplanets is potentially one of the biggest scientific revolutions in history. It had major implications on humanity's perception of our place in the universe. What was once believed only by a few (the existence of exoplanets), soon came to be the norm. Before the massive explosion in discovered exoplanets, we had little to no idea if the Solar system was unique. The pace at which the field expanded is simply astonishing. In 30 years we went from thinking that Earth could be unique, to now knowing that statistically there is **at least one** planet for every star in the universe. The variety of discovered planets was inconceivable to most of mankind. We are nonetheless one step closer to being able to answer the profound question about the origins of life.

Even with the close to 5000 confirmed exoplanets, a lot of work remains to be done in the field. We are yet to discover Earth analogues that can be studied in detail[1]. Unfortunately, the intrinsic signals of stars induced by stellar activity can induce RV variations that hide or mimic planetary signals. This makes finding these planets extremely challenging, highlighting the continued need for better tools and methods to correct for stellar variability.

Another area that requires improvement is our understanding of the formation and evolution of planets. For this, we need to be able to characterise young planetary systems, where the initial conditions are still imprinted into the planetary parameters. Although *K2* and *TESS* were able to discover young planets for years, it has only been recently that were able to measure their masses. Even today, there are only a handful of young systems with measured masses.

1.2 Contribution

The work presented in this thesis focuses on the above two points: mitigating stellar activity, extracting precise radial velocities; and measuring the masses of young transiting planets. As such, I have developed an alternative method for extracting precise radial velocities, directly from stellar spectra, measured the masses of 2 young transiting planets, and further developed current techniques for exoplanet detection by introducing 2 extensions to the generalised Lomb-Scargle periodogram, which in turn I use to place detection constraints for long-period planets around AU Mic.

1.3 Thesis structure

This thesis contains two chapters covering the background material, separated into astrophysical background, and statistical and numerical methods respectively. Chapter 2 presents an overview of exoplanetary science in general, formation and evolution as well as the importance of young planets. In addition, it presents the radial velocity method used extensively in this thesis, followed by a discussion

[1]The Kepler mission did find a few planets around Sun-like stars that could be Earth analogues, but they are too far to study in detail

on stellar signals and how we can correct for stellar variability. Chapter 3 covers a general overview of the widely used periodogram approach, followed by an introduction to Gaussian processes (GPs). In addition, this chapter provides a description of the GP framework formalism, used to jointly model the stellar activity indicators and the radial velocities in order to disentangle the magnetic activity induced signals from planet induced variations.

In Chapter 4, I present the results from our year-long intensive monitoring campaign of AU Mic. We measure the masses for the two extremely young transiting planets. This is the only system ($\sim$ 22 Myr) younger than 500 Myr that has mass measurements for relatively low-mass planets[2]. The RV signals of the two planets around AU Mic are around 50 times smaller than the activity signals.

In Chapter 5, I present two extensions to the generalised Lomb-Scargle periodogram, namely the linear activity-corrected periodogram (LACP) and Gaussian process based GdG periodogram. I demonstrate the effectiveness of these models in correcting for activity induced RV variations on simulated datasets. In addition, I presented the detection limits for long period planets ($\geq$ 20 days) around AU Mic.

Chapter 6 presents a Gaussian process based method that I developed for extracting precise radial velocities directly from the stellar spectra, offering an alternative to the traditionally used cross-correlation method. This GP RV extraction method is encoded in my publicly available *python* package called BRAVE that I present in this chapter. I show the benchmarking of this method on simulated synthetic spectra, testing its capabilities and robustness. In addition, I present two applications of this method, first, on the M50 open cluster, followed by CHIRON observations of TOI-813.

Finally, Chapter 7 presents the conclusions and future work.

[2]All the other systems that have similar masses are 600-800 Myr - see K2-100, TOI-1201, TOI-560.

1.4 Personal note

Ever since I can remember, I have been a curious person. I was always asking my parents questions about the universe and the world that surrounds us[3]. I recall sitting in front of the TV as a child, at times for hours, astonished, watching documentaries about the universe and physics. It is something that has fuelled my curiosity for many years to come.

My first encounter with exoplanets came at the University of Chicago where I took a class by Daniel Fabrycky. I was instantly hooked. The idea of discovering and characterising far-away worlds was just too exciting to resist[4]. This was the catalyst that eventually led me to pursuing a PhD in exoplanets. Although the road, at times, has not been easy, I wouldn't want to change it. It made the PhD a unique experience, from which I have learnt a tremendous amount. It often involved going back and forth between projects, making progress here and there, whilst discovering something new. As such, the topics presented in this thesis represent the result of numerous iterations and are not presented in chronological order.

[3] At some point they got tired of me and told me to go out into the world and find the answers myself, and so I did.

[4] And of course potentially finding aliens! What can be more exciting than that?

The good thing about science is that it's true whether or not you believe in it.

— Neil deGrasse Tyson (2014)

2 Astrophysical background

Contents

This chapter aims to provide an overview of background materials, that are pertinent to the core focus areas of this thesis. A brief history and overview of exoplanetary science will be covered. First, a concise summary of detection methods is described, focusing specifically on Doppler spectroscopy (radial velocity) which forms the fundamental topic of the thesis. Followed by a discussion around stellar variability and its effects on exoplanet detection and characterisation is presented. In addition, a short sketch about planet formation and evolution is set out together with an examination of young planets and their scientific significance. This discourse seeks to supply context and colour to latter chapters and analysis by providing a

foundation of background knowledge and literature that currently exists.

Considering the broad extent of exoplanetary science, it is inevitable that some subjects may be omitted or not covered in detail. Thankfully, there are countless resources available, such as excellent books and reviews paper that cover the full breadth of current research. I refer the interested reader to the following materials that I have found the most useful.

Exoplanetary science in general. In my opinion the books that i have found to be most useful for a general review of all major research topics in modern exoplanetary science are *The Exoplanet Handbook* (Perryman, 2018) and *Exoplanets* (Seager, 2010), which has chapters contributed by 34 authors. A particularly relevant resource for this thesis is the chapter on Radial Velocity (Lovis & Fischer, 2010). Both of these books cover topics ranging from instrumentation and detection methods to planet formation, interiors and atmospheres, dynamics, and more. For exoplanetary atmospheres I recommend *Exoplanetary Atmospheres: Theoretical Concepts and Foundations* (Heng, 2017). An excellent review on planet formation and evolution is *Formation, Orbital and Internal Evolutions of Young Planetary Systems* by Baruteau et al. (2016). Two vital online sources that are regularly updated are the NASA Exoplanet Archive and Exoplanet.eu. They provide catalogues of all published exoplanets together with all the relevant literature for each exoplanet, as well as visualisation tools. In addition to all these helpful written sources, I can only recommend the interested reader to check out the publicly available videos published by the Sagan Summer Workshop. These cover all the topics of exoplanetary science and are presented by world leading experts.

Stellar astrophysics. *An Introduction to Modern Astrophysics* by Carroll & Ostlie (2006) offers a practical introduction stellar structure and evolution. For a detailed exploration of the origin, evolution and effects of magnetic fields I refer the reader to *Solar and Stellar Magnetic Activity* (Schrijver & Zwaan, 2000). An addition source of excellent review papers is published by the Evry Schatzman School.

Statistics and numerical methods. *Bayes in the sky: Bayesian inference and model selection in cosmology* (Trotta, 2008) gives a great introduction to statistics

and its applications in astrophysics. For modelling, inference and signal processing, I recommend the book *Pattern Recognition and Machine Learning* (Bishop, 2006) and the review article *Data analysis recipes: Fitting a model to data* (Hogg et al., 2010). When it comes to numerical methods the best source is almost always *Numerical Recipes: The Art of Scientific Computing* (Press, 2007). In the context of Gaussian processes, my go to book is always *Gaussian Processes for Machine Learning* by Rasmussen & Williams (2006).

2.1 Exoplanets

What can be defined as a 'planet'? Since 2006, the International Astronomical Union (IAU) has defined a planet (in the Solar System) as being a celestial body that fulfils the following requirements[1]:

1. it orbits around the Sun
2. it has sufficient mass to assume a hydrostatic equilibrium (a spherical shape)
3. it has 'cleared the neighbourhood' around its orbit (i.e. the body becoming dominant gravitationally, resulting in no other bodies of comparable size other than its natural satellites or those otherwise under its gravitational influence.)

There are eight planets in the Solar System that meet the above requirements and can therefore be classified as planets; Mercury, Venus, Mars, Jupiter, Saturn, Uranus, Neptune and of course Earth. The first five aforementioned planets are known as the 'naked-eye planets', due to their brightness, resulting in the ability for them to be seen from Earth. The latter two planets (Uranus and Neptune) were first discovered by telescope. A non-satellite body that fulfils the first two requirements of the IAU definition of a planet, is classified as a 'dwarf planet' (e.g. Pluto).

To date, there is no formally accepted definition of exoplanets. The IAU has adopted only a working definition of an exoplanet, subject to change based on new knowledge and information. The current official working definition of an

[1]Refer to https://www.iau.org/static/resolutions/Resolution_GA26-5-6.pdf

exoplanet, as amended by IAU Commission F2: Exoplanets and the Solar System in August 2018, is as follows:

- Objects with true masses below the limiting mass for thermonuclear fusion of deuterium (currently calculated to be 13 Jupiter masses for objects of solar metallicity) that orbit stars, brown dwarfs or stellar remnants and that have a mass ratio with the central object below the L4/L5 instability ($M/M_{central} < \frac{2}{(25+\sqrt{621})} \approx \frac{1}{25}$)
- The minimum mass/size required for an extrasolar object to be considered a planet should be the same as that used in our Solar System.

For a field that some might argue, did not formally exist 30 years ago, exoplanetary science has grown immensely and was recognised with the award of the 2019 Nobel Prize in Physics (Michel Mayor and Didier Queloz), marking a significant milestone for the exoplanet community.

2.1.1 A brief history

The roots of the conceptual idea of exoplanets can be traced back to the metaphysical argument of cosmic pluralism (i.e. the belief that there are numerous 'worlds' out there, similar to our own), as early as the time of Anaximander (c. 610-564 BCE). The debate of cosmic pluralism has continued, in a variety of forms, until the modern era. A key turning point in this debate came around during the 16th century, as part of the Copernican revolution, stemming from Nicolaus Copernicus, who formulated a heliocentric model of the universe (Copernicus, 1543). In addition to this, the telescope provided evidence that celestial bodies like the Moon and the solar system planets were all worlds in much the same way Earth was, and that they potentially might be inhabitable.

These two key discoveries suggested that that the Earth was not fundamentally unique in the cosmos. Principal advocates for Copernicus' model included Kepler and Galileo, although the majority at the time, continued to subscribe to geocentric models. The next evolution in the Copernican model came from Giordano Bruno,

who proposed that 'fixed stars' were in fact other suns, surrounded by their own planets, and that these planets may harbour life of their own. Moreover, Bruno also insisted the universe to be infinite and could therefore possess no 'center'.

Fast forward some centuries, the advancement in science and technology has allowed us to seek answers to those questions surrounding worlds beyond our own. Exoplanetary science, like many other fields, also experienced its own setbacks. The earliest claims of exoplanet detection were made in the 19th century, by William Jacob (Jacob, 1855). In 1855, he claimed that he saw deviations in the orbits within the nearby 70 Ophiuchi binary star system. Thomas See's work (See, 1895) which surfaced later that century also appeared to confirm this, with a proposed 36 year orbital period of a dark object. These have since been disproved, showing that they were false positives. However, this was a clear sign within the field of science, that exoplanets, and more specifically the detection of them, were finally getting the attention they deserved.

The next turning point came nearly a century later, when in 1952 Otto Struve proposed a spectroscopic survey to detect the radial velocity RV) variations induced by planetary companions. Struve showed that high precision stellar radial velocity observations could be used to search for planets orbiting nearby stars. He made the controversial assertion that Jupiter-like planets could reside as close as 0.02 AU from their host stars. In addition to this, he also highlighted that if such close-in planets were ten times the mass of our Jupiter, the reflex stellar velocity for an edge-on orbit would be about 0.2 $\mathrm{km\,s^{-1}}$ and detectable with 1950's Doppler precision (Struve, 1952). Struve's proposal and work catalysed several RV monitoring surveys over the next decades, including those of Campbell and Walker (Campbell et al., 1988), Latham et al.(1989), and Marcy and Butler (1992).

Unfortunately, the first few spectroscopic surveys proved to be unsuccessful in detecting exoplanets, in part due to the technological limitations. However, the wait was finally over, when in 1992, radio astronomers Aleksander Wolszczan and Dale Frail announced the discovery of two rocky planets orbiting PSR B1 1257+12, a pulsar in the Virgo constellation. They used pulsar timing variations to detect

these. A year later, the planet PSR B1620-26 b was discovered. It is orbiting a binary system composed of a pulsar and a white dwarf. This was the first planet found in a stellar cluster (globular cluster M4) (Wolszczan & Frail, 1992). This marked a major milestone in the development of exoplanetary science[2]. Granted that these planets were orbiting stellar remnants rather than a main sequence star.

Finally, the long wait for spectroscopic surveys came to an end in 1995, when Didier Queloz and Michel Mayor announced their discovery of the first planet orbiting 51 Pegasi (Mayor & Queloz, 1995). This was a major breakthrough as the host star is a Sun-like (G5V) star, demonstrating without a doubt that planets exist around main-sequence stars. The presence of the hot Jupiter was inferred from observations with the ELODIE spectrograph (Baranne et al., 1996), showing periodic variations in the star's radial velocity. This discovery confirmed what Struve had presented back in 1952. This was finally the moment that exoplanetary science had been waiting for, catalysing the trajectory of science in this space for many years to come.

2.1.2 Detection methods

Within exoplanetary science, there are a variety of widely used detection methods, each with their advantages and disadvantages. To date, there are 4947 exoplanets known, of which an overwhelming majority (4481), have been discovered using RV and transit methods[3]. In contrast to RV discoveries which very quickly came to dominate exoplanet detections in the early years, the transit method had a much slower start, with the first transit observations taking place in 1999 of HD 209458 b (Henry et al., 1999; Charbonneau et al., 2000). The first exoplanet 'discovered' by the transit method occured only in 2002, when OGLETR-56 b was accidentally discovered as part of a microlensing campaign (Udalski et al., 2002). Nonetheless, the transit method is now the most successful method to detect exoplanets, in part due to the immense success of the *Kepler* (Borucki et al., 2008) and *K2* (Howell et al., 2014) missions. A legacy which inspired many more missions, including *TESS* (Ricker et al., 2015) and the upcoming *PLATO* (Rauer et al., 2014) mission.

[2]For a detailed timeline of events please refer to NASA's historic timeline here.
[3]As of January 26, 2022 - Exoplanet.eu

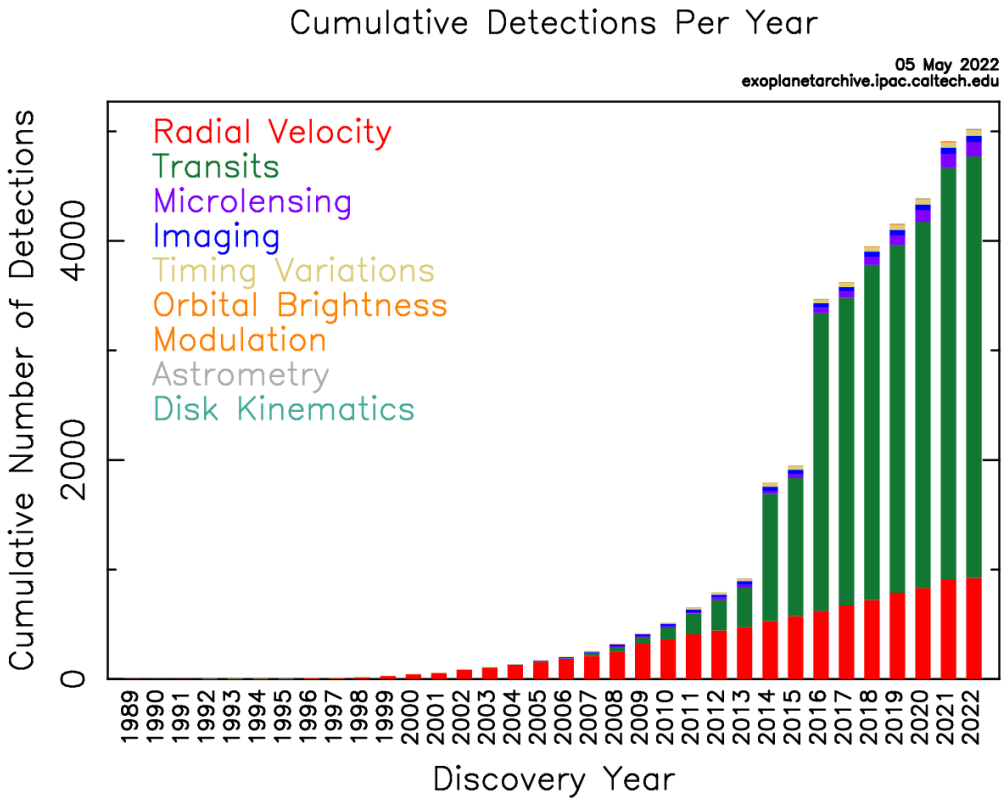

Figure 2.1: Detected exoplanets over the years colour coded by detection method. Image credit: NASA Exoplanet Archive.

Other less frequently 'successful' methods, but nonetheless crucial (complementing each other), include direct imaging (Marois et al., 2008; Lagrange et al., 2009), pulsar timing (Wolszczan & Frail, 1992), astrometry (Benedict et al., 2002) and microlensing (Bond et al., 2004). The cumulative distribution of exoplanets detected by the various methods as a function of year is shown in Figure 2.1.

The focus of this thesis is on Doppler spectroscopy (radial velocity) and as such it is presented in more detail in Section 2.3. However, for context and completeness, a brief overview of transit photometry, radial velocity and direct imaging is presented below.

Transit photometry

By definition an eclipse is when a celestial body is obscured by a second one. In general, when talking about two astronomical objects, there is a primary eclipse and a secondary eclipse. The primary eclipse (also referred to as a transit in the

case of exoplanets) occurs when the less massive of the two objects passes in front of the larger object, periodically blocking some of the light. The secondary eclipse is when the less massive object goes behind the primary target.

The fundamental idea behind transit photometry, or the transit method, is to observe these periodic dips in luminosity (caused by an exoplanet transiting between Earth and the host star). It is important to note, that this requires the orbital inclination to be close to 90°. Assuming that planetary orbits are randomly distributed, then the probability of a transit to occur at semi-major axis a scales as (Cameron, 2016):

$$0.0046(R_\star/R_\odot)(1\mathrm{AU}/a)$$

where $R_\star$ is the host star's radius in solar units (see Units at the beginning of the thesis, page xix). This means that the probability of observing the transit of an Earth analogue around a Sun-like star is 0.46%, and the probability of observing a planet like Jupiter is only 0.09%. According to Cameron (2016), the probability of observing short period planets ($P < 10d$) is in the $2 - 10\%$ range. To counteract the low geometric probability of transits, modern transit searches observe a large number of targets simultaneously. The depth and duration of the transit can be used to infer the planet-to-star radius ratio $R_\mathrm{p}/R_\star$ and the impact parameter b which quantifies the distance at which the transit occurs relative to the star's equator[4]. The period between successive transits determines the planet's orbital period P. The transit depth scales as:

$$(\frac{R_p}{R_*})^2$$

and as such the transit depth of Jupiter around the Sun is $\sim 1\%$. An advantage of studying transiting exoplanets is that if the stellar radius is known, then transits provide us with the planet radius, which is one of the fundamental parameters required to characterise these planets. Furthermore, the transit constraints the

[4]The transit duration scales as $\mathrm{T_{duration}} = \frac{P}{\pi}\sin^{-1}\left(\frac{\sqrt{(R_*+R_P)^2-(bR_*)^2}}{a}\right)$, where P is the period, and a is the semi-major axis. The impact parameter is given by $b = \frac{a\cos i}{R_*}$.

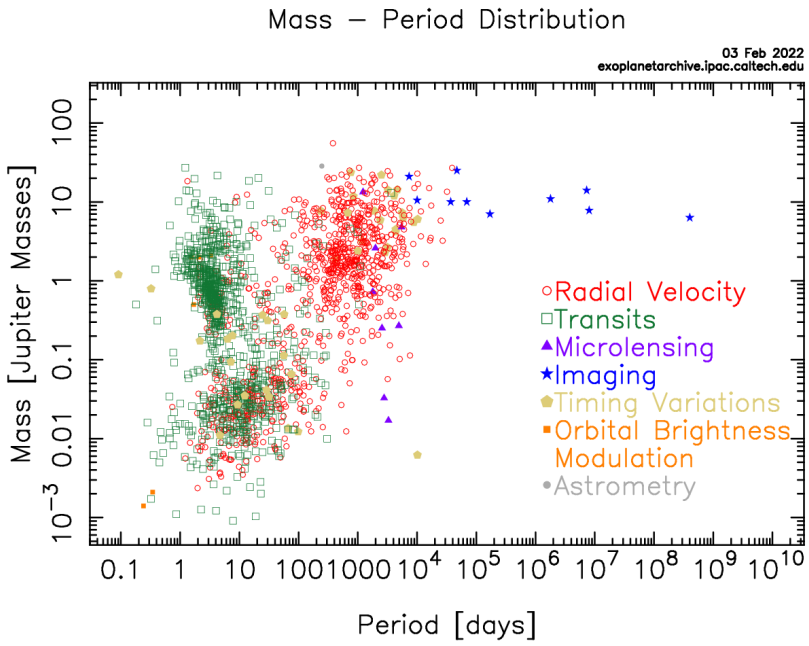

Figure 2.2: Mass-Period distribution of confirmed exoplanets, colour coded by detection method. Image credit: NASA Exoplanet Archive.

orbital inclination and breaks the $M \sin i$ degeneracy in RV. Another advantage is that it allows to study the atmospheres of these worlds by studying the light that passes through the upper atmosphere of the planet, or by studying the difference of the observed light between the secondary eclipse (when the planet is blocked by the star) and out-of-transit (Heng, 2017). Some of the disadvantages include that it requires observing a large number of stars, the risk of false positives due to stellar variability and the lack of mass determination of the planets[5] (Seager, 2010). I show the currently known transiting planets (green) which have mass measurements from other methods in Figure 2.2.

Radial Velocity method

A star that is orbited by a planet (or multiple) will move around in its own small orbit, as a response to the planet's gravity. This results in small, but detectable variations in the speed with which the star either moves towards or away from Earth. Using this information, the RV method is based on distinguishing these tiny

[5]With the exception of multi-transiting-planet systems, where transit-timing-variations (TTVs) can be used to constrain the masses.

but recurring Doppler shifts in the light emitted by these stars that are affected by the gravitational force of a surrounding orbiting body, e.g. an exoplanet. The main advantage of the RV method is its ability to constrain the mass of a planet: if the inclination angle i of a planet's orbital plane relative to the sky is unknown, the RV method is able to yield the planet's minimum mass, $m \sin i$. However, in the case of follow up observations for a transiting planet, the orbital inclination i is well constrained and it provides the *true* mass of a planet. The planet mass is the other fundamental parameter required to characterise these exotic worlds. The mass and radius of a planet provide clues about its composition, atmosphere (and scale height) and formation history. As such, radial velocity is an indispensable method not only to discover planets, but also to confirm the planetary nature of candidates from other techniques (Lovis & Fischer, 2010). Possibly the biggest disadvantage of Doppler spectroscopy is the fundamental stellar variability, which hinders our ability to study planets using RV data. Other disadvantages of high resolution spectroscopic observations include requiring a bright target, as well as the fact that only one star can be observer at a time.

Direct imaging

In the case of direct imaging the presence of a planet is inferred from its emitted thermal light (with a fractional contribution from reflected light). This method consists of using a coronagraph to block out the direct light from the host star, so that nearby objects can be resolved. The two biggest challenges are that the contrast ratio is usually $\sim 10^6$ in the best case scenarios (Lagrange et al., 2009), and the angular/spatial separation in these systems. As such, direct imaging is mostly sensitive to young massive planets that still retained the thermal heat from formation and are usually found in face-on orbits at large separations (Traub & Oppenheimer, 2010). Some of the currently imaged objects (Bowler, 2016) are shown in Figure 2.3, together with 'hot-start'[6] formation and evolution models

[6]The two competing formation theories are core-accretion and disc instability. In the case of core-accretion, it is believed that once a large enough core is formed $\sim 10 M_\oplus$, gas accretion can occur very fast. As such, the surrounding gas flows inwards and forms an accretion shock near the planetary boundary. This shock is believed to be luminous and allows for the falling gas to

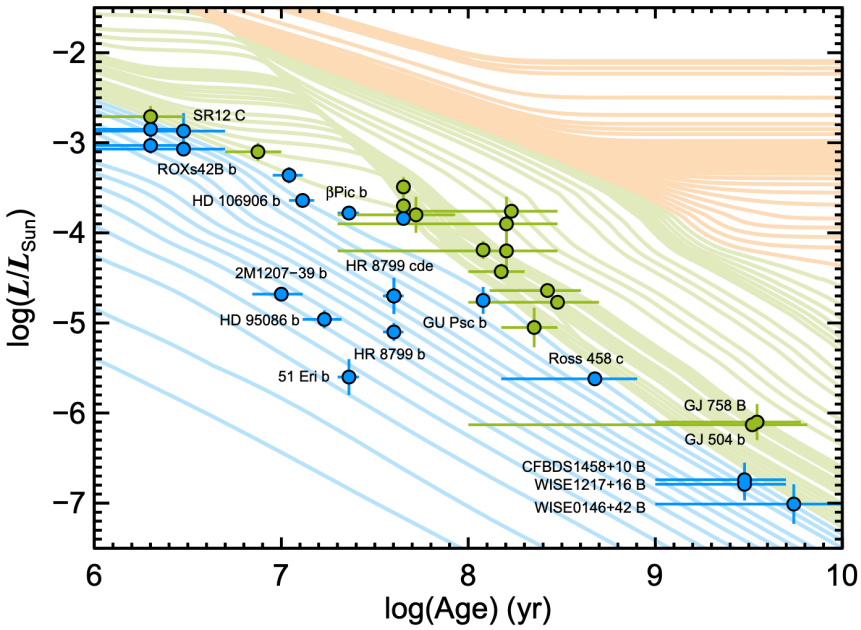

Figure 2.3: A sample of imaged objects in the brown dwarf (green) and planetary (blue) mass regimes for which the age and luminosity is known. It is worth noting that many of these objects lie close to the deuterium fusing limit, with only a few objects clearly in the planetary-mass regime. 'Hot-start' evolutionary models from Burrows et al. (1997) are shown with orange ($> 80 M_{Jupiter}$), green ($14 - 80 M_{Jupiter}$) and blue ($< 14 M_{Jupiter}$) tracks. Figure from Bowler (2016).

from Burrows et al. (1997). This figure also highlights that young planets cool and contract very fast. In the case of imaged planets is is essential to understand the formation and evolution processes involved (see the next section for an overview).

The period-mass diagram of confirmed exoplanets is shown in Figure 2.2, colour-coded by detection method. Note that the mass of transiting planets is provided by follow-up observations using RVs (or TTVs in some cases). This figure highlights the intrinsic biases (limitations) of each method, how they complement each other and how it is necessary to combine them to obtain the full picture. Planets discovered by photometry (shown in green) tend to be on short orbits due to the low geometric probability of transits, planets discovered by RVs tend to have bigger masses due to the dependence of the induced Doppler variations on the planetary mass, whilst imaged planets (blue) are on long period orbits and are more massive.

radiate away its heat energy. Therefore, core accretion is sometimes referred to as a "cold start" mechanism. By contrast, in the case of disc instability, the collapse leads the gas to retain a larger amount of its initial entropy, leading to a "hot start" scenario.

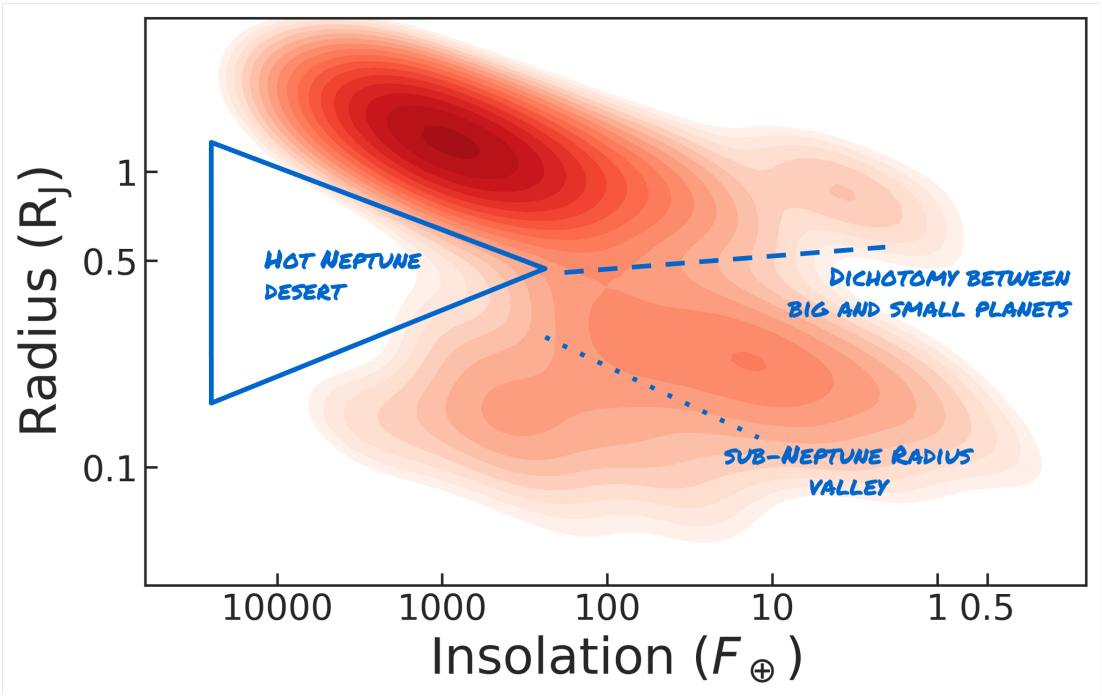

Figure 2.4: Figure showing planet population contours from currently confirmed planets. In this figure the x-axis is the stellar insolation of the observed planet (related to semi-major axis) against the observed planetary radius in units of $R_{Jupiter}$. There are three regions highlighted where a lack of planets is observed. The 'hot Neptune desert' (on the left) is where no Neptune-sized planets orbiting close to the host star are observed. The second observed separation is the dichotomy between big and small planets are larger separations from the host star. Finally the 'sub-Neptune radius valley', also called the evaporation valley is where we observe a bi-modal distribution in the radii of smaller planets between $1 - 1.8R_\oplus$ and $1.8 - 4R_\oplus$. Figure by Oscar Barragán.

2.1.3 Formation and evolution

In order to draw rational conclusions about the detected planets and decipher planet populations, it is necessary to understand the formation and evolution process. I note, that this process also happens vice versa. Observations prompt theorists to refine the current theories to be able to explain the observations. This is especially important at young ages as planets evolve most rapidly during the first few Myrs. In this section I aim to provide an overview of the current state of the field (Baruteau et al., 2016), noting that this is an active area of research in which I am not an expert as my PhD focuses on providing observational data to validate and refine these theories.

The current planet population is shown in Figure 2.4, plotting planet insolation

against planetary radius. This plot shows the planet population contours and highlights three regions of interest, where we observe a lack of planets. The three regions are the 'hot Neptune desert' (a lack of Neptune sized planets at high insolation - this is due to the effects of photoevaporation), a valley between big and small planets at larger separations (smaller insolation) and the 'evaporation valley' (Owen & Wu, 2017). In the following sections I provide the current theories that aim to explain these observations.

Formation

Planet formation is believed to begin in protoplanetary discs with the growth of dusts grains and formation of planetesimals. Unfortunately, the formation of planetesimals is poorly understood and as such most studies about planet formation start at a later phase (Baruteau et al., 2016). Most theories make the assumption that planetesimals have already formed and focus on the growth of planetesimals into protoplanets. When protoplanets grow to a moderately high mass before the disc dispersion, they become the cores of giant planets and accrete the surrounding gas. This is called the 'core accretion' model. For an in-depth description of planetasimal growth I recommend the book *Astrophysics of Planet Formation* by Armitage (2010). The currently adopted theory is that of pebble accretion, in which mm and cm-sized grains collide to form bigger and bigger planetesimals, eventually forming protoplanets, which in turn will become the rocky planets if the disc dispersed, or can grow into gas giants.

Evolution

When it comes to evolution an important consideration is the initial condition of the newly formed planet. In the literature there is a distinction between 'cold-start' and 'hot-start' (Burrows et al., 1997; Spiegel & Burrows, 2012), which relate to the temperature of the planet just after formation. As the name suggests, 'cold-start' assumes that the planet was able to dissipate a large amount of heat from formation, whilst in the case of 'hot-start' the planet is still at a high temperature. This has major implications for the starting radius of the planet and its evolution. Spiegel &

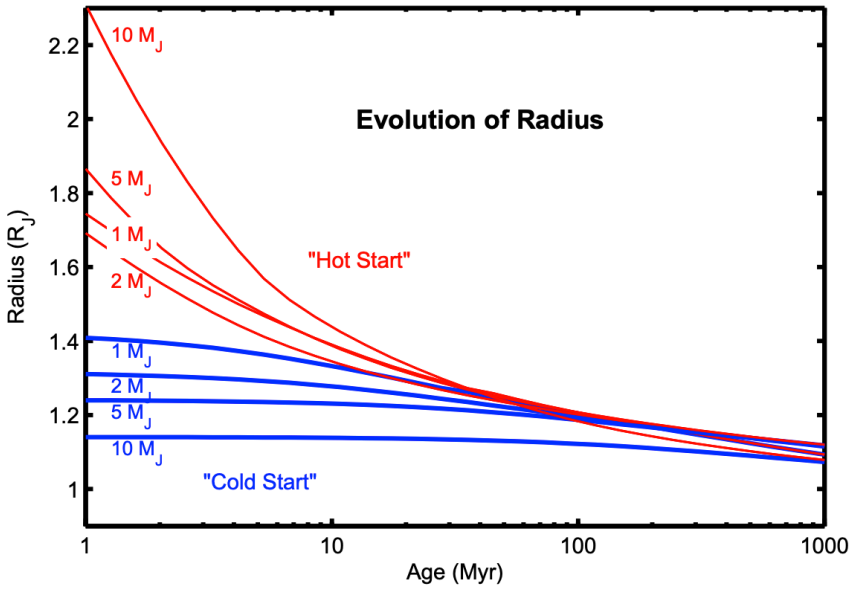

Figure 2.5: The figure shows the planetary radius contraction for massive planets in the range of 1, 2, 5, and 10 $M_{Jupiter}$ for a 'hot-start' (red) and 'cold-start' (blue) scenario. It can be noticed that there are major differences at early times between the two scenarios. Figure from Spiegel & Burrows (2012).

Burrows (2012) has shown that the difference in radius between a 'hot-start' and 'cold-start' objects "is dramatic at early times", especially in the case of massive planets (see Figure 2.5). During the first few Myrs these massive planets are contracting rapidly and the two formation scenarios can easily be separated. At later times (100 Myrs), both of these scenarios converge to the same radius and as such the imprints of the initial conditions can no longer be distinguished.

In the case of low-mass planets Owen (2020) has shown that the planet radius contraction is dependent on the Kelvin-Helmholtz contraction timescale (see Figure 2.6). In addition, Owen (2020) states that there is a degeneracy between the internal entropy and envelope mass fraction and thus they cannot be constrained, except for very specific cases. One such example might be AU Mic b due to its young age ($\sim$ 22 Myr), if we were to constrain its mass beyond what we have been able to do so far (see Chapter 4).

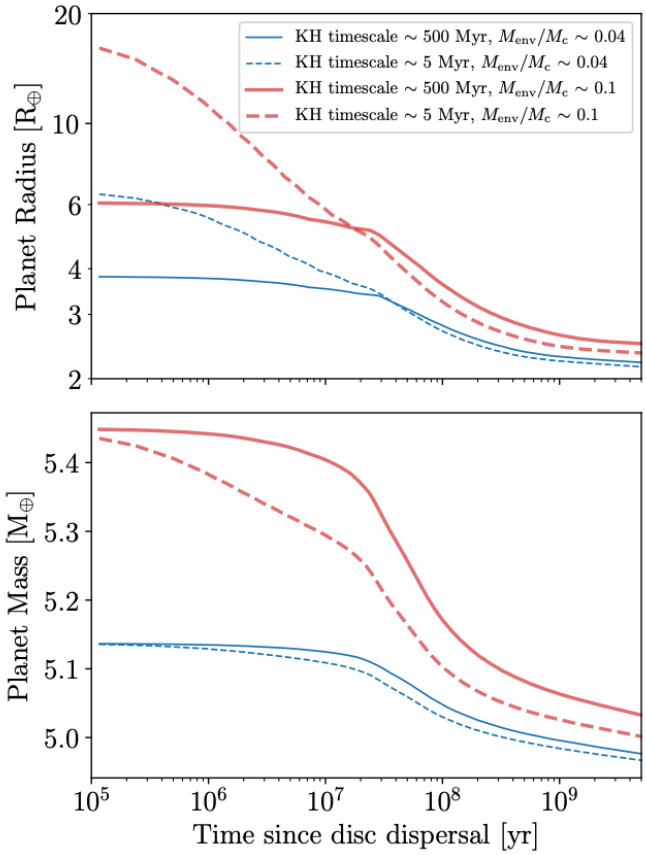

Figure 2.6: The figure shows the radius (top panel) and total mass (bottom panel) evolution for a planet with core mass of $\sim 5\ M_\oplus$ located at 0.1 AU around a Sun-like star. The solid and dashed lines show the cases with Kelvin-Helmholtz contraction timescales of 500 and 5 Myr respectively. The red lines show the planet with initial envelope fraction ($M_{envelope}/M_{core}$) of 0.1, and blue lines show the planet with an envelope fraction of 0.04. Figure from Owen (2020).

Migration

In the case of planet migration, there are three different scenarios that are separated in the literature and these scenarios depend on the mass of the planet (Baruteau et al., 2016). In the case of low-mass planets, the migration process is called *type I migration*. In the case of massive planets that are able to clear the neighbourhood around their orbit and open a gap in the disc, the migration process is called *type II migration* and finally for planet masses similar to Saturn the migration process is called *type III migration*. In all three cases, the migration is due to the interaction between the planet and the protoplanetary disc. This interaction leads to a wake

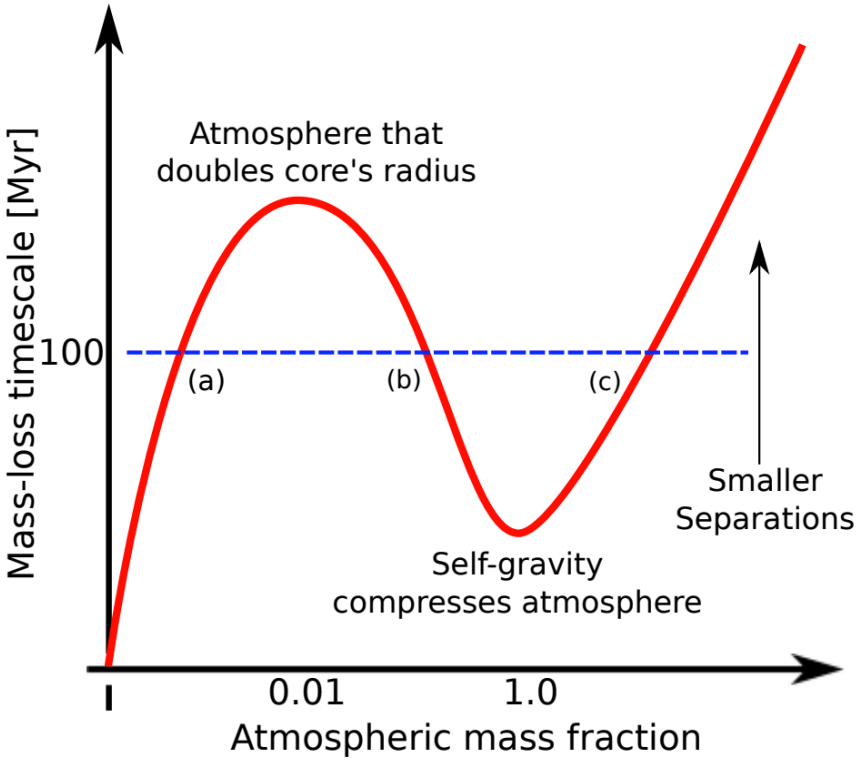

Figure 2.7: The dependence of the mass-loss timescale on the atmospheric mass fraction for a planet with fixed core mass. In blue dashed line is a fixed timescale ($\sim$ 100 Myr) for mass-loss to occur. This timescale moves up in the diagram as the planet moves to smaller separations or the core mass is reduced. Figure from Owen (2019).

torque and corotation torque. The planet mass determines the balance of these forces and as such the type of migration. For details see Baruteau et al. (2016).

A different mechanism than can lead to migration and/or eccentricity excitation is the Kozai-Lidov mechanism (Shevchenko, 2017). This is a dynamical interaction by which a binary system is perturbed by a distant third body, which can drive initially near-circular orbits to high eccentricities. Orbital circularisation or migration can also occur due to the interaction of gravitational tides (Bolmont & Mathis, 2016).

Observed planet populations explained

Owen (2019) argues that the origin of both the 'hot Neptune desert' and 'evaporation valley' can be explained by the dependence of the mass-loss timescale on the atmospheric mass fraction. This relationship is shown in Figure 2.7 as described in Owen & Wu (2017). The key point is that as it can be seen in the figure, this function

has two turning points, depending on the envelope mass fraction ($M_{envelope}/M_{core}$). The first turning point (between (a) and (b) in the figure) is when the radius of the atmosphere is big enough to double the core's radius (usually when the mass of the atmosphere is $\sim 1\%$ of the core mass). In this case, the radius of the planet is mostly controlled by the atmosphere radius and it is rapidly increasing. The energy from the accretion of new material balances the effect of the increasing atmosphere mass. As a result, the mass-loss timescale decreases up to the point where the envelope mass becomes comparable to the core mass and its gravity compresses the atmosphere to an approximately fixed radius. With additional accretion, the mass-loss timescale starts to increase again (marked as (c) in the figure). Any planet with an atmosphere mass that is below the blue dashed line in the figure is unstable to atmospheric mass-loss and will continue to lose its atmosphere until its completely barren or it reaches a stable point. As a consequence, the 'hot Neptune desert' is formed by planets that originally were between (b) and(c) but lost some of their envelope, whilst the 'photo-evaporation valley' is caused by planets residing to the left of point (a) that lose their envelopes completely. In layman terms, the planet population observed is a natural consequence of photoevaporation. In the case of low-mass planets they are just unable to retain their atmospheres leading to a bi-modal distribution. In the case of the hot Neptune desert, we talk about planets which are more strongly irradiated and thus even though they have larger atmospheres to start with (and also larger cores) they still can't hold on to them.

In turn, the dichotomy between small and big planets at larger separations is argued to be explained by run-away core accretion (Raymond, 2015). As such cores that grow to a given size will quickly proceed to grow into gas giants before disc dissipation.

2.2 Planets around young stars

Even though young planets present a unique environment to test and refine the formation and evolution theories, up to 2019 there were no known small planets younger than 1 Gyr (the key timescale at which the initial conditions are still

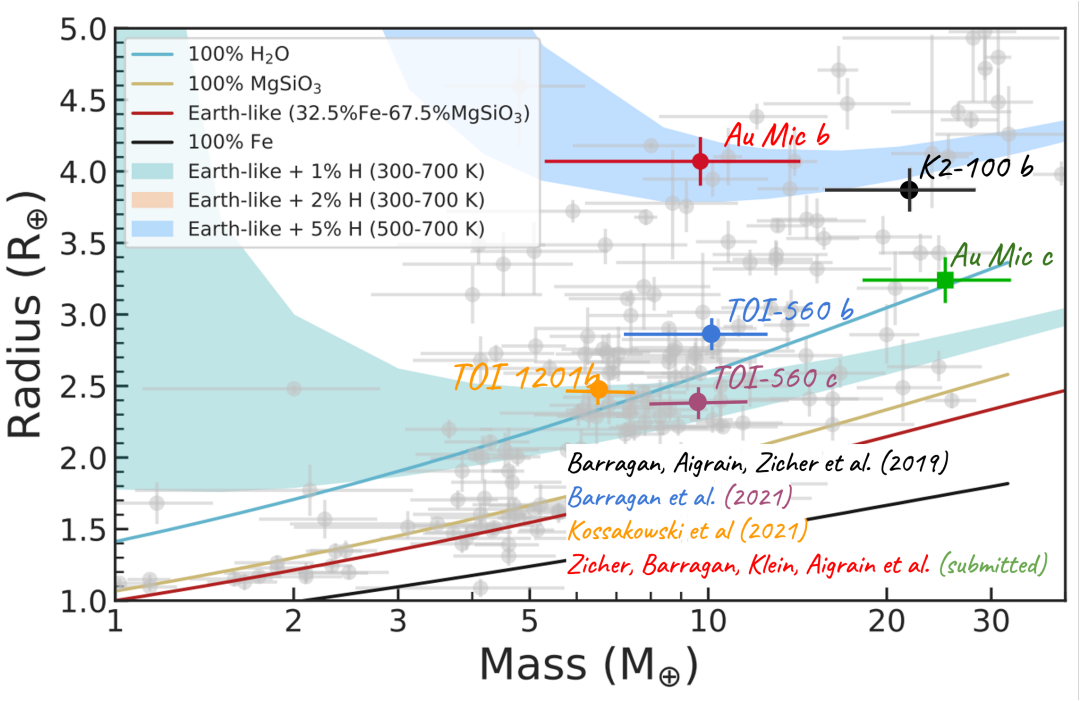

Figure 2.8: Mass-radius diagram showing the known young planets with measured masses as of December 2021. Figure by Oscar Barragán.

imprinted on the planets) with measured masses[7]. This changed when Barragán et al. (2019b) published the results of K2-100 b. Another young system with 2 planets, AU Mic b and c, is presented in Chapter 4, with a discussion about how the results compare to current theoretical predictions. Thankfully in recent years a handful of young planets with known masses have been published (see Figure 2.8).

It is worth noting that while *K2* and *TESS* have been able to detect young small planets in transit for a few years now, it's only very recently that we have been able to measure their masses in RVs, and not without a lot of effort (as highlighted above by the fact that the first measurement came in 2019). Currently there are only two systems with measured masses that are younger than 500 Myr, namely V1298 Tau (Suárez Mascareño et al., 2021) and AU Mic (see Chapter 4). To find out why, we must look to activity signals in RVs - discussed in the remainder of this chapter.

[7]I exclude ultra-hot Jupiters and other large planets from this discussion and focus only on small planets

2.3 The radial velocity method

According to Newton's universal law of gravity, the force acting on two bodies is directly proportional to their masses m_1 and m_2 and inversely proportional to the square of the separation r between their centres. As such, this force is given by

$$F = \frac{\mathrm{G}m_1 m_2}{r^2} \tag{2.1}$$

where $\mathrm{G} = 6.67428 \times 10^{-11}$ m^3 kg^{-1} s^{-2} is the universal gravitational constant. Newton's third law states 'for every force in nature there is an equal and opposite reaction'. As such, when a planet is orbiting a star due to the force of gravity, the star is affected by the gravity of the planet too. This means that the orbital motion of the planet causes a reflex motion in the star around the system's barycentre. This motion results in periodic perturbations to the stars radial velocity, the arrival time of some periodic signal (e.g. pulsar timing), and the angular projection on the sky of the star (astrometry). This thesis focuses on the stellar radial velocities and their observations using a spectrograph.

As stated by Kepler's first law, the closed orbit of a planet around the systems barycentre is defined by an ellipse, which in polar coordinates is:

$$r(t) = \frac{a\,(1 - e^2)}{1 + e\cos\nu(t)} \tag{2.2}$$

where r is the planet-barycentre separation, a is the semi-major axis of the ellipse, e is the eccentricity of the orbit and $\nu(t)$ is the true anomaly. By definition the true anomaly is the angle between the point of periapsis (closest approach) and the position of the planet at any given time t. In general, T_0 is defined as the time when the planet is at the periapsis, but in the case of circular orbits, T_0 is defined as the time of minimum conjunction (midpoint of the transit). The semi-major axis a is the parameter that defines the period of the orbit and is given by Kepler's third law[8]:

$$P^2 = 4\pi^2 a^3 / G\,(M_\star + M_\mathrm{p})$$

[8]Open orbits are described by a parabola or hyperbola

Following the work of Murray & Dermott (2000), we can define two complementary angles called eccentric anomaly ϵ and mean anomaly μ[9], and as such, the true anomaly $\nu(t)$ is given by:

$$\nu = 2\arctan\left[\sqrt{\frac{1+e}{1-e}}\tan\left(\frac{\epsilon}{2}\right)\right] \tag{2.3}$$

where the eccentric anomaly ϵ relates to the mean anomaly μ as:

$$\mu = \epsilon - e\sin(\epsilon) \tag{2.4}$$

and μ only depends on time t and a reference time T_0 which is the periastron passage, such that:

$$\mu = \frac{2\pi}{P}(t - T_0) \tag{2.5}$$

Then, the true anomaly can be expressed in terms of time by solving equations 2.5, 2.4 and 2.3. It is important to note that equation 2.4 cannot be solved analytically for non-zero eccentricities and numerical methods are used. This non-linear equation is usually referred to as Kepler's equation:

$$\epsilon - e\sin(\epsilon) = \frac{2\pi}{P}(t - T_0) \tag{2.6}$$

A Keplerian orbit in 3-D is fully described by 6 orbital elements: a, e, T_0, i, Ω, and ω. The visual representation of all these definitions is shown in Figure 2.9 [10]. The three angular parameters (i, Ω, and ω) relate the projection of the 2-D orbit onto the observed orbit and depend exclusively on the geometrical orientation of the observer (vernal point) relative to the orbit. The orbital inclination i is defined between $0 \leq i \leq \pi$ and represents the inclination of the orbit compared to the reference plane (gray in figure). An inclination of 0 corresponds to a face-on-orbit whilst an inclination of 90° is an edge-on-orbit. By definition, the longitude of the ascending node Ω , specifies the angle between the reference direction and ascending node. The argument of periapsis ω specifies the angle between the periapsis point

[9]The derivation of these angles is beyond the scope of this thesis. I refer the reader to Murray & Dermott (2000) or Perryman (2018) for details.

[10]This Figure is by Lucas Snyder, his personal website is here.

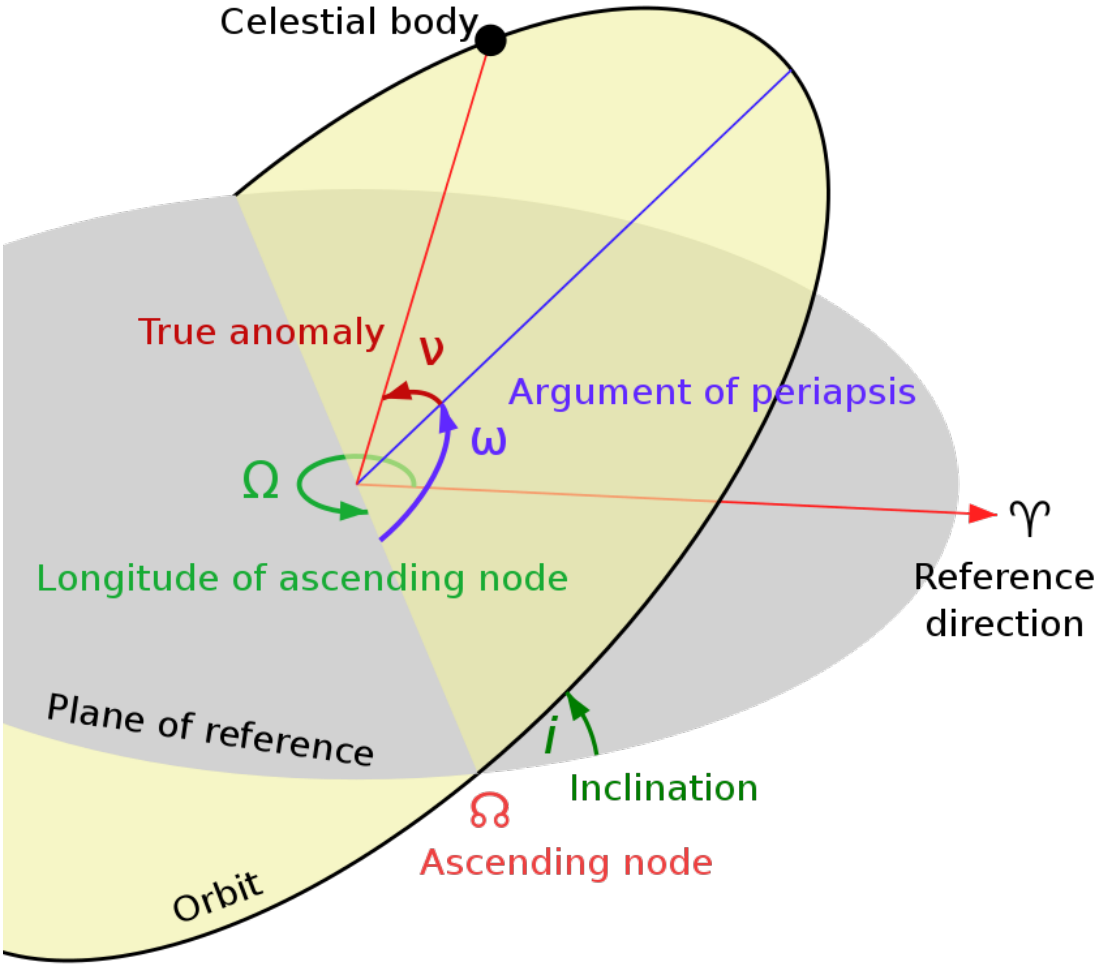

Figure 2.9: Diagram illustrating the various orbital elements. The orbital plane is shown in yellow, while the reference plane is shown in gray. The vernal point (reference direction) is shown pointing towards the observer. Figure by Lucas Snyder.

and the ascending node in the plane of the orbit - measured in the direction of the motion. Because of symmetry, the Keplerian elements for the star will be identical, except for ω which is shifted by π radians, and the semi-major axis a which is reduced by a factor $\mathrm{M_{planet}}/\mathrm{M_*}$.

Then, following the work of Murray & Dermott (2000), the star's radial velocity is defined as:

$$\mathrm{RV}(t) = K[\cos(\omega + \nu(t)) + e\cos\omega] \tag{2.7}$$

where the RV semi-amplitude K, is given by[11]:

$$\mathrm{K} = \frac{1}{\sqrt{1-e^2}} \frac{\mathrm{M_p} \sin \mathrm{i}}{(\mathrm{M_\star} + \mathrm{M_p})^{2/3}} \left(\frac{2\pi G}{P}\right)^{1/3} \tag{2.8}$$

Usually it is safe to assume that $\mathrm{M_p} \ll \mathrm{M_*}$. In the case of Earth, it induces a $\mathrm{K} \approx 9\mathrm{cm\,s^{-1}}$ signal in the Sun.

Then, there are five parameters that are required to fit for a single orbit based on the RV observations: e, P, $\mathrm{T_0}$, ω and $\mathrm{K} = \mathrm{K}(a, e, \mathrm{P}, i, \mathrm{M_\star}, \mathrm{M_P})$. In the case of multiple planets, it can be approximated that the RV signal is the sum of N Keplerian terms defined in equation 2.7 (Perryman, 2018).

2.3.1 Extracting RV's from stellar spectra

Measuring a star's RV is equivalent to determining the tiny wavelength shift in the lines of the stellar spectrum. If a star is moving away with velocity v in the observers reference frame, at an angle θ relative to the line-of-sight (reference plane), then the change in wavelength is $\Delta\lambda := \lambda_{\mathrm{em}} - \lambda_{\mathrm{obs}}$. Which is related to the relativistic Doppler equation by:

$$\lambda_{\mathrm{obs}} = \lambda_{\mathrm{em}} \frac{(1 + \frac{v}{c}\cos\theta)}{\sqrt{1 - (\frac{v}{c})^2}} \tag{2.9}$$

where λ_{em} and λ_{obs} are the emitted and observed wavelengths. Because in general $v \ll c$ and $\theta \ll \frac{\pi}{2}$, the above equation reduces to:

$$\mathrm{RV} = v\cos\theta \approx \left(\frac{\Delta\lambda}{\lambda_{\mathrm{em}}}\right) c \tag{2.10}$$

where positive values indicate a red-shift (object moving away). The relativistic corrections become important at the sub $\mathrm{m\,s^{-1}}$ level (Lindegren & Dravins, 2003).

I will now rewrite the above equation in $\ln\lambda$ space. As such:

$$\mathrm{z} = \frac{\Delta\lambda}{\lambda_{\mathrm{em}}} = \frac{\lambda_{\mathrm{obs}} - \lambda_{\mathrm{em}}}{\lambda_{\mathrm{em}}} = \frac{v}{c} = \frac{1}{\mathrm{R}} \tag{2.11}$$

[11] I prefer the more practical equation: $\mathrm{K} = \frac{28.4329\ \mathrm{m\ s^{-1}}}{\sqrt{1-e^2}} \frac{\mathrm{M_P}\sin\mathrm{i}}{M_{\mathrm{Jup}}} \left(\frac{\mathrm{M_*}+\mathrm{M_P}}{M_\odot}\right)^{-2/3} \left(\frac{1\mathrm{yr}}{\mathrm{P}}\right)^{1/3}$.

where R is the spectral resolution. Then using the Taylor expansion $\ln(1+x) = x - \frac{x^2}{2} + \frac{x^3}{3} - \frac{x^4}{4} + \ldots$, we can write:

$$\ln \lambda_{\rm obs} = \ln \lambda_{\rm em} + \ln(1 + \frac{v}{c}) = \ln \lambda_{\rm em} + \frac{v}{c} \tag{2.12}$$

Because the wavelength shift $\Delta\lambda$ is wavelength dependent, it makes more sense to work in ln space, where the Doppler shift corresponds to an addition (rather than multiplication). This is the formalism that I adopt in Chapter 6, where I extract radial velocities directly from the stellar spectra. This approximation holds for velocities up to < 17 km s^{-1}. For details about the full reasoning and derivation please see Gullberg & Lindegren (2002) or Zechmeister et al. (2018).

In practice, the information about the Doppler shift is encoded in the thousands of absorption and emission lines contained in the spectra of the stars. Traditionally this information is extracted using a cross-correlation of the observed spectrum with a template (binary mask) Baranne et al. (1996). Formally, the cross-correlation between two functions f and g, $(f \star g)(\tau)$ is defined as:

$$(f \star g)(\tau) := \int_{-\infty}^{+\infty} f^*(t) g(t+\tau) dt \tag{2.13}$$

The computed cross-correlation function (CCF), $f \star g$, by definition aims to quantify the similarity between the two functions as a function of lag τ. Then, from the cross-correlation function in velocity space (velocity steps corresponding to lag τ) it is possible to extract the RV shifts between the two spectra. This method was originally proposed by Fellgett (1955) and is now the default extraction method for many of the modern RV instruments (e.g. ESO data reduction software (DRS) for HARPS, HARPS-N and ESPRESSO).

Because the CCF is measuring the similarity of the two functions shifted by lag τ, with the use of a proper template, it can be assumed that the information in all spectral lines is condensed into the shape of the CCF with the location of the peak representing the stellar RV. The RVs are then inferred by fitting a Gaussian to the CCF. In addition, the projected equatorial rotational velocity of the star,

$v \sin i$ can be approximated from the width of the CCF (rotational broadening) (Gullberg & Lindegren, 2002; Pepe et al., 2002; Queloz et al., 2001).

To put into perspective how small the wavelength shifts are, let us consider the case of a $1\,\mathrm{m\,s^{-1}}$ shift. This would correspond to shifts of $\sim 2 \cdot 10^{-5}$ Å at $\lambda = 500\,\mathrm{nm}$. This is orders of magnitude smaller than the size of a single Silicon atom which has typical sizes of 2.1 Å. For a modern, relatively high spectral resolution spectrograph that has R = 100 000, we usually have a pixel sampling resolution of R = 400 000, which means that the shift is still only $\sim 1/750^{\mathrm{th}}$ of a CCD pixel.

A few of the non-trivial requirements for extracting accurate RVs include the necessity of accurate and precise wavelength calibrations. These are usually performed using a ThAr (Thorium-Argon) lamp or a laser frequency comb for modern spectrographs (Murphy et al., 2007; Araujo-Hauck et al., 2007). Another important consideration is correcting for the Solar System barycentre, and stabilising the spectrograph inside a temperature controlled vacuum vessel, as changes to the refractive index of air may introduce several $\mathrm{m\,s^{-1}}$ shifts. Defects or inhomogeneities in the CCD pixels, varying point-spread function (PSF), chromatic aberrations and fringing pattern, and other instrumental drifts and imperfections can lead to RV variations of tens if not hundreds of $\mathrm{m\,s^{-1}}$. For a comprehensive radial velocity error budget I refer the reader to Halverson et al. (2016).

2.4 Stellar activity - Nuisance signals

Instruments like HARPS and HARPS-N have nominal precisions of $\sim 30\ \mathrm{cm\,s^{-1}}$ (Mayor et al., 2003; Motalebi et al., 2015) and have been observing for almost three decades between them. In addition, in recent years, due to the numerous advancements in instrumentation, next generation spectrographs are able to reach nominal precisions of $\sim 10\ \mathrm{cm\,s^{-1}}$ (e.g. ESPRESSO - Pepe et al. 2010, 2021, and EXPRES - Jurgenson et al. 2016). As such, one would expect that detecting low-mass planets would be straightforward. However, this has not been the case, with only a handful of planets having semi-amplitudes at the sub-$\mathrm{m\,s^{-1}}$ level. As it has become so apparent over the past decade, detecting low-mass planets is no longer

an instrumental limitation, but a restriction of our understanding, and ability to model stellar signals that contaminate the RV time-series and hinder our detection capabilities. As such, numerous new methods have been in development in recent years to try and correct for these nuisance signals (Collier Cameron et al., 2020; Dumusque, 2018; Jones et al., 2017; Rajpaul et al., 2015, 2020). Unfortunately, some of these methods that try to correct for the activity signal in the RVs require dense time-sampling and large datasets, something that historically has been limited. This motivated new projects such as the *The Terra Hunting Experiment* (Hall et al., 2018; Thompson et al., 2016), or *The EXPRES Stellar-signals Project* (Zhao et al., 2020, 2022) which aim to provide an unprecedented quality of data, allowing for the robust testing and development of new tools to mitigate the effects of stellar variability. A great development in this field has also come from observations of the Sun as a star (Dumusque et al., 2021; Collier Cameron et al., 2019). For a great review of current techniques I would point the reader to Zhao et al. (2022), which is a project aimed at bringing together numerous research groups to analyses the same dataset and compare the different approaches. For a comprehensive review of stellar activity and its implication on both Doppler spectroscopy but also photometry, I point the reader to the review article by Rackham et al. (2022). There are a variety of different stellar phenomena that induce RV variations. These phenomena can range from minutes to several years. A brief introduction to the most significant ones is presented below.

Stellar oscillations

Stars that have a convective outer layer can excite acoustic p-modes due to turbulent convection (Bouchy & Carrier, 2001; Christensen-Dalsgaard, 2002). These oscillations typically have periods of a few minutes and induce signals of a few tens of $\mathrm{cm\,s^{-1}}$. However, it was shown by Schrijver & Zwaan (2000) that the superposition of multiple of these convective envelope oscillations can produce signals of several $\mathrm{m\,s^{-1}}$. The frequency of these oscillations scales as the square root of the stellar density and the induced RV variations is dependent on stellar luminosity-to-mass ratio (Christensen-Dalsgaard, 2002). Cegla (2019) has shown that it is possible to average

out these p-mode oscillations by taking observations with exposure times over a few oscillation periods, focusing on integrating over an integer number of periods.

Granulation and super-granulation

Granulation is the photospheric manifestation of the convective currents that take place directly below the photosphere (in the outer layers) of Sun-like stars. The granulation pattern is due to the large number of cells ($\sim 10^6$) that show bright/hot upflows in their cores and darker intergranular lanes at the edges where the cooler plasma is descending back into the convective zone (see the top left part of Figure 2.10 for the granulation pattern)[12]. These convective cells have typical diameters of $\sim$ 1500km and cover the stellar surface. In the case of the Sun, the typical vertical flows have velocities of 1-2 $\mathrm{km\,s^{-1}}$ but because of large number of cells that average out, the effective velocity leads to a constant net blueshift of circa 200 $\mathrm{m\,s^{-1}}$. This is because the bright upflows have a greater photometric contribution than the cooler, darker downflows of material. It is estimated that the variability of this blueshift is at the level of a few $\mathrm{m\,s^{-1}}$ in the case of Sun-like stars. The typical evolution timescale of granules is roughly 10 min, but there are larger scale structures called super-granules that evolve on timescales of a few hours to a day (Michel et al., 2008; Carroll & Ostlie, 2006). Similar to p-mode oscillations, granulation becomes significant in the case of low-mass planets where precise RVs are required. Luckily it is possible to minimise their impact by taking multiple RV observation during the night, separated by a few hours (Dumusque et al., 2011; Meunier et al., 2015).

Magnetic activity - flares, spots, plages, and faculae

One the the biggest source of variability in Solar-type stars and M-dwarfs is attributed to the presence of magnetic fields. These magnetic fields cause inhomogeneities on the stellar disc that are called active regions as they comprise of areas of intense magnetic activity, and include starspots (dark spots), plages and faculae. Dark spots designate areas where the magnetic flux tubes emerge from the star and

[12]This figure is by Kelvin Song, for more illustrations by him here.

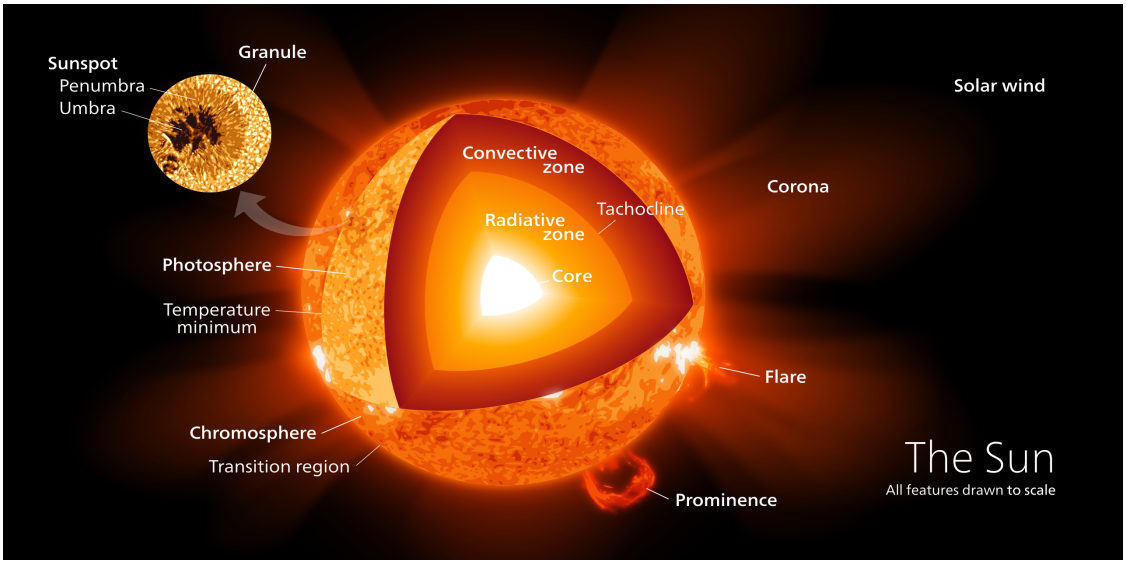

Figure 2.10: Figure showing the structure of the Sun and the different phenomena that dominate the stellar surface. Figure by Kelvin Song.

in general form in pairs, corresponding to opposite polarities. A darkspot is shown in the top left corner of Figure 2.10. In the bottom right a prominence is shown, which are structures of tens of thousands of km, where material is travelling along the magnetic field lines. Faculae by contrast, are bright regions that are found in the photospheric intergranular lanes and are associated with strong magnetic fields (Hale, 1908). In general faculae form networks and have longer lifetimes than spots. Plages are large bright zones in the chromosphere of stars and are closely related to the faculae from the photosphere. From observations, it is believed that starspots are always accompanied by faculae and plages, but it is thought that faculae can exist without darkspots (Schrijver & Zwaan, 2000).

It is intuitive to understand how starpots may induce photometric variability (due to them being rotationally-modulated), but the RV variability deriving from them is less-trivial. A toy model scenario is presented in Figure 2.11, that shows how the presence of this active region induces a line asymmetry, shifting the centroid by a small amount in the blueshifted direction. As the active region is rotating on the stellar surface it will produce an apparent RV signal on time-scales similar to the stellar rotation rate (Dumusque et al., 2015).

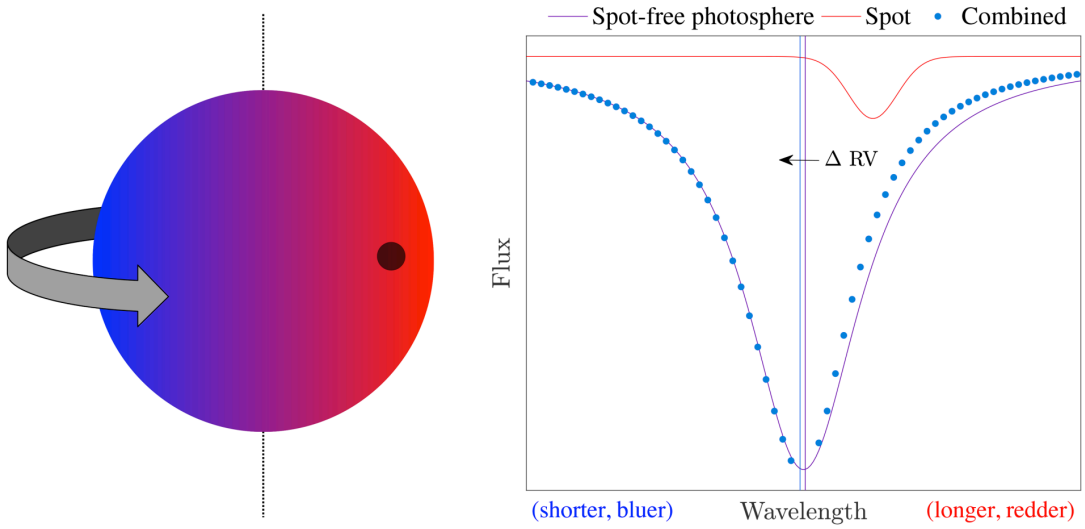

Figure 2.11: Figures showing the affects of a starspot on the radial velocity measurements. Assume a single starspot on the rotating stellar surface as shown in the left panel. As such, this will induce an asymmetry in the stellar spectrum shown in the right panel. Consequently, this asymmetry in the line profile will lead to a small RV variation. In the example shown in this figure, the darkspot is rotating away from us and therefor it lowers the contribution of the redshifted hemisphere, leading to a small net blueshift . Figure from Rajpaul (2017).

The current understanding is that these active regions appear in a stochastic manner, and as they rotate in and out of sight on the stellar surface they evolve and migrate across latitudes. As a consequence, the signal produced by these magnetic field induced inhomogeneities is quasi-periodic in nature. An interesting point is that the main contributor to the RV variability in Sun-like stars doesn't actually come directly from the flux deficit or excess attributed to the active region, but from the strong magnetic fields that are associated with them. These magnetic fields interact with the ionised plasma, leading to locally suppressing the net blueshift typically linked to convective cells (Borgniet et al., 2015; Meunier & Lagrange, 2013; Lagrange et al., 2010).

The level of RV variability due to activity varies greatly from star to star, and depends mostly on the mean magnetic activity level. This in turn is influenced by spectral type and stellar age. In the case of Sun-like stars, due to magnetic braking the rotational velocity decreases as they get older (Mestel, 1968). In general they

start out with rotation periods of a few days at 10 Myr, but tend to slow down to about 40-50 days at 5 Gyr. According to Mestel (1968) the stellar rotational velocity scales with stellar age as $t^{-1/2}$. As it is believed that the magnetic dynamo is tied to the rotation rate, the mean magnetic activity of the stars decrease. In the case of M-dwarfs, which are fully convective, the stellar activity levels can vary vastly.

The stellar activity presented above is exacerbated in the case of young stars ($\leq$ 1 Gyr) where the rotating active regions can induce RV variability of 100s of $\mathrm{m\,s^{-1}}$ (see Chapter 4).

2.4.1 Activity indicators

Stellar nuisance signals can be split into two categorise. One category, where the RV variability can be corrected in a straightforward way. For example, p-mode oscillations can be averaged out by choosing the right exposure time for the observations as shown by Cegla (2019). On the other hand, activity induced signals are non-trivial to correct for. Their periodic or quasi periodic nature can sometimes be mistaken for planetary signals and lead to false-positive detections (Bonfils et al., 2007; Haywood et al., 2014; Santos et al., 2014). This means that in the case of low-mass planets, the limiting factor for detection is the presence of these activity induced nuisance signals. Because of the timescales over which these signals change and operate, it is crucial to disentangle them from the dataset.

Knowing that these active regions are associated with strong magnetic fields and that they distort the line profiles allows us to use this to our advantage and come up with activity-sensitive indicators. As such, it is possible to extract ancillary parameters or time-series from the stellar spectra simultaneously with the RVs, that are able to offer us some information about the level of activity induced variations. Some of the used activity indicators include the full-width-half-maximum (FWHM), which measures the width of the CCF, the line asymmetry, which can be measured from the CCF bisector, as well as chromospheric activity indicators such as $\log R'_{\mathrm{HK}}$ or S_{HK}. All of these are sensitive to the signals induced by stellar activity, but are left unchanged by the reflex motion induced by a planet.

Chromospheric indicators : $\mathcal{S}$-index and $\log R'_{\rm HK}$

Two of the most commonly used chromospheric indicators are the $\mathcal{S}$-index and $R'_{\rm HK}$. They both rely on the Ca II H and K lines (3 967 Åand 3 933 Å) which are the strongest and broadest lines in the visible part of the Solar spectrum. It is important to note that emission in the core of these lines is sensitive to chromospheric magnetic activity levels and as such it can be a great proxy (Schrijver & Zwaan, 2000).

By definition, the $\mathcal{S}$-index is defined as:

$$S = \alpha \frac{\Psi_{\rm H} + \Psi_{\rm K}}{\Psi_{\rm V} + \Psi_{\rm R}} \tag{2.14}$$

where $\Psi_{\rm H}$ and $\Psi_{\rm K}$ is the flux in the cores of the H and K lines, and $\Psi_{\rm V}$ and $\Psi_{\rm R}$ is the flux of the continuum in a 20 Å bandpass on either side of the H and K lines. As such, it is a ratio of flux counts and it is a dimensionless quantity. Because the normalisation is compared to the local continuum, the $\mathcal{S}$-index cannot be used to compare stars of different spectral type as the continuum is dependent on this. Similarly, it is challenging to compare the $\mathcal{S}$-index between two instruments as the put through of the two instruments might be different in those reference bands.

By comparison, the $R'_{\rm HK}$ index was introduced such that it is independent of spectral type and instrumental specifics. Similarly to the $\mathcal{S}$-index, it uses the H and K lines, and is defined as:

$$R'_{\rm HK} = \frac{\Psi'_{\rm H} + \Psi'_{\rm K}}{\sigma_{\rm B} {\rm T}_{\rm eff}^4} \tag{2.15}$$

where $\sigma_{\rm B}$ is the Stefan-Boltzmann constant, $\rm T_{eff}$ is the stellar effective temperature, and $\Psi'_{\rm H}$ and $\Psi'_{\rm K}$ are the fluxes of the H and K line cores, but measured at the stellar surface as opposed to the observer. This means that it measures the excess in the H and K lines compared to the star's bolometric luminosity. The $R'_{\rm HK}$ is most commonly used in logarithmic units (i.e. $\log R'_{\rm HK}$). Following the classification used by Maldonado et al. (2010), stars can be defined as 'very inactive' for $\log R'_{\rm HK} < -5.1$; 'inactive' for $-5.1 < \log R'_{\rm HK} < -4.75$; 'active' for $-4.75 < \log R'_{\rm HK} < -4.2$; and 'very active' when $\log R'_{\rm HK} > -4.2$.

For a few other chromospheric activity indicators see Chapter 4.2.4, where we used these to determine if the observations were affected by flares.

CCF related indicators

The CCF FWHM is defined as the width of the CCF function at half-maximum. As such, it is closely related to the mean width of the spectral lines. Then, because of Doppler broadening of the spectral lines, the FWHM is closely connected to the rotation rate of the star ($v \sin i$). Knowing that younger, faster rotating stars tend to have stronger magnetic activity, the FWHM can be used as a proxy for the magnetic activity level. Haywood (2015) showed that the RV perturbations originating from starspots breaking the symmetry in the flux of the two hemispheres will be correlated to variations in the FWHM (see Figure 2.11, the FWHM changes due to the asymmetry caused by the darkspot).

The CCF bisector is defined as the array of points that bisect the CCF function, such that at every equal intensity the widths are the same (see the right panel in Figure 2.12). As such, the bisector is used to quantify the line asymmetry of spectral lines. Because of granulation in cool stars, the CCF bisector get a characteristic 'C' shape. This is because there is a superposition of blueshifted (hot upflow) and redshifted (colder downflow) (see the right panel of Figure 2.12). Then, whenever an active region alters the balance between the blueshifted and redshifted lines, there is a small distortion in the shape of the bisector.

Many similar metrics were established, for example the bisector velocity span (Toner & Gray, 1988), the bisector curvature (Hatzes, 1996), and the bisector inverse slope (Queloz et al., 2001).

2.4.2 Correcting/Mitigating activity-induced RV variability

Having established that there are ancillary time-series and indicators that are able to track the stellar activity induced RV variations, let us explore a few approaches that could either help mitigate the effects of activity or explicitly try and model it in order to disentangle activity signals from signals that are planetary in nature.

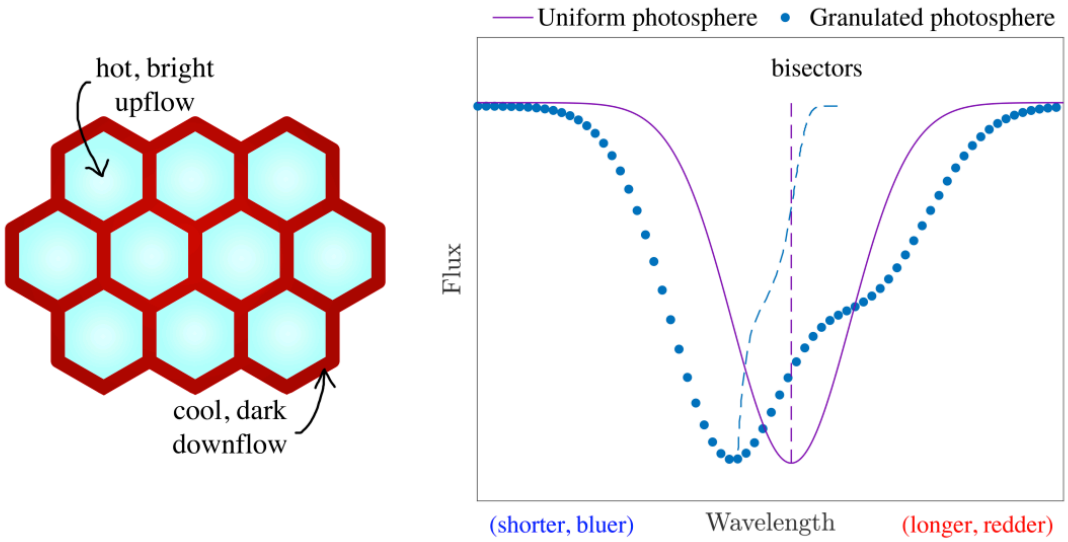

Figure 2.12: Figure showing the effects of granulation on the CCF bisector. The left panel shows a schematic drawing for granulation. The right panel shows the bisector for a Gaussian shown in purple, and a Sun-like star in blue, where the characteristic 'C' shape can be seen. Figure from Rajpaul (2017).

Observational approaches

Let us start with observational approaches as these are the most trivial of the cases presented. It is well established that the contrast of spots is lower in the infrared than it is in the visible (Quirrenbach et al., 2014), as such the effects of stellar activity induced variations is smaller. This is particularly interesting in the case of M-dwarfs, because they are brightest in the infrared. Other observational approaches include binning the data, but the big drawback of this is that the binning process discards information from the individual observations, in addition to requiring a lot of telescope time.

Zeeman-Doppler imaging

Zeeman-Doppler imaging (ZDI) uses time-series spectropolarimetry in order to try an reconstruct the stellar magnetic fields using a maximum entropy approach. As such, it generates the simplest magnetic field geometry that is able to explain the data Marsh & Horne (1988). In general this method works best for young, active and rapidly rotating stars that have have large Doppler broadening. Klein

et al. (2021) successfully applied ZDI to SPIRou observations of AU Mic, measuring the mass of then known transiting planet AU Mic b, and was able to reconstruct the stellar surface topology.

Pre-whitening and linear correlation models

An approach sometimes adopted involves using Fourier analysis to find the strongest periodic signal in the data, and then subtracting a sinusoidal fit of this signal from the dataset, repeating the process until no significant signals remain. This is called pre-whitening and it is a quick way to reveal any potential periodic signals in the RV time-series. In some instances, this approach is used with sinusoids corresponding to the estimated stellar rotation period (and its harmonics), aiming to remove the stellar activity induced RV variations.

Another approach that is widely adopted involves fitting simple linear correlations between the RV measurements and the activity indicators, in order to remove the stellar activity induced variations from the RVs. This approach however is reliant on the RVs being strongly correlated with one of the ancillary time-series, meaning that it can be applied only in specific cases.

F F' method

Aigrain et al. (2012, hereafter A12) has shown that there is an inherent connection between the stellar-induced RV variations and the surface of the star that is covered by active regions. In their formalism, they demonstrate that it is possible to use the photometric brightness of the star to predict the RV variations.

They define the relative drop in flux due to a spot on the stellar surface as:

$$\mathrm{F}(t) = f\,\mathrm{MAX}\{\cos\beta(t); 0\} \tag{2.16}$$

where $f = 2(1-c)(1-\cos\alpha)$ is the relative flux drop for a dark spot at the disc centre, c is the contrast ratio of the spot, α is the angular radius of the spot on the stellar surface (it is assumed that $\alpha \ll 1$), and $\beta(t)$ is the angle between the spot normal and the line of sight. As such, this angle is defined as:

$$\cos\beta(t) = \cos\phi(t)\cos\delta\sin i + \sin\delta\cos i \tag{2.17}$$

where i is the inclination, δ is the latitude of the spot relative to the star's rotational equator, and $\phi(t) = 2\pi/P_{\rm rot} + \phi_0$ is the phase of the spot compared to the observer. Then the relative drop in flux and its time derivative can be written as:

$$\mathrm{F(t)} = 1 - \frac{\Psi(\mathrm{t})}{\Psi_0} \quad \dot{\mathrm{F}}(\mathrm{t}) = -\frac{\mathrm{d}\Psi/\mathrm{dt}}{\Psi_0} \tag{2.18}$$

A12 showed that the perturbations to the stellar RV due to activity (spots) can be separated into two terms, and can be written as:

$$\Delta\mathrm{RV}(t) = \Delta\mathrm{RV}_{\rm rot}(t) + \Delta\mathrm{RV}_{\rm c}(t)$$

where $\Delta\mathrm{RV}_{\rm rot}$ is the RV induced by the spot's rotation and $\Delta\mathrm{RV}_{\rm c}(t)$ is the RV induced from the spot's suppression of the convective blueshift.

Following the work of A12 and using the previously introduced definition for the flux, we can define these two contributions as:

$$\Delta\mathrm{RV}_{\rm rot}(t) = -F(t)\,\dot{F}(t)\,\frac{R_\star}{f} \tag{2.19}$$

$$\Delta\mathrm{RV}_{\rm conv}(t) = \mathrm{F}^2(t)\,\frac{\delta V_{\rm c}\kappa}{f} \tag{2.20}$$

where R_* is the stellar radius, f is the relative flux drop (defined above), $\delta V_{\rm c}$ is the difference in convective blueshift between the spotted and unspotted photosphere, and κ is the ratio between the unspotted and spotted area (usually $\kappa \gg 1$).

As the spot induced RVs can be written terms of the stellar flux and its time derivative, this method is called F F' method. A12 has shown the method's effectiveness by reproducing the RV variations of the Sun from high cadence photometry to the sub-m s^{-1} level. However, the fallback of this method is that it requires contemporaneous RV and photometric observations and it doesn't use any information available in the activity indicators.

The above mentioned linear decorrelation method is at the foundation of my linear activity-corrected periodogram that is presented in Chapter 5.2. The F F' method is the basis on which the more complicated multi-dimensional GP framework is built on (see Chapter 3.3 for details) as well as the Gaussian process corrected GdG periodogram (see Chapter 5.4) approach.

Nothing in life is to be feared, it is only to be understood. Now is the time to understand more, so that we may fear less.

— Marie Skłodowska Curie

3 Statistical methods

Contents

This chapter aims to introduce some key statistical and numerical methods methods used in the thesis. First, I introduce the widely popular tools classified as periodograms. In the context of exoplanetary science their main application is to study the presence of periodic signals in time-series, but they can also be used to define detection limits for planetary companions (see Chapter 5.3). Next, I introduce Gaussian processes, a key foundation for the work presented in this thesis. I use Gaussian process regression extensively throughout the thesis, including

modelling stellar spectra (see Chapter 6) and stellar variability. For this, I introduce the Gaussian process framework used in Chapter 4, to simultaneously model the RV and activity indicator time-series. Finally, I present a brief discussion around posterior sampling methods, focusing on Markov chain Monte Carlo (MCMC) and nested sampling.

3.1 Periodograms - classical, generalised and extensions

The first technique defined as a 'periodogram' was introduced by Arthur Schuster (Schuster, 1898). Also known as the 'classical' or Schuster periodogram, it is based on the discrete-time Fourier transform (DTFT)[1]. It represents one of the most widely adopted methods to analyse periodic variations in time-series and there is extensive literature available on this topic. Unfortunately, it has some limitations when it comes to analysing astrophysical data, especially radial velocity time-series. Due to the fact that it requires numerous samples of the signal with even time sampling, it is usually unsuitable for exoplanet searches (low-cadence data with irregular time sampling).

3.1.1 The Lomb-Scargle and generalised Lomb-Scargle

A generalisation of the Schuster periodogram known as the Lomb-Scargle (Barning, 1963; Lomb, 1976; Scargle, 1982) or least-squares periodogram was developed in order to handle the irregular time sampling. This is achieved by using a pair of phase offset sinusoidal basis functions that are orthogonal[2] . It is equivalent to fitting sine waves of the form $y = a\sin(\omega t + \phi) = b\sin\omega t + c\cos\omega t$. While fitting sine waves requires solving linear equations at each sampled frequency, the

[1]The power spectral density of a continuous function $x(t)$, is the Fourier transform of its auto-correlation function, such that $\mathcal{F}\{x(t) \circledast x^*(-t)\} = X(f) \cdot X^*(f) = |X(f)|^2$. When evaluating the function using DTFT it can be written as the summation of periodic components: $S\left(\frac{k}{NT}\right) = \left|\sum_n x_N[n] \cdot e^{-i2\pi\frac{kn}{N}}\right|^2$. When evaluated over all integer values of k (0,N-1) the result is the Schuster periodogram.

[2]Two functions are orthogonal if $\langle f, g\rangle = \int_{x_1}^{x_2} f(x)g(x)\mathrm{d}x$. Computing the integral for $\sin(x) \cdot \cos(x)$ we obtain $-1/2\cos^2(x)$, which evaluated from 0 to 2π gives 0.

Lomb-Scargle method provides an analytic solution, making it computationally more efficient and arguably more convenient. Using the original notation from Lomb (1976), for a time-series (t_i, y_i) with zero mean ($\bar{y} = 0$), the Lomb-Scargle periodogram at frequency ω is defined as:

$$\hat{p}(\omega) = \frac{1}{\sum_i y_i^2} \left\{ \frac{\left[\sum_i y_i \cos\omega\left(t_i - \hat{\tau}\right)\right]^2}{\sum_i \cos^2\omega\left(t_i - \hat{\tau}\right)} + \frac{\left[\sum_i y_i \sin\omega\left(t_i - \hat{\tau}\right)\right]^2}{\sum_i \sin^2\omega\left(t_i - \hat{\tau}\right)} \right\} \tag{3.1}$$

where $\hat{\tau}$ is defined as:

$$\tan 2\omega\hat{\tau} = \frac{\sum_i \sin 2\omega t_i}{\sum_i \cos 2\omega t_i} \tag{3.2}$$

However the above method has two major shortcomings when it comes to analysing time-series in the exoplanetary context. First, it assumes that the observations are noise-free and hence the measurement errors are not taken into account. This was solved with the introduction of weighted sums by Irwin et al. (1989). Second, it assumes that the data has 0 mean (mean subtracted), implying that the mean of the data and the mean of the sinusoids are the same - this is not always the case. A solution for this problem is to introduce an offset c that is able to capture this (Cumming et al., 1999). Incorporating these generalisations is equivalent to that of a χ^2 fit, where the model is of the form : $y = a\sin\omega t + b\cos\omega t + c$.

A generalised Lomb-Scargle (GLS) periodogram accounting for measurement errors and a non-zero mean was introduced by Zechmeister & Kürster (2009). Following their notation, for a time-series (t_i, y_i) with N observations and errors σ_i, we fit the following model:

$$y(t) = a\sin\omega t + b\cos\omega t + c \tag{3.3}$$

Hence, we try to minimise the following function:

$$\chi^2 = \sum_{i=1}^{N} \frac{\left[y_i - y\left(t_i\right)\right]^2}{\sigma_i^2} = W \sum w_i \left[y_i - y\left(t_i\right)\right]^2 \tag{3.4}$$

where the observation are weighted by inverse-variance as:

$$w_i = \frac{1}{W}\frac{1}{\sigma_i^2} \quad \left(W = \sum \frac{1}{\sigma_i^2} \quad \sum w_i = 1\right)$$

In order to minimise equation 3.4, partial derivatives must be calculated and solved. This in turn corresponds to solving a system of linear equations (3 equations in this case). Re-normalising the solution to unity by χ^2_0 (the χ^2 of the weighted mean) in turn leads to the following equation for $p(\omega)$:

$$p(\omega) = \frac{\chi^2_0 - \chi^2(\omega)}{\chi^2_0} \tag{3.5}$$

The GLS periodogram defined above, implies that the so called power $p(\omega)$ must obey $0 \leq p(\omega) \leq 1$. In the aforementioned condition, $p = 0$ corresponds to no improvement to the fit, whilst $p = 1$ would correspond to a 'perfect' fit to the data. In practice a 'perfect' fit is unattainable due to the observational noise.

Due to its convenience and efficiency, the GLS periodogram has been widely adopted in the astrophysics community and it is one of the most widely used tools in exoplanet studies, including Doppler spectroscopy. There is a very easy to use *Python* implementation available with the `astropy` package (Astropy Collaboration et al., 2013, 2018). It has been applied to the study of both planetary and stellar signals (see,e.g., Pepe et al., 2011; Wright, 2018, and references therein). Namely, GLS periodograms are often used in order to estimate the stellar rotation period of stars from the activity indicators (e.g. FWHM, $\log R'_{\rm HK}$ $S_{\rm HK}$ etc.). Knowing the rotation period of the host star can help disentangle stellar and planetary signals from each other, but also, it can help 'clean' the RV time-series.

3.1.2 Limitations

Unfortunately, the GLS periodogram relies on a few fundamental assumptions that are not always fulfilled and thus can make the results unreliable. It assumes that the studied signal is a *single* sinusoid affected by Gaussian noise. In other words, it not only requires a strictly periodic signal, but also it has to take the shape of a sine/cosine function. Although this might be the case for a single planet on a circular orbit, it does not necessarily apply to Keplerian signals. Due to this limitation, the GLS periodogram is also unable to properly account for any time-correlated noise or nuisance signal. Even something as simple as a linear

trend will cause distorted results, not to mention more complex activity induced variations that tend to be quasi-periodic in nature.

Another shortcoming of the GLS periodogram is that in the case of exoplanet studies, there are usually multiple signals that interfere and should be accounted for. Not only are there quasi-periodic activity induced signals in the data, but also potentially multiple Keplerian signals (non-sinusoidal signals). Adding to this the usual complexity of astrophysical window functions, it becomes a very complex system. One can expect that all these signals will interfere in complex ways and the combination of them cannot be simply treated as a single sine wave. For example, Fig 3.1 shows the interference pattern caused by the interaction of simple periodic functions of the form $f = \sin(\frac{2\pi}{P_i} + \phi_i)$. It is clear, that regardless of the amount of white Gaussian noise ('jitter') that is added to a single sine wave, it cannot explain the observed interference pattern. Assuming such a model could lead to heavily biased results about the amplitude and frequency of the assumed sinusoid. Furthermore, in exoplanet searches the stellar activity component present in the data is usually not a strictly periodic function, but rather has a quasi-periodic nature.

Another key point when it comes to dealing with periodic signals is the importance of how the modelling is performed. There are major differences between doing an iterative fitting versus fitting the entire model simultaneously. For example, let us take the toy model presented in Fig 3.2. In this example, let us assume that we have two sinusoidal functions with periods 19 days and 33 days and amplitudes of 1 $\mathrm{m\,s^{-1}}$. We sample the sum of these two waves at 150 random points, not adding any noise. Let us now assume that we know the period and phase of these signals, and we want to try to fit for their amplitudes. In the panel on the right, the results of this fitting procedures can be seen. First, we fit for the 33 day period and remove it from the observations, leaving us with the blue residuals. It is important to note that the residuals are non-sinusoidal. Next, we fit for the remaining signal at 19 days and subtract it, leaving us with the residuals shown in orange. These residuals are an artefact of the iterative fitting. There is no 3$^{\mathrm{rd}}$ hidden signal (or in the case of exoplanet searches, this is not a planet hidden

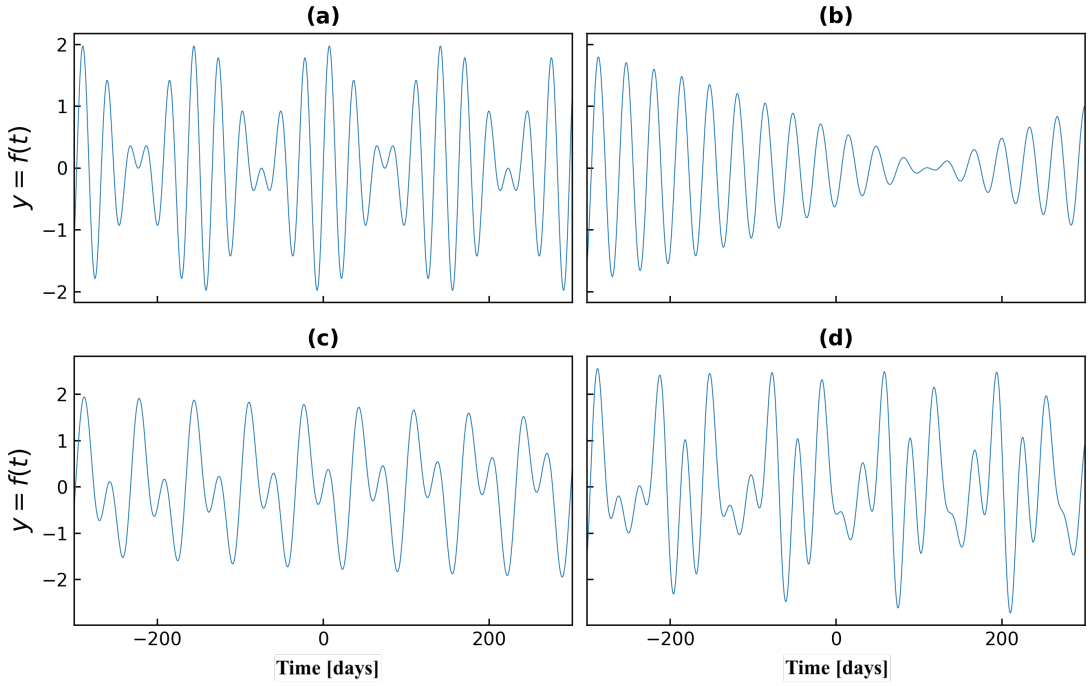

Figure 3.1: Interference between periodic signals. The functions presented above have the form $f = \sum_i^N \sin(\frac{2\pi}{\mathrm{P}_i} + \phi_i)$. In panels **a**, **b**, and **c**, $N = 2$, where $\mathrm{P}_1 = 33$ days and P_2 is 27 days, 34 days and 67 days respectively. Panel **d** shows the interference of 3 signals with periods: 27 days, 34 days and 67 days.

in the data). Finally, the results of fitting for both signals simultaneously are shown in green. These, as expected, are flat.

A popular tool that highlighted and addressed these affects, was the **Period04** program. It was widely used to analyses RV time-series, as well as time-series in helio and asteroseismology. It finds signals iteratively, but every time a new signal is found, it re-fits the original data with all the signals at the same time.

Furthermore, the time sampling of observations can play a key role in the robustness of any detection. It is crucial to account for the window-function (WF) of the time-series, especially when modelling multiple signals. Due to the sparse and irregular time sampling, 'ghost' signals can be observed. Without properly testing for these biases, distorted results can be obtained (for example, see Dumusque et al. (2012); Rajpaul et al. (2016)).

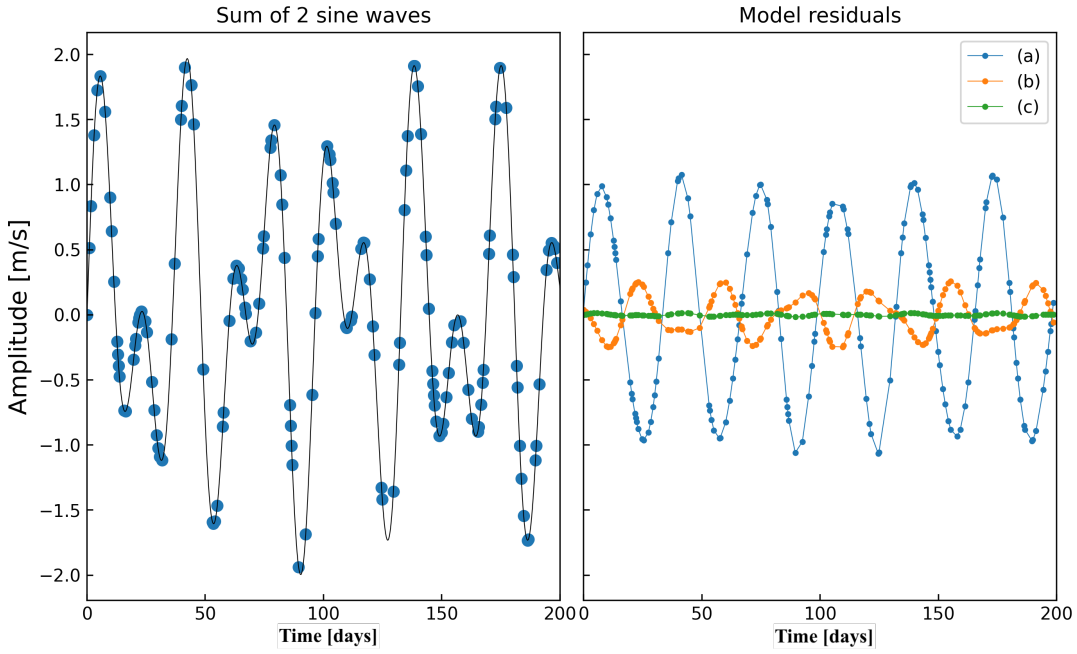

Figure 3.2: Interference pattern between 2 periodic signals and the importance of fitting procedures. The function presented on the left has the form $f = \sum_i^2 \sin(\frac{2\pi}{P_i} + \phi_i)$ and $P_1 = 19$ days and $P_2 = 33$ days, each with amplitude 1 $m\,s^{-1}$. The signal has been randomly sampled 150 times, not including any noise (blue dots). The panel on the right shows the result of fitting for these two signals in a simultaneous vs. iterative way. In blue, I show the result of subtracting the best fit model with fixed period 33 days from the observations. In orange, this is the residual of subtracting the 19 days signal from blue. The residuals of performing the fit of both signals simultaneously are shown in green.

3.1.3 Extensions

Over the years, a few extensions to the generalised Lomb-Scargle periodogram have been developed (Mortier et al., 2015; Mortier & Collier Cameron, 2017; Hara et al., 2017) that try to account for some of these shortcomings. For instance, the Bayesian generalised Lomb-Scargle (BGLS) (Mortier et al., 2015) periodogram rather than providing a power it provides a probability for each frequency being present in the data, making it much easier to compare peaks. It 'builds up' the periodogram by 'forward modelling' the data and taking the likelihood of the prediction instead of the power. This also allows the user to incorporate any prior knowledge about the system into the analysis. The idea was further developed with the introduction of the stacked Bayesian generalised Lomb-Scargle (Mortier & Collier Cameron, 2017) periodogram. It starts out by applying the BGLS periodogram on a limited number

of data and adding more observations. The idea behind it is that as we add more and more data points, any planetary signal should become stronger, whilst nuisance signals should become less relevant due to their quasi-periodic nature resulting in a smaller likelihood. Both the original BGLS and stacked BGLS have an openly available *Python* implementation. In contrast, the L1 periodogram (Hara et al., 2017) is able to model multiple signals at the same time and it uses a clever regularisation method (L1 - Lasso regression) to determine their significance. An easy to use *Python* implementation of the L1 periodogram is also available (Hara & Mari, 2021).

3.1.4 Assessing significance

When using a periodogram to determine the presence of a periodic component in the data, an essential factor is to asses the significance of the periodogram peaks. The simplest way to do this is to express it in terms of a false alarm probability (FAP). The values obtained for the false alarm probability are often misinterpreted or misused, making it crucial to understand what they actually mean. In layman terms, the FAP computes the probability of obtaining a peak of a given power (or bigger) assuming that the data consists only of white Gaussian noise and no periodic component. A small value for the FAP can be used as an indication that a periodic component can be found in the data. It is important to note however that it is conditioned on the data being purely white noise, hence the FAP should be used with caution. For example, a FAP of 1% can correspond to a much higher probability of false detection in real datasets (see Figure 3.3). As such, a number of ways to compute FAPs exist. Some of these include using approximations such as the Baluev method (Baluev, 2008) or Davies bound (Davies, 1987), which provide a pessimistic bound on the FAP. By contrast the 'naive estimate' provides an an optimistic estimation. A more realistic estimate can be obtained using bootstrap methods that are based on the noise properties of the data, but at a much higher computational cost. The comparison of the most common implementations to compute FAPs are shown in Figure 3.3 for a dataset consisting of 100 observations[3].

[3]Figure from `astropy` documentation here

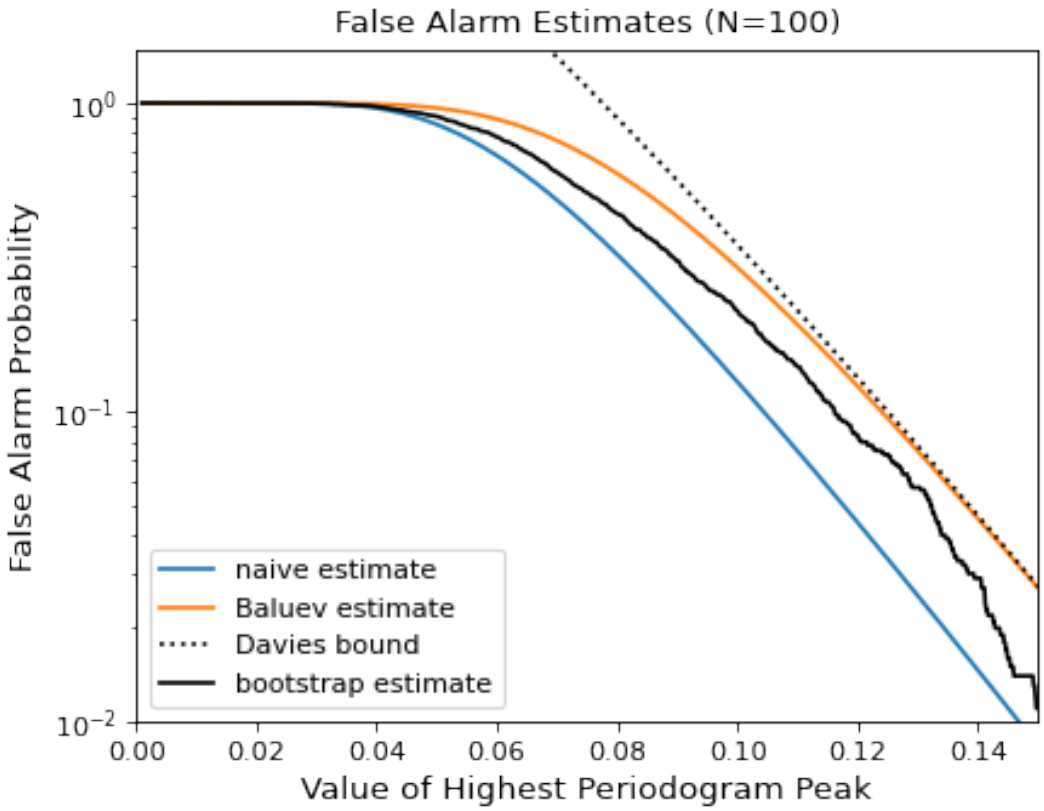

Figure 3.3: Comparison of different methods used to compute false alarm probabilities at a given frequency for a dataset of 100 observations. The x-axis shows the power value of the highest peak, whilst the y-axis shows the corresponding false alarm probability. The different methodologies used to compute them are shown in blue for 'naive' method, orange for 'Baluev' method, dotted black line for Davies bound and solid black line for bootstrap estimation. Figure from `astropy` documentation.

As computing the false alarm probabilities of periodograms and interpreting the peak significance was known to be challenging, I opted to not use them and rely on injection-recovery tests instead (see Chapter 5.3). However, there is an extensive literature available on the subject (VanderPlas, 2018) and the assessment of periodogram peaks remains and active area of research (Delisle et al., 2020a; Hara, 2021).

In Chapter 5, I present two extensions to the GLS periodogram that I have developed. They are able to address some of the shortcoming that were mentioned. The first approach involves including a linear trend into the model that allows to 'clean' the RV and is able to account for multiple signals, fitting everything at the same time. The second extension takes a different approach to account for the

stellar variability and it has similarities to the Gaussian process(GP) framework developed by Rajpaul et al. (2015) (presented in Chapter 3.3).

3.2 Gaussian process regression

An elegant solution to the flaws of traditional approaches to model stellar activity is the introduction of Gaussian processes (GPs). Whilst classical regression methods focus on inferring the parameters of a function that is fitted to the data, Gaussian processes take a different approach. This data-driven route is non-parametric/semi-parametric by comparison (depending on the exact interpretation). Gaussian processes allow us to perform Bayesian inference on a family of functions with given properties, controlled by the hyper-parameters. As such, I will define them as semi-parametric as opposed to purely non-parametric. Although a GP model has many parameters (one for each observation), they are marginalised over analytically, and as such we fit directly for the hyper-parameters of a GP. As the hyper-parameters are one level removed from the data, the model has more freedom/flexibility.

3.2.1 Introduction

By definition, a Gaussian process is a stochastic process (e.g. random variables in a time-series), such that any finite subset can be described by a multivariate normal distribution. The joint distribution of the infinitely many random variables is the distribution of a Gaussian process. As such, a GP is a distribution over functions with a continuous domain, e.g. time or space (Rasmussen & Williams, 2006). In simpler terms, a GP can be thought of as an infinite-dimensional generalization of the multivariate normal distribution .

This rather complex definition does not make it obvious as to why, or how GPs can be a powerful tool in modelling stellar activity signals. I aim to provide a brief and relatively simple introduction to Gaussian processes, focusing on their direct applicability in the context of regression and exoplanet science. By no means is it meant to be a comprehensive introduction. For this, I recommend the GP 'Bible' by Rasmussen and Williams (Rasmussen & Williams, 2006).

Parametric and semi-parametric modelling

In order to understand the motivation behind GPs, it is crucial to understand the difference between parametric and semi-parametric modelling. Whilst parametric modelling focuses on fitting *a single* functional form (assumed to be the correct one), to the data and infer the best fit parameters, a semi-parametric approach implies assuming that it is not possible (or fitting due to lack of knowledge) to choose one specific functional form, as there is a family of functions that are able to fit the data just as well. Meaning, that in semi-parametric modelling the focus is on determining the characteristics and properties of these functions that could fit the data.

A simple example to help understand parametric modelling and also illustrate its shortcoming is the following thought experiment. Assume we have 3 data points, at x = 1,2,3 and correspondingly y = 1,2,3. It is easy to see that a simple linear model is able to fit the data with a function of the form $f(x) = y = ax + b$. This however is not the only possible function that is able to explain this data. It is trivial that there is an infinite number of polynomial functions that are able to fit the 3 data points just as well. The curves arising from these functions differ significantly from each other and from the straight line, but all of them are able to go exactly through the data. This gives rise to the question of which of these functions is the right one? Of course, in real world cases it is possible to incorporate prior knowledge that helps choose the 'right' model, but it illustrates that in cases where a complex dataset is modelled that includes stochastic processes, it is not straight forward to write a a parametric model. Even when a parametric model is formulated, it raises the question 'is it the right one?'.

On the other hand, semi-parametric models do not try to infer parameters of a function. In turn they use a distribution of functions that have characteristics consistent with the data (controlled by the hyper-parameters). It is possible to perform the modelling by refining the probability distributions of these functions by selecting the ones that offer the strongest match with the data. Gaussian processes represent a practical and powerful example of such semi-parametric models.

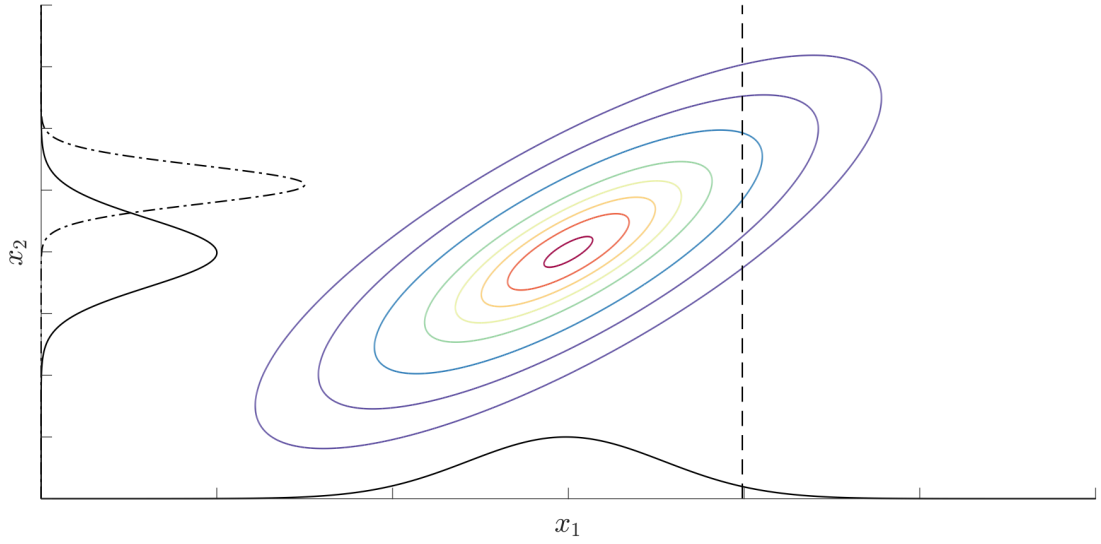

Figure 3.4: The bivariate Gaussian distribution for two variables x_1 and x_2 is shown with coloured covariance ellipses. The marginal distributions (projections) for the two variables are shown in black (solid lines). Observing x_1 at the value shown with the dashed line, updates our belief about x_2, leading to the conditional distribution shown in black dash-dotted line. The covariance allows us to update our knowledge about a variable with information provided by observing the other. Figure from Rajpaul (2017).

A caveat that must be stated is that in situations where the behaviour of the underlying process is well understood, invoking Occam's razor argument, it is completely reasonable to use a simple parametric model. The key distinction being, that in situations where we lack this information, a GP with only 2 hyper-parameters, the same number of free parameters as fitting a straight line, in turn can describe an infinity of function shapes.

3.2.2 Multivariate Gaussian distribution

To understand how Gaussian processes work and in order to develop an intuition for working with probability distributions over functions (as opposed to parameters), it is helpful to first consider the multivariate Gaussian distribution. The simplest scenario that can be studied is the bivariate Gaussian distribution from which we will build up to Gaussian processes.

Let us examine a bivariate Gaussian distribution defined for two variables x_1 and x_2. This distribution can be fully described by a mean vector μ and a covariance

matrix Σ (dimension [2,2]). An example of a bivariate Gaussian distribution is shown in Figure 3.4 as elliptical contours, corresponding to the joint probability distribution $p(x_1, x_2)$. The marginal distributions, $p(x_1)$ and $p(x_2)$, are shown on the x_1 and x_2 axis respectively. Observing x_1 at the location of the dashed line affects our knowledge about x_2. This associated conditional distribution $p(x_2|x_1)$ is shown by the dash-dotted line. This 'updated' distribution looks very different from the original distribution. This is due to the relationship set by the covariance. Information about one variable will constrict the uncertainty in the other.

Formally, the bivariate Gaussian distribution is defined as:

$$\begin{bmatrix} x_1 \\ x_2 \end{bmatrix} \sim \mathcal{N}\left(\begin{bmatrix} \mu_1 \\ \mu_2 \end{bmatrix}, \begin{bmatrix} \Sigma_{11} & \Sigma_{12} \\ \Sigma_{21} & \Sigma_{22} \end{bmatrix}\right) \tag{3.6}$$

The conditional distribution for x_1 given x_2 is then:

$$(x_1 \mid x_2 = a) \sim \mathcal{N}\left(\mu_1 + \Sigma_{12}\Sigma_{22}^{-1}\left(a - \mu_2\right), \Sigma_{11} - \Sigma_{12}\Sigma_{22}^{-1}\Sigma_{21}\right) \tag{3.7}$$

Generalising these equations to the multivariate Gaussian case, we can write:

$$\begin{bmatrix} \mathbf{x} \\ \mathbf{y} \end{bmatrix} \sim \mathcal{N}\left(\begin{bmatrix} \boldsymbol{\mu}_x \\ \boldsymbol{\mu}_y \end{bmatrix}, \begin{bmatrix} \boldsymbol{\Sigma_{xx}} & \boldsymbol{\Sigma_{xy}} \\ \boldsymbol{\Sigma_{yx}} & \boldsymbol{\Sigma_{yy}} \end{bmatrix}\right) \tag{3.8}$$

where $\mathbf{x} = [x_1, x_2, \ldots, x_n]$ and $\mathbf{y} = [y_1, y_2, \ldots, y_m]$, n and m are the number of variables.

The conditional distribution for $\mathbf{x}$ given $\mathbf{y}$ is then:

$$(\mathbf{x} \mid \mathbf{y} = \mathbf{a}) \sim \mathcal{N}\left(\boldsymbol{\mu}_x + \boldsymbol{\Sigma}_{xy}\boldsymbol{\Sigma}_{yy}^{-1}\left(\mathbf{a} - \boldsymbol{\mu}_y\right), \boldsymbol{\Sigma}_{xx} - \boldsymbol{\Sigma}_{xy}\boldsymbol{\Sigma}_{yy}^{-1}\boldsymbol{\Sigma}_{yx}\right) \tag{3.9}$$

Expending on this idea and applying the same methodology to more variables allows us to start formulating the basis of the multivariate Gaussian distribution. In addition, in this sample example, we represented the two variables plotted against each other, but there is no reason stopping us from actually assuming that the two data points are from a time-series. In the same way, observing one of these variables (points) will condition our knowledge about the other.

Let us now consider the case of a 10-dimensional example, where the 10 variables correspond to evenly spaced points of a time-series defined between times [1,10]

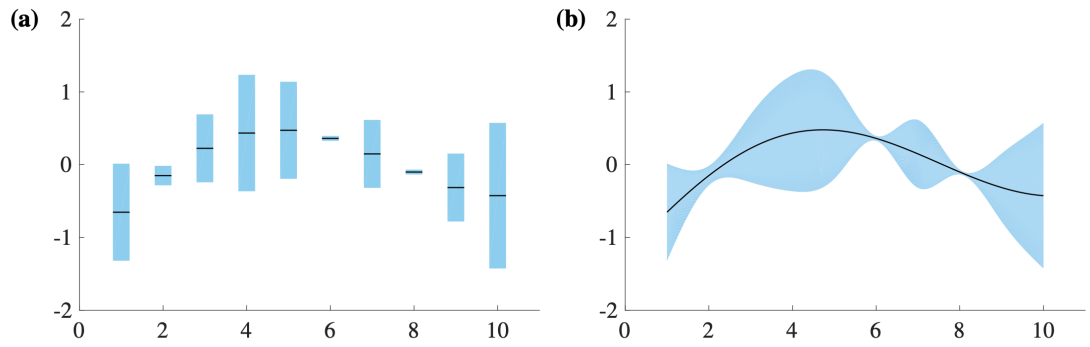

Figure 3.5: Left panel shows the distribution for 10 variables, with observations taken at 2, 6, and 8. The black lines show the posterior mean and blue shading shows the $\pm\sigma$. The right panel shows the same data, but with a dense evaluation of the posterior over the [1,10] interval. This shows how evaluation the posterior at a large number of points leads to a continuous posterior distribution. Figure from Rajpaul (2017).

(see Figure 3.5). In this case, the relationship between the variables is quantified by a [10,10] covariance matrix. Assuming that we take observations at times 2, 6, and 10, we can compute the conditional distribution of all these points as shown in the left panel of Figure 3.5, where the mean is shown with a black line and the $\pm\sigma$ is represented by the blue shaded area. Naturally, it is possible to extend this further, and rather than having 10 points we can have an arbitrary number (e.g. thousands). The posterior distribution of this is shown in the right panel of Figure 3.5. It can be seen that the posterior distribution appears to be continuous as opposed to discrete. It is possible to increase the number of points to infinity, meaning that x_i are infinitely close. In turn this means that the joint distribution over the infinitely many points x_i is equivalent to a distribution over a function space.

Formally, the multivariate Gaussian distribution is given by:

$$\mathbf{P}_{\mathbf{X}}\left(x_1,\ldots,x_n\right) = \frac{1}{\sqrt{(2\pi)^n|\mathbf{\Sigma}|}}\exp\left[-\frac{1}{2}(\mathbf{x}-\boldsymbol{\mu})^{\mathrm{T}}\mathbf{\Sigma}^{-1}(\mathbf{x}-\boldsymbol{\mu})\right] \tag{3.10}$$

Since there is nothing restricting the positions of these observations and points at which we can investigate the function, it can be said that we are working over a continuous space when using a Gaussian process. In contrast to the multivariate normal distribution $\mathcal{N}(\mu,\Sigma)$, which is defined by mean vector μ and

covariance matrix Σ, a Gaussian process, $\mathcal{GP}$, is defined by a mean function and a covariance function.

Realistically, thanks to the remarkable properties of Gaussian distributions, it is not necessary to use infinite-dimensional spaces. It is enough to asses the probability distribution of a finite number of points of interest and include any finite number of observations that we may have.

As previously mentioned, in the case of Gaussian processes it necessary to define a covariance function. In line with the standard formulation used, the *covariance kernel function* $k(x_i, x_j)$ will give us the covariance between any two points x_i, x_j. Because the covariance between i and j must be symmetric, it is required to fulfil the following condition $k(x_i, x_j) = k(x_j, x_i)$. In the case of GPs, an additional stipulation is that all linear combinations of variables have non-negative variances. As a consequence of this, the covariance function $k(x_i, x_j)$ must be positive semi-definite.

Using the above mentioned covariance function, it is then possible to compute the covariance matrix for the points that we are interested in. Assuming n points of interest (noted as $\mathbf{x}$), then the covariance matrix is defined as:

$$\mathbf{K}(\mathbf{x}, \mathbf{x}) = \begin{pmatrix} k(x_1, x_1) & k(x_1, x_2) & \cdots & k(x_1, x_n) \\ k(x_2, x_1) & k(x_2, x_2) & \cdots & k(x_2, x_n) \\ \vdots & \vdots & \ddots & \vdots \\ k(x_n, x_1) & k(x_n, x_2) & \cdots & k(x_n, x_n) \end{pmatrix} \tag{3.11}$$

As a consequence of the way we defined the covariance kernel function, by construction the covariance matrix $\mathbf{K}$ will be symmetric and positive semi-definite.

Learning an unknown function from data

Having defined the fundamental theory behind Gaussian processes, let us put it in practice and demonstrate how it can be used for semi-parametric modelling. For this let us define a dataset (n observations) $\mathcal{D} = \{(x_i, y_i)\}_{i=1}^{n} = (\mathbf{x}, \mathbf{y})$. Our goal is to find the relationship between the inputs x_i and outputs y_i. For simplicity, let us assume that:

$$y_i = g(x_i) + \epsilon_i \tag{3.12}$$

where $\epsilon_i \sim \mathcal{N}(0, \sigma^2)$ and $g(x)$ is an unknown function but with known properties. Hence, we can define a Gaussian process prior on the function g, incorporating any prior knowledge about g into the covariance structure of the GP:

$$g \sim \mathcal{GP}(0, k) \tag{3.13}$$

In the cases where we are able to quantify the mean of the relationship between x and y, such that $g(x) = \mu(x) + f(x)$, we can actually use a GP prior on f instead:

$$f \sim \mathcal{GP}(\mu, k) \tag{3.14}$$

where $\mu(x)$ is the GP mean function and k is the covariance kernel function (incorporating the known information about the covariance of the data). A key point is that the GP prior doesn't depend on the data, it only incorporates the general properties of the function f. A discussion about how to choose the mean and covariance functions is presented later in this chapter.

It is possible to include the observation errors into our model by simply adding them to the covariance function like:

$$k(x_i, x_j) \to k(x_i, x_j) + \sigma_i^2 \delta_{ij}$$

By definition, our dataset can be explained by the multivariate Gaussian distribution:

$$p(\mathbf{y}) = p(\mathbf{f}(\mathbf{x})) = \mathcal{N}(\boldsymbol{\mu}(\mathbf{x}), \mathbf{K}(\mathbf{x}, \mathbf{x})) \tag{3.15}$$

where $\mathbf{f}$ is our unknown function, $\boldsymbol{\mu}$ is the GP mean function and $\mathbf{K}$ is our covariance matrix as defined in equation 3.11.

Assume we want to evaluate the posterior distribution at position x_* which is not included in $\mathbf{x}$. Then, the joint probability distribution between the data and the added point can be written as[4]:

$$p\left(\begin{bmatrix} \mathbf{y} \\ y_* \end{bmatrix}\right) = \mathcal{N}\left(\begin{bmatrix} \boldsymbol{\mu}(\mathbf{x}) \\ \boldsymbol{\mu}(x_*) \end{bmatrix}, \begin{bmatrix} \mathbf{K}(\mathbf{x}, \mathbf{x}) & \mathbf{K}(\mathbf{x}, x_*) \\ \mathbf{K}(x_*, \mathbf{x}) & \mathbf{K}(x_*, x_*) \end{bmatrix}\right) \tag{3.16}$$

[4]By construction $\mathbf{K}(x_*, \mathbf{x}) = \mathbf{K}(\mathbf{x}, x_*)^{\mathrm{T}}$

This implies that the posterior distribution over y_* is a Gaussian distribution[5], with mean:

$$m_* = \mu(x_*) + \mathbf{K}(x_*, \mathbf{x})\,\mathbf{K}(\mathbf{x}, \mathbf{x})^{-1}(\mathbf{y} - \boldsymbol{\mu}(\mathbf{x})) \tag{3.17}$$

and covariance:

$$\sigma_* = K(x_*, x_*) - \mathbf{K}(x_*, \mathbf{x})\,\mathbf{K}(\mathbf{x}, \mathbf{x})^{-1}\mathbf{K}(\mathbf{x}, x_*)^{\mathrm{T}} \tag{3.18}$$

In general, it is desired to evaluate the posterior distribution at multiple positions, $\mathbf{x}_*$, as opposed to just one point. Then,by construction we want to evaluate $\mathbf{y}(\mathbf{x}_*)$. Extending equation 3.16 and following the steps presented in Eaton (1983), leads to:

$$p(\mathbf{y}_* \mid \mathbf{y}) = \mathcal{N}(\mathbf{m}_*, \mathbf{C}_*) \tag{3.19}$$

with

$$\mathbf{m}_* = \boldsymbol{\mu}(\mathbf{x}_*) + \mathbf{K}(\mathbf{x}_*, \mathbf{x})\,\mathbf{K}(\mathbf{x}, \mathbf{x})^{-1}(\mathbf{y} - \boldsymbol{\mu}(\mathbf{x})) \tag{3.20}$$

and

$$\mathbf{C}_* = \mathbf{K}(\mathbf{x}_*, \mathbf{x}_*) - \mathbf{K}(\mathbf{x}_*, \mathbf{x})\,\mathbf{K}(\mathbf{x}, \mathbf{x})^{-1}\mathbf{K}(\mathbf{x}, \mathbf{x}_*)^{\mathrm{T}} \tag{3.21}$$

A crucial point of the above equations is that it actually allows us to learn the unknown function f from the observations subject to the assumptions we have made about its mean and covariance. Noting the generalisation that defining a GP on the function f allows us to compute the GP posterior distribution:

$$f \mid \mathcal{D} \sim \mathcal{GP}(\mu_{\mathcal{D}}, k_{\mathcal{D}})$$

where $\mu_{\mathcal{D}}$ is the vector of mean values corresponding to each x_i, and $k_{\mathcal{D}}$ provides the uncertainty on the posterior estimate. These are defined as:

$$\mu_{\mathcal{D}}(x) = \mu(x) + \mathbf{K}(x, \mathbf{x})\mathbf{K}^{-1}(\mathbf{y} - \boldsymbol{\mu}(\mathbf{x})) \tag{3.22}$$

and

$$k_{\mathcal{D}}(x_i, x_j) = k(x_i, x_j) - \mathbf{K}(x_i, \mathbf{x})\,\mathbf{K}^{-1}\mathbf{K}(\mathbf{x}, x_j) \tag{3.23}$$

Using these equations we can now learn an unknown function from the data and evaluate it at at any desired location with the expected errors.

[5]For the proof I direct the reader to page 116-117 in the book titled *Multivariate Statistics: a Vector Space Approach* (Eaton, 1983).

3.2.3 Gaussian process covariance function

Knowing how to choose the covariance kernel function for a Gaussian process is a complex matter. I showed how a GP can be used to model an unknown function, and stated that any prior knowledge about the general properties of the function should be incorporated into the covariance function. As such it is necessary to elaborate what we mean by these properties. In the context of astrophysics and especially exoplanets, we usually work with time-series, and as such, consider the following thought experiment. Assume we are measuring the flow rate of a river and take some observations. It is intuitive, that two measurements taken minutes apart will be strongly correlated, whilst measurements taken 1000 years apart may have little significance on each other. This is because there are lot of variables that can drastically alter the results (quantity of rainfall, climate change, changes in the landscape, or even human intervention - e.g. the building of a dam). As such, it can be established that the important component is the distance between observation x_i and x_j. This behaviour can be quantified using the so called 'stationary' covariance functions, which only depend on $|x_i - x_j|$. This family of functions includes some of the most commonly used covariance functions including the squared exponential (SE) kernel and the Matérn class kernels.

Whereas in parametric modeling the functions are governed by parameters, in the case of Gaussian processes the covariance functions are controlled by so called 'hyper-parameters'. These hyper-parameters control the main behaviour of the kernel and incorporate information about the covariance, not affecting the functional form of functions drawn from the GP.

Let us explore the most popular kernels and introduce the kernels of particular importance for the research presented in this thesis.

White noise kernel

The simplest covariance matrix is computed using the white noise kernel:

$$k_{\mathrm{WN}}\left(x_i, x_j\right) = \sigma_i^2 \delta_{ij} \tag{3.24}$$

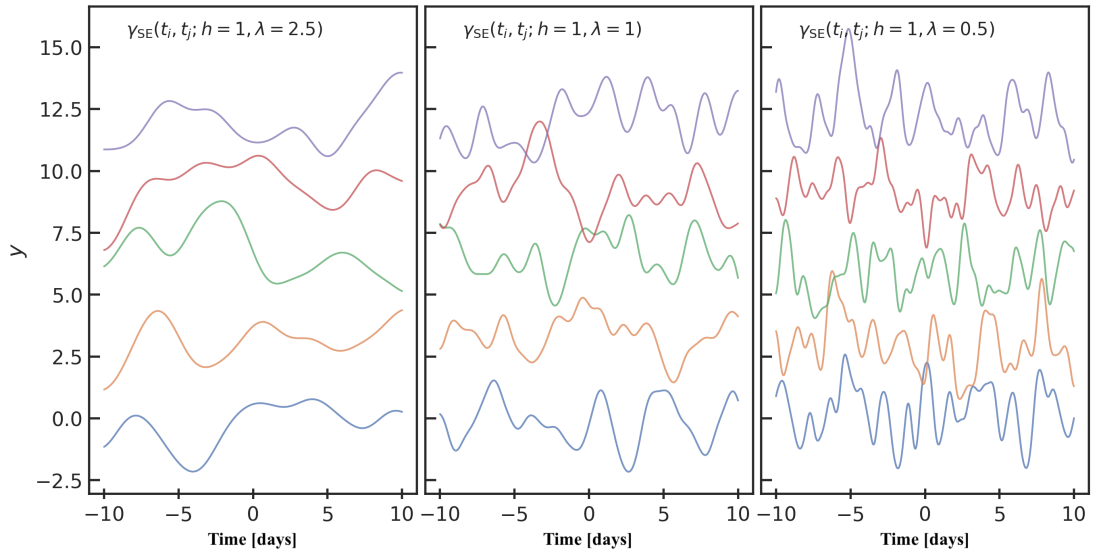

Figure 3.6: SE kernel GP samples created with different length scale hyper-parameter. The three different hyper-parameter sets used to create the 5 SE GP samples are ($h = 1$, $\lambda = 2.5$),($h = 1$, $\lambda = 1$),($h = 1$, $\lambda = 0.5$) respectively. Note that in all three cases the mean function is 0. It is easy to notice that the GPs in the left panel are the 'smoothest' (as in vary slower) and as λ decrease, the drawn functions become more chaotic.

where σ_i is the error of observation x_i, and δ_{ij} is the Kronecker delta function. This kernel assumes that the observations are independent (no covariance) and it creates a diagonal covariance matrix. It is used to account for uncertainties in the data.

Squared exponential kernel

A widely popular kernel is the squared exponential kernel, defined as:

$$k_{\text{SE}}(x_i, x_j) = h^2 \exp\left(\frac{-(x_i - x_j)^2}{2\lambda^2}\right) \tag{3.25}$$

where h and λ are the two hyper-parameters. In this case, h is the output scale parameter. Also possible to define it as an amplitude that can be thought of as a scale factor that controls the typical deviation from the mean. Meanwhile, λ is the length scale, this can be interpreted as the characteristic distance for which two points are strongly correlated. These functions are very smooth, thus arguably not suitable for modelling some physical processes (Stein, 1999). I illustrate the effect of changing the length scale hyper-parameter in Figure 3.6. It shows how

increasing the length scale leads to functions that vary slowly and decreasing it, we obtain functions that behave more chaotically.

Matérn class kernels

The Matérn class kernels are defined as:

$$k_{\mathrm{M},\nu} = h^2 \frac{2^{1-\nu}}{\Gamma(\nu)} \left(\frac{\sqrt{2\nu}\,|x_i - x_j|}{\lambda} \right)^{\nu} \mathbb{B}_\nu \left(\frac{\sqrt{2\nu}\,|x_i - x_j|}{\lambda} \right) \tag{3.26}$$

where h and λ are the output and length scales, $\Gamma()$ is the standard Gamma function, and $\mathbb{B}()$ is modified Bessel function of second order. The hyper-parameter ν controls the degree of differentiability, which in turn affects the smoothness of these functions.

For half integer values of ν, and assuming the notation $D_\nu = |x_i - x_j|$, the kernel functions can be simplified to:

$$k_{\mathrm{M},\nu} = h^2 \exp\left(-\frac{D_\nu \sqrt{2\nu}}{\lambda} \right) \frac{(\nu - 1/2)!}{(2\nu - 1)!} \sum_{i=0}^{\nu} \frac{(\nu - 1/2 + i)!}{i!(\nu - 1/2 - i)!} \left(\frac{2D_\nu \sqrt{2\nu}}{\lambda} \right)^{\nu - 1/2 - i} \tag{3.27}$$

In the limit of $\nu \to \infty$, the Matérn kernel becomes equivalent to the SE kernel. The simplest Matérn kernel is for $\nu = \frac{1}{2}$, which is called the Ornstein–Uhlenbeck (OU) kernel:

$$k_{\mathrm{M12}}(x_i, x_j) = h^2 \exp\left(\frac{-|x_i - x_j|}{\lambda} \right) \tag{3.28}$$

The functions produced by this covariance function can be differentiated only once and are very 'rough'.

The other Matérn functions of interest are given by setting $\nu = \frac{3}{2}$ and $\nu = \frac{5}{2}$ and are defined as:

$$k_{\mathrm{M32}} = h^2 \left(1 + t_{3/2}\right) \exp\left(-t_{3/2}\right) \tag{3.29}$$

with $t_{3/2} \equiv \sqrt{3}\,|x_i - x_j|\,\lambda^{-1}$

$$k_{\mathrm{M52}} = h^2 \left(1 + t_{5/2} + \frac{t_{5/2}^2}{3}\right) \exp\left(-t_{5/2}\right) \tag{3.30}$$

with $t_{5/2} \equiv \sqrt{5}\,|x_i - x_j|\,\lambda^{-1}$. These are the two kernel functions used in Chapter 6 to model stellar spectra. Specifically the Matérn 3/2 function is adopted as the default covariance kernel function.

Building new kernels

A beautiful property of Gaussian processes is that any linear combination or product of covariance kernels will produce a valid kernel. As such, it is possible to define a covariance kernel over multidimensional input spaces (n-dimensions).

$$k\left(x_i, x_j\right) = \prod_n k^n\left(x_i^{(n)}, x_j^{(n)}\right) \tag{3.31}$$

where k^n is a kernel over the n^{th} input dimension, $x_i^{(n)}$ and $x_j^{(n)}$ denote the values of the input in the n^{th} dimension at positions i and j respectively. As the product of covariances is a valid covariance, equation 3.31 is a valid covariance over the multi-dimensional input space.

In a similar manner, following the work of Osborne (2010), it is possible to model the relationship between multiple time-series in order to obtain multidimensional outputs. To define this, let us assume we have multiple time-series (each with x observations). Then, using an artificial multidimensional input space [l,x], with label l as the index for the outputs, we can write:

$$k\left(\left[l_m, x_i\right], \left[l_n, x_j\right]\right) = k_x\left(x_i, x_j\right) k_l\left(l_m, l_n\right) \tag{3.32}$$

where $l_m$and l_n are the labels of the corresponding time-series.

Periodic kernels

Another family of kernels are the periodic kernels, which allow us to formulate prior distributions over periodic functions. For example, one of these is the periodic squared exponential function originally derived by David MacKay in 1988, and it is defined as:

$$k_{\text{per-SE}}\ \left(x_i, x_j\right) = h^2 \exp\left(\frac{-2\sin^2\left(\frac{\pi(x_i - x_j)}{P}\right)}{\lambda^2}\right) \tag{3.33}$$

where h is similar to an amplitude and P is the period. The hyper-parameter λ in this case controls the harmonic complexity of the functions. In layman terms, it controls the 'smoothness' of the variations within one period. This means that large values correspond to sinusoidal functions, meanwhile small values add complexity to

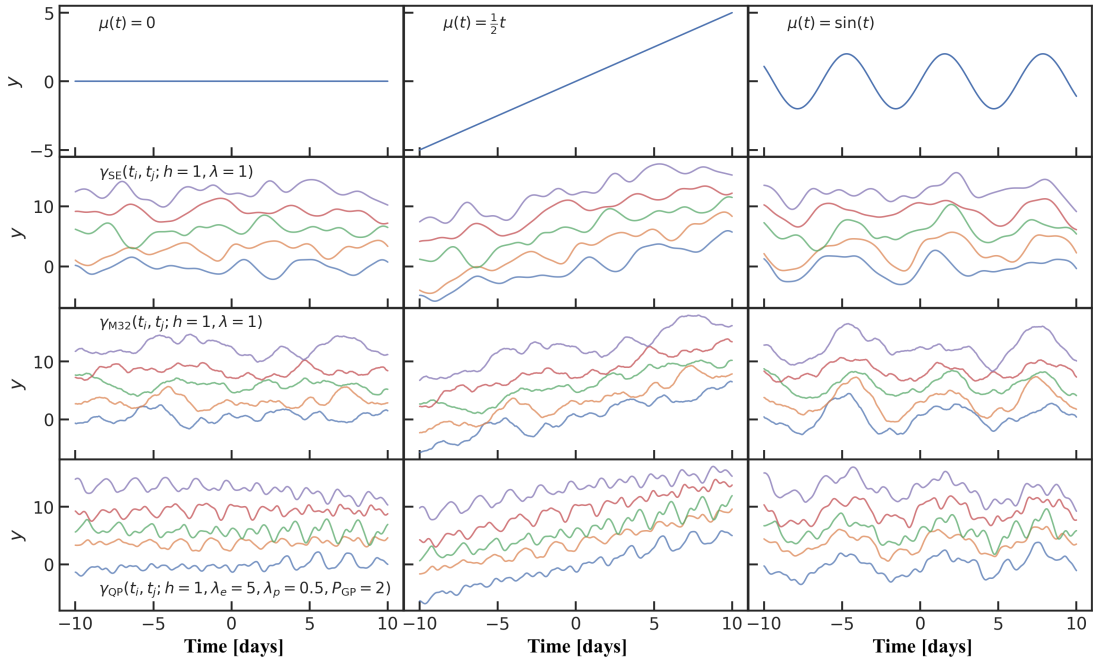

Figure 3.7: GP samples created with different mean and covariance functions. The left, middle, and right panels corresponds to GPs with mean functions $\mu = 0$, $\mu = 1/2t$, and $\mu = \sin(t)$) respectively. Top panel shows a plot with only the mean functions. The second, third, and fourth panels show five GPs samples for the squared exponential (with $h = 1$, $\lambda = 1$), Matérn 3/2 (with $h = 1$, $\lambda = 1$), and quasi-periodic kernels (with $h = 1$, $\lambda_e = 5$, $\lambda_p = 0.5$, and $P_{\text{GP}} = 2$) respectively. Note that although the 5 samples are defined by the same hyper-parameters, the drawn function can be very different.

the underlying functions. Thanks to the built in flexibility of this kernel, it is possible to model periodic functions without the the limitation of purely sinusoidal functions.

Quasi-periodic kernel

Combining periodic and stationary kernels allows us to model periodic signals that can change over time. This is exactly what we want in exoplanetary science when modelling stellar variability. The simplest quasi-periodic kernel is obtained from multiplying the periodic squared exponential kernel with the simple squared exponential kernel, and is defined as:

$$k_{\text{QP}-\text{SE}}(x_i, x_j) = h^2 \exp\left(-\frac{\sin^2\left(\frac{\pi(x_i - x_j)}{P}\right)}{2\lambda_{\text{p}}^2} - \frac{(x_i - x_j)^2}{2\lambda_{\text{e}}^2}\right) \tag{3.34}$$

where the 4 hyper-parameters can be described as: h can be thought of as the amplitude, P is the period of the signal, λ_p is the harmonic complexity - structure

within one period, and λ_e controls how quickly the periodic signal evolves.

A few examples of drawn GP functions are shown in Figure 3.7, for the SE, Matérn 3/2 and quasi-periodic kernels. The top row shows three different selections for the mean function, corresponding to $\mu = 0$, $\mu = 1/2t$, and $\mu = \sin(t)$), respectively. The second, third and fourth rows show the samples for the SE kernel, the Matérn 3/2 and the quasi-periodic kernel respectively. It shows that even when the mean function and the GP hyper-parameters are the same, the functional form of the GPs drawn can vary.

3.2.4 Gaussian process mean function

In general, the mean function of the Gaussian process is used to model any known physical processes that are well understood and can be separated out from the stochastic or unknown variations of the underlying function. In layman terms, this means that all the parametric model components are incorporated into the mean function, whilst the less understood signals are accounted for by the covariance function. For example, in the case of exoplanet searches in RV time-series, we are interested in modelling two physical process. The first one is the periodic signals induced by the presence of planets, which can very easily be parametrised as the sum of Keplerian functions. The second process involves the modeling of stellar activity signals, which is less understood and difficult to parametrise. As such, it makes sense to incorporate the Keplerian signals into the mean function and allow for the GP covariance function to model the stellar variability. In practice, due to the way the likelihood of a Gaussian process is defined, it is permitted to subtract any known signals from the data and then compute the likelihood for a zero mean GP. I tend to use this approach as it is more convenient from a 'coding' point of view, it allows the code to be modular and also less complex.

3.2.5 Hyper-parameter and model inference

In the case of Gaussian processes models, inference is used to refine the GP prior distributions that are defined over a family of functions, to distributions that have

a more accurate representation of the observations. Let us assume the case of a Gaussian process that has a mean function defined by hyper-parameters $\boldsymbol{\theta}$, and covariance function governed by hyper-parameters $\boldsymbol{\Phi}$. Then, the log marginal likelihood, $\ln \mathcal{L} = \ln p(\mathbf{y} \mid \mathbf{x}, \boldsymbol{\theta}, \boldsymbol{\Phi})$, of our observations $\mathbf{y}$ can be obtained by marginalising over the functions, and is defined as (Rasmussen & Williams, 2006):

$$\ln \mathcal{L}(\boldsymbol{\theta}, \boldsymbol{\Phi}) = -\frac{1}{2}\left(N_{\text{obs}} \ln 2\pi + \ln |\mathbf{K}| + \mathbf{r}^{\top}\mathbf{K}^{-1}\mathbf{r}\right) \tag{3.35}$$

where $\mathbf{r} = \mathbf{y} - \boldsymbol{\mu}$ is the residual vector of the data $\mathbf{y}$ and the mean function $\boldsymbol{\mu} = \mu(\mathbf{t})$ evaluated at the times $\mathbf{t}$. N_{obs} is the number of observations, $|\mathbf{K}|$ is the determinant of the covariance matrix, and covariance matrix $\mathbf{K}$ is given by kernel function $\gamma(t_i, t_j)$. Notice that I have changed notation from $k(x_i, x_j)$ to $\gamma(t_i, t_j)$ in order to avoid confusion between the covariance function and covariance elements. An interesting observation is that $-1/2 \ln|\mathbf{K}|$ is a penalty term that quantifies the complexity of the model. As such, GPs have a built in tool to prevent over-fitting.

To infer the posterior distributions of $\boldsymbol{\theta}$ and $\boldsymbol{\Phi}$, we rely on Bayesian statistics[6]. As such, we simply multiply the log-likelihood with prior $p(\boldsymbol{\theta}, \boldsymbol{\Phi})$, resulting in $p(\boldsymbol{\theta}, \boldsymbol{\Phi}|\mathbf{y}) \propto p(\mathbf{y}|\boldsymbol{\theta}, \boldsymbol{\Phi})\, p(\boldsymbol{\theta}, \boldsymbol{\Phi})$

In order to compute the Bayesian evidence it is required to marginalise over all model parameters. Let us assume a given model $\mathcal{M}_*$, defined by a mean and covariance function, characterised by hyper-parameters $\boldsymbol{\Psi}_*$ (combination of $\boldsymbol{\theta}_*$ and $\boldsymbol{\Phi}_*$), then the marginal likelihood is:

$$p(\mathbf{y} \mid \mathcal{M}_*) = \int p(\mathbf{y} \mid \boldsymbol{\Psi}_*, \mathcal{M}_*)\; p(\boldsymbol{\Psi}_* \mid \mathcal{M}_*)\; d\boldsymbol{\Psi}_* \tag{3.36}$$

For model comparison, we are usually interested in the ratio of posteriors of the two models ($\mathcal{M}_*$ and $\mathcal{M}_1$), also called posterior odds(Gregory, 2005):

$$\frac{p(\mathcal{M}_* \mid \mathbf{y})}{p(\mathcal{M}_1 \mid \mathbf{y})} = \frac{\frac{p(\mathbf{y}|\mathcal{M}_*)\cdot p(\mathcal{M}_*)}{p(\mathbf{y})}}{\frac{p(\mathbf{y}|\mathcal{M}_1)\cdot p(\mathcal{M}_1)}{p(\mathbf{y})}} = \frac{\int p(\mathbf{y} \mid \Psi_*, \mathcal{M}_*)\, p(\Psi_* \mid \mathcal{M}_*)\, d\Psi_*}{\int p(\mathbf{y} \mid \Psi_1, \mathcal{M}_1)\, p(\Psi_1 \mid \mathcal{M}_1)\, d\Psi_1} \cdot \frac{p(\mathcal{M}_*)}{p(\mathcal{M}_1)} \tag{3.37}$$

[6]Bayes' theorem: $P(A \mid B) = \frac{P(B|A)P(A)}{P(B)}$

In above equation, the ratio of marginal likelihoods is the so called called Bayes factor (Jeffreys, 1939) $\mathcal{K}$ and is defined as:

$$\mathcal{K} = \frac{p\left(\mathbf{y} \mid \mathcal{M}_{*}\right)}{p\left(\mathbf{y} \mid \mathcal{M}_{\mathbf{1}}\right)} = \frac{\int p\left(\mathbf{y} \mid \Psi_{*}, \mathcal{M}_{*}\right) p\left(\Psi_{*} \mid \mathcal{M}_{*}\right) d\Psi_{*}}{\int p\left(\mathbf{y} \mid \Psi_{1}, \mathcal{M}_{1}\right) p\left(\Psi_{1} \mid \mathcal{M}_{1}\right) d\Psi_{1}} \tag{3.38}$$

Another way to compare different models is to use the Bayesian Information Criteria, given by:

$$\mathrm{BIC} = k \ln(n) - 2 \ln(\widehat{L}) \tag{3.39}$$

where k is the number of parameters, n is the number of observations and $\widehat{L}$ is the maximum likelihood.

A discussion around how to evaluate the posteriors and the marginal likelihood is presented in Section 3.4.

3.3 GP framework

Using Doppler spectroscopy for detecting and characterising exoplanets can be challenging. This because the physical processes that take place in stars or on their surface generate signals (nuisance signals) contaminate the RV time-series. These signals are often very complex and it is difficult to model using traditional approaches. In the case of young stars the situation is even worse as the stellar activity induced variations are often much bigger than the reflex motion induced by the planets. As shown later in this thesis (see Chapter 4), in the case of AU Microscopii, the stellar variability is almost 100 times bigger than the signal of the orbiting exoplanets, making detection extremely challenging.

In order to model the stellar activity, Rajpaul et al. (2015) proposed a GP framework that models the RV time-series simultaneously with the activity indicators in an effort to filter the stellar contamination (see Figure 3.8 for a schematic of the assumed model). This is achieved using a multidimensional GP approach which is detailed in this section.

In general, a GP activity model assumes that the stellar induced signals present in the observations can be described by a Gaussian process. The GP framework,

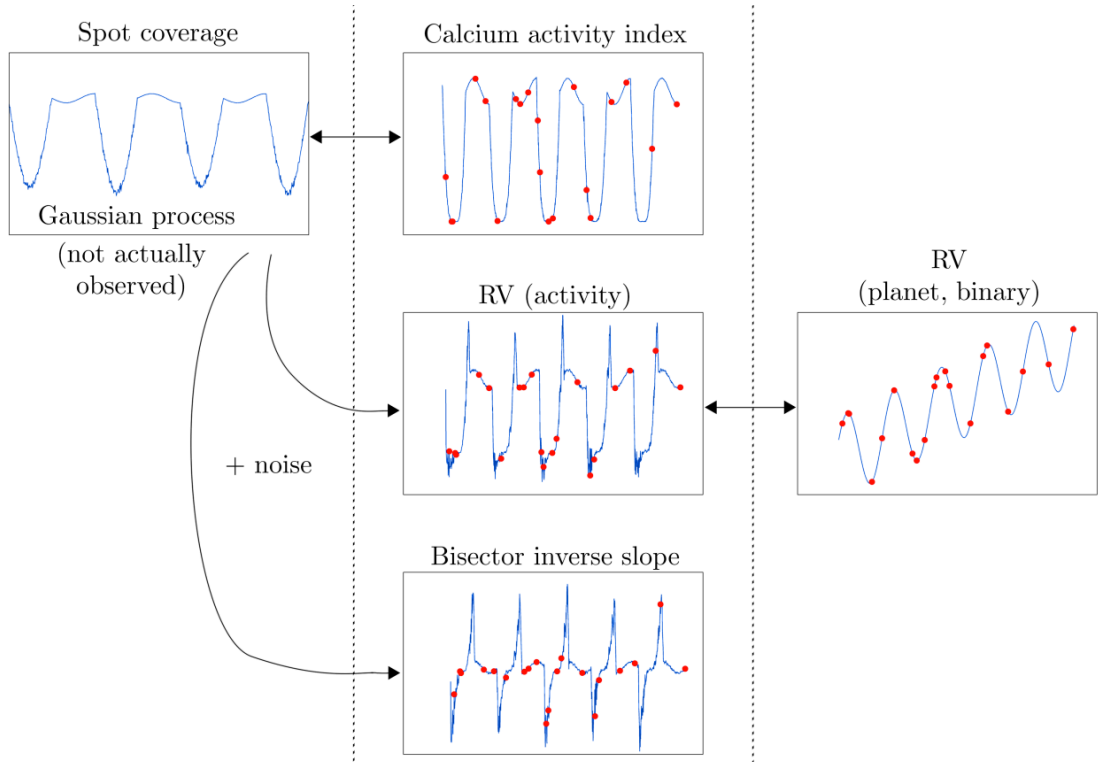

Figure 3.8: Schematic sketch of the GP framework for joint modelling of RVs with ancillary activity indicators. Figure from Rajpaul et al. (2015).

constrains this model further, by assuming that all time-series (activity indicators and RVs) can be explained by the same latent GP and its time derivative. Extensions to this model were proposed by Jones et al. (2017) and Gilbertson et al. (2020), which add higher derivative terms and generalise the work to include an arbitrary set of activity indicators.

Physical motivation

A12 has shown that there is an inherent connection between the stellar-induced RV variations and the surface of the star that is covered by active regions. Building on the ideas presented in the F F' method (see Chapter 2.4.2 for details), it can be assumed that some function $G(t)$ (not directly observed) is able to quantify as a function of time the fraction of the stellar surface that is covered by active regions. These active regions will induce different variations in the photometric and spectroscopic observations of the star (RVs and the different activity indicators).

As presented in Aigrain et al. (2012), some are only affected by the projected area (hence $G(t)$), whilst others are also affected by the local radial velocity at the location of the spots, meaning that they can be described as linear combinations of this underlying function and its time derivatives. Note that in the notation and formalism adopted next, it is assumed that the GP function $G(t) = F^2$ (from the original work) and thus the time derivative $\dot{G}(t) = F\dot{F}$.

Defining the GP framework

Building on the description of how each time-series depends on the stellar surface covered in active regions presented in Chapter 2.4.2, it is easy to notice that contemporaneous time-series (RVs, activity indicators) can be modelled simultaneously. The assumption here being that they are all described by the same underlying function and its derivatives. The advantage of modelling everything together is that whilst RVs contain both stellar signals and planet-induced variations, the ancillary time-series are only dependent (sensitive) to activity. As such, this connection can be exploited to constrain the activity signal and help our efforts of separating activity induced signals from planetary signals.

Let us consider the case of a dataset that consists of N time-series ($\mathcal{A}_{i=1}, \ldots, N$), each comprising of M individual observations. Then, following the above mentioned conditions, we can say:

$$\begin{aligned} \mathcal{A}_1 &= A_1 G(t) + B_1 \dot{G}(t) \\ &\vdots \\ \mathcal{A}_N &= A_N G(t) + B_N \dot{G}(t) \end{aligned} \tag{3.40}$$

where $A_1, B_1, \cdots, A_N, B_N$ are the free parameters of our model that describe the dependence of each time-series on the latent GP function $G(t)$ and its time derivative $\dot{G}(t)$. Thanks to the flexible property of GPs that any affine operation on a GP results in a GP, each of these time-series is a GP. Then, using the work of Osborne (2010) presented in the context of building new kernels, we can define the relationship

between the different time-series. As such, the covariance between two observations t_i and t_j and time-series A_l and A_m, is given by:

$$\begin{aligned} k^{l,m}(i,j) = A_l A_m \gamma^{G,G}(i,j) + B_l B_m \gamma^{dG,dG}(i,j) \\ + A_l B_m \gamma^{G,dG}(i,j) + A_m B_l \gamma^{dG,G}(i,j) \end{aligned} \tag{3.41}$$

where $\gamma^{G,G}(i,j)$ is the covariance between observations of G at times t_i, t_j; $\gamma^{dG,dG}(i,j)$ is the covariance between an observation of G at time t_i and and observation of $\dot{G}$ at time t_j; similarly, $\gamma^{G,dG}(i,j)$ describes the covariance between $\dot{G}(t_i)$ and $G(t_j)$; and $\gamma^{dG,G}(i,j)$ denotes the covariance of two observations of $\dot{G}$ at times t_i, t_j.

For simplicity and making it easier to follow let us state the quasi-periodic kernel again:[7]:

$$\gamma_{\mathrm{QP}}\left(t_i, t_j\right) = h^2 \exp\left[-\frac{\sin^2\left[\pi\left(t_i - t_j\right)/P_{\mathrm{GP}}\right]}{2\lambda_{\mathrm{p}}^2} - \frac{\left(t_i - t_j\right)^2}{2\lambda_{\mathrm{e}}^2}\right] \tag{3.42}$$

Then, assuming the notation $\tau \equiv \frac{2\pi(t_i - t_j)}{P_{\mathrm{GP}}}$, and ignoring the amplitude term which is absorbed by the free parameters (A_i and B_i), the covariance terms between the different observations for the QP kernel can be defined as:

$$\gamma_{\mathrm{QP}i,j}^{G,G} = \exp\left[-\frac{\sin^2(\tau/2)}{2\lambda_{\mathrm{p}}^2} - \frac{\left(t_i - t_j\right)^2}{2\lambda_{\mathrm{e}}^2}\right] \tag{3.43}$$

$$\gamma_{\mathrm{QP}i,j}^{G,dG} = -\gamma_{\mathrm{QP}i,j}^{dG,G} = \gamma_{\mathrm{QP}i,j}^{G,G}\left[\frac{\pi \sin\tau}{P_{\mathrm{GP}}\, 2\lambda_{\mathrm{p}}^2} + \frac{t_i - t_j}{\lambda_{\mathrm{e}}^2}\right] \tag{3.44}$$

$$\gamma_{\mathrm{QP}i,j}^{dG,dG} = \gamma_{\mathrm{QP}i,j}^{G,G}\left[-\left(\frac{\pi \sin\tau}{P_{\mathrm{GP}}\, 2\lambda_{\mathrm{p}}^2}\right)^2 - \frac{\tau \sin\tau}{2\lambda_{\mathrm{p}}^2\lambda_{\mathrm{e}}^2} + \frac{\pi^2\cos\tau}{P_{\mathrm{GP}}^2\lambda_{\mathrm{p}}^2} - \left(\frac{t_i - t_j}{\lambda_{\mathrm{e}}^2}\right)^2 + \frac{1}{\lambda_{\mathrm{e}}^2}\right] \tag{3.45}$$

Then the joint covariance matrix of all the time-series we want to model can be constructed, such as:

$$\boldsymbol{K}_{\mathrm{activity}} = \begin{pmatrix} \boldsymbol{k}^{1,1} & \boldsymbol{k}^{1,2} & \cdots & \boldsymbol{k}^{1,N} \\ \boldsymbol{k}^{2,1} & \boldsymbol{k}^{2,2} & \cdots & \boldsymbol{k}^{2,N} \\ \vdots & \vdots & \ddots & \vdots \\ \boldsymbol{k}^{N,1} & \boldsymbol{k}^{N,2} & \cdots & \boldsymbol{k}^{N,N} \end{pmatrix} \tag{3.46}$$

[7]Note the slightly different notation used.

where each $\mathbf{k}^{l,m}$ is computed using equation 3.41 for any valid kernel γ. Note that $\mathbf{k}^{l,m}$ is a covariance matrix itself of dimension $[M, M]$ (assuming M observations).

By construction $\mathbf{K}$ has to be a valid covariance matrix and as such we can use it for GP regression. In addition, by default it is symmetric and positive semi-definite[8]. As a consequence it is only ever necessary to compute the upper triangle ($\boldsymbol{k}^{j,i} = (\boldsymbol{k}^{i,j})^\top$).

Having built a valid covariance function for the joint modelling of multiple time-series, we can infer the parameters of the multidimensional GP by using equation 3.35 for the marginal log-likelihood.

It is possible to apply the same methodology to different kernels, the only requirement is that $\gamma_{i,j}^{G,G}$ is a valid covariance kernel. For an implementation of different kernels please refer to `pyaneti` and `spleaf` (Rajpaul et al., 2015; Barragán et al., 2022; Delisle et al., 2020b).

3.4 Posterior distribution - posterior sampling

Bayes' Theorem (Bayes & Price, 1763) provides a robust framework to compute the posterior (conditional probability), defined as:

$$P(M \mid D) = \frac{P(D \mid M)P(M)}{P(D)}$$

where we aim to compute the probability of model M (defined by parameters Φ_i), based on data D.

In general, we are often interested in the posterior distribution of each parameter Φ_i not just the posterior distribution of the full model. As such, the parameter estimation can be computer by ignoring the Bayesian evidence $P(D)$. Hence, we can use $P(D|M)P(M)$ to obtain posterior distribution over each parameter, marginalised over the other parameters. It is important to note that the Bayesian evidence is crucial when comparing between different models (see, e.g., Gelman et al., 2004).

[8]Depending on the chosen covariance kernel it can be a Hermitian matrix. (e.g. SE kernel, this is not the case for the QP kernel)

In order to compute the posterior distribution for a desired parameter Φ_i, we can marginalise over it by integrating $P(D|M)P(M)$ over the remaining $\Phi_{j\neq i}$ parameters. In this manner we are able to calculate the marginal posterior distribution for each parameter Φ_i. This can be done either analytically or numerically. However, in astrophysics this is mostly done numerically. As such, there numerous numerical methods that are commonly used to sample the parameter space in order to compute the marginal posterior distributions from a collection of data points.

Two of the most common sampling methods are *Markov chain Monte Carlo* and *nested sampling* algorithms which are briefly presented below.

3.4.1 Markov-chain Monte Carlo

Adopting the definition used by Sharma (2017), a Markov chain is defined as a sequence of stochastic variables $X_1, \ldots, X_n$, so that the probability of each only depends on the previous one, implying that past and future states are independent. When using random numbers to create the Markov chain, it is called Markov chain Monte Carlo (MCMC). As such we can take a random sample of points described by the vector $\mathbf{\Phi}$ from the parameter space that we want to sample.

There is an extensive literature available on MCMC sampling methods, with numerous 'flavours' available. The simplest MCMC algorithm relies on the Metropolis-Hastings algorithm (Metropolis et al., 1953; Hastings, 1970). This simple implementation of Markov chain Monte Carlo draws new samples for the parameters randomly and computes the likelihood for the proposed 'step'. It accepts the move if the ratio of the likelihoods , $\frac{P(M(\Phi)|D)}{P(M(\Phi)_{new}|D)}$[9], is smaller or equal to a random number between 0 and 1. Other approaches to MCMC include the ensemble sampler algorithm (Goodman & Weare, 2010) that is implemented in `pyaneti` (Barragán et al., 2019a) and **emcee** (Foreman-Mackey et al., 2013), as well as Hamiltonian Monte Carlo (Duane et al., 1987). The ensemble sampler uses multiple chains that evolve in order to compute the posteriors. Hamiltonian Monte Carlo introduces an additional 'momentum vector' in order to try and avoid random walk behaviour.

[9]This reduces to $\frac{P(D|M(\Phi))}{P(D|M(\Phi_{\rm new})}$

This should ensure that the parameters are sampled in bigger steps and the chains converge to the target distribution faster.

In the case of MCMC methods it is necessary to test for convergence (meaning that the posterior distribution from the chains reflects the true posterior). The most commonly used convergence diagnostic is the Gelman-Rubin test (Gelman & Rubin, 1992). This involves running M different chains with different starting conditions. We than define *burn-in period*, in which we allow the chains to evolve to search for the highest likelihood. Once we are confident that the chains reached the parameter space with the highest likelihood, we discard these steps that were part of the burn-in and allow the MCMC to sample the posterior. In the cases where the chains are highly correlated, we *thin* them, meaning that we discard some data points such that the remaining N steps are independent. After this we compute the posterior mean for each parameter for each chain:

$$\hat{\Phi}_{\mathrm{m}} = \frac{1}{\mathrm{N_m}} \sum_{i}^{\mathrm{N_m}} \Phi_i^{\mathrm{m}}$$

and the intra-chain variance:

$$\sigma_{\mathrm{m}}^2 = \frac{1}{\mathrm{N_m} - 1} \sum_{i}^{\mathrm{N_m}} \left(\Phi_i^{\mathrm{m}} - \bar{\Phi}_{\mathrm{m}} \right)^2$$

Next, the mean of all the chains is calculated:

$$\bar{\Phi} = \frac{1}{\mathrm{M}} \sum_{\mathrm{m}}^{\mathrm{M}} \bar{\Phi}_{\mathrm{m}}$$

together with how individual means vary around the joint mean:

$$B = \frac{\mathrm{N}}{\mathrm{M} - 1} \sum_{\mathrm{m}=1}^{\mathrm{M}} \left(\bar{\Phi}_{\mathrm{m}} - \bar{\Phi} \right)^2$$

and the averaged variance of all the chains:

$$\mathrm{W} = \frac{1}{\mathrm{M}} \sum_{\mathrm{m}=1}^{\mathrm{M}} \sigma_{\mathrm{m}}^2$$

Finally, we define:

$$\bar{\mathrm{V}} = \frac{\mathrm{N} - 1}{\mathrm{N}} \mathrm{W} + \frac{\mathrm{M} + 1}{\mathrm{MN}} \mathrm{B}$$

which is an unbiased estimator for the true variance. Under the assumption that the chains converged, W should be an unbiased estimator too. As such we compute:

$$\mathrm{R} = \sqrt{\bar{\mathrm{V}}/\mathrm{W}}$$

which in the case of convergence should be ≈ 1.

3.4.2 Nested Sampling

Originally developed by John Skilling (Skilling, 2006), the nested sampling algorithm focuses on approximating marginalization integrals. It allows to numerically compute the Bayes factor for model comparison in addition to generating samples from the posterior distribution, $P(\Phi|D, M)$. In summary, the algorithm relies on iteratively computing the likelihood and evaluating its weight. The smallest likelihood value is saved together with the corresponding weight, after which an MCMC run is used to sample higher likelihood regions. Two widely used implementations of this algorithm include **Multinest** (Feroz et al., 2009; Buchner, 2016) and **PolyChord** (Handley et al., 2015).

In general MCMC algorithms are faster than nested sampling techniques, but in the case of multi-modal distributions they risk getting stuck and not exploring the parameter space properly. By contrast, nested sampling algorithms albeit slower, they have been optimised to deal with multi-modal distributions (sampling each peak individually) and are able to deal with a bigger number of parameters. Another difference between the two algorithms is that whilst nested sampling provides the evidence for the models, MCMC in general is unable to provide it and as such it makes model comparison challenging.

In this thesis, I have originally used **Multinest** and **PolyChord** for exploring the posteriors of the GP framework, but transitioned to using `pyaneti` for the final analysis of the AU Mic dataset. In addition, I have used **emcee** for posterior sampling in the case of extracting radial velocities using GPs.

The risk of a wrong decision is preferable to the terror of indecision.

— Moses ben Maimon (Maimonides)

4

AU Mic - measuring the masses of two young planets

Contents

In this chapter we report on the results of a 10-month intensive monitoring

campaign on AU Mic with HARPS, which aims to characterise the activity-induced RV signal of the host star sufficiently to detect the two transiting planets. Although activity signals are larger in the optical than in the near-IR, they are also better characterised, as standard RV pipelines extract a number of chromospheric and line-shape indices that can be used as activity indicators. As our approach relies on modelling the effects of stellar activity alongside the planetary signal, rather than filtering one to reveal the other, working in a regime where activity signals are strong can be an advantage rather than an impediment.

This chapter is structured as follows. Section 4.1 introduces the AU Mic system and provides context for the presented work. Section 4.2 describes the details of the observations and data reduction, as well as the identification of epochs affected by stellar flares, which were discarded from the rest of the analysis. The description of the GP framework we use to model the RVs and activity indicators is presented in Chapter 3.3. In Section 4.3, a detailed description of the exact model that we selected is presented, as well as simulations done to optimise the observing strategy ahead of time. We discuss our results and confront them with theoretical models of early planet evolution in Section 4.5. Finally, we conclude and discuss future prospects for the characterisation of planetary signals orders of magnitude below the stellar noise in Section 4.6.

4.1 Introduction & context

Planets orbiting young stars offer a unique window into the formation and evolution of planets and planetary systems. The first few hundreds of Myr, when the planets evolve most rapidly, and their observable parameters are still affected by initial conditions, offer the most sensitive tests of theoretical models. Planets whose masses and radii can be measured directly are particularly valuable in that respect, but only a few are known to date. This is in large part due to the rapid rotation and enhanced magnetic activity of the host stars, which hinders both transit detection and radial velocity (RV) follow-up.

In recent years, the *K2* (Howell et al., 2014) and *TESS* (Ricker et al., 2015) space missions have enabled the detection of a number of planets transiting young stars in nearby open clusters and associations, including (David et al., 2016b,a, 2019a; Mann et al., 2016b,a, 2017, 2018, 2020; Gaidos et al., 2017; Pepper et al., 2017; Vanderburg et al., 2018; Rizzuto et al., 2018, 2020; Newton et al., 2019, 2021; Kossakowski et al., 2021), but most of them currently lack mass determinations. Dedicated spectroscopic surveys have also uncovered a number of non-transiting planets around very young stars (including (Quinn et al., 2012; Donati et al., 2016; Yu et al., 2017)), but these lack radius estimates. The combination of measured radius and mass gives access to the planet's mean density, which in turn contains clues regarding its bulk and atmospheric composition. Specifically, young planets ($\lesssim 100$ Myr) with orbital periods $\lesssim 30$ days and known mean densities are particularly valuable, as this is the period range where planets are most strongly effected by atmospheric mass-loss over their lifetimes (e.g. Lopez & Fortney, 2013; Owen, 2019). Therefore, young planets provide the opportunity to probe the amount of primordial gas these planets accreted from their parent protoplanetary discs before the majority of it is lost. In addition, for those planets that are either close enough to their star, or have low enough mass that mass-loss is important on timescales comparable to their age, then constraints can be placed on their initial entropy (Owen, 2020). Knowledge of the amount of primordial gas these planets accreted, and in what thermodynamic state, is extremely valuable as the origin of close-in planets remains uncertain (e.g. Bean et al., 2021). To date, there are only a few planets with well-determined masses *and* radii orbiting stars with well-determined ages below 1 Gyr (Mann et al., 2017; David et al., 2019b; Barragán et al., 2019b, 2021; Plavchan et al., 2020; Klein et al., 2021; Kossakowski et al., 2021; Suárez Mascareño et al., 2021).

Two of them, K2-100b (Mann et al., 2017; Barragán et al., 2019b) and TOI-1201b (Kossakowski et al., 2021), orbit stars with ages in the range 600–800 Myr. K2-100b is a $3.88 \pm 0.16\,R_\oplus$, $21.0 \pm 6.2\,M_\oplus$ planet on a 1.67 d orbit around an early G-dwarf in the ~ 750 Myr-old Praesepe open cluster, whose transits were discovered in data from the *K2* space mission (Howell et al., 2014), and whose

mass was measured using HARPS-North (Pepe et al., 2010). Photo-evaporation models suggest that K2-100b is likely still losing its atmosphere (see Barragán et al., 2019b, and references therein), but any estimate of both its original and its final composition depends critically on assumptions regarding the UV flux of the host star and how it has evolved throughout its lifetime. TOI-1201b is a $2.42 \pm 0.09\,R_\oplus$, $6.3 \pm 0.9\,M_\oplus$ planet on a 2.49 d orbit around an early M-dwarf whose gyrochronological age lies in the range 600–800 Myr and which is a likely kinematic member of the Hyades super-cluster. Its transits were discovered in data from the *TESS* space mission (Ricker et al., 2015), and its mass was measured using CARMENES (Quirrenbach et al., 2014). Both host stars are relatively faint in the optical, so additional follow-up to refine the planets' masses or detect their atmosphere is best pursued with infrared instruments.

By contrast, another of these planets orbits AU Mic, the brightest M-dwarf in the Southern sky (V = 8.73 Torres et al. 2006). Plavchan et al. (2020, hereafter P20) discovered the transits of AU Mic b in the first month of data from the Transiting Exoplanet Survey Satellite (TESS, Ricker et al. 2015), reporting an orbital period of 8.46 d and a planetary radius of $4.2 \pm 0.2\,R_\oplus$. Due to its young age ((22 ± 3 Myr; Mamajek & Bell, 2014)), the AU Mic system provides a much more direct test of planet formation and evolution models, but its intense magnetic activity also exacerbates the challenges of detecting both the transits and the RV signal of any planetary companions. In addition, AU Mic hosts an edge-on debris disc (e.g., Kalas et al., 2004; Boccaletti et al., 2015), which shows peculiar fast moving features, still unexplained (Boccaletti et al., 2018). The *TESS* light curve exhibits significant variability (∼0.1 mag) due to starspots, from which P20 determined the star's rotation period, $P_{\rm rot} = 4.863$ d, as well as frequent flares, which hinder the detection and modelling of the transits. P20 combined data from several optical and near-infrared spectrographs, obtained over several years (starting long before the discovery of the transits) in an effort to constrain the planet's mass, but obtained only an upper limit. A more intensive observing campaign using the SPIRou near-infrared spectropolarimeter (Donati et al., 2020), focusing on several consecutive

rotational cycles, enabled Klein et al. (2021, hereafter K21) to measure a mass of $17.1^{+4.7}_{-4.5}\,M_\oplus$ for AU Mic b, recently refined at $20.1^{+1.7}_{-1.6}\,M_\oplus$ in Cale et al. (2021).

P20 also reported an additional transit-like event from a possible second transiting planet. *TESS* re-observed the system two years later, enabling Martioli et al. (2021, hereafter M21) to confirm the detection of AU Mic c, with a radius of $3.24 \pm 0.16\,R_\oplus$ planet and a period of 18.859 d, though no more than a 5σ upper limit of $20.13\,M_\oplus$ has been reported for its mass (Cale et al., 2021). Note that the existence of more than one transiting planet around AU Mic is not altogether surprising, given that AU Mic hosts an edge-on debris disc, and that observations of the transits of AU Mic b have shown its orbit to be aligned (including Addison et al., 2021; Martioli et al., 2020; Szabó et al., 2021; Hirano et al., 2020). The parameters of AU Mic and its two transiting planets that are relevant in the present work, as reported in the literature at the time of writing, are listed in Table 4.1.

Together with AU Mic's youth and proximity, the fact that it hosts not one but two transiting planets opens up the possibility of comparative exoplanetology. It is thus the target of a number of ongoing ground- and space-based observing campaigns aiming to measure the planets' masses more precisely, as well as to detect the planet's atmosphere and exosphere in transmission[1]. Knowing the planet's mass is important not only to understand its bulk composition, but also to interpret any transmission spectrum observations, as it helps break degeneracies in the atmospheric retrieval process (Batalha et al., 2019).

4.2 Observations

AU Mic has been monitored by a number of optical and near-IR RV spectrographs over the past decade, both before and after the discovery of the transiting planets, including: HARPS, iShell, HIRES, CARMENES, SPIRou, CHIRON, IRD, TRES, Minerva Australis (P20; K21; Cale et al., 2021, hereafter C21). However, none of the individual datasets so far have sufficient time-sampling to constrain both the activity signals and the orbits of the transiting planets on their own. Combining

[1]See e.g. HST Programme 15836, PI E. Newton.

Table 4.1: Parameters of the AU Mic host star and transiting planets gathered from the literature.

Parameter	Value	Reference/Notes
Au Mic stellar parameters		
Distance	9.7248 ± 0.0046 pc	Gaia Collaboration et al. (2021)
$T_{\rm eff}$	3700 ± 100 K	Afram & Berdyugina (2019)
Radius ($R_\star$)	0.75 ± 0.03 $R_\odot$	White et al. (2019)
Mass ($M_\star$)	$0.50^{+0.03}_{-0.03}$ $M_\odot$	P20
$\log g$	4.39 ± 0.03	computed from $R_\star$ & $M_\star$
Luminosity	0.09 ± 0.02 $L_\odot$	Plavchan et al. (2009)
Age	22 ± 3 Myr	Mamajek & Bell (2014)
$P_{\rm rot}$	4.86 ± 0.01 days	P20
$i_{\rm orb}$	89.5 ± 0.4	P20
$v \sin i$	7.8 ± 0.3 km s^{-1}	K21
Linear limb dark. coef.	0.2348	Claret (2018)
Quadratic limb dark. coef.	0.3750	Claret (2018)
Au Mic b		
Transit epoch T_0	8330.39051 ± 0.00015 days	M21
Period	8.463000 ± 0.000002 days	M21
Semi-major axis	0.0645 ± 0.0013 au	Kepler's law
Impact parameter	0.18 ± 0.11 $R_\star$	M21
Planet radius	4.07 ± 0.17 $R_\oplus$	M21
Velocity semi-amplitude	$8.5^{+2.3}_{-2.2.}$ m s^{-1}	K21
Planet Mass	$17.1_{-4.5}$+4.7 $M_\oplus$	K21
Equilibrium temperature	593 ± 21 K	M21
Au Mic c		
Transit epoch T_0	8342.2223 ± 0.00015 days	M21
Period	18.859019 ± 0.000016 days	M21
Semi-major axis	0.1101 ± 0.0022 au	Kepler's law
Impact parameter	0.51 ± 0.21 $R_\star$	M21
Planet radius	3.24 ± 0.16 $R_\oplus$	M21
Velocity semi-amplitude	$0.6 < K_c < 9.5$ m s^{-1}	K21
Planet Mass	$2.2 < M_c < 25$ $M_\oplus$	M21
Equilibrium temperature	454 ± 16 K	M21

data from multiple instruments is possible, and can in principle be advantageous, if the chromaticity of the activity signal is explicitly accounted for when modelling the data (C21). However, combining data from multiple instruments with different wavelength ranges is also challenging because each instrument has different zero-point and noise characteristics, as well as qualitatively distinct activity indicators. Furthermore, the sparse time-sampling of many of these datasets compared to the rotation period of AU Mic, as well as the orbital period of both planets, makes them of limited use to constrain the planetary masses and orbits. We therefore opted to carry out a dedicated, intensive survey using a single instrument, namely HARPS, and focused exclusively on this new dataset in this chapter. I defer any attempt to combine the new data with archival datasets in the context of the GP framework to future work, but a Lomb-Scargle analysis is presented in Chapter 5.2.

4.2.1 Previous HARPS observations

The system has been observed since late 2013 with HARPS (under programmes 192.C-0224, 098.C-0739, 099.C-0205, 0104.C-0418, PI Lagrange), as part of a wider, long-term monitoring survey aiming to detect Jovian planets at intermediate separations (Grandjean et al., 2020) around targets of the SPHERE direct imaging survey (Beuzit et al., 2019). In total there are 54 archival spectra taken on 29 individual nights between 2 October 2013 and 2 November 2019. As these observations were primarily intended to search for giant planets beyond the snow line, their time sampling is too sparse to constrain the orbits of the transiting planets effectively, but we extracted the RVs and activity indicators from the ESO archive when planning our own programme, in order to evaluate the magnitude of the activity-induced RV variations and to estimate the number of new observations required. We note that neither this HARPS programme, nor the SPHERE survey have reported any planet detections at wide separations around AU Mic so far (Lannier et al., 2017). Chapter 5.2 combines both new and archival HARPS datasets to place limits on the presence of additional planets in the system.

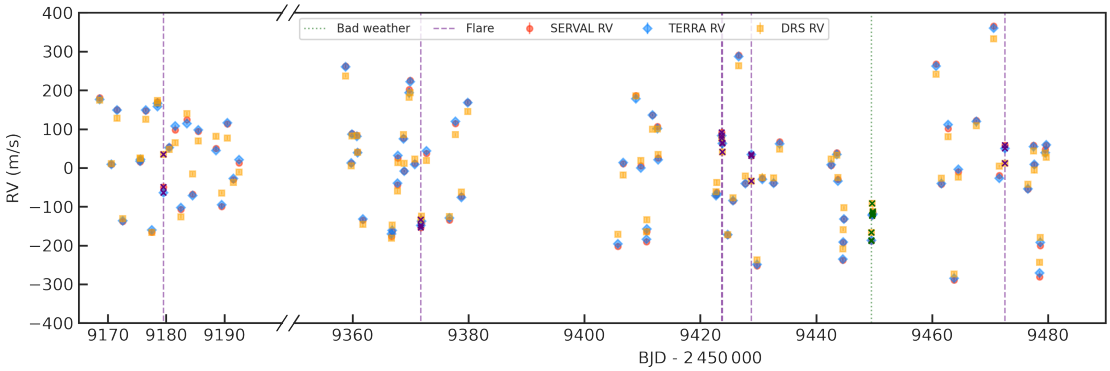

Figure 4.1: Mean-subtracted RV time-series as extracted with SERVAL (red circles), TERRA (blue diamonds), and the DRS (yellow squares). Note the gap in the x-axis corresponding to a $\sim$ 5-month break in the observations. The vertical lines show the observations affected by flares (purple dashed) and clouds (green dotted), which are also marked by 'x' symbols, and were discarded from the rest of the analysis (see Section 4.2.4 for details).

4.2.2 New HARPS observations

The new HARPS observations were collected during ESO Periods 106 & 107 under programmes 0105.C-0288[2] & 0106.C-0852 (PIs Aigrain and Zicher). In total, we obtained 91 individual spectra: 22 observations on 20 individual nights in P106 (between 15 November and 9 December 2020), and 69 observations on 49 individual nights in P107 (between 24 May and 22 September 2021). All observations were taken in High-Accuracy Mode (HAM), with resolution $R = 115,000$ (Mayor et al., 2003). The exposure time was initially set to 900s, but increased to 1200s as the seeing became more variable from June 2021 (onset of Chilean winter), resulting in a typical signal to noise ratio (SNR) at 550 nm of 80 to 100. Both programmes were carried out under the auspices of the HARPS time-share programme organised by F. Bouchy and X. Dumusque.

4.2.3 Data reduction and time-series extraction

The data were reduced using version 3.8 of HARPS Data Reduction Software (DRS). DRS RVs were extracted from the Cross-Correlation Function (CCF) obtained using an M4 mask. We also extracted RVs using two alternative pipelines which have been

[2]The P105 observations were delayed because of the COVID-19 pandemic and taken in P107.

shown to outperform the DRS for M-dwarfs: `SERVAL` (Zechmeister et al., 2018) and `HARPS-TERRA` (Anglada-Escudé & Butler, 2012). `SERVAL` and `HARPS-TERRA` both compute a template spectrum from the observations themselves, rather than using a pre-existing digitized mask to compute the CCF as in the DRS. In the case of `SERVAL`, the template is constructed by co-adding the observed spectra in the barycentric rest-frame. In the case of `HARPS-TERRA`, the template is initially computed by co-adding high SNR observations, allowing preliminary estimates of the RVs to be made, then a new, higher SNR template is produced by co-adding all the spectra in the stellar rest frame, and the RVs are evaluated again. All three time-series are qualitatively similar, as shown in Figure 4.1. The median RV uncertainties for the DRS, `SERVAL` and `HARPS-TERRA` were 5.2, 3.6 and 3.4 $\mathrm{m\,s^{-1}}$, respectively, while the Root Mean Square (RMS) RV variations are 121, 130 and 132 $\mathrm{m\,s^{-1}}$, respectively.

We also extracted a number of ancillary time-series which might serve as activity indicators. These fall into two categories: those that quantify changes in the mean line profile, and those that measure chromospheric emission in the cores of certain spectral lines. In the former category, we include the Full Width at Half Maximum (FWHM) and Bisector Inverse Slope (BIS) of the CCF provided by the DRS, as well as the Differential Line Width (DLW) computed by the `SERVAL` pipeline. The DLW is obtained by correlating the fit residuals with the second derivative of the template (Zechmeister et al., 2018). The chromospheric indicators we consider include the Mt Wilson S_{HK} and H_α indices computed by the `HARPS-TERRA` [3], which measure emission in the cores of the CA II H & K and the H_α lines, respectively. As presented in Sections 4.2.4 and 4.3.3, the chromospheric activity indicators were used to identify observations affected by flares, while the line-shape indicators were most useful to model the activity-induced signals in the RVs.

All the HARPS RVs and activity indicators after June 2015 (after the HARPS fibre upgrade (Lo Curto et al., 2015) are given in Appendix B.1 - the full version

[3]Note that the chromospheric metrics provided by the `SERVAL` pipeline and the DRS are entirely consistent with that provided by `HARPS-TERRA`, with Pearson correlation coefficients systematically larger than 0.99.

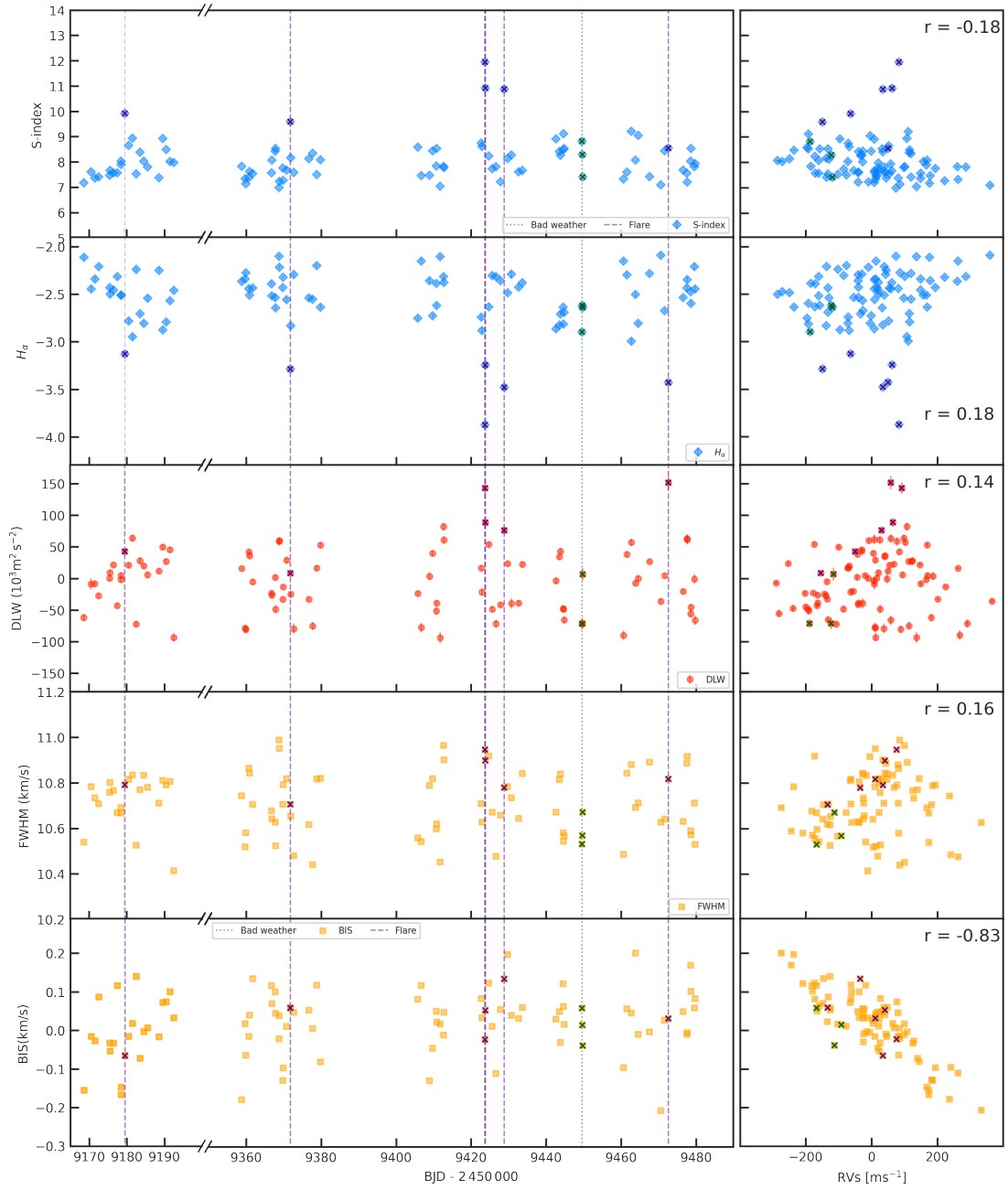

Figure 4.2: Activity indicators versus time (left) and versus the RVs produced by the corresponding pipeline (right). From top to bottom: DRS FWHM and BIS, `SERVAL` DLW, `HARPS-TERRA` $S_{\rm HK}$ and Hα index. The colour indicates the pipeline used to extract each indicator: blue for `HARPS-TERRA` red for `SERVAL` and yellow for the DRS. Significant outliers in either $S_{\rm HK}$ or $\rm H_\alpha$, which indicate that the corresponding observations were affected by flaring, are marked by purple dashed vertical lines in the left column. Along with one observation affected by clouds (green dotted vertical line), these observations (marked as 'x' symbols in all panels) were discarded from the rest of the analysis (see Section 4.2.4 for details).

of which is available in machine-readable format. The activity indicator time-series are shown in Figure 4.2.

4.2.4 Removing flares and clouds

As well as displaying significant rotational modulation of starpots, the ground-based and *TESS* light curves of AU Mic show frequent white-light flares (e.g., Hebb et al. 2007; P20; M21). These flares can significantly affect the measured radial velocities as they distort the line profiles. The distorted line profiles are shown in Figure 4.3 in units of blaze-corrected flux. As our current models are not equipped to account for the RV effects of flares, we flagged the observations affected by flares and discarded them from the analysis. The procedure used to identify observations strongly affected by flares is described in detail in the companion paper Klein et al. (submitted). In short, we computed a chromospheric emission metric for 7 different chromospheric lines (see Figure 4.3, namely Ca II H & K (3968.47 & 3933.66 Å), H_α (6562.808 Å), H_β (4861.363 Å), Na I D1 & D2 (5895.92 & 5889.95 Å respectively) and He I D3 (5875.62 Å) using the easy-to-use method of Zechmeister et al. (2018) and the integrations windows of Gomes da Silva et al. (2011). As the effects of stellar flares might change from one chromospheric line to the other, we defined a master index by taking the median-normalized average of all chromospheric emission indices. We finally applied a 3σ-clipping process to the resulting time-series, flagging a total of 6 observations likely affected by a stellar flare which were then removed from the following analysis (see Figure 4.2). Note that the RVs affected by flares do not stand out as outliers in the raw RVs, but would do so after subtracting the activity model described in Section 4.3.1.

After removing the observations affected by flares, one substantial outlier ($4-\sigma$) remained when looking at the time-series residuals (after subtraction of the best-fit stellar activity plus planetary signals model, as described in Section 4.3). We inspected images from the Danish all-sky camera at La Silla, which showed that variable, high cirrus were present that entire night. We then inspected all three observations of AU Mic taken that night, and found the spectra to be strongly

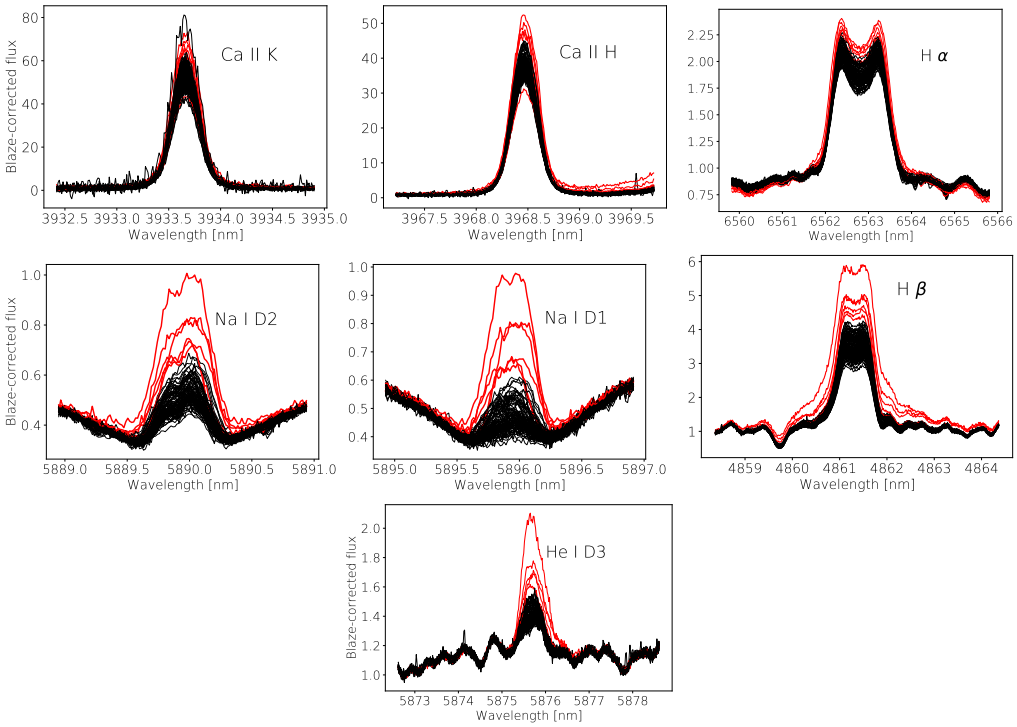

Figure 4.3: Observed emission reversals of Ca H & K, H_α, Na D1&D2 , H_β and He I chromospheric lines for AU Mic. In each panel, profiles shown in red were flagged as affected by a stellar flare (6 observations). Note that the cloud/Moon-polluted observations (2021–08–23) are not shown in these plots. Figures by Baptiste Klein.

contaminated by the Moon. We thus removed them from further analysis. Although only one of the three observations taken that night was a significant RV outlier, the spectra were all affected by the Moon so we deemed it safer to remove them all. We checked that no other spectra taken on other nights were affected in the same way by dividing each spectrum by the median spectrum across all observations. The three observations from that night were the only ones which showed strong evidence of Moon contamination.

All the observations affected by flares or clouds are indicated in Table B.1. The total number of epochs remaining and included in our final analysis, shown in Figure 4.1, was therefore 82.

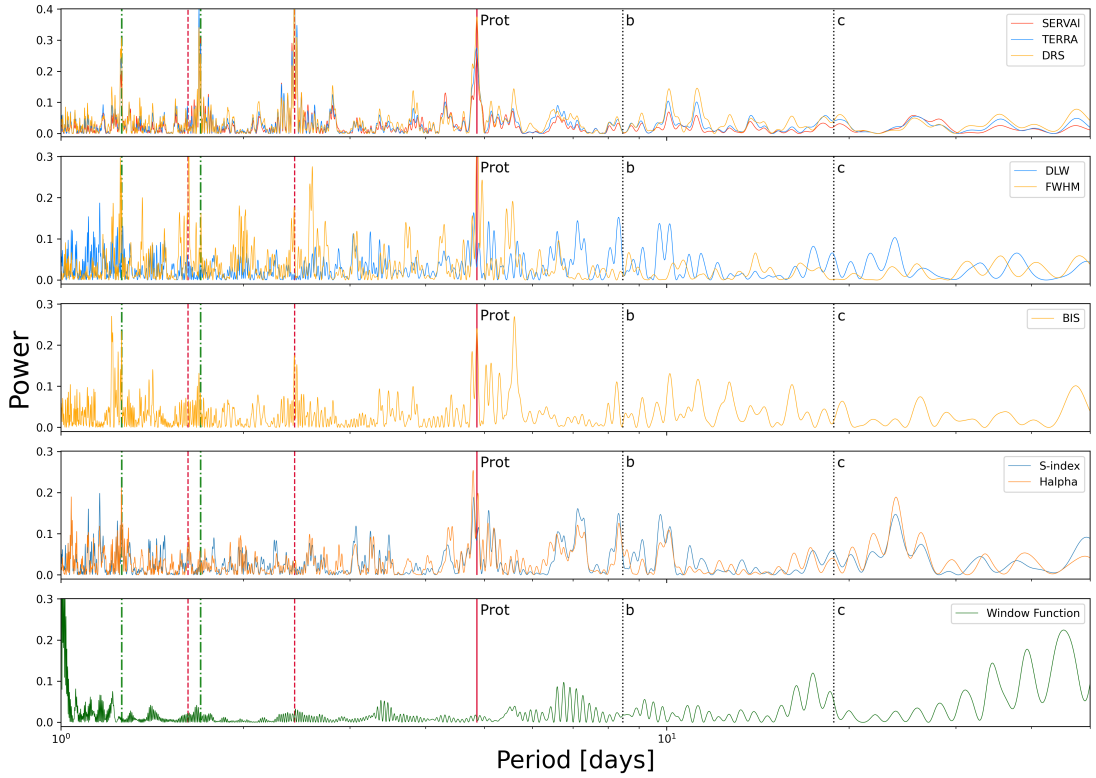

Figure 4.4: Lomb-Scargle periodograms of the 3 RVs time-series (top), DLW & FWHM (2^{nd} panel), BIS (3^{rd} panel), S-index & H_α(4^{th} panel) and the window function of the observations (bottom). Vertical crimson lines denote the stellar rotation period and its first two harmonics, vertical green lines denote 1-d aliases of the stellar rotation period, while vertical black dotted lines denote the orbital periods of AU Mic b and c.

4.2.5 Correlations and periodograms

In the right-hand column of Figure 4.2, we show the correlation between each activity indicator and the RVs extracted using the corresponding pipeline. Each plot is annotated with the corresponding Pearson correlation coefficient. Although all the time-series are dominated by activity signals, this does not result in a clear correlation between the activity indicators and the RVs, with the exception of the BIS, which is anti-correlated with the RVs. This is fully expected, as the other activity indicators depend only on the projected area of the active regions, their contrasts, and (for FWHM and DLW) on the absolute value of the surface radial velocity at the location of the active regions relative to the stellar rest frame, but the RVs and BIS also depend on the sign of this quantity.

Lomb-Scargle periodograms of the RVs and activity indicators time-series are

shown in Figure 4.4, along with that of the observation window function. Both RV and DLW time-series show strong peaks at the rotation period and its first harmonic. There is also a peak in both periodograms near, but not exactly at, the second harmonic ($P_{\rm rot}/3$). Peak splitting around the rotation period and its harmonics can indicate differential rotation or active region evolution (see e.g., Aigrain et al. 2012; K21). The raw RVs do not display significant peaks at the orbital period of either planet. There are no prominent peaks in the window function, although there is a little excess power around, but not exactly at, the period of AU Mic c. These periodograms were calculated using the `astropy` package (Astropy Collaboration et al., 2013, 2018).

4.3 Modelling the RVs

In this section, we describe the way we analysed the data, which involved jointly modelling activity and planet signals in the RVs and the activity indicators simultaneously, using the multidimensional Gaussian Process model (presented in Chapter 3.3) introduced by Rajpaul et al. (2015) as implemented in the `pyaneti` package (Barragán et al., 2022, hereafter B22).

4.3.1 Activity model

We model the activity signals in the RVs, $V(t)$ and one or two activity indicators, $\alpha(t)$ and optionally $\beta(t)$ as

$$\begin{aligned} V(t) = &\ A_V G(t) + B_V \dot{G}(t) + C_V \\ \alpha(t) = &\ A_\alpha G(t) + C_\alpha, \\ \beta(t) = &\ A_\beta G(t) + B_\beta \dot{G}(t) + C_\beta, \end{aligned} \tag{4.1}$$

where the function $G(t)$ is a latent variable, loosely representing the projected area of the visible hemisphere covered by active regions, and is modelled as a quasi-periodic GP with covariance function:

$$\gamma(t_i, t_j) = \exp\left[-\frac{\sin^2[\pi(t_i - t_j)/P_{\rm GP}]}{2\lambda_{\rm P}^2} - \frac{(t_i - t_j)^2}{2\lambda_{\rm e}^2}\right], \tag{4.2}$$

where $P_{\rm GP}$ is the characteristic period of the GP, and corresponds to the stellar rotation period, $\lambda_{\rm p}$ the inverse harmonic complexity, and $\lambda_{\rm e}$ is the evolution timescale, and is related to the lifetime of the active regions. The parameters A_V, B_V, A_α, A_β and B_β are free parameters, which control the relationship between the latent GP variable and the observables, while C_V, C_α and C_β are constant offsets for each time-series, which are also free parameters. The interested reader is referred to Rajpaul et al. (2015) and B22 for a full description of the activity model.

Chromospheric activity indicators, such as $S_{\rm HK}$ or $\rm H_\alpha$, depend primarily on the fraction of the visible disc that is covered in active regions, and are thus expected to be approximately proportional to $G(t)$ and were thus modelled under the form $\alpha(t)$ in Equation (4.1). The same is true of the FWHM and DLW, which measure the width of the spectral lines. On the other hand, the BIS, which measures the asymmetry of the spectral lines, is expected to depend on $\dot{G(t)}$, and was thus modelled like $\beta(t)$ in Equation (4.1).

4.3.2 Joint activity and planet model

To model the activity signal alongside the signals of the known transiting planets, we subtract from the RVs the sum of two Keplerian signals, and compute the likelihood of the GP applied to the residuals (see Equation 7 in B22). This introduces a further 6 or 10 free parameters into the model (depending on whether the orbits are assumed to be circular or not).

The measurement uncertainties on the RVs and DLWs at each epoch were accounted for by adding a term to the diagonal of the GP covariance matrix. In addition, we add a separate 'jitter' term to the diagonal of the covariance for each time-series (in effect, a constant term added in quadrature to the formal uncertainties on each observation, see Equation 13 in B22). This term absorbs any imperfections in our activity plus Keplerian models and ensures that the resulting uncertainties are propagated to the final parameter estimates.

4.3.3 Choice of RV version and activity indicator(s)

We performed a number of runs using different versions of the RV time-series, and different combinations of activity indicators. We focused on the DRS FWHM & BIS and the `SERVAL` DLW because their periodograms (shown in Figure 4.4) display prominent peaks at the rotation period of AU Mic and its harmonics. The $S_{\rm HK}$ of the chromospheric activity index has a more complex periodogram, and proved to be less useful in constraining the activity signal in the RVs. For the RV time-series, we tried using both the DRS and the `SERVAL` versions, but we note that the `HARPS-TERRA` RVs would give results that are essentially identical to those obtained with the `SERVAL` RVs.

We tried the following models:

1) $V(t) = \mathrm{RV(DRS)}$, $\alpha(t) = \mathrm{FWHM}$ and $\beta(t) = \mathrm{BIS}$;

2) $V(t) = \mathrm{RV(SERVAL)}$, $\alpha(t) = \mathrm{DLW}$ and $\beta(t) = \mathrm{BIS}$;

3) $V(t) = \mathrm{RV(SERVAL)}$ and $\alpha(t) = \mathrm{DLW}$;

All three models give mutually consistent results, although model 1 does not yield a 3σ detection of AU Mic c whereas models 2 and 3 do. In other words, the `SERVAL` RVs and DLWs result in slightly better sensitivity to the planetary signals compared to the DRS RVs and FWHMs. The results of models 2 and 3 are essentially equivalent. In principle, including the BIS in the modelling should help constrain $G(t)$, but in this specific case the BIS does not seem to provide additional information that the RV and DLW time-series do not already contain. For the remainder of this chapter, we therefore adopt model 3 as our fiducial model, since it is simple and has 3 fewer free parameters. For completeness, I show the results for the three runs in Appendix B.2.

4.3.4 Model comparison for different planet configurations

For completeness, we also test if the planetary signals are recovered individually in the data (using our fiducial Model 3). We ran three different setups: one including only planet b, one only planet c, and the last one including both signals. The results of this test are summarised in Table 4.2. We found that we are able to recover each planetary signal individually, even if the signal of the other planet is not included in the model. In addition, we found that the model producing the highest likelihood is the one including both planetary signals. However, we note, that if we use standard model comparison parameters such as Akaike Information Criterion and Bayesian Information Criterion, the preferred model is the one including AU Mic c signal only. This is expected given that the detection of AU Mic b is not well constrained. In addition, it is challenging to assess how we are penalising for the 5 extra parameters. We are practically fixing the ephemerides and eccentricity, meaning that we are only adding one parameter, the semi-amplitude. Nonetheless, we adopt the two planet model given that this is physically motivated. We know a priori that both planets are present from the transit observations. Therefore, the results presented in the remainder of this chapter are Model 3 with both planetary signals.

Table 4.2: Model comparison for different configurations

Model	$N_{\rm pars}$	K_b [m s^{-1}]	K_c [m s^{-1}]	$\ln \mathcal{L}$	AIC^a	BIC^b
Planet b signal only	15	$6.1^{+2.9}_{-2.8}$	...	336	-641	-595
Planet c signal only	15	...	8.4 ± 2.6	339	-648	-601
Both planetary signals	20	5.8 ± 2.5	8.5 ± 2.5	342	-643	-581

Note – $^{(a)}$ Akaike Information Criterion (AIC $= 2N_{\rm pars} - 2\ln\mathcal{L}$). $^{(b)}$ Bayesian Information Criterion (BIC $= N_{\rm pars}\ln N_{\rm data} - 2\ln\mathcal{L}$).

4.3.5 Exploration of the parameter space

The full model has 20 parameters: 5 per Keplerian signal, 8 for the activity model, and 2 jitter parameters. These are listed in Table 4.3, which gives the prior adopted for each parameter. The period and time of transit for each planet are tightly constrained by the *TESS* light curve and we adopted Gaussian priors based on

the ephemerides reported by M21. We also adopt a uniform prior between 4.8 and 4.9 days for the GP period $P_{\rm GP}$, based on the rotation period reported by P20. For the orbital eccentricities of the planets, we adopt a beta distribution prior, as advocated by Van Eylen et al. (2019) for multiplanet systems. For all the other parameters, we adopted minimally informative priors.

We then explored the parameter space with a Markov chain Monte Carlo (MCMC) sampler (see Barragán et al., 2019a, for details) to evaluate the joint posterior distribution over all the parameters. We iterated 250 independent Markov chains in sets of 5000 steps, checking for convergence using the auto-correlation length of the chains after each set of 5000 steps. If the chains were not converged, we iterated for a further set of 5000 steps, repeating the process until convergence was reached. We then used the last 5000 steps, thinning the chains by a factor of 10 so that samples are uncorrelated, to create the final posterior distribution (corresponding to 125 000 independent samples for each parameter). The resulting 'corner' plot, showing 1D and 2D posterior densities for all the parameters, is shown in Figure 4.5). Except for the longitude of periastron ω, which is unconstrained for both planets, the marginal posterior distributions for each of the sampled parameters are uni-modal, indicating that there are no pathological degeneracies between the parameters.

4.4 Results

We report fitted values and upper and lower uncertainties for each parameter in the final column of Table 4.3, using the median and $16^{\rm th}$ and $84^{\rm th}$ percentiles of the marginal posterior distributions. The inferred model is shown alongside the data in Figure 4.6. Figure 4.7 shows the phase-folded individual RV signal for each planet. The signals of AU Mic b and AU Mic c are detected at the 2.3 and 3.4σ level respectively, with amplitudes of 5.8 ± 2.5 m s^{-1} and 8.5 ± 2.5 m s^{-1}. While AU Mic c is detected at high confidence, the detection of AU Mic b is more tentative in this dataset. The eccentricities are consistent with zero.

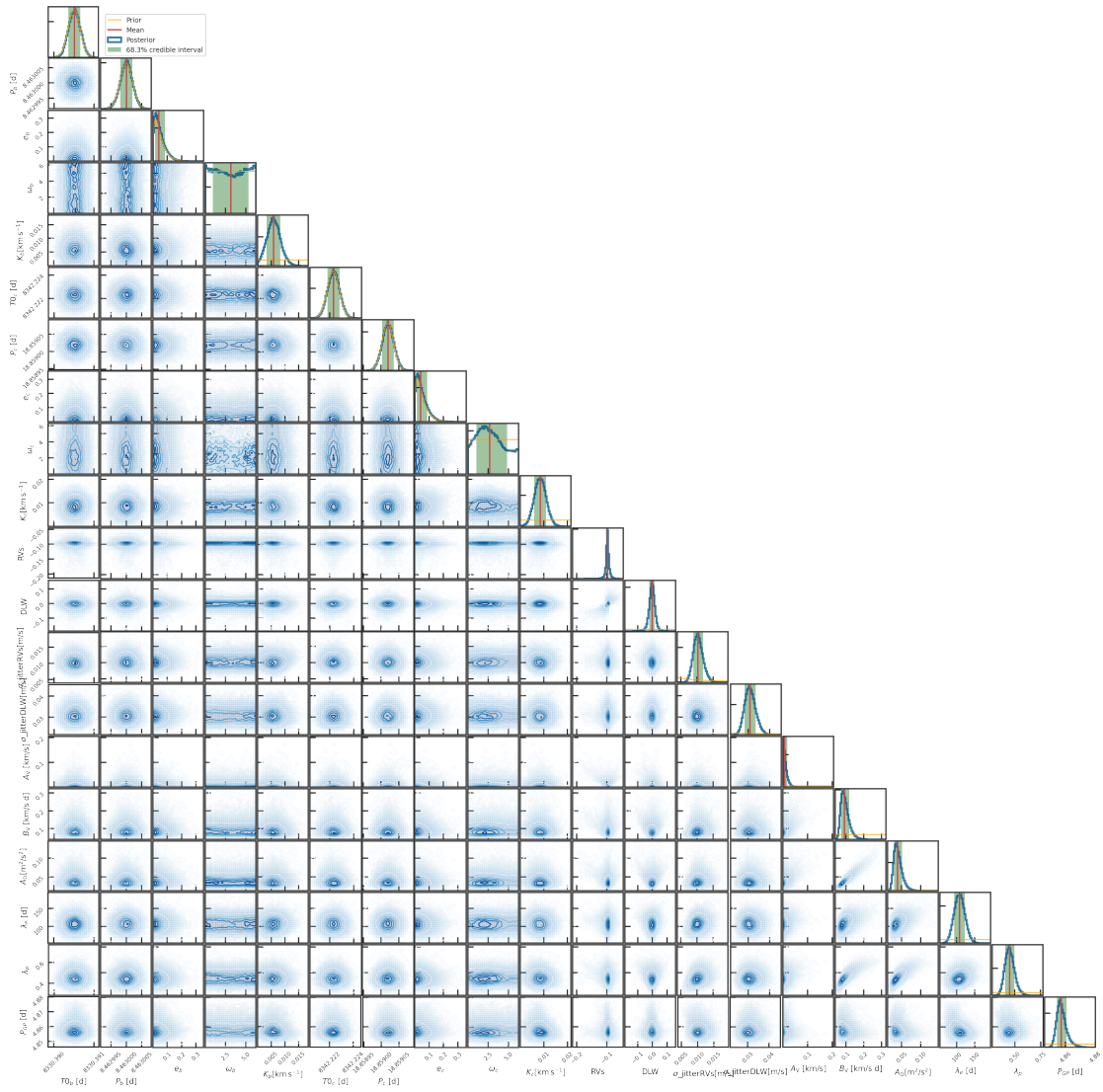

Figure 4.5: Posterior and correlation plots for the sampled parameters (MCMC corner plot). The inferred parameters from these posteriors are given in Table 4.3

The GP hyper-parameters are well constrained, and consistent with prior information about the rotation and activity behaviour of AU Mic. The GP period is $P_{\rm GP} = 4.857^{+0.004}_{-0.003}$ d, consistent with the rotation period $P_{\rm rot} = 4.863 \pm 0.010$ d reported by P20. The GP evolution time-scale $\lambda_{\rm e} = 108 \pm 15$ d is 20 times the rotation period and is consistent with estimates from previous studies where a GP was used to describe the RVs only (P20; K21; C21). The inverse harmonic complexity $\lambda_{\rm p} = 0.449^{+0.049}_{-0.043}$ is relatively low. This can arise for a number of reasons: if the distribution of active regions on the stellar surface was relatively complex at the time of the observations, or if the latent variable $G(t)$ displays beat patterns caused

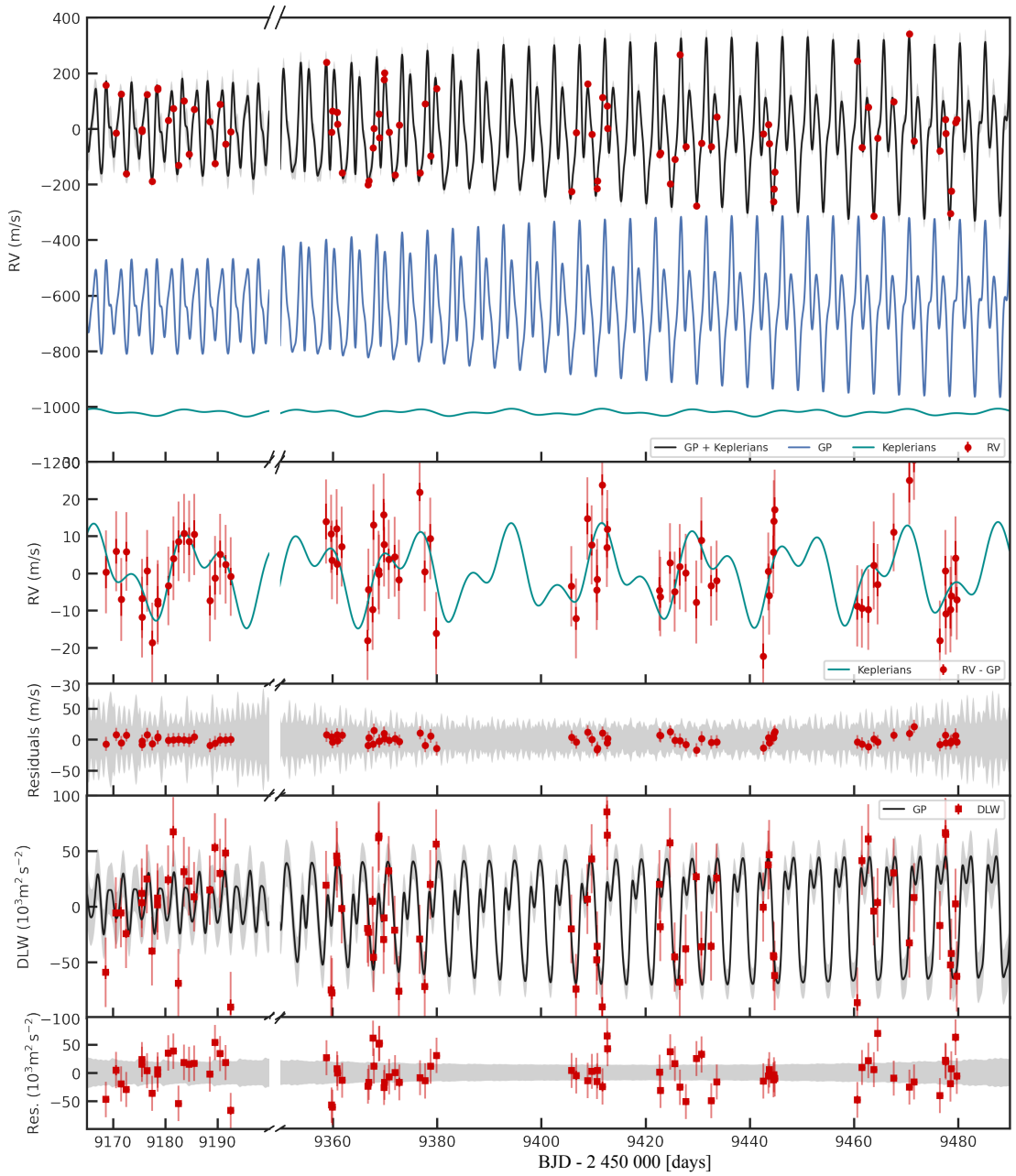

Figure 4.6: Radial velocity and DLW time-series (red symbols with error bars) with the best-fit model (solid lines) and 3σ confidence intervals (shaded grey areas). Note the break in the x-axis corresponding to a $\sim$ 5-month break in the observations. The top panel shows the RV data with the full model in black. The activity and Keplerian components are also shown separately, in blue and cyan respectively, vertically offset for clarity. The second panel shows the data after subtracting the activity model, with the Keplerian component over-plotted. The final RV residuals are shown in the third panel. The fourth panel shows the DLW time-series, with the activity model in black, and the DLW residuals are shown in the fifth panel. In all the panels, the nominal error bars are in solid colour, and the error bars taking into account the jitter are semi-transparent.

by either differential rotation or the evolution of individual active regions (we note K21 detected solar-like differential rotation using Doppler Imaging with SPIRou).

We now examine the behaviour of the parameters A_V, B_V, and A_α, which control the relationship between the observables and the underlying latent variable $G(t)$. As shown in Table 4.3 and Figure 4.5, the posterior for A_V is consistent with zero at the 1.5σ level, while those for B_V and A_α are significantly non-zero. In other words, the RV time-series behaves primarily like $\dot{G}(t)$ while the DLW time-series behaves primarily like $G(t)$. This is consistent with the prediction of Aigrain et al. (2012) and with what has been observed for other young, rapidly rotating, active stars including K2-100 (Barragán et al., 2019b) and HD 73583 (Barragán et al., 2021).

The jitter terms, $\sigma_{\rm RV}$ and $\sigma_{\rm DLW}$, can be used as diagnostics of the effectiveness (or otherwise) of our model at explaining the full dataset. In both cases, the posteriors medians are approximately ten times smaller than the amplitude of the dominant activity term (B_V and A_α, respectively), but roughly twice the nominal measurement uncertainties. This illustrates the fact that our activity model explains most of the RV and DLW variations, but is not perfect.

A widely used test of the quality of a model fit is to compare the root-mean-square (RMS) before and after subtracting the best-fit model. Caution must be used in interpreting such a comparison, as a low residual RMS can result from over-fitting as readily as from a particularly good model. On the other hand, an anomalously high residual RMS would be a robust indication that the model cannot fully explain the observations. The initial RMS of the RV observations is $137\,{\rm m\,s^{-1}}$, compared to $7.5\,{\rm m\,s^{-1}}$after we subtracting our best-fit, combined activity and planetary signal model. The DLW time-series has an initial RMS of $45 \times 10^3\,{\rm m^2\,s^{-2}}$ which shrinks to $30 \times 10^3\,{\rm m^2\,s^{-2}}$ after subtracting the best-fit model (which, in the case of DLW, includes activity only). Thus, the RMS of both time-series is reduced by 94% for the RVs and 33% for the DLW, indicating that our model explains most of the variability seen in the RVs and a significant fraction of that seen in the DLWs. The residual RMS is nonetheless significant compared to the median formal uncertainty of each time-series ($3.6\,{\rm m\,s^{-1}}$ and $4.8\,{\rm m^2\,s^{-2}}$, respectively). This highlights that

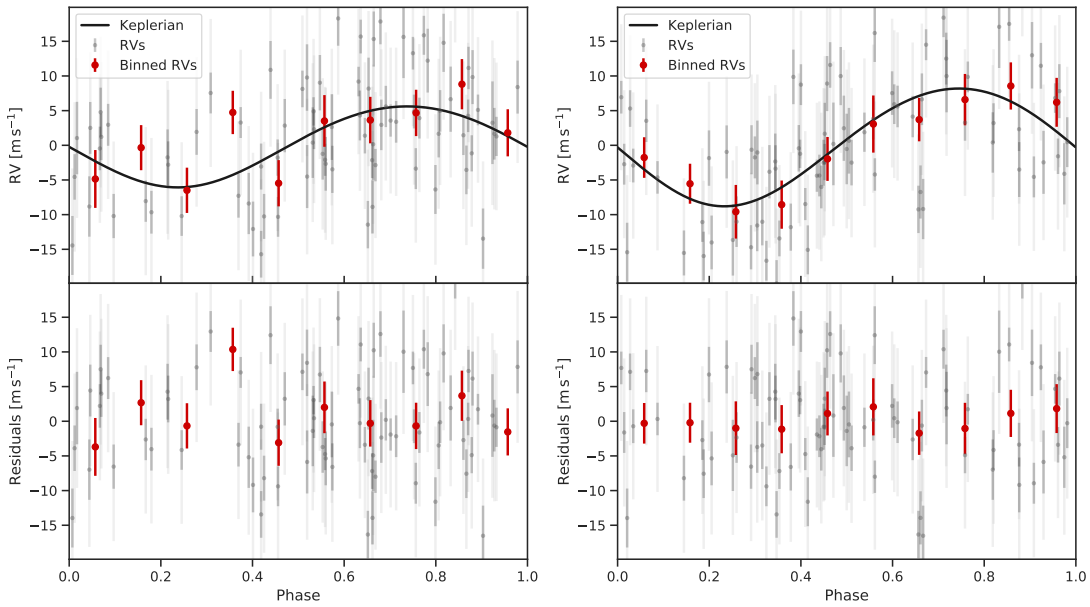

Figure 4.7: Phase-folded RV signals for AU Mic b (left) and AU Mic c (right) after subtracting the systemic velocity, the activity signal, and the other planet. Grey circles with error bars show the HARPS measurements, and the error bars taking into account the jitter are shown with lighter grey. The black line show the best-fit Keplerian model. Red circles show binned RVs to facilitate comparison between data and models.

our model, while useful, is incomplete. The remaining variability might be due to stellar signals which our model cannot account for, or to instrumental systematics. Either way, it is absorbed by the jitter terms which, as we can see from Table 4.3, have values similar to the residual RMS (as one would expect).

4.5 Discussion

In this Section, we discuss the implications of the results presented in Section 4.4 for the masses, orbits, composition and evolution of AU Mic b and c.

4.5.1 Planet masses

From our estimates for $K_\mathrm{b} = 5.8 \pm 2.5$ m s^{-1} and $K_\mathrm{c} = 8.5 \pm 2.5$ m s^{-1}, we directly obtain mass estimates for the two planets of $M_\mathrm{b} = 11.7 \pm 5.0\ M_\oplus$ and $M_\mathrm{c} = 22.2 \pm 6.7\ M_\oplus$. This represents a 3.4σ detection of planet c, but only a tentative, 2.3σ detection of planet b.

Table 4.3: Priors and posterior median and confidence intervals for the parameters of the joint RV & DLW model. The posterior distributions from which we infer these parameters are shown in Figure 4.5

Parameter	Prior[(a)]	Posterior value[(b)]
AU Mic b's parameters		
Orbital period $P_{\rm orb}$ (days)	$\mathcal{N}[8.463000, 0.000002]$	8.463000 ± 0.000002
Transit epoch	$\mathcal{N}[8330.39051, 0.00015]$	8330.39051 ± 0.00015
Eccentricity e	$\mathcal{B}[1.52, 29]$[(c)]	$0.04^{+0.045}_{-0.025}$
Angle of periastron ω (deg)	$\mathcal{U}[0, 360]$	179^{+128}_{-125}
Semi-amplitude K ($\mathrm{m\ s^{-1}}$)	$\mathcal{U}[0, 50]$	5.8 ± 2.5
AU Mic c's parameters		
Orbital period $P_{\rm orb}$ (days)	$\mathcal{N}[18.859019, 0.000016]$	18.859019 ± 0.0000016
Transit epoch	$\mathcal{N}[8342.2223, 0.0005]$	8342.22231 ± 0.00050
Eccentricity e	$\mathcal{B}[1.52, 29]$[(c)]	$0.041^{+0.047}_{-0.026}$
Angle of periastron ω (deg)	$\mathcal{U}[0, 360]$	153^{+124}_{-94}
Semi-amplitude K ($\mathrm{m\ s^{-1}}$)	$\mathcal{U}[0, 50]$	8.5 ± 2.5
Multidimensional GP parameters		
GP Period $P_{\rm GP}$ (days)	$\mathcal{U}[4.5, 5.5]$	$4.8571^{+0.0037}_{-0.0027}$
$\lambda_{\rm p}$	$\mathcal{U}[0.1, 2]$	$0.449^{+0.049}_{-0.043}$
$\lambda_{\rm e}$ (days)	$\mathcal{U}[10, 500]$	108 ± 15
$A_{\rm V}$ ($\mathrm{m\,s^{-1}}$)	$\mathcal{U}[0, 100]$	$7.5^{+10.9}_{-05.5}$
$B_{\rm V}$ ($\mathrm{m\,s^{-1}\,d}$)	$\mathcal{U}[-1000, 1000]$	91^{+27}_{-18}
A_α ($1000\ \mathrm{m^2\,s^{-2}}$)	$\mathcal{U}[0, 1000]$	$38.7^{+12.3}_{-08.5}$
Other parameters		
C_v (Offset RV,$\mathrm{km\,s^{-1}}$)	$\mathcal{U}[-0.82, 0.71]$	$-0.0982^{+0.0047}_{-0.0043}$
C_α (Offset DLW,$\mathrm{m^2\,s^{-2}}$)	$\mathcal{U}[-1, 1]$	$-0.003^{+0.018}_{-0.019}$
Jitter term $\sigma_{\rm RV}$ ($\mathrm{m\,s^{-1}}$)	$\mathcal{J}[0, 1000]$	$10.3^{+1.6}_{-1.4}$
Jitter term $\sigma_{\rm DLW}$ ($1000\ \mathrm{m^2\,s^{-2}}$)	$\mathcal{J}[0, 1000]$	$30.7^{+2.7}_{-2.4}$
Derived Parameters		
AU Mic b's derived Parameters		
Planet mass $M_{\rm p}$ ($M_\oplus$)	$\cdots$	11.7 ± 5.0
Planet density $\rho_{\rm p}$ ($\mathrm{g\,cm^{-3}}$)	$\cdots$	0.97 ± 0.43
AU Mic c's derived Parameters		
Planet mass $M_{\rm p}$ ($M_\oplus$)	$\cdots$	22.2 ± 6.7
Planet density $\rho_{\rm p}$ ($\mathrm{g\,cm^{-3}}$)	$\cdots$	3.66 ± 1.28

Note – [(a)] $\mathcal{U}[a, b]$ refers to uniform priors between a and b, $\mathcal{N}[\mu, \sigma]$ to Gaussian priors with mean μ and standard deviation σ, $\mathcal{B}[a, b]$ to a beta distribution with shape parameters a and b, and $\mathcal{J}[a, b]$ is the modified Jeffrey's prior as defined by Gregory (2005, eq. 16). [(b)] Inferred parameters and errors are defined as the median and 68.3% credible interval of the posterior distribution. [(c)] Beta distribution to inform eccentricity sampling using the beta distribution for multi planetary systems as defined by Van Eylen et al. (2019).

K21 reported a mass estimate of $17.1 \pm 4.6\,M_\oplus$ for planet b, which is consistent at the 1σ level with our estimate. We note that K21 did not include AU Mic c in their analysis, since the second planet was not confirmed at the time.

More recently, C21 reported a mass of $20.1 \pm 1.6\,M_\oplus$ for planet b and a 5σ upper limit for planet c of $M_c < 20.1\,M_\oplus$, using a combination of data from multiple optical and near-IR spectrographs, and a model which includes only the RVs, but exploits the chromaticity of the activity signal. Our results are not consistent with these values. Although it is difficult to identify the exact source of the discrepancy, several factors are likely at play. The first is the difference in the wavelength coverage; including both optical and near-IR data should in principle give a better handle on the activity signals, though it also necessitates an increase in the number of free parameters in the model. Another difference is the time-sampling of the datasets used, which is much sparser in the case of C21 than in the present work. Sparser time sampling severely limits the ability to model the activity signal. The third is the fact that we model an activity indicator simultaneously with the RVs, which again should help constrain the activity component of the model. We note that C21 performed two different analyses, with different assumptions about the chromaticity of the activity signal, and that these gave mutually inconsistent results, particularly for the mass of planet c.

Another difference is that C21 use a Gaussian prior with mean 0.19 and standard deviation 0.04 for the eccentricity of planet b, derived from *Spitzer* secondary eclipse observations. As the latter are not yet published, we did not incorporate this prior in the analysis presented in Section 4.4, but we did carry out an additional model run with the same eccentricity prior for planet b as used by C21. This did not appreciably affect our mass estimates for either planet.

Finally, exploring the parameter space for such complex, activity plus Keplerian models, is in general challenging. To check how robust our results are to the details of the model, we carried out simple tests including only planet b or only planet c, and found that the resulting RV semi-amplitudes were consistent with the values obtained from the model including both planets. We also carried out a number of additional

tests using simulations, described in Section 4.5.4, to further establish confidence in our results. Overall, however, it is clear that continued RV monitoring of the system, as well as independent analyses of all the available datasets by different teams, would be desirable to resolve the discrepancies between the published mass estimates.

4.5.2 TTV analysis

As AU Mic b and c are close to a 2:1 mean-motion resonance, transit timing variations (TTVs) can be used to constrain their masses and eccentricities. Szabó et al. (2021) and Gilbert et al. (2021) report tentative TTVs for AU Mic b at the level of 3–4 min and 80 s, respectively, using *TESS* and *CHEOPS* observations. Although the measurement of transit times is somewhat difficult because of AU Mic's frequent flaring, these results indicate that strong TTVs, with amplitudes in excess of $\sim$ 10 min, are not present in the system. This can be used to provide a sanity check on the mass and eccentricity estimates derived in this work and in previous RV analyses, and to motivate future TTV follow-up.

Using the TTVFast package (Deck et al., 2014) we forward modelled the TTVs expected from a two-planet configuration as observed in the AU Mic system. TTV amplitudes are most sensitive to planetary mass and eccentricity, so we varied those on a grid over a plausible range for these parameters, noting the amplitude of the TTV signal in each case. Our predictions are summarised in Figure 4.8. Even for the most extreme mass ratio and eccentricities compatible with the results of our RV analysis, the maximum amplitude of the TTVs never exceeds a few minutes, with a super-period of 80 days. We therefore conclude that our mass estimates are consistent with existing transit observations.

4.5.3 Dynamical analysis

We used `mercury6` (Chambers, 1999) to test the dynamical stability of the AU Mic system. We used the masses and orbital parameters reported in Table 4.3, assuming that both planets have co-planar orbits. Starting from this configuration, we evolved the system for 1 Gyr with steps of 0.5 d per integration. We found that the

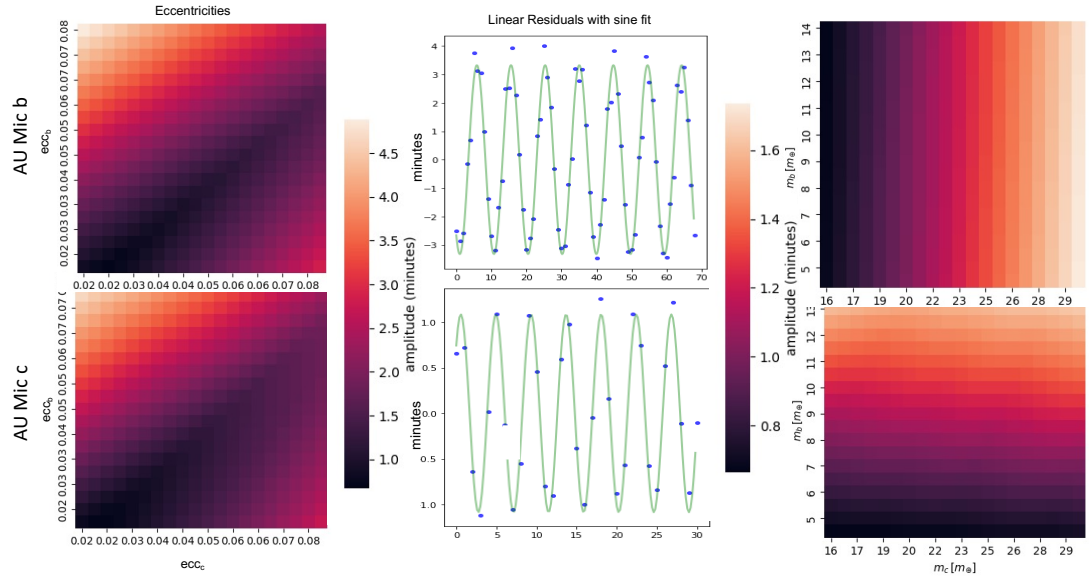

Figure 4.8: Expected TTV amplitudes for varying the eccentricities with fixed masses (left) and varying masses but fixed eccentricities (right). Expected TTV amplitudes for our reported masses and eccentricities for AU Mic b and c are reported in the middle panel. The x-axis corresponds to transit number.

eccentricity and semi-major axis of both planets display periodic fluctuations with a period of $\sim$ 1000 years, but these fluctuations are contained and the system appears stable over the full duration of the simulation. The eccentricity of AU Mic b oscillates between 0.05 and 0.25, and its semi-major axis varies by 8×10^{-5} AU. The eccentricity of AU Mic c remains < 0.10 and the maximum departure of its semi-major axis from the starting value is 1.3×10^{-4} AU. We conclude that the orbital parameters and masses derived for AU Mic planets are consistent with a dynamically stable system.

4.5.4 Tests to establish detection robustness

It has been shown that the combination of complex models and the window function of the observations can create spurious planet-like signals in RV time-series, specially for active stars (e.g., Rajpaul et al., 2016). In order to check the reliability of our RV detection, we performed numerical simulations similar to Barragán et al. (2019b). We used `citlalatonac` (B22) to simulate an RV and DLW time-series containing only the best-fit activity model as obtained from the real data. We decided to use the median values of our derived parameters given that the posteriors are

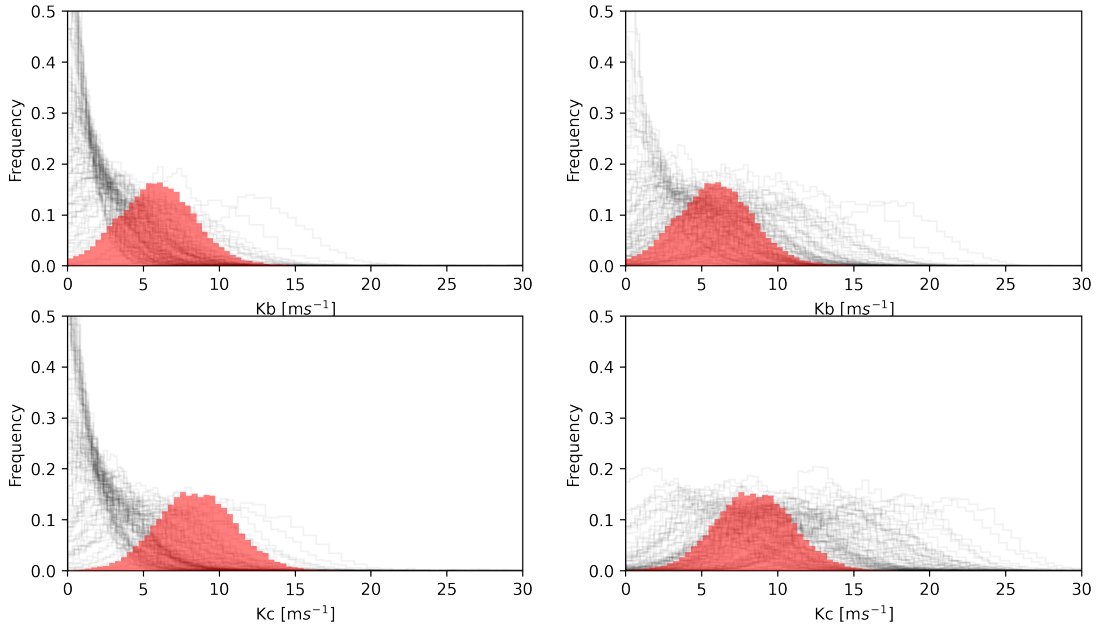

Figure 4.9: Results of the activity-only (left) and activity plus Keplerian (right) simulations (see Section 4.5.4 for details). In each panel, the red histogram shows the posterior derived from the original data, and the thin grey lines show the posteriors obtained from the simulations. Figures by Oscar Barragán.

quasi-Gaussian uni-modal distributions. We then added correlated noise using a squared exponential kernel with a length-scale of one day, and the same amplitude as the jitter term obtained from the real data, plus white noise for each observation according to its nominal measurement uncertainty. We did this 100 times to obtain 100 simulated activity-only time-series, with similar noise properties and the same time-sampling as the real data.

We modelled each activity-only synthetic dataset using a two-planet and 2-dimensional GP configuration as described in Sect. 4.3.5. For each simulation, we plot the posterior over the semi-amplitudes for both 'planets' in the left column of Figure 4.9, compared to the posterior obtained from the real dataset. We then count the fraction of the simulations where the recovered semi-amplitude for planets b and c equals or exceeds the median value obtained from the actual observations. For planet b, this occurred 11% if the time in the 100 simulations. For planet c, it occurred in 2% of the cases. Taking Poisson counting errors into account, this is fully consistent with the confidence intervals that we derived for the real observations.

We then repeat the same exercise, creating another 100 synthetic datasets, but this time, injecting two Keplerian signals with the median planet parameters obtained from the real dataset, as reported in Table 4.3. Again, we modelled these synthetic datasets using `pyaneti` with the same configuration as described in Sect. 4.3.5. The resulting posteriors are shown in the right column of Figure 4.9. In this case, we are interested in two distinct questions. First, how often are AU Mic b and AU Mic c detected at a given confidence level from these simulations? For this purpose, we consider that a detection has occurred if the median of the posterior is larger than 2σ, where σ is half the interval between the 16.5^{th} and 83.5^{th} percentiles. We find that AU Mic b is detected 42% of the time, and AU Mic c 88% of the time. This confirms that, if the planet masses are similar to the maximum a posteriori values we derived from the real data, more data is needed for a robust detection of planet b. Second, we asked what fraction of the time the recovered semi-amplitude is within 2σ of the injected value? We find that this happens 91% and 89% of the time, for AU Mic b and AU Mic c respectively. For Gaussian posteriors, we would expect these numbers to be around 95%. Again, accounting for Poisson counting errors, this result is thus consistent with what we expect.

4.5.5 Composition and evolution

Having measured radii and masses for both planets allows to place them in a mass-radius (M-R) diagram, as shown in Figure 4.10. Also shown on that figure are other planets with well-determined masses and radii and theoretical mass-radius relations for terrestrial and ocean worlds (Zeng et al., 2016), and for *evolved* planets with H/He envelopes (Zeng et al., 2019) accounting for 1–5% of the total mass, at a temperature of 500 K, which is close to the equilibrium temperatures of both AU Mic b and c (593 ± 21 K and 454 ± 16 K respectively, see Martioli et al. 2020 and Table 4.1). We note that although it is not ideal to directly compare these young planets with their older counterparts, this is standard practice in the field.

Comparison to these theoretical composition curves for evolved, $\sim$ Gyr old planets indicates that planet c is compatible with a pure H_2O world, and planet b

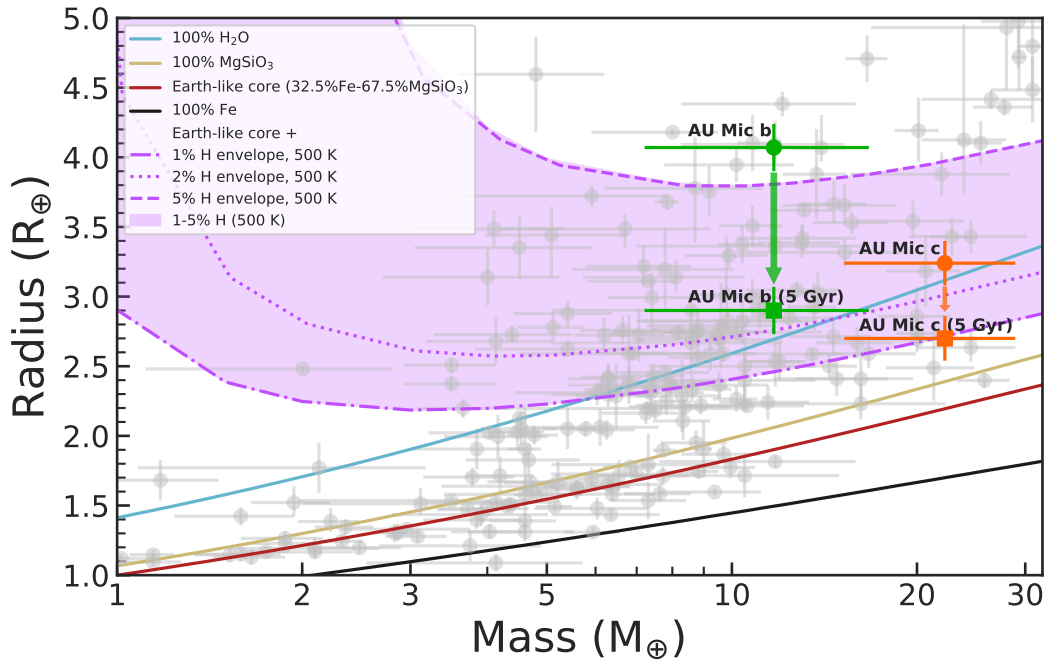

Figure 4.10: Mass *vs* radius diagram for small exoplanets ($1 < R_\mathrm{p} < 5R_\oplus$ and $1 < M_\mathrm{p} < 32M_\oplus$). Grey points with error bars show planets with mass and radius measurements better than 50% (As in the TEPCAT catalogue, https://www.astro.keele.ac.uk/jkt/tepcat/, Southworth et al., 2007). AU Mic b and c are shown with a green and orange circle, respectively. The green and orange arrows indicate the expected evolutionary pathway for the planets and their final state after 5 Gyr. The green and orange squares show the expected position of AU Mic b and c after 5 Gyr, respectively. Solid lines represent two-layer models as given by Zeng et al. (2016) with a different colour corresponding to a different mixture of elements. Purple non-solid lines correspond to Earth-like rocky cores surrounded by a Hydrogen envelope of 1% (dash-dotted line), 2% (dotted line), and 5% (dashed) Hydrogen mass for *evolved* exoplanets assuming an equilibrium temperature of 500 K (Zeng et al., 2019). Figure by Oscar Barragán. **Note**: One should compare the expected evolved position of the planets with the composition curves, rather than their current position.

requires an atmosphere containing some H/He. However, it is difficult to imagine how a pure H_2O planet could form. Coupled with the fact planet b hosts an atmosphere containing H/He, we consider it more likely that both planets possess voluminous H/He atmospheres. However, comparison to these evolved mass-radius relationships is indicative only. Young planets still contain considerable thermal energy left over from their assembly (e.g. Ginzburg et al., 2016), resulting in significantly larger planetary radii compared to evolved planets with the same composition (e.g. Owen, 2020).

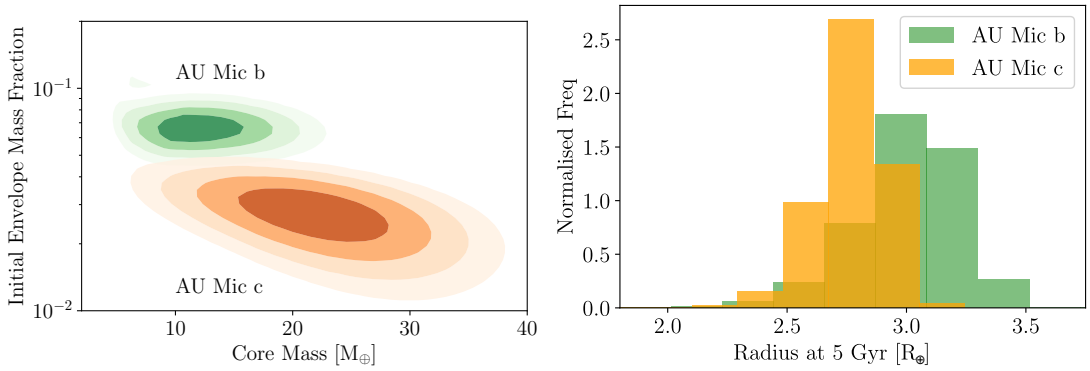

Figure 4.11: Initial envelope mass fractions and core masses (left - with contours shown at 0.5σ intervals) and radii after 5 Gyr (right) for AU Mic b and c (in green and orange, respectively) compatible with the measured masses and radii, based on evolutionary calculations including cooling and contraction and photo-evaporation (see Section 4.5.5 for details). Figures by James Owen.

Thus, we compare the measured masses and radii to evolutionary models for close-in exoplanets, that include the impact of cooling and contraction of any H/He atmosphere and photoevaporative loss using MESA models (Owen & Wu, 2013). The evolutionary calculations are identical to those used in Owen (2020) and Mann et al. (2021). In this manner, the measured masses and radii of planets b and c, can be used to constrain their possible evolutionary pathways, and hence their composition and thermodynamic state both today and at their formation. The evolutionary calculations were performed by James Owen.

We find that both planets formed with voluminous, but low mass H/He dominated atmospheres and as such are likely progenitors of the ubiquitous super-Earth/sub-Neptune population. This is further evidenced when we evolve these planets forward to an age of 5 Gyr finding that in the vast majority of cases these planets retain a fraction of their H/He atmosphere, reaching a radius of ~ 2.9 and ~ 2.7 $R_\oplus$ for b and c respectively, see Figure 4.11. However, there are two standout results. The first is that the amount of H/He these planets accreted from their parent discs is significantly less than predicted from standard models of core-accretion (e.g. Lee & Chiang, 2015). The second is the trend between the two planets, whereby planet c has a higher inferred core-mass, but accreted less H/He

than planet b. This is exactly the opposite of what is expected from core-accretion, where more massive cores accrete more H/He (e.g. Pollack et al., 1996).

There have already been indications that close-in planets may accrete less H/He than predicted by core-accretion, based on a sample of old individual planets (Jankovic et al., 2019), and from inferences about the population of planets discovered by *Kepler* (Rogers & Owen, 2021). However, this is the first time it has been directly identified in young planets that have not been significantly affected by atmospheric mass-loss. Possible mechanisms to resolve this tension with core-accretion include forming the planets late in the disc's lifetime, during the dispersal phase (e.g. Ikoma & Hori, 2012; Lee & Chiang, 2016), or the conclusion from 3D simulations that high-entropy gas is continually recycled into the forming atmosphere, preventing it from cooling and accreting more gas (e.g. Ormel et al., 2015; Chen et al., 2020; Ali-Dib et al., 2020). Finally, additional mass-loss during disc dispersal can dramatically remove accreted material, as the disc's pressure confinement of the proto-atmosphere is rapidly removed (e.g. Owen & Wu, 2016; Ginzburg et al., 2016).

However, none of these proposed mechanisms can reconcile core-accretion with the observation that planet c, with its more massive core, started off with a smaller H/He atmosphere. This is even more curious as planet c appears massive enough to have undergone run-away accretion, even at its current short-period orbit, and formed a giant planet (e.g. Rafikov, 2006; Lee et al., 2014). However, it only had an initial H/He mass fraction of a few percent.

One possible explanation is that the two planets formed further from the star than their present-day locations, then migrated inwards. Standard core accretion models predict that the mass of the accreted atmosphere grows with core mass as $\sim M_{\rm core}^{1.7}$ (as evidenced by Lee & Chiang (2015)), and is approximately logarithmically sensitive to the disc pressure (e.g. Piso & Youdin, 2014). Applying these scaling laws directly to the core and envelope masses we infer for AU Mic b and c, it would imply that the two planets formed in regions of the disc with extremely different densities (by a factor $\gtrsim \exp(10)$). Such a scenario would also require that planet c did not start migrating inwards until the disc dispersed (otherwise it would have

accreted more gas). It is then difficult to see how the planet would have reached its current orbit by the present age of the system, in the absence of a gas disc. On the other hand, the critical core mass for runaway gas accretion depends on the rate at which the core is accreting solid material , which itself depends on location within the disc (Terquem, 2014). This opens up the possibility of a scenario where the planets form at different locations in the disc, but less extremely so, and migrate inwards during the late stages of the disc's dispersal. Exploring this scenario further using detailed calculations is, however, beyond the scope of the present work.

Another possible explanation would be that planet c started forming later, and thus acquired its envelope over a shorter time, than planet b. However, the accreted mass has a very weak dependence on accretion time ($M_{\rm env} \propto t^{0.4}$, Lee & Chiang 2015). Following the same logic as the gas surface density arguments given above, this would require planet c to form over a time period $10^{1/0.4} \sim 300$ times shorter than planet b. Again, this would require a great deal of fine tuning.

A second, speculative scenario that would reconcile both c's large core-mass and lower H/He atmosphere mass compared to b, is that c is the product of a post-disc-dispersal giant impact. Giant impacts are not an unlikely outcome for planets that find themselves on short period orbits after disc-dispersal (e.g. Poon et al., 2020; Bonomo et al., 2019). Giant impacts can remove large amounts of H/He in any collision (e.g. Liu et al., 2015; Inamdar & Schlichting, 2016) in addition to the fact that the collision inflates any residual H/He atmosphere resulting in enhanced photoevaporation (Biersteker & Schlichting, 2019). Planets in multiple systems found by *Kepler* tend to have similar radii (e.g. Weiss et al., 2018) and masses (e.g. Millholland et al., 2017) to each other. This has been interpreted as evidence for uniformity in the underlying core-mass within each system (Millholland & Winn, 2021). Thus, if AU Mic formed three planets with properties similar to b, and two underwent a giant impact, a planet with properties similar to c would be the natural outcome. One way to test this speculative scenario is to measure the obliquity of planet c. Any indication of difference between the spin-orbit angles of the two planets (the orbital plane having been found aligned with the stellar rotation axis;

Addison et al., 2021; Martioli et al., 2020; Szabó et al., 2021; Hirano et al., 2020) would indicate that significant dynamical interaction between planets in the system took place after disc-dispersal. The amplitude of the Rossiter-McLaughlin (RM) effect induced by planet c is typically of the order of $v \sin i \, (R_\mathrm{p}/R_\mathrm{s})^2 \sqrt{1 - b_\mathrm{p}^2}$, where R_p and R_s refer to the planet and star radii, and where b_p is the impact parameter of the planet transit. We thus expect an RM effect of $\sim 10\,\mathrm{m\,s^{-1}}$ for AU Mic c, which is feasible with current high-precision spectrographs.

The scenarios presented above are based on the suggestions and expertise of James Owen and Caroline Terquem.

4.6 Conclusions

We have analysed data from an intensive monitoring campaign using HARPS with multidimensional GP framework (B22), and measured the masses of AU Mic b and c to be $11.7 \pm 5.0\ M_\oplus$ and $22.2 \pm 6.7\ M_\oplus$. We detect planet c at 3.4σ confidence and planet b at 2.3σ confidence. The results are insensitive to the choice of RV time-series (DRS, `SERVAL`, `HARPS-TERRA`) and to the specific activity indicators used, though this choice affects the degree of confidence in the detections slightly. The mass measurements, combined with literature radius estimates, indicate that AU Mic b has a significant H/He envelope and may have an internal heat source. On the other hand, we find that AU Mic c is denser and compatible with either a rocky core surrounded by a $\sim 2\%$ H/He envelope or a pure H_2O composition. These results are in tension with current core-accretion models, which predict that planet c, with a more massive core, should have the larger H/He envelope of the two. We provide a possible, speculative explanation for this discrepancy involving a giant impact, but stress that additional observations are needed to further refine the mass measurements and constrain the obliquity of planet c.

The RV signals of the two planets around AU Mic are around 50 times smaller than the activity signals. Disentangling the former from the latter is very challenging, as highlighted by the discrepancies between our results and those of other teams working on the same system using different instruments and methods, which need

to be better understood. Further observations of this system and independent analyses of the available datasets are needed to resolve these discrepancies. However, the fact that these detections were possible at all is very encouraging for the continued characterisation of the increasing number of young transiting planets being discovered by surveys such as *K2* and *TESS*. The characterisation of planets around young stars also provides an extreme test case for activity mitigation techniques in RVs. The methods being developed in this context will prove useful for future searches for smaller and cooler planets around less active stars, where the amplitude ratios between planetary and activity signals are similar.

Statement of Authorship for joint/multi-authored papers for PGR thesis

Title of paper: One year of AU Mic with HARPS: I - measuring the masses of the two transiting planets
Publication status: Submitted for publication
Journal: Monthly Notices of the Royal Astronomical Society (MNRAS)

Publication details: This paper is the first in a series of papers aimed at presenting the analysis of the AU Mic observations gathered during European Southern Observatory (ESO) periods P106 & 107. The aim of this paper is to measure the masses of the two transiting planets in the AU Mic system.

Paper contributions:

Contributions by author: Norbert Zicher: lead author, principal investigator (PI) for observations, RV analysis & modelling, and interpretation. Oscar Barragan: RV analysis, dynamical analysis, robustness testing. Baptiste Klein: flare analysis, composition, and evolution interpretation. Suzanne Aigrain: principal investigator (PI) for observations, modelling recommendations and interpretation. James Owen: composition and evolution analysis and interpretation. Laurel Kaye: TTV analysis. Louise Dyregaard: data reduction with DRS. Davide Gandolfi & Luisa Serrano: data reduction with *serval* and *terra*.

Student Confirmation:

Student name: Norbert Zicher

Contributions to the paper: lead author, principal investigator (PI) for observations, RV analysis & modelling, and interpretation

Signature: Zicher Date: 27.01.2022

Supervisor Confirmation:

Student name and title: Prof. Suzanne Aigrain

Supervisor comments: I confirm the author contributions are as described above

Signature: Date: 28/1/22

All that is gold does not glitter,
Not all those who wander are lost;
The old that is strong does not wither,
Deep roots are not reached by the frost.

From the ashes a fire shall be woken,
A light from the shadows shall spring;
Renewed shall be blade that was broken,
The crownless again shall be king.

— J.R.R. Tolkien, from
The Fellowship of the Ring (1954)

5 Modified Periodograms

Contents

Periodograms represent one of the classical go-to methods for analysing time-series data. Historically, astronomers have used techniques similar to the Generalised Lomb-Scargle periodogram to search for planets around bright stars by looking for peaks (local maxima) in the power spectrum of the RV time-series. In this chapter, I present two extensions to the Generalised Lomb-Scargle periodogram (see Chapter 3.1 for more information) that are able to account for nuisance signals arising from the host star, hence improving planet detection capabilities. I apply these methods to the AU Mic dataset to obtain detection limits around the target, as well as to compare the results with the more complex GP framework (see Chapter 4).

5.1 Introduction and context

Analysing time-series data for periodic variations is one of the cornerstones for exoplanet searches, especially in Doppler spectroscopy. Arguably one of the most widely used tools for this are periodograms. Since their introduction in 1898, they have been intensely studied and a large variety of 'adaptations' exist in the literature. In the case of radial velocity searches, one of the most widely adopted versions is the generalised Lomb-Scargle periodogram as introduced in Chapter 3.1. Due to its ease of use and simplicity, it is part of every astronomer's toolkit, particularly in RV searches for exoplanets. Observers look for peaks in the power distribution of the periodograms. These peaks correspond to periodic signals that are present in the data and are potentially induced by planetary companions orbiting the target. However, with the continuous improvement of instruments and their precision, it has become apparent that variations induced by the host star can not only mimic that of planets, but also are often stronger than their planetary counterparts. Fortunately, with the help of activity sensitive indicators, it is possible to separate these two signals, allowing us to detect exoplanets.

Despite its wide range of applicability, the GLS also has some shortcomings. As mentioned previously in Chapter 3.1, an important limitation is its inability to properly account for signals arising from stellar variability. This is a critical point, as these nuisance signals can often mimic the behaviour of planetary signals and it is crucial to remove them. This shortcoming can be improved by accounting for correlations between the RV time-series and activity-sensitive time-series that track the stellar variability. In this chapter, I present two extensions to the GLS periodogram. The first extension called 'Linear activity-corrected periodogram' (LACP), takes into account any linear correlation between the RV time-series and activity indicators, reducing the impact of the stellar signal on the dataset. The second extension relies on using Gaussian processes (GPs) in order to model the activity induced variations and isolate it from any genuine signals that could be induced by a companion.

The first of these periodograms was conceptualised after my visit to IPAG (Institut de Planétologie et d'Astrophysique de Grenoble) in France, where I worked with the group of Prof. Anne-Marie Lagrange on young systems. Their initial approach to searching for planets around young stars led me to develop the linear activity-corrected periodogram fitting method. Originally, they would subtract a linear correlation from the data such that $\mathrm{RV}_{\mathrm{residuals}} = \mathrm{RV}_{\mathrm{obs}} - s \cdot \beta_{\mathrm{Activity}}$, where $\mathrm{RV}_{\mathrm{obs}}$ are the observed radial velocities, $\beta_{\mathrm{activity}}$ is an activity indicator time-series (such as BIS or FWHM), and s is a constant (the slope of the linear correlation obtained from a least-squares fit between the RVs and the ancillary time-series). Then, using the residuals they would place detection limits on the presence of any planets. They would do this using the Local Power Analysis (LPA) (Meunier et al., 2012), which determines the minimum $m \sin i$ (minimum mass) for which a companion on a circular orbit with period P would lead to a signal consistent with the data. The way 'consistent' is defined here is the following, the LAP method provides the maximum power of the pure planetary signal at period P (sampled at the observations) and compares it to the maximum power of the data (residuals) periodogram within a small period range around period P (Grandjean et al., 2020, 2021).

Considering the drawbacks of sequential fitting, the importance of time sampling and also the robustness of FAP/peak significance, I thought that the way they were doing things was sub-optimal. I believe that the sequential fitting is susceptible to artefacts, and as a consequence of this modelling the detection limits may be biased. I showed that fitting simultaneously for the trend performs at least as well as the linear detrending method they employed. In some cases it is able to return more accurate results for the planet amplitude than a sequential approach. I have not explored the robustness of the LPA method and as such I refrain from making any comments about its performance. However, I believe that using injection tests is a more robust way of placing constraints on the presence of planets and as such I adopt it for my analysis in this chapter. A toy model test case is presented in Section 5.2.1 which shows how both of these approaches do significantly better than a simple GLS and it also compares the results from the two approaches.

An additional incentive behind developing the two periodogram-like approaches comes from the fact that although the GP framework presented in Chapter 3.3 and applied to the AU Mic dataset in Chapter 4 does a great job at mitigating the affects of stellar activity, it requires a tight time-sampling and/or constraints on the ephemeris. In cases where those requirements are not met, the GP framework breaks down. This is due to the fact that the likelihood function is highly multi-modal in orbital space and that the activity signal cannot be properly constrained. As such it is necessary to explore alternative, less complex approaches to perform 'blind' searches for planets in RV datasets, particularly when the time-sampling is fairly sparse compared to the periods of interest.

The structure of this chapter is as follows. Section 5.2 focuses on the linear activity-corrected periodogram, with Subsection 5.2.1 providing the theoretical basis and Subsection 5.2.2 testing the performance on a toy model. Section 5.3 presents the results of applying the LACP method to the AU Mic dataset (introduced in Chapter 4) in order to place detection limits for any 'long' period planets. Section 5.4 details the G-dG periodogram which uses a GP, similar to the GP framework, in order to model the stellar activity and remove it from the data. Finally, Section 5.5 summarises the results and their implications.

5.2 LACP - Linear activity-corrected periodogram

Analysing datasets of young active stars is extremely difficult. In these cases, it is crucial to account for the stellar variability signals as this can often be much bigger than the signal induced by planets. For example, in the case of AU Mic, as shown in Chapter 4, the signal of the two transiting planets is buried in the data and are roughly 50 times smaller than the stellar signals. For systems where there is a clear correlation with one or more of the activity indicators, these can easily be used to 'clean' the RVs and unveil the presence of any potential exoplanets. In some instances, it is not possible to use complex models such as the GP framework because of the sparse time-sampling of the data. In situations like this, less complex models must be used in order to remove the stellar variability. A few examples of these

include pre-whitening, harmonic decomposition or linear detrending. However, due to the flaws of iterative fitting and signal interference, it is best to fit for everything at the same time. This motivated the development of the linear activity-corrected periodogram. Note that I do not adopt the $\hat{\tau}$ notation from the LS periodogram (see Chapter 3.1. It might be possible to provide a contracted form of the equations, similar to the LS/GLS periodogram, but this has not been explored.

5.2.1 Theory

Let us assume the following model:

$$\mathrm{RV}_{\mathrm{model}}\left(t_i\right) = a\sin\left(\frac{2\pi}{P}t_i\right) + b\cos\left(\frac{2\pi}{P}t_i\right) + c\cdot\beta_i + d \tag{5.1}$$

where β_i represents one of activity time-series (e.g. FWHM, BIS, etc.) that shows a strong linear correlation with the RVs.

In order to account for the observational errors, an inverse-variance weighting is introduced into the model. Fitting the model to the data can be achieved using a least-squares approach. For simplicity, I adopt the notation, $\mathrm{RV}_{\mathrm{obs}}(\mathrm{t_i}) = \alpha_{\mathrm{i}}$ for the radial velocity observations:

$$\chi^2 = \sum_i \frac{\left[\alpha_i - \mathrm{RV}_{\mathrm{model}}\left(\mathrm{t_i}\right)\right]^2}{\sigma_i^2} \tag{5.2}$$

Then:

$$\chi^2 = \sum_i \left[\alpha_i^2 + \mathrm{RV}_{\mathrm{model}}^2\left(\mathrm{t_i}\right) - 2\alpha_{\mathrm{i}}\mathrm{RV}_{\mathrm{model}}\left(\mathrm{t_i}\right)\right]/\sigma_i^2$$

Minimising the above equation, is equivalent to taking the partial derivative with respect to all the free parameters of the model and setting them to 0.

$$\frac{\partial\chi^2}{\partial a} = \frac{\partial\chi^2}{\partial b} = \frac{\partial\chi^2}{\partial c} = \frac{\partial\chi^2}{\partial d} = 0$$

Taking the derivatives, results in the following set of equations:

$$\begin{aligned}
\tfrac{\partial\chi^2}{\partial a} &= \textstyle\sum_i \tfrac{2}{\sigma_i^2}\left[a\sin^2 x_i + b\cos x_i\cdot\sin x_i + c\cdot\beta_i\cdot\sin x_i + d\sin x_i - \alpha_i\sin x_i\right] \\
\tfrac{\partial\chi^2}{\partial b} &= \textstyle\sum_i \tfrac{2}{\sigma_i^2}\left[a\sin x_i\cdot\cos x_i + b\cos^2 x_i + c\cdot\beta_i\cdot\cos x_i + d\cos x_i - \alpha_i\cos x_i\right] \\
\tfrac{\partial\chi^2}{\partial c} &= \textstyle\sum_i \tfrac{2}{\sigma_i^2}\left[a\sin x_i\cdot\beta_i + b\cos x_i\cdot\beta_i + c\cdot\beta_i^2 + d\cdot\beta_i - \alpha_i\cdot\beta_i\right] \\
\tfrac{\partial\chi^2}{\partial d} &= \textstyle\sum_i \tfrac{2}{\sigma_i^2}\left[a\sin x_i + b\cos x_i + c\cdot\beta_i + d - \alpha_i\right]
\end{aligned} \tag{5.3}$$

These can be collected into the follow system of linear equations:

$$Ax + B = 0; \quad Ax = -B$$

Where:

$$A = \sum_i \frac{2}{\sigma_i^2} \begin{pmatrix} \sin^2 x_i & \cos x_i \cdot \sin x_i & \beta_i \sin x_i & \sin x_i \\ \sin x_i \cdot \cos x_i & \cos^2 x_i & \beta_i \cos x_i & \cos x_i \\ \sin x_i \cdot \beta_i & \cos x_i \cdot \beta_i & \beta_i^2 & \beta_i \\ \sin x_i & \cos x_i & \beta_i & 1 \end{pmatrix}$$

and:

$$B = \sum_i \frac{2}{\sigma_i^2} \begin{pmatrix} -\alpha_i \cdot \sin x_i \\ -\alpha_i \cdot \cos x_i \\ -\alpha_i \cdot \beta_i \\ -\alpha_i \cdot 1 \end{pmatrix}$$

Now that the system of linear equations is defined, it is just a matter of computing χ^2 at each trial period P_j in order to obtain a periodogram. I adopt the normalisation $p(\omega) = \frac{\chi_0^2 - \chi^2(\omega)}{\chi_0^2}$, where χ_0^2 is the χ^2 of the activity only model ($\mathrm{RV_{model}}\ (\mathrm{t_i}) = \mathrm{c} \cdot \beta_\mathrm{i} + \mathrm{d}$) and $\omega = \frac{2\pi}{P_j}$, with P_j being the trial period. This way, the resulting power $p(\omega)$ must obey $0 \leq p(\omega) \leq 1$, following the same formalism as the generalised Lomb-Scargle.

5.2.2 Feasibility

Having presented the theoretical basis behind the linear activity-corrected periodogram, it is pivotal to test its applicability and effectiveness. For this, I create a toy example with synthetic data that I can use to evaluate it. In this experiment, I define the full time-series such that it is between 'time' 0 and 100 days and consists of 200 evenly spaced data points. This noise-free time-series are used to create the synthetic data, from which I then randomly select a subset of 25 points and add noise to construct the observed time-series. I will show how both the linear-activity corrected periodogram and the method used by the Grenoble team greatly improve detectability over a simple GLS periodogram. I addition, I also compare the performance of the two.

First, I generate two synthetic time-series. One corresponding to an activity indicator time-series y_1, that will contain the activity signal and y_2 corresponding

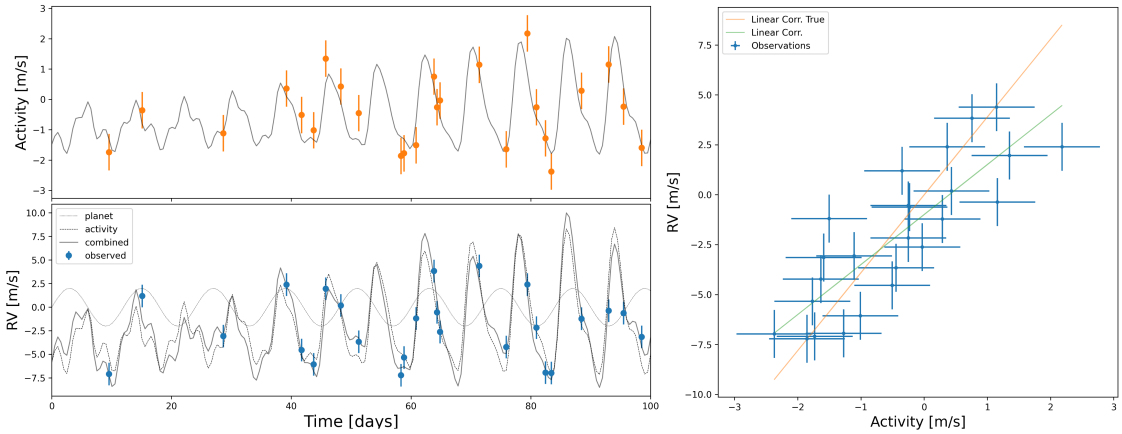

Figure 5.1: Simulated time-series. Left: Simulated activity (top panel) and RV time-series (bottom panel) with the injected planet. Right: Linear correlation between the two. The orange solid line shows the true linear correlation, whilst in green I show the linear correlation computed using a linear fit using polyfit.

to the RVs induced by the stellar variability plus a planetary signal added on top. I do this with the help of a Gaussian process G and its derivative $\dot{G}$, defined using the QP kernel (see equation 3.34) to generate a quasi-periodic time-series. I compute the covariance of the zero-mean Gaussian process on the full 200 data points and draw a random sample (as such obtaining G and $\dot{G}$). The GP hyper-parameters used in this exercise are $P_{\rm GP} = 7.9$ days, $\lambda_{\rm p} = 0.8$ and $\lambda_{\rm e} = 91$ days, corresponding to the rotation period of the 'star', the harmonic complexity and the evolution timescale. Then:

$$y_1 = \nu_1 \cdot G + \nu_2 \cdot \dot{G}$$

$$y_2 = \nu_3 \cdot G + \nu_4 \cdot \dot{G} + \mathrm{RV}_{\rm planet}$$

Where $\nu_1 = 3.0$, $\nu_2 = 1.1$, $\nu_3 = 11.7$, and $\nu_4 = 5.3$ are the parameters controlling the dependence of the simulated data on the GP. The injected planet parameter is defined by a sinusoidal function with amplitude $A = 2\ \mathrm{m\,s^{-1}}$, period $P = 12$ days and phase $\phi = 0$:

$$\mathrm{RV}_{\rm planet}(\mathrm{t_i}) = \mathrm{A} \cdot \sin(\frac{2\pi}{\mathrm{P}}\mathrm{t_i} + \phi)$$

Afterwards, I sample these functions at 25 random epochs (the same for both) and add white noise to obtain realistic observations:

$$\mathrm{Activity(t)} = \mathrm{y_1(t)} + \sigma_1(\mathrm{t})$$

Table 5.1: Model comparison of the linear activity-corrected periodogram best fit values. Constant model corresponds to just an offset, and activity-only is a linear trend + an offset.

Parameter	Constant model	Activity-only	LACP model	True
χ^2	207.63	62.68	24.97	...
Offset ($m\,s^{-1}$)	-2.01	-0.99	-1.03	0
Linear corr.	...	2.50	2.81	3.9
Period [days]	...	...	11.95	12
Amplitude ($m\,s^{-1}$)	...	...	2.05	2
Phase	...	...	0.09	0
BIC	210.85	69.12	41.06	...

$$\mathrm{RV(t)} = \mathrm{y_2(t)} + \sigma_2(\mathrm{t})$$

where $\sigma_1 = \mathcal{N}[0, 0.6]$ and $\sigma_2 = \mathcal{N}[0, 1.2]$ are just randomly drawn values from Gaussian distributions. The two synthetic time-series and sampled observations are shown in Figure 5.1, together with their linear correlation.

Figure 5.2 shows the periodograms for the two simulated time-series (top 2 rows), the LACP periodogram of the RVs (3$^{\mathrm{rd}}$ row), a comparison between the GLS periodograms for three different models (4$^{\mathrm{th}}$ row) and the window function (final panel). Each plot is briefly presented below with a discussion around their significance in the text that follows. The top two rows show the `astropy` GLS periodogram of the simulated activity time-series and RV time-series respectively. The third row shows the periodogram obtained from applying the linear activity-corrected method. The fourth row shows the GLS periodograms of three different RV time-series for comparison purposes. In navy, I show the GLS periodogram of the original RV time-series. In blue, I show the GLS periodogram of the corrected RV time-series (subtracted the best fit linear trend) from the LACP, and in orange I show the GLS periodogram of the RV time-series after subtracting the linear fit obtained from polyfit (see green line in the right panel of Figure 5.1). In addition, I provide a zoomed-in version around the injected planet period of the periodogram to make the differences easier to see. The bottom row shows the window function of the simulated dataset. In each panel, I show the stellar rotation period with a solid black line and the injected planet period with a dashed green line.

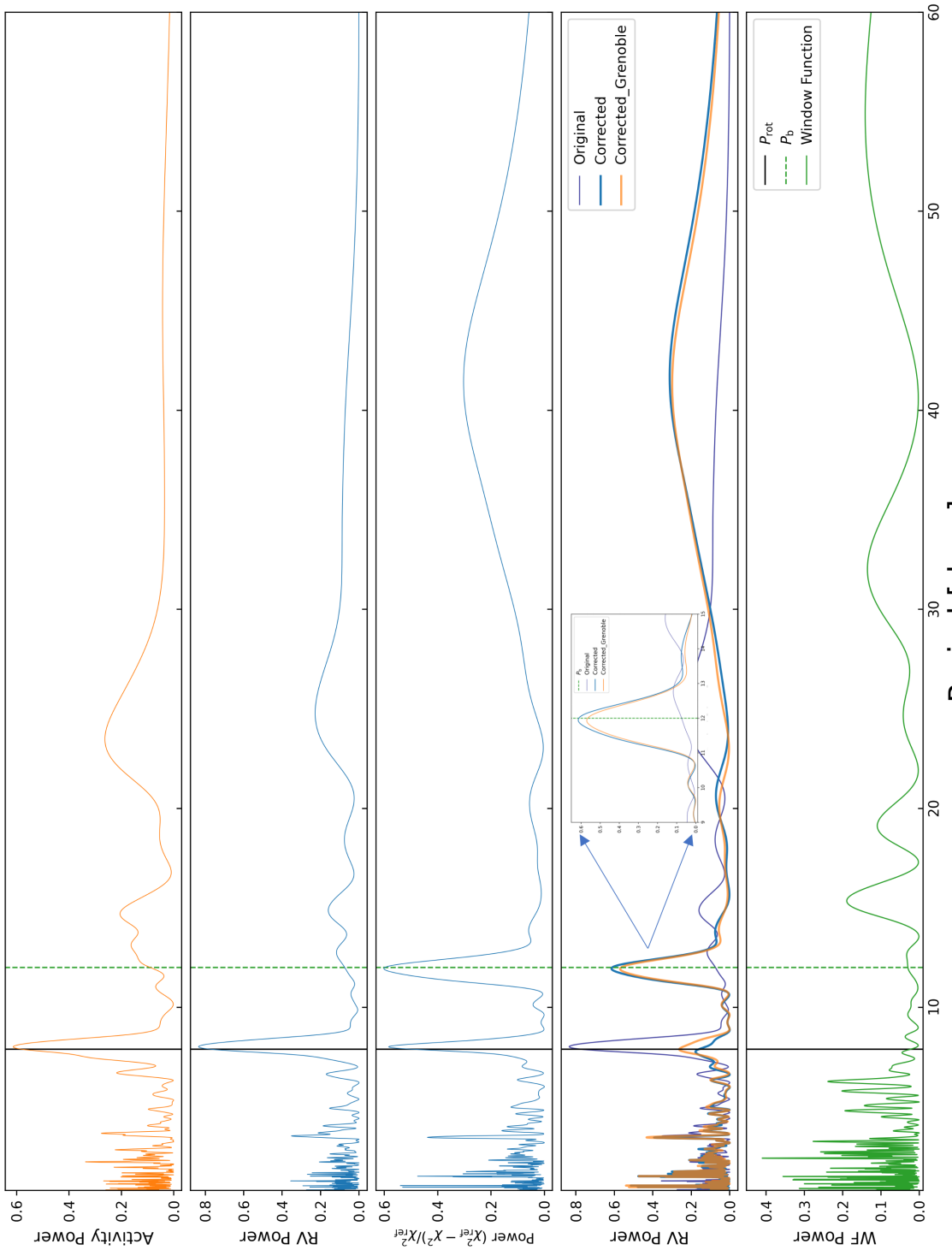

Figure 5.2: Periodograms of the simulated data. Refer to text for details, due to size limitations.

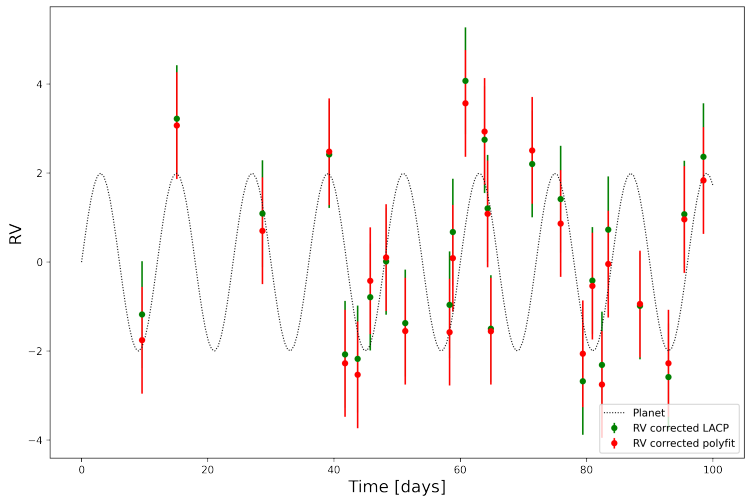

Figure 5.3: Residuals after subtracting the best fit linear activity model. In red I show the residuals after removing the best fit linear fit from a least-square fit, whilst in green I show the residuals after subtracting the best fit linear model from the linear-activity corrected periodogram.

Before analysing this dataset, let us have a look at the `astropy` GLS periodograms of the synthetic time-series (see top 2 rows of Figure 5.2). It is clear that the highest peak in the periodograms is the rotation period of the star as expected. It is worth noting that the injected planet is 'hidden' in the RV periodogram and the probability of finding this signal in the uncorrected RV time-series is 'limited'.

Applying the linear activity-corrected periodogram to the simulated data vastly improves the detection capabilities. The middle panel (third row) of Figure 5.2 shows the periodogram obtained using this custom method. It is obvious that the signal at the rotation period of the star has decreased and the highest peak now corresponds to the planets rotation period. The exact values returned by the linear activity-corrected method are shown in Table 5.1. In order to compare the models returned by the LACP we can use the BIC, which clearly shows that the best fit model is the full LACP model (linear activity + sinusoidal). Although this model is not perfect, it allows us to push the detection boundaries in a thoughtful and sensitive way.

For comparison purposes, Figure 5.3 shows the RV residuals together with the injected signal after subtracting the linear trend. This is done in two different ways.

First, in green I show the residuals after subtracting the best fit linear model obtained from my linear activity-corrected periodogram, whilst in red I show the residuals after subtracting the linear fit using `numpy` (Harris et al., 2020) package's polyfit[1].

In order to compare the periodograms of post & prior correction, I fit these residuals with the `astropy` GLS. The results are shown in the fourth row of Figure 5.2. The difference between the two corrected RV time-series is that in the case of 'corrected', the linear model subtracted was fitted simultaneously with a sinusoidal in LACP, whilst 'corrected_Grenoble' corresponds to simply fitting a linear trend and removing it. This is what the Grenoble team used to do. It can be seen in the zoomed-in part of the figure that the LACP performs slightly better, although in this particular case the differences are small. In addition to providing similar or better detection capabilities, fitting the linear trend simultaneously also allows us to better recover the amplitude of the injected signal. By comparison, the GLS periodogram predicts a 1.98 $\mathrm{m\,s^{-1}}$ signal for the LACP corrected RVs and 1.90 $\mathrm{m\,s^{-1}}$ for the sequential fitting (the method employed by the Grenoble team), giving marginal evidence that it is preferable to perform the fitting simultaneously. I note that this is a rather idealistic scenario in which there are no other signals in the dataset and as such the difference between a sequential and simultaneous modeling is small. The later injection-recovery tests in real data showed a clearer improvement, though there was neither space nor time to detail them here.

Even though the presented case is only a toy model and arguably not as complex as any real world dataset, it clearly shows that there is a significant gain in correcting for the nuisance signal of the host star whenever possible. It is important to note that although the linear detrending helped, by no means did it offer a 'perfect' picture. This motivated the development of the GdG periodogram presented later in the chapter.

[1]See the numpy package documentation here.

5.3 AU Mic detection limits

Building on the framework presented in the previous chapter, it is possible to extend it to account for any known planetary signals in the data. This makes it suitable to study the full AU Mic dataset, not just the data presented in Chapter 4. As a result, it is possible to apply a linear detrending to the RV on the full 145 observations collected between 2013 and 2021. Discarding the 9 contaminated spectra identified in Chapter 4 results in a total of 136 points used to compute detection constraints on the presence of any long period signals. The full AU Mic data is presented in Figure 5.4. As previously mentioned, due to the sparse sampling of the archival data, it is not suitable to be studied with a GP framework, but this is not a problem when using periodograms. Even though it is not as complex and ultimately will not perform as well as a GP approach, the linear activity-corrected method is able to correct for some of the stellar variability improving the final result. Therefore, in order to extend the LACP framework with a known signal (for simplicity), let us assume the following model:

$$\mathrm{RV}_{\mathrm{model}}\ (\mathrm{t_i}) = \mathrm{a}\sin\left(\frac{2\pi}{\mathrm{P_b}}\mathrm{t_i} + \phi\right) + \mathrm{b}\sin\left(\frac{2\pi}{\mathrm{P}}\mathrm{t_i}\right) + \mathrm{c}\cos\left(\frac{2\pi}{\mathrm{P}}\mathrm{t_i}\right) + \mathrm{d}\cdot\beta_\mathrm{i} + \mathrm{e}$$

Where the first term corresponds to a known planetary signal with period P_b and known phase ϕ, b and c are the free parameters of the fitted sinusoidal signal at period P, d is the linear correlation with an activity time-series represented by β_i and e in an offset. Following the formalism presented in Chapter 5.2.1, this model is equivalent to solving a system of linear equations of the form:

$$Ax + B = 0; \quad Ax = -B$$

Where:

$$A = \sum_i \frac{1}{\sigma_i^2} \begin{pmatrix} \sin^2\gamma_i & \sin\gamma_i\cdot\sin x_i & \cos x_i\cdot\sin\gamma_i & \beta_i\cdot\sin\gamma_i & \sin\gamma_i \\ \sin\gamma_i\cdot\sin x_i & \sin^2 x_i & \cos x_i\cdot\sin x_i & \beta_i\cdot\sin x_i & \sin x_i \\ \sin\gamma_i\cdot\cos x_i & \sin x_i\cdot\cos x_i & \cos^2 x_i & \beta_i\cdot\cos x_i & \cos x_i \\ \sin\gamma_i\cdot\beta_i & \sin x_i\cdot\beta_i & \cos x_i\cdot\beta_i & \beta_i^2 & \beta_i \\ \sin\gamma_i & \sin x_i & \cos x_i & \beta_i & 1 \end{pmatrix}$$

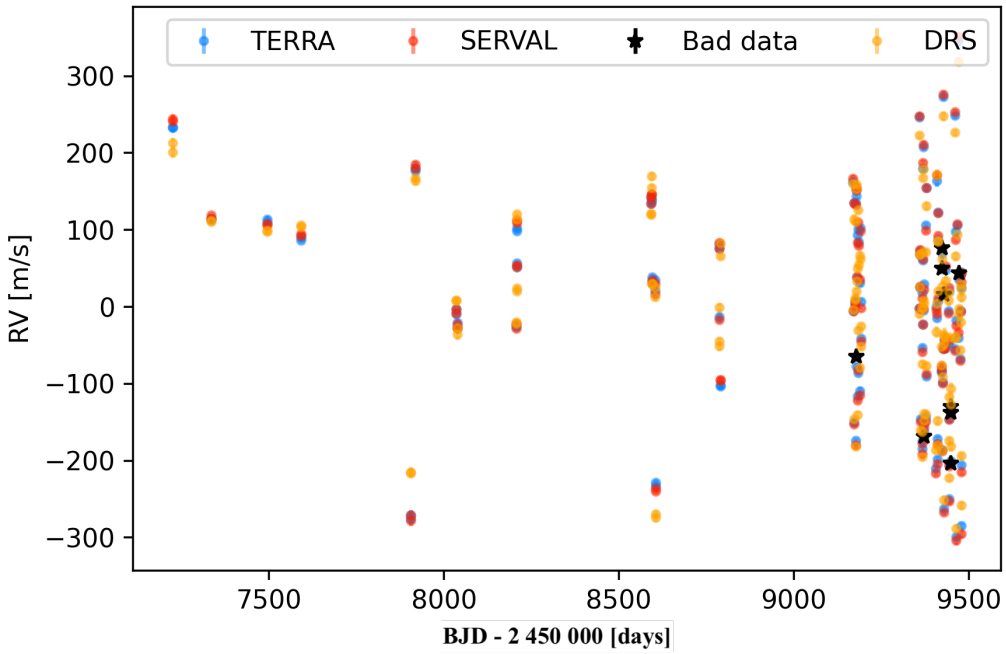

Figure 5.4: Mean-subtracted RV time-series as extracted with SERVAL (red), TERRA (blue), and the DRS (yellow). Black stars mark the nights that were discarded due to contamination and stellar flares. Note that the observations presented in Chapter 4 from the intense monitoring program begin at BJD - 2 450 000 equal to 9170 (See Figure 4.1).

and

$$B = \sum_i \frac{1}{\sigma_i^2} \begin{pmatrix} -\alpha_i \cdot \sin \gamma_i \\ -\alpha_i \cdot \sin x_i \\ -\alpha_i \cdot \cos x_i \\ -\alpha_i \cdot \beta_i \\ -\alpha_i \cdot 1 \end{pmatrix}$$

Where γ_i corresponds to the known signal and x_i is the additional periodic signal that we are fitting for.

When applying this extended LACP method to the AU Mic system, we have two known signals (the two transiting planets) and thus include 2 additional terms rather than just one as presented in the equations above (including only one for simplicity), but the basis is the same. In order to detrend the RVs, it is necessary to find an activity time-series that shows a clear correlation with the observed RVs. The full activity time-series are shown in Figure 5.5. The same colour coding as previously adopted in Chapter 4 is used (orange for DRS, red for `SERVAL` and blue for `HARPS-TERRA`). The left panel shows the activity time-series plotted against DRS

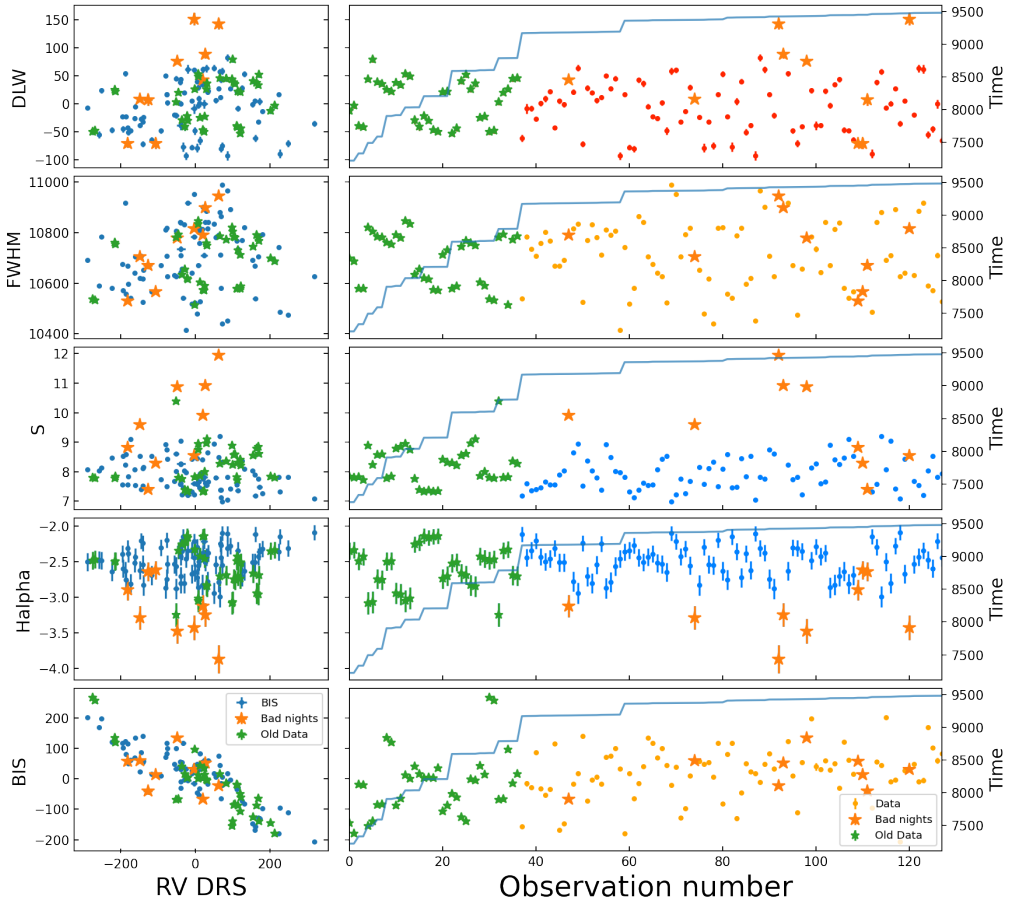

Figure 5.5: Left panel shows the activity indicators versus RVs produced by the DRS pipeline. The right panel shows activity indicators vs observation number (and time with the second axis showed by blue line). From top to bottom: DRS FWHM and BIS, `SERVAL` DLW, `HARPS-TERRA` S_{HK} and Hα index. The colour indicates the pipeline used to extract each indicator: blue for `HARPS-TERRA` red for `SERVAL` and yellow for the DRS. Contaminated observations are marked with orange stars. Archival observations are marked in green.

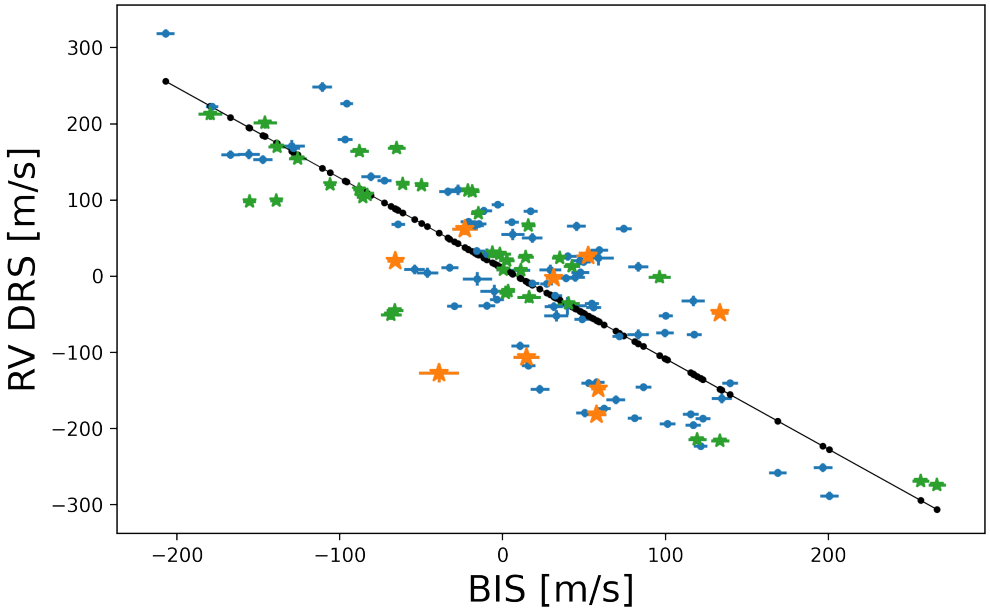

Figure 5.6: Linear trend between the DRS RVs and the Bisector Span activity indicator used to 'correct' the radial velocities. Blue dots show the 'new' observations, archival data in green and contaminated observations are shown with orange stars.

RVs. The right panel plots the activity time-series against observation number due to the big gaps. In addition, the corresponding time is plotted on the second y-axis. Whenever there is a jump in the blue line, that means there is a big gap between the observations. In contrast to the plots presented in Chapter 4, the fiducial RV time-series in this chapter is the DRS version. This is because the activity indicator that shows the best correlation is the BIS (see Figure 5.6), and this is extracted with the DRS pipeline, hence it makes most sense to use the values obtained from the DRS. The strong linear trend between the RVs and BIS can be exploited, allowing the RVs to be corrected for the activity. Unfortunately, even with this strong linear trend, the corrected RVs have a lot of scatter, illustrating that this simplistic model is unable to account for all the variation from stellar activity. Inspecting the periodogram of the corrected RV reveals that even after subtracting the linear trend, there is a strong peak at the stellar rotation period and its aliases and harmonics.

A stark difference between the full dataset and the 82 epochs used before can be seen when looking at the `astropy` GLS periodogram of the data(shown in

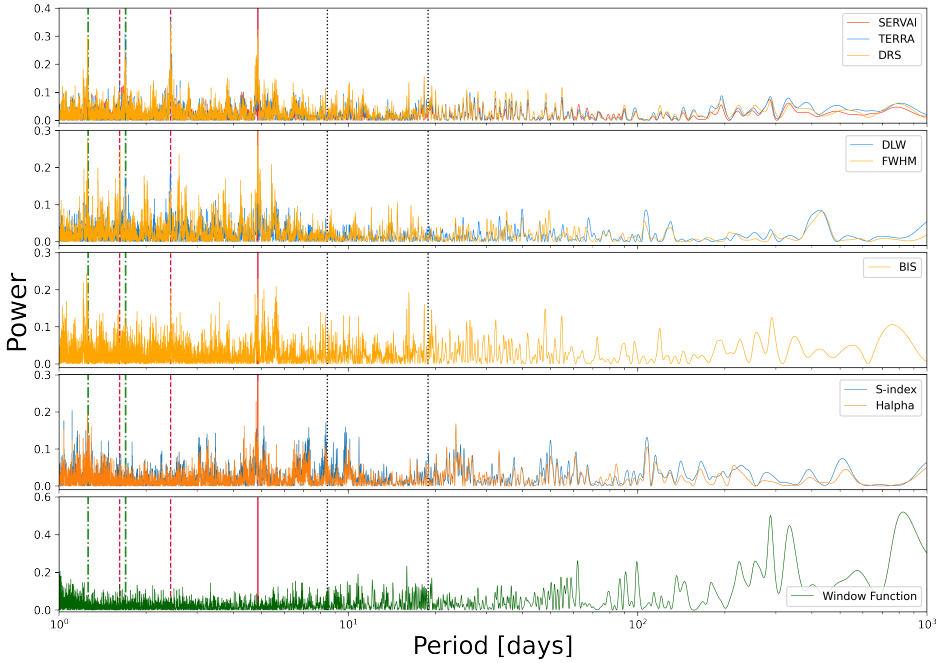

Figure 5.7: Lomb-Scargle periodograms of the 3 RVs time-series (top), DLW & FWHM (2nd panel), BIS (3rd panel), S-index & H_α(4th panel) and the window function of the observations (bottom). Vertical crimson lines denote the stellar rotation period and its first two harmonics, vertical green lines denote 1-d aliases of the stellar rotation period, while vertical black dotted lines denote the orbital periods of AU Mic b and c. The periodograms are a lot noisier compared to Figure 4.4.

Figure 5.7). The periodograms of the full time-series are a lot 'noisier', indicating the challenges of this dataset. Note that these periodograms are computed over a much bigger period range (1 to 1000 days), because in this chapter I am interested in the presence of any long period planets.

Focusing on the periodogram of the DRS RVs shown in the lower panel of Figure 5.8, there is no indication of any clear peaks. This means that it is not possible to infer the presence of any obvious long period planets (or signals). In order to actually quantify this statistically, I perform an injection-recovery test on the AU Mic dataset. I do this by injecting planets at certain periods, amplitudes and phases and try to recover them to constrain what should be detectable 'if it was present in the data'. For each selected period, amplitude, and phase, I generate

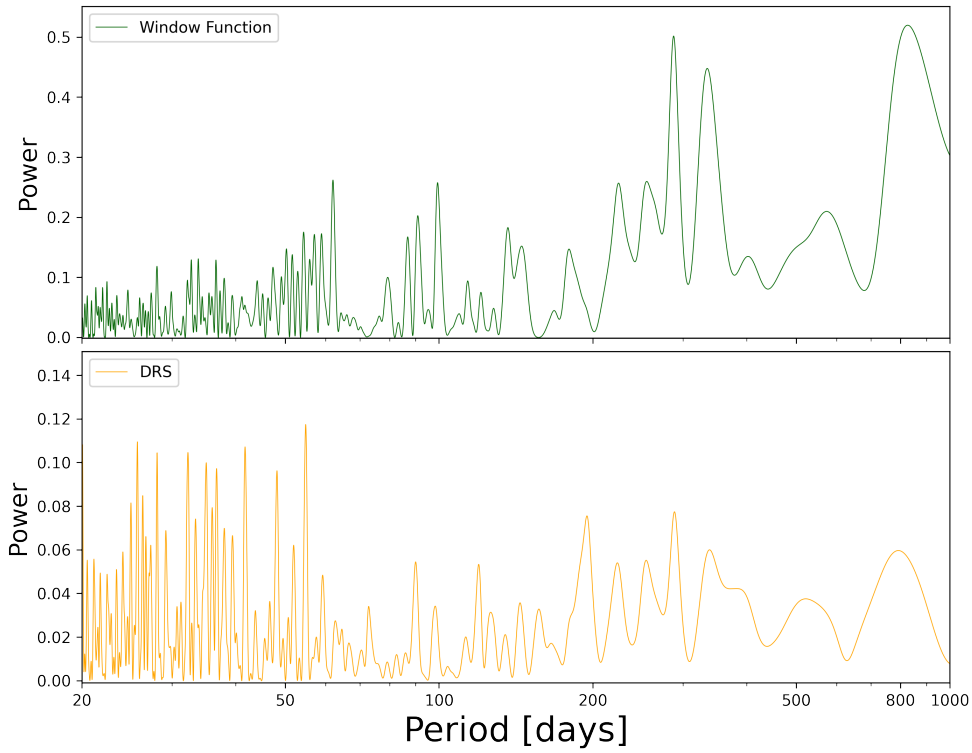

Figure 5.8: Lomb-Scargle periodogram of the window function and uncorrected DRS RVs over the period range where planets were injected.

the corresponding sinusoid and add it to the original DRS RVs. I then run the linear activity-corrected periodogram, fitting for the two known planets, a linear trend with the BIS, and an additional signal. The way I define the successful recovery of a signal, is by requiring one of the top 5 peaks in the computed LACP to be the same as the injected period ±2%. The period range sampled with the LACP is 20 to 1000 days. In total, I inject planets at 60 unique periods and 30 different amplitudes (evenly spaced in log amplitude between 10 and 200 $\mathrm{m\,s^{-1}}$). For each pair of period-amplitude I run the injection-recovery test at 100 different phases, resulting in a total of 1800 period-amplitude pairs and 180 000 test cases. The results of the injection-recovery tests are summarised in Figure 5.9. In this heatmap, the injected amplitudes are shown on the x-axis and the injected periods are presented on the y-axis. The heatmap is colour-coded corresponding to the

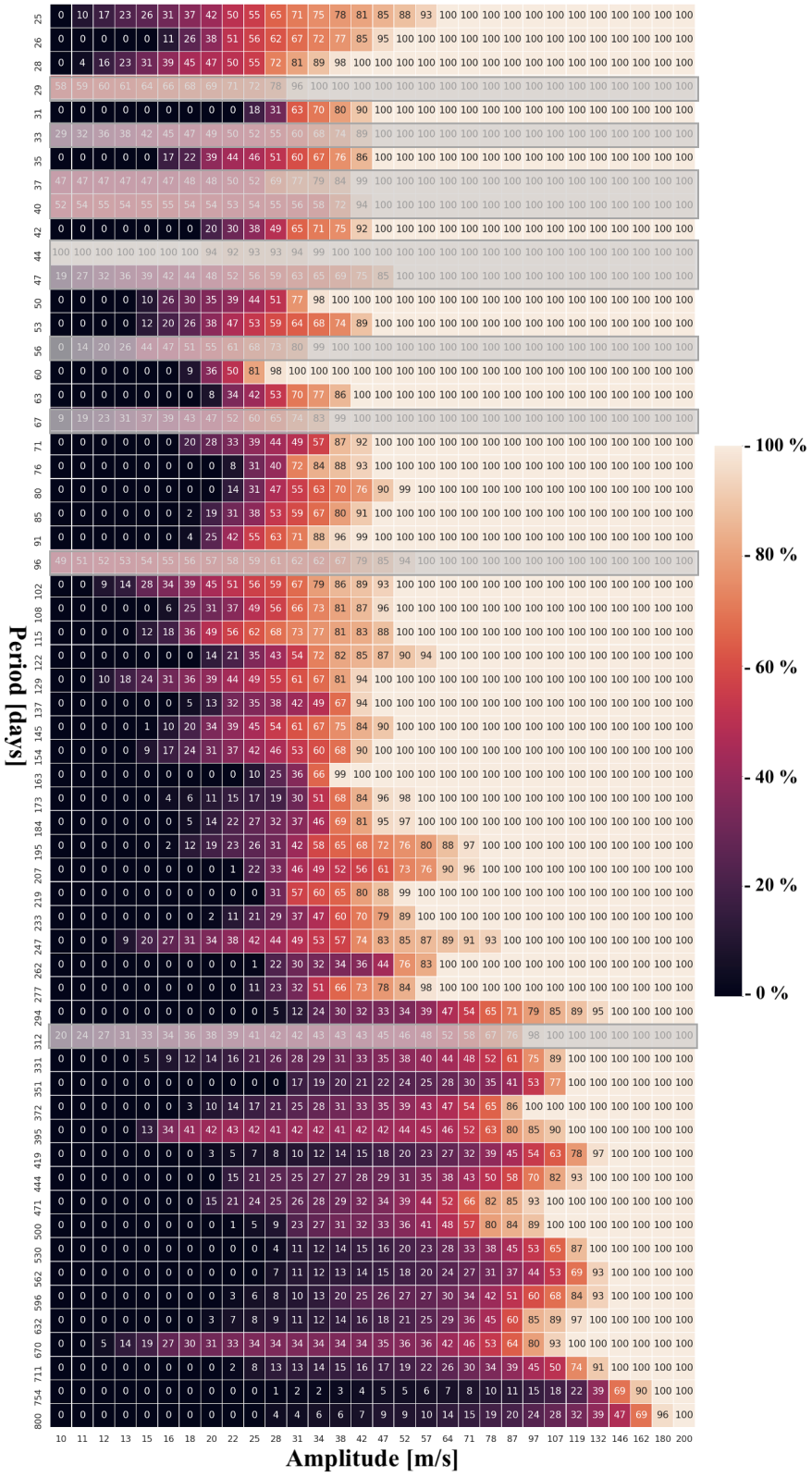

Figure 5.9: Heatmap of detection limits from injection tests for AU Mic. The y-axis shows the injected period, x-axis is he injected amplitude in $\mathrm{m\,s^{-1}}$. Recovery fraction is colour-coded from black to beige, corresponding to 0% and 100% recovery respectively. Injected periods affected by the window-function (see Figure 5.8) are grayed out as these results are distorted.

fraction of recovered signals, where black means 0% and beige means a 100% recovery rate. The individual recovery fraction is also shown in each cell. Periods that were affected by either the window-function or peaks in the original RVs have been grayed out as these give biased results making their interpretability extremely challenging. See top panel of Figure 5.8 for the window-function, and bottom panel for the periodogram of the uncorrected RVs. The shaded out periods correspond to peaks, making their interpretation difficult. From the injection-recovery test, it can be comfortably concluded that there are no signals with amplitudes bigger than 50 $\mathrm{m\,s^{-1}}$in the 20 to 220 day range, and no signals with amplitudes of 100 $\mathrm{m\,s^{-1}}$ or more at any of the sampled periods. Although these limits seem vague when compared to the impressive results presented in Chapter 4, they have key implications for planet formation and migration and are important. For example, being able to eliminate the presence of any big planets on these longer orbits allows to close the gap between RVs and direct imaging surveys. In addition, it implies that the fast moving features that were observed in the debris-disk or the gaps that were seen, must be explained by some other physical process.

5.4 GdG Periodogram

To this date, the gold standard in radial velocity searches for exoplanets is the GP framework (with the caveat that new, very promising methods such as *SCALPELS* (Collier Cameron et al., 2020), or extracting RVs on individual lines (Dumusque, 2018) have not reached full maturity yet). This allows us to model the activity signal in a way that is able to account for the quasi-periodic nature of the activity signal, whilst also trying to constrain the general freedom and flexibility of a simple Gaussian process model. Unfortunately, even in the cases where it is possible to use a Gaussian process to model the activity signal, it can be computationally expensive. Often, using a simple quasi-periodic GP fit to model the RVs results in over-fitting the data, making it crucial to use the ancillary time-series not only to constrain the GP hyper-parameters, but also constrain the underlying functional shape that is drawn from that GP family. In some instances, due to their complexity, a black-box

approach is used, where people blindly apply a Gaussian processes model to the radial velocities, leading to numerous flawed or misguided results. A simpler and more natural approach is to use periodograms, but unfortunately, as I showed before, at the moment there is no periodogram that is able to compete with the performance of a well applied GP model. This is the motivation behind developing the 'GdG' periodogram. Following the same idea as with any Gaussian process model, I will use a constrained GP to model the activity in the RV time-series with the help of the ancillary data. Doing this in a periodogram framework not only makes it more accessible to the general user but also it is much faster than a full GP framework.

5.4.1 Theory

Following the same formalism as in the case of the LACP method, let us assume the following model:

$$\mathrm{RV_{model}}\ (\mathrm{t_i}) = \mathrm{a}\sin\left(\frac{2\pi}{\mathrm{P}}\mathrm{t_i}\right) + \mathrm{b}\cos\left(\frac{2\pi}{\mathrm{P}}\mathrm{t_i}\right) + \mathrm{c}\cdot\mathrm{G}(\mathrm{t_i}) + \mathrm{d}\cdot\dot{\mathrm{G}}(\mathrm{t_i}) + \mathrm{e} \tag{5.4}$$

Where the first two terms are the sinusoidal signal that we are fitting for at period P, $G(t)$ and $\dot{G}(t)$ are a zero-mean quasi-periodic Gaussian process and its derivative (unobserved latent variable - similar to the GP framework - see Chapter 3.3 for details) used to model the activity, and e is an offset. Then, fitting for this model is equivalent to a χ^2 minimisation (or maximising the likelihood), where:

$$\chi^2 = \sum_i \frac{\left[\mathrm{RV_{obs}}\,(\mathrm{t_i}) - \mathrm{RV_{model}}\,(\mathrm{t_i})\right]^2}{\sigma_i^2} \tag{5.5}$$

In order to keep the equations simple and readable, let us use the following notation: S for $\sin x_i$, C for $\cos x_i$, G for $G(t_i)$, dG for $\dot{G}(t_i)$ and $\mathrm{RV_{obs}(t_i)} = \alpha_\mathrm{i}$. Computing the derivatives with respect to the free parameters of this model, results in the following set of equations:

$$\begin{aligned}
\frac{\partial\chi^2}{\partial a} &= \textstyle\sum_i \frac{2}{\sigma_i^2}\left[a\cdot S^2 + b\cdot C\cdot S + c\cdot G\cdot S + d\cdot dG\cdot S + e\cdot S - \alpha_i\cdot S\right]\\
\frac{\partial\chi^2}{\partial b} &= \textstyle\sum_i \frac{2}{\sigma_i^2}\left[a\cdot S\cdot C + b\cdot C^2 + c\cdot G\cdot C + d\cdot dG\cdot C + e\cdot C - \alpha_i\cdot C\right]\\
\frac{\partial\chi^2}{\partial c} &= \textstyle\sum_i \frac{2}{\sigma_i^2}\left[a\cdot S\cdot G + b\cdot C\cdot G + c\cdot G^2 + d\cdot dG\cdot G + e\cdot G - \alpha_i\cdot G\right]\\
\frac{\partial\chi^2}{\partial d} &= \textstyle\sum_i \frac{2}{\sigma_i^2}\left[a\cdot S\cdot dG + b\cdot C\cdot dG + c\cdot G\cdot dG + d\cdot dG^2 + e\cdot dG - \alpha_i\cdot dG\right]\\
\frac{\partial\chi^2}{\partial e} &= \textstyle\sum_i \frac{2}{\sigma_i^2}\left[a\cdot S + b\cdot C + c\cdot G + d\cdot dG + e - \alpha_i\right]
\end{aligned} \tag{5.6}$$

this can be contracted to solving a system of linear equations of the form:

$$Ax + B = 0; \quad Ax = -B$$

Where:

$$A = \sum_i \frac{2}{\sigma_i^2} \begin{pmatrix} S^2 & C \cdot S & G \cdot S & dG \cdot S & S \\ S \cdot C & C^2 & G \cdot C & dG \cdot C & C \\ S \cdot G & C \cdot G & G^2 & dG \cdot G & G \\ S \cdot dG & C \cdot dG & G \cdot dG & dG^2 & dG \\ S & C & G & dG & 1 \end{pmatrix}$$

and:

$$B = \sum_i \frac{2}{\sigma_i^2} \begin{pmatrix} -\alpha_i \cdot S \\ -\alpha_i \cdot C \\ -\alpha_i \cdot G \\ -\alpha_i \cdot dG \\ -\alpha_i \cdot 1 \end{pmatrix}$$

In contrast to the previously presented linear activity-corrected periodogram, before being able to solve the system of linear equations, $G(t)$ and $\dot{G}(t)$ need to be computed from the ancillary time-series. This is done is a similar manner to the GP framework. First, I fit the activity time-series in order to obtain the best fit GP hyper-parameters and the corresponding free variables. Assuming the two (or more) activity time-series are $y_1 = \gamma_1 \cdot G + \gamma_2 \cdot \dot{G}$, and $y_2 = \beta_1 \cdot G + \beta_2 \cdot \dot{G}$, we fit these two simultaneously using a log-Likelihood maximisation algorithm. For the optimisation problem, bounds can be set to act as priors, ensuring that the results are reasonable. This process results in obtaining the best fit values for P_{GP}, λ_p and λ_e, together with free parameters γ_1, γ_2, β_1, and β_2 that quantify the dependence of the ancillary data on the GP function (they can also be thought of as variables quantifying the covariance of the data). Next, we use the best hyper-parameters and the two time-series to predict $G(t)$ and $\dot{G}(t)$. Once these have been computed, the problem reduces to simply solving the system of linear equations. Note, this method assumes that we keep $G(t)$ and $\dot{G}(t)$ fixed between the different computations for the periodogram. Although this is not exactly accurate, in most cases the underlying GP function will not change much and it is not necessary to explore the hyper-parameter space, meaning the drawn GP function should not change drastically between runs. By computing the χ^2 at each trial period P_j, the activity corrected

periodogram is obtained. Again, I adopt the normalisation $p(\omega) = \frac{\chi_0^2 - \chi^2(\omega)}{\chi_0^2}$, where χ_0^2 is the χ^2 of the activity only model ($\mathrm{RV_{model}\,(t_i) = c \cdot G(t_i) + d \cdot \dot{G}(t_i) + e}$) and $\omega = \frac{2\pi}{P_j}$, with P_j being the trial period. This way, the resulting power $p(\omega)$ must obey $0 \leq p(\omega) \leq 1$, following the same formalism as before.

5.4.2 Feasibility

In order to quantify the effectiveness of the Gaussian process GdG periodogram approach, let us first create a toy model that can be used to assess its validity and applicability. To set up our toy model, I take a time-series with 200 data points that are evenly spaced over 100 days. This time-series is used to compute the Gaussian process $G(t)$ and $\dot{G}(t)$. In turn, I use these to create 3 time-series, 2 activity indicators and an RV time-series. All three contain an activity signal, y_1 depends only on $G(t)$ while y_2 and y_3 depend on both $G(t)$ and $\dot{G}(t)$. In addition, y_3 contains a sinusoidal planetary signal. To allow for nice plots, we start by simulating the noise-free dataset at tight time sampling, then randomly select a subset of 50 points and add noise to construct the observed time-series. The Gaussian process G is a zero-mean GP with the quasi-periodic kernel and hyper-parameters $P_{\mathrm{GP}} = 10$ days, $\lambda_p = 0.8$ and $\lambda_e = 56$. The planet signal is defined as $\mathrm{RV_{planet} = A \cdot \sin(\frac{2\pi}{P} t_i + \phi)}$, with amplitude $A = 2\ \mathrm{m\,s^{-1}}$, period $P = 21.6$ days and phase $\phi = 0.5$. The 3 generated time-series are defined as:

$$\mathrm{Activity_1(t) = \gamma_1 \cdot G(t) + \gamma_2 \cdot \dot{G}(t) + \sigma_1(t)}$$

$$\mathrm{Activity_2(t) = \beta_1 \cdot G(t) + \beta_2 \cdot \dot{G}(t) + \sigma_2(t)}$$

$$\mathrm{RV(t) = \alpha_1 \cdot G(t) + \alpha_2 \cdot \dot{G}(t) + RV_{planet} + \sigma_3(t)}$$

where, the parameters controlling the covariance of the time-series (one could say their dependence on G and $\dot{G}$) are $\gamma_1 = -5$, $\gamma_2 = 0$, $\beta_1 = 2$, $\beta_2 = 5$, $\alpha_1 = 4.3$, $\alpha_2 = 2.1$. The added observational noise is given by white Gaussian noise defined by $\sigma_1 = \sigma_2 = \sigma_3 = \mathcal{N}[0, 0.2]$.

Using the GP as defined above together with the covariance terms, I compute the big covariance matrix $\mathbf{K}$ of the simulated data (shown in Figure 5.10). The

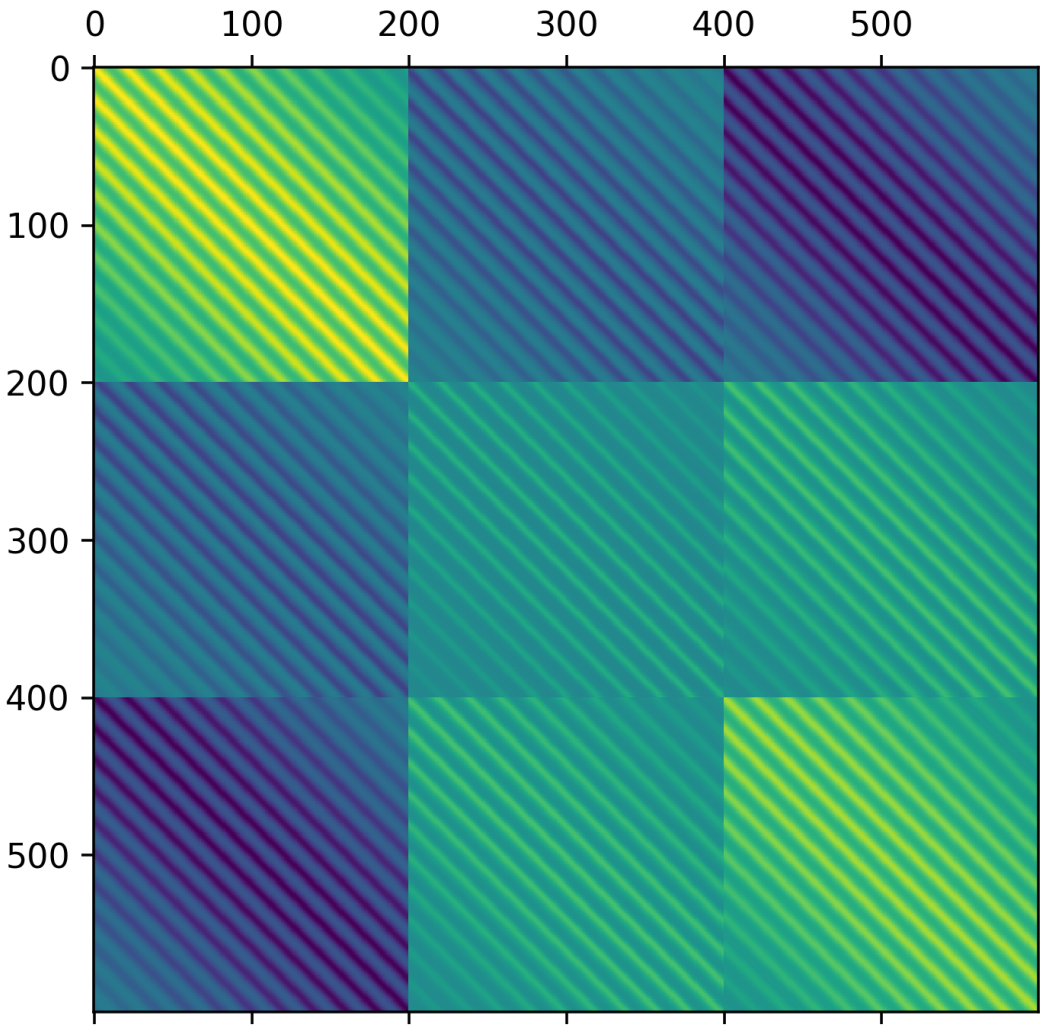

Figure 5.10: Covariance matrix of the simulated data. Each matrix is [200,200] corresponding to the number of simulated data points. The diagonal matrices correspond to activity time-series 1, activity time-series 2 and RV respectively.

formalism adopted here is the same as in the case of the GP framework, making it identical to the way $\mathbf{K}_{\rm act}$ is defined (see equation 3.46). It is composed of the smaller $\mathbf{k}_{\rm act}^{ij}$ covariance matrices corresponding to each time-series and their relationship. These covariance matrices encompass the quasi-periodic nature of the activity signal. In the big matrix, each time-series is represented by a smaller [200,200] matrix (hence the [600,600] matrix). The diagonal matrices represent the covariance of each individual time-series, whilst the off-diagonal matrices highlight their correlations. Next, I generate the 3 time-series using the covariance matrix

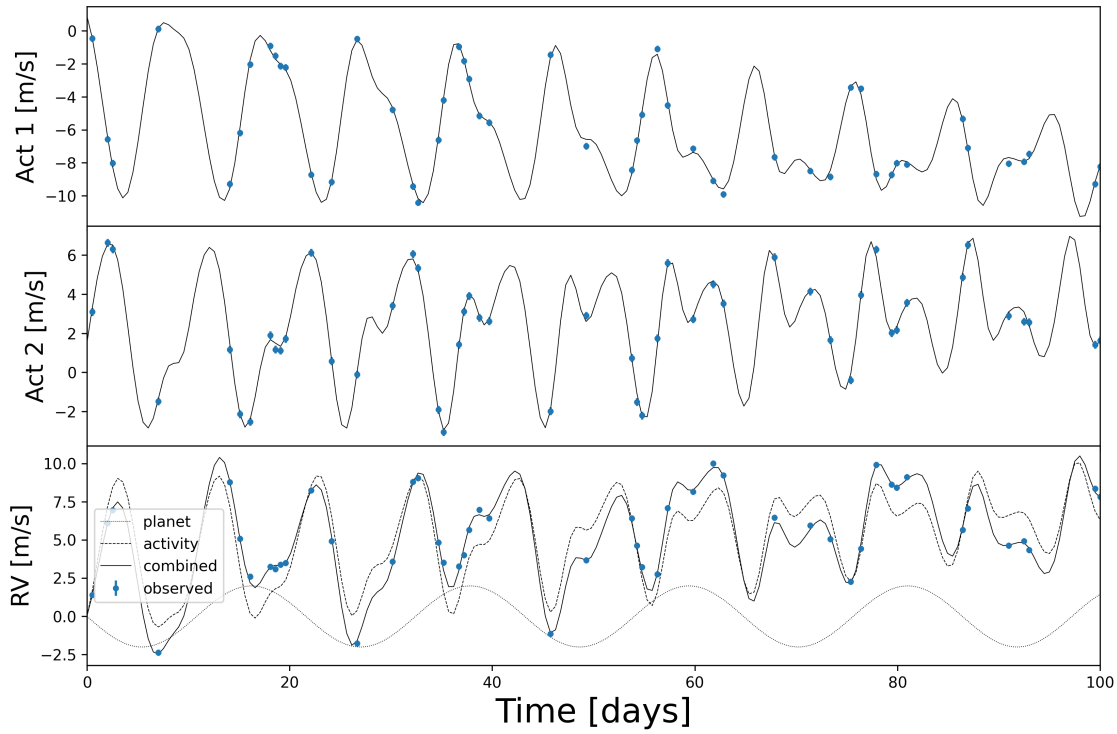

Figure 5.11: Simulated time-series. The top two panels show the two synthetic activity time-series. RVs are presented in the bottom panel with a solid line, the injected planetary signal showed with dotted line, activity signal with a dashed line. Blue circles show the sampled observations with errorbars.

K. From the simulated time-series I randomly sample 50 observations and add the white Gaussian noise to obtain the observed time-series. The generated data and the drawn samples are is shown in Figure 5.11 together with the added planetary signal.

Now that the synthetic data is created, I proceed to apply the GdG methodology. In this toy example, I take some extra steps (that in principle are not required) in order to ensure that the fit obtained is sensitive and perform a full assessment of the underlying principle. First, I fit a quasi-periodic GP to the two activity time-series simultaneously in order to recover the GP hyper-parameters and the 4 free parameters (γ_1, γ_2, β_1, β_2). I do this by minimising the negative log-Likelihood of the GP fit. To ensure that the fit is robust and to incorporate any prior knowledge, I place bounds on the limits for each parameter (note that only γ_2 has a tight bound, this is because, this time-series is meant to mimic the behavior of DLW for example, and this is expected to depend only on G). The resulting fit is shown in Figure 5.12 and the exact numerical values are summarised in Table 5.2. It is

Table 5.2: Table presenting the best fit GP hyper-parameters from fitting the two activity time-series

Parameter	Set bounds (lower,upper)	Fitted value	True
P_{GP} [days]	(2,20)	9.96	10
λ_p	(0.4,1)	0.97	0.8
λ_e [days]	(2,120)	60.72	56
$\gamma_1(\mathrm{m\,s^{-1}})$	(-20,20)	- 6.93	-5
$\gamma_2(\mathrm{m\,s^{-1}})$	(-0.25,0.25)	-0.02	0
$\beta_1(\mathrm{m\,s^{-1}})$	(-5,5)	2.71	2
$\beta_2(\mathrm{m\,s^{-1}})$	(-15,15)	7.04	5

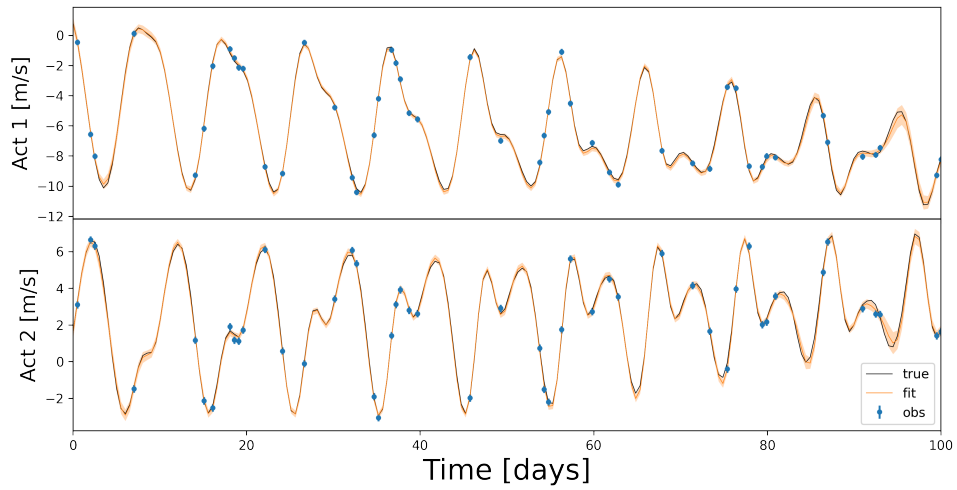

Figure 5.12: Gaussian process fit to the data with the best fit hyper-parameters. The true function is shown with a black line, GP mean is shown with orange line and confidence intervals shaded in orange. Blue circles show the observations.

easy to see from the figure that we are able to reproduce the injected functions extremely well. Comparing the returned values, it can be noted that we are able to recover the GP hyper-parameters really well and obtain comparative values for the 4 free parameters.

In principle, in order to apply the GdG method, we only need the GP hyper-parameters. Knowing the hyper-parameters, the Gaussian process fit can be conditioned on the ancillary time-series, providing a more robust model for the activity signal than modelling it directly in the RVs. Having computed the GP

Table 5.3: Model comparison of the GdG periodogram best fit values

Parameter	Constant model	Activity-only	GdG model	True
χ^2	10200.88	2497.64	383.80	...
Offset ($\mathrm{m\,s^{-1}}$)	0	0	0	0
G coeff. ($\mathrm{m\,s^{-1}}$)	...	5.32	5.75	4.3
dG coeff. ($\mathrm{m\,s^{-1}}$)	...	1.93	2.78	2.1
Period [days]	...	...	22.03	21.6
Amplitude ($\mathrm{m\,s^{-1}}$)	...	...	2.12	2
Phase	...	...	-0.42	-0.5
BIC	10204.79	2509.38	407.27	...

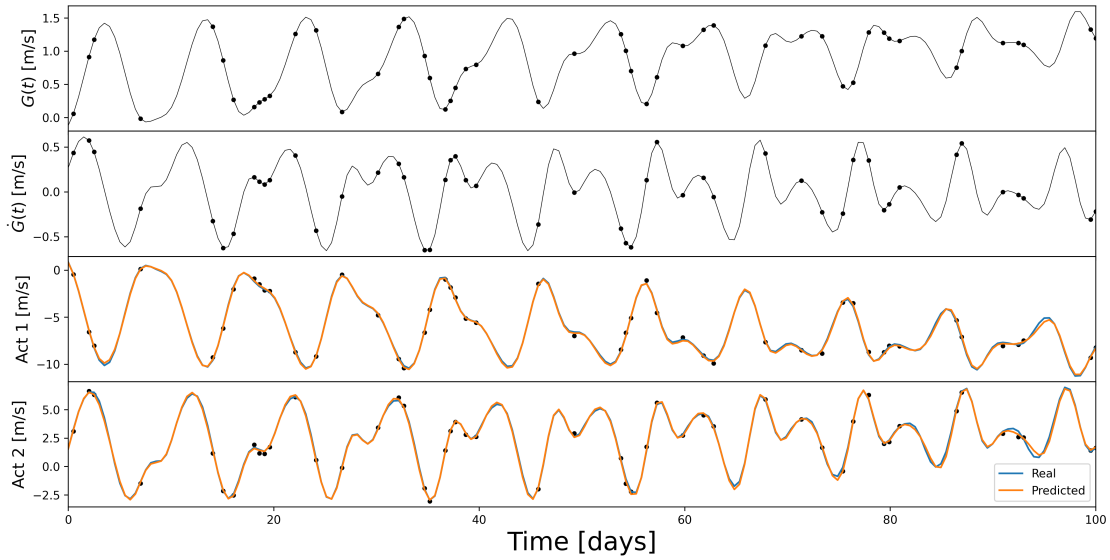

Figure 5.13: Computed Gaussian Process functions for $G(t)$ and $\dot{G}(t)$ and the resulting prediction for the two synthetic activity time-series.

hyper-parameters, I use these together with the two activity time-series to predict G and $\dot{G}$. Figure 5.13 shows the predicted GP functions (G and $\dot{G}$) obtained from the data. In addition, it also shows the predicted ancillary time-series computed from the predicted G and $\dot{G}$ using the 4 free parameters that we obtained during the previous step. In the case of the two activity datasets, the predictions overlap almost perfectly with the simulated functions. This is anticipated, as the same behaviour is observed in Figure 5.12. It is worth mentioning that the first activity time-series behaves almost exclusively as G, as expected. Meanwhile, the second activity time-series is predominantly controlled by the time derivative component.

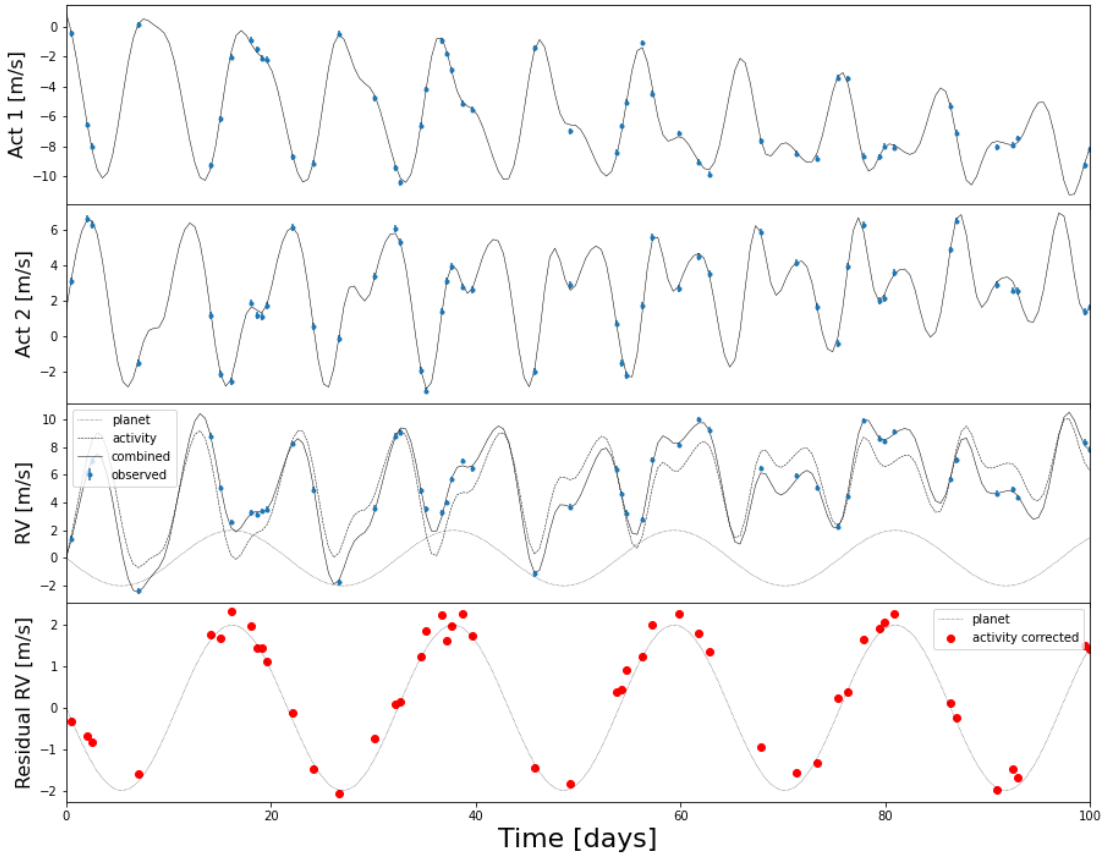

Figure 5.14: The full simulated dataset with the bottom panel showing the residuals after subtracting the best fit GP model from the RVs.

Knowing the shape of G and $\dot{G}$, it becomes a matter of simply plugging in the values into the GdG framework as presented in the theory section. The results from running the periodogram on the synthetic data are summarised in Table 5.3. The recovered planetary parameters match up very well with the injected signal. It is also obvious, that the full GdG model is by far the best fit according to the BIC. This can also be seen in Figure 5.14, where I show the full dataset as well as the residuals after subtracting the best fit activity model predicted by the periodogram using the GP functions. For completeness, I compute the `astropy` GLS periodogram of the synthetic RVs before and after correcting for activity using the best fit activity model from the GdG periodogram. The resulting periodograms are shown in Figure 5.15. The periodogram of the original RV time-series is shown in blue, whilst the corrected RVs are shown in orange, with vertical lines showing the stellar rotation period (dotted) and injected planet period (dashed). It can be

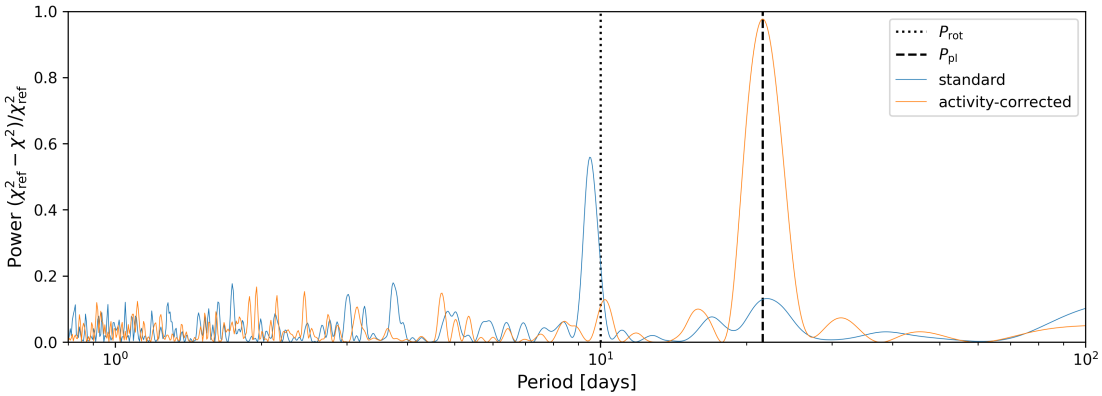

Figure 5.15: Lomb-Scargle periodograms computed with the `astropy` package for the simulated RVs. The original RV time-series is shown in blue, whilst the corrected RVs (best fit GP activity model subtracted) is shown in orange, showing a clear peak at the period of the injected planet.

seen that the GLS is unable to detect the injected planet in the original time-series, but shows an obvious peak in the activity corrected RVs.

These results clearly demonstrate the power of the GdG periodogram and its ability to account for complex correlated nuisance signals. Even if the toy model example is not 100% realistic and representative of real world datasets, I am confident that the methodology is robust and presents a massive improvement over currently available techniques.

5.4.3 Benchmarking

In order to truly assess the ability of the GdG periodogram to remove the stellar variability from the RV time-series it is necessary to benchmark its performance compared to well established methods. For this purpose, one of the best datasets available is the data for AU Mic presented in Chapter 4. This also allows us to benchmark the results to the more complex GP framework, highlighting the advantages and disadvantages of this technique. Obviously in this dataset we know that there are two transiting planets that need to be accounted for. Similar to the extension presented for the LACP (see Chapter 5.3 for details), it is possible to add any known planets to the GdG framework.

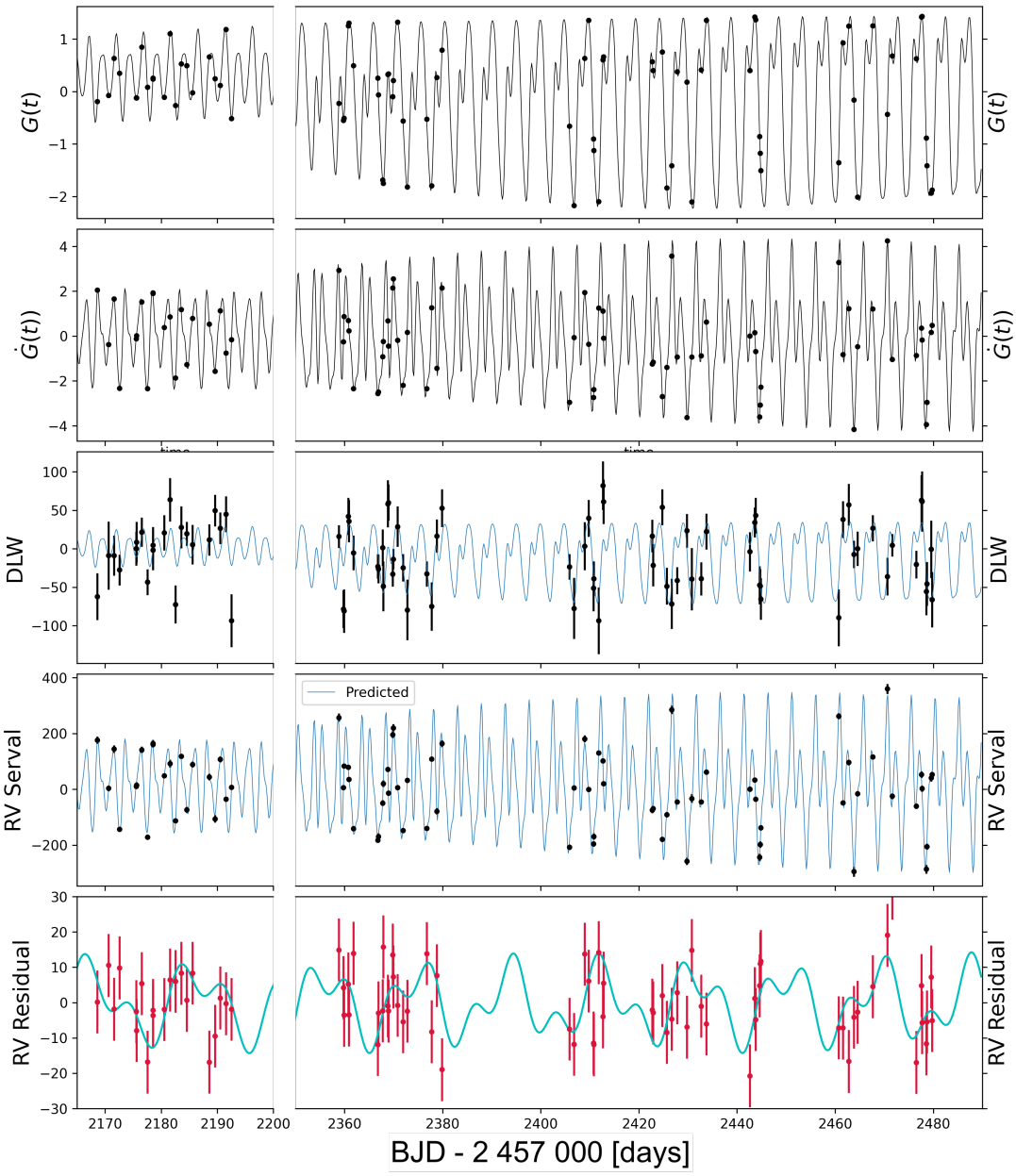

Figure 5.16: The computed Gaussian process functions for $G(t)$ and $\dot{G}(t)$ and the resulting predictions for the DLW activity time-series and RVs are shown in the top panels. The bottom panel shows in red the RV residuals after subtracting the best fit GP model predictions. The predicted signal induced by the two transiting planets is shown in cyan.

Table 5.4: Table presenting the best fit GP hyper-parameters from fitting of DLW and RV `SERVAL` time-series.

Parameter	Set bounds (lower,upper)	Fitted value	GP framework
$P_{\rm GP}$ [days]	(4.8,4.9)	4.857	4.863
λ_p	(0.4,0.6)	0.429	0.449
λ_e [days]	(80,120)	107.84	108
β_1 ($\mathrm{m\,s^{-1}}$)	(-None,None)	28.99	38.7
β_2 ($\mathrm{m\,s^{-1}}$)	(-0.05,0.05)	-0.05	...
G coeff. ($\mathrm{m\,s^{-1}}$)	(0,None)	0	7.5
dG coeff. ($\mathrm{m\,s^{-1}}$)	(-None,None)	75.2	91
Offset DLW ($\mathrm{m^2\,s^{-2}}$)	...	-6.99	-3
Offset `SERVAL` ($\mathrm{m\,s^{-1}}$)	...	21.84	-98.2

Before applying the GdG framework, I have tested various combinations of activity time-series and RVs to see which one performs the best. As previously reported, the simplest and best performing case is using the DLW and `SERVAL` RVs simultaneously in order to condition the GP fit for the activity. As a consequence, I will adopt the same fiducial model as presented in Chapter 4. To make the two test cases as similar as possible it is necessary to slightly adapt the dataset. Because the GdG framework doesn't fit for extra observational noise (jitter), I artificially enlarge the errors 5 fold for the DLW observations and 3 fold for the RVs. This is equivalent to the jitter term that we obtained with the Gaussian process framework, ensuring that the two models are trying to fit for data with the same observational error.

Prior to being able to run the GdG periodogram, it is necessary to compute G and $\dot{G}$. This is performed in an identical manner to the toy model case. The only difference is that rather than fitting just ancillary time-series, in this case I fit the RVs and DLW simultaneously. This is necessary because the activity indicators by themselves are unable to provide a good GP fit. In part, this is due to the massive activity induces variations in the RVs, making it necessary to include them in the modelling. The GP fit parameters are summarised in Table 5.4 together with the values obtained in Chapter 4. The GP hyper-parameters are almost identical, and the free parameters are quite similar as well. The computed values for the GP

Table 5.5: Model comparison of the GdG periodogram best fit values .

Parameter	Constant model	Act. only	Act. + 2planets	GdG model	GP Framework
χ^2	4221.17	222.38389862091074	20.15	16.411445170248 1	...
Offset ($\mathrm{m\,s^{-1}}$)	-3.24	-3.37	21.04	21.33	-98.2
G coeff. ($\mathrm{m\,s^{-1}}$)	...	1.99	0.22	0.77	7.5
dG coeff. ($\mathrm{m\,s^{-1}}$)	...	72.26	75.16	75.12	91
K_b ($\mathrm{m\,s^{-1}}$)	...	...	3.33	3.6	5.8
K_c ($\mathrm{m\,s^{-1}}$)	...	...	4.72	5.1	8.5
Period [days]	...	...	2.19	...	
Amplitude ($\mathrm{m\,s^{-1}}$)	...	...	4.68	...	
Phase	...	...	0.04	...	
BIC	4225.58	235.60	42.18	51.66	...

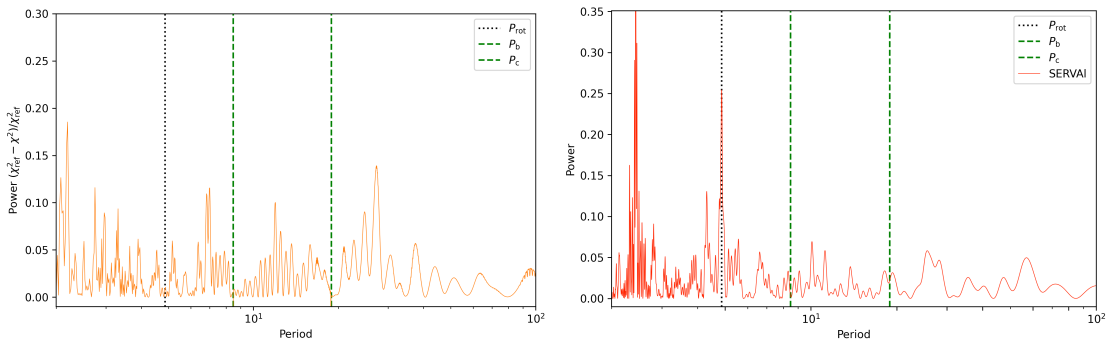

Figure 5.17: Periodograms for RV time-series. Left panel shows the GdG periodogram of the dataset (fitting for the GP activity model, 2 known transiting planets and an additional signal). The right panel shows the `astropy` GLS periodogram of the original RVs extracted with `SERVAL`. It is hard to directly compare the two because of normalisation. It wouldn't be very robust to compute the `astropy` GLS periodogram of the RVs after subtracting the computed GdG GP activity model and fitted amplitudes for the two planets as this iterative fitting could alter the results. It is clear that the GdG periodogram model (activity + 2 planets) removes almost all the signals.

functions are shown in Figure 5.16, together with the DLW and RV time-series. The bottom panel shows in red the residuals after subtracting the predicted activity component of the RVs. In cyan I show the expected planetary signal using the values computed with the GP framework in Chapter 4 ($K_b = 5.8 m\,s^{-1}$and $K_c = 8.5$ $m\,s^{-1}$). Comparing Figure 5.16 and Figure 4.6, shows that the obtained residuals are identical to the eye for the two techniques. This is highly encouraging for the purpose of benchmarking the technique.

The results obtained from plugging in the values of G and $\dot{G}$ into the GdG framework are shown in Table 5.5. It is worth noting, that the best fit model according to the BIC is the GP activity model with the 2 known planets. Adding an additional sinusoidal signal doesn't further improve the fit by that much. This leads me to believe that the probability of a 3rd signal in the data is rather small but cannot be fully excluded. The fitted parameters are in agreement with the results obtained from the more complex GP framework (see Chapter 4. Being able to detect the 2 planetary signals with the GdG approach is a great sign to its applicability. Considering that the GdG framework is much simpler (and exponentially faster) when compared to the full GP framework, it performs extremely well.

For completeness, I show the comparison between the periodogram obtained with the GdG periodogram (left panel) and a GLS periodogram (right panel) computed on the uncorrected `SERVAL` RVs (see Figure 5.17). It is easy to see that the GdG periodogram completely removes the activity signal at the stellar rotation period, as well as the power at the periods corresponding to the two transiting planets. Noting, that even after removing the activity signal there are peaks at aliases of the stellar rotation period, meaning that although the activity model is able to remove a lot of the variability ($\sim 90\%$) it is not perfect. In comparison, the GLS periodogram is completely dominated by the stellar rotation period and its aliases and harmonics. It would be extremely difficult to recover the two transiting planets using this approach.

5.5 Discussion and conclusion

I presented two extensions to the generalised Lomb-Scargle periodogram, namely the linear activity-corrected periodogram and the GdG periodogram. Both of these are able to account for stellar variability, either by using a linear detrending or a Gaussian process activity model respectively. These methods overcome some of the shortcomings of the original approaches by not only performing the activity correction, but by doing so simultaneously with the signal detection. I also showed how both frameworks can be extended to account for any known signals in the dataset, as well as their ability to model multiple sinusoidal signals concomitantly. Furthermore, although not explicitly shown in this chapter, it is possible to model data from multiple instruments, further improving on the classical capacities of periodograms.

The toy models clearly demonstrate that these added features are a valuable addition and greatly improve the performance of detection capabilities. In both cases, the GLS fails to show a peak at the period of the injected planets, whilst the LACP and GdG methods are easily able to recover them. Noting that most astronomers (in my experience) are more comfortable with using periodograms over other methods, I hope that these improved tools will prove to be of great value to the community. I also hope that due to their ease of use they are able to eliminate

some of the misuses of more complex models that can lead to spurious results. Even though the two periodograms bring numerous advantages, they still have their limitations. These methods have their own niches. The GdG periodogram is a very strong tool that is able to model extremely complex activity signals, but has the shortcoming that it requires good time sampling in order to be able to constrain the GP model. In contrast, the LACP is a simpler model that can be used in almost all instances, but it doesn't have the complexity and 'resolving' power of the GP model. Thanks to being computationally inexpensive compared to other models, they provide a great set of tools not only for detection, but also injection-recovery tests, allowing the user to have more robust results.

When comparing the GdG method to the GP framework, its performance is extremely good. The parameters recovered match up very well, and the recovered planetary signals are consistent with each other. I do believe however that the best way is to use a full model such as the GP framework. This is because the periodogram is only able to search for purely sinusoidal signals and this is not always the case for exoplanets. Sadly, due to its computational cost, the GP framework can be difficult to use on a large quantities of datasets. In comparison, the GdG periodogram is a 'cheap' tool that can easily be used on vast amount of data whilst not sacrificing much of the performance.

In addition to providing the theoretical basis for these methods and assessing their feasibility and performance, I presented the detection limits for long period planets ($>$ 20days) around AU Mic . The results from the injection-recovery test show that it can be concluded with confidence that the probability of having any additional planets with amplitudes greater than $50\,\mathrm{m\,s^{-1}}$ is very small. These detection limits have important implications, such as helping us bridge the gap between RV and direct imaging surveys.

A person who never made a mistake never tried anything new.

— Albert Einstein

6 Brave

Contents

This chapter focuses on a method I developed that allows to extract radial velocities directly from the stellar spectrum, without the need for a stellar template. First, I present the context and motivation behind developing this technique. The theoretical description is presented in Section 6.2. A *Python* package that I have developed called "BRaVe" is presented Section 6.3. The package encodes the presented method together with a few simple tools (my own implementation of a CCF RV extraction, data manipulation, barycentric correction, etc.) which allow for easier diagnostics and analysis. I also present the benchmarking of this method on simulated datasets in Section 6.3.4. Applications of this GP RV extraction are

presented in Section 6.4, followed by discussion and conclusion in Section 6.5.

6.1 Context and motivation

Over the past decades RV spectrographs have improved significantly, going from formal precisions of 100s $\mathrm{m\,s^{-1}}$ in the 1970s to ~ 10 $\mathrm{cm\,s^{-1}}$ for current instruments (e.g., *ESPRESSO* - Pepe et al. 2021, and *EXPRES* - Jurgenson et al. 2016). Even though the instrument precision improved greatly, the way RVs are extracted from the observed spectrum have remained borderline unchanged - i.e., masked, weighted cross-correlation of the stellar spectrum with a template spectrum (usually a binary mask that has peaks corresponding to absorption lines and that are inversely proportional to the depth of the line).

This approach to extracting RVs leaves a few areas to improve on. First, it makes the assumption that the template spectrum is a good match to the stellar spectrum, which might not always be the case. Second, it doesn't leverage the additional constrained from computing RVs for multiple observations. For example, if we obtain a relative shift RV_1 for 'spectrum 1' compared to the template and we obtain RV_2 for 'spectrum 2' relative to the same template, there is an additional constraint that requires that the relative RV shift of 'spectrum 1' to 'spectrum 2' must be $\mathrm{RV}_1 - \mathrm{RV}_2$. Given that the two observations will potentially have different wavelengths, it is not always expected that the error in $\mathrm{RV}_1 - \mathrm{RV}_2$ (obtained from the CCF relative to the template) to correspond directly to the error in the RV obtained from cross-correlating the two spectra.

This motivated the development of a technique to extract RVs directly from the stellar spectrum using Gaussian processes. As such, it is not necessary to use a template as the star's exact spectrum is used as reference. An added benefit of using GPs to model the stellar spectrum is that it allows to evaluate the the flux and associated uncertainty at any wavelength, as opposed to discrete wavelengths determined by the detector pixels. This in turn allows us to extract relative radial velocities without having to resample the spectra or worry about propagating uncertainties.

6.2 Gaussian processes on spectra

The underlying principle of using GPs to extract radial velocities is sketched below, with the detailed mathematical model presented afterwards:

(i) Assume each observed spectrum can be modelled with a Gaussian process, more precisely each order of each spectrum;

(ii) Align all the observations relative to the first observation and fit a GP to the whole dataset to evaluate the likelihood. This allows to infer the relative RV shifts and associated errors using an MCMC method where we sample for different relative shifts;

(iii) For each observation combine the RVs from all the orders to obtain the relative RV shift for that observation;

A fundamental assumption of this approach is that the intrinsic stellar spectrum should not change drastically between different observations.

This approache differs from other template-free methods such as HARPS-TERRA (Anglada-Escudé & Butler, 2012) and SERVAL (Zechmeister et al., 2018), both of which create a high SNR template from the observations using an iterative process, and use this template to compute the radial velocities. The method is similar to the pair-wise GP RVs by Rajpaul et al. (2020), which extracts RVs by measuring pair-wise radial velocities for all possible combinations of the observations before collecting them into the final RVs. My approach was developed at the same time as the approach of Rajpaul et al. (2020).

Let us assume that we have a set of N spectroscopic observations defined as $\mathcal{D} = \{\mathcal{S}_1, \ldots, \mathcal{S}_N\}$, where each spectrum $\mathcal{S}_i$ is defined by $\mathcal{S}_i = \{(\lambda_{ij}, \mathrm{flx}_{ij}, \sigma_{ij})\}_{j=1}^{M}$. In this case, M is the number of pixels in a single spectrum, λ_{ij} are the wavelengths, flx_{ij} are the fluxes, and σ_{ij} are the associated errors in the fluxes. Computationally simulated experiments show that simply cross-correlating observed spectra with each other leads to poor results in the RVs that can be extracted (Rajpaul, 2017). This is likely due to the fact that the cross-correlation function is very sensitive

to noise. Although there is a large number of absorption lines, the overall result from the CCF is going to be heavily affected by the noise of parts of the spectrum that offer limited information about the RVs. As such the RV estimates from comparing pairs of spectra is a poor representation.

In order to correct for this, let us build a model f_i that summarises the available information in the spectrum. As such, model f_i summarises the pixel-level noise and covariance between nearby data points to produce a lower noise spectrum for the cross-correlation. This is possible because in the case of spectral lines, nearby pixels are not independent from each other (and even in the case of continuum it can help filter some of the noise). For this, we will use a GP prior $f_i(\lambda) \sim \mathcal{GP}(\mu_i, \gamma_i)$, where the mean function $\mu_i(\lambda)$ will describe the continuum (usually set to 1, as the stellar spectra are normalised) and the covariance function will be used to fit for the spectral absorption elements.

In the GP RV extraction framework I developed I chose to adopt the Matérn 3/2 class kernel[1](with $\nu = \frac{3}{2}$), which is described by[2]:

$$\gamma_{\mathrm{M32}}(\lambda_i, \lambda_j) = h^2 \left(1 + \frac{\tau_{3/2}}{\rho}\right) \exp\left(\frac{-\tau_{3/2}}{\rho}\right) \tag{6.1}$$

with $\tau_{3/2} \equiv \sqrt{3}\,|\lambda_i - \lambda_j|$, where $|\lambda_i - \lambda_j|$ is just the separation of the two wavelength positions, h is the output scale (related to the depth of spectral lines) hyper-parameter and ρ is the length scale (connected to the shape and typical spacing of lines) hyper-parameter.

Experiments carried out by Rajpaul (2017) found that the two best kernels for fitting spectra are the Matérn 3/2 and Matérn 5/2 kernel functions. These results show that the Matérn 3/2 class kernel can be slightly too flexible resulting in fitting the noise. In order to counteract this, I impose bounds on the h and ρ hyper-parameters, ensuring that this is never the case. These bounds were determined from extensive testing. For these tests, I take a theoretical stellar spectrum (R =

[1]This is because in order to model all the spectra at once, I need to take advantage of the approximation implemented in `celerite` , allowing this kernel to scale linearly, $\sim \mathcal{O}(M)$, as opposed to $\sim \mathcal{O}\left(M^3\right)$

[2]Note that I have changed the notation of the length scale hyper-parameter from λ to ρ in order to not confuse it with wavelength

800 000) between 450 and 800 nm, resample it to a lower pixel resolution (R = 50 000 - 300 000), split it into 80 orders (each spanning $\sim$ 5 nm), and generate a few simulated realisations (adding random noise to the flux values at each wavelength corresponding to a given SNR = [10, 30, 100, 500]) of observations of this theoretical spectrum. As such, in total I simulate 36 spectra ($3 \cdot 3 \cdot 4 = 36$ - 3 resolutions [50k, 100k, 300k], 3 draws for the noise, 4 SNR values). I then use the GP with Matérn 3/2 kernel to fit these simulated spectra. For each resolution and each realisation I try various combinations of the GP hyper-parameters to find an ideal fit. Of course, there is a degeneracy between the two hyper-parameters which is considered for the final bounds. I compare these fits to the original 'perfect' spectrum to see how the GP fits the stellar spectrum. An example of this is shown in Figure 6.1, where the stellar synthetic spectrum is (R = 100 000, SNR = 30). Note that the x-axis is in ln wavelength and has been renormalised to be between 0 and 1. I show a small sample from $\sim$ 525 nm. It can be seen that the GP fits shown in red, green and orange are completely unable to fit the spectrum. The GP shown in brown does a better job, but it is unable to account for absorption lines that are close to each other. The GP shown in cyan is overfitting the data. The ideal fit is shown in pink with the uncertainty shown by the shaded pink region.

The hyper-parameters can be determined through finding the maximum likelihood, where the likelihood is given by:

$$\ln \mathcal{L}(\boldsymbol{\theta}, \boldsymbol{\Phi}) = -\frac{1}{2}\left(N_{\text{obs}} \ln 2\pi + \ln |\mathbf{K}| + \mathbf{r}^{\top}\mathbf{K}^{-1}\mathbf{r}\right) \tag{6.2}$$

Once the hyper-parameters are computed, we can compute the GP predictive distribution $g_i := f_i(\lambda) \mid \mathcal{S}_i \sim \mathcal{GP}(\mu_i, \gamma_i)$, where μ_i^* and γ_i^* can be computed using (see Chapter 3.2 for details):

$$\mu_i\star(x) = \mu(x) + \mathbf{K}(x, \mathbf{x})\mathbf{K}^{-1}(\mathbf{y} - \boldsymbol{\mu}(\mathbf{x})) \tag{6.3}$$

and

$$\gamma_i^{\star}(x_j, x_l) = \gamma(x_j, x_l) - \mathbf{K}(x_j, \mathbf{x})\,\mathbf{K}^{-1}\mathbf{K}(\mathbf{x}, x_l) \tag{6.4}$$

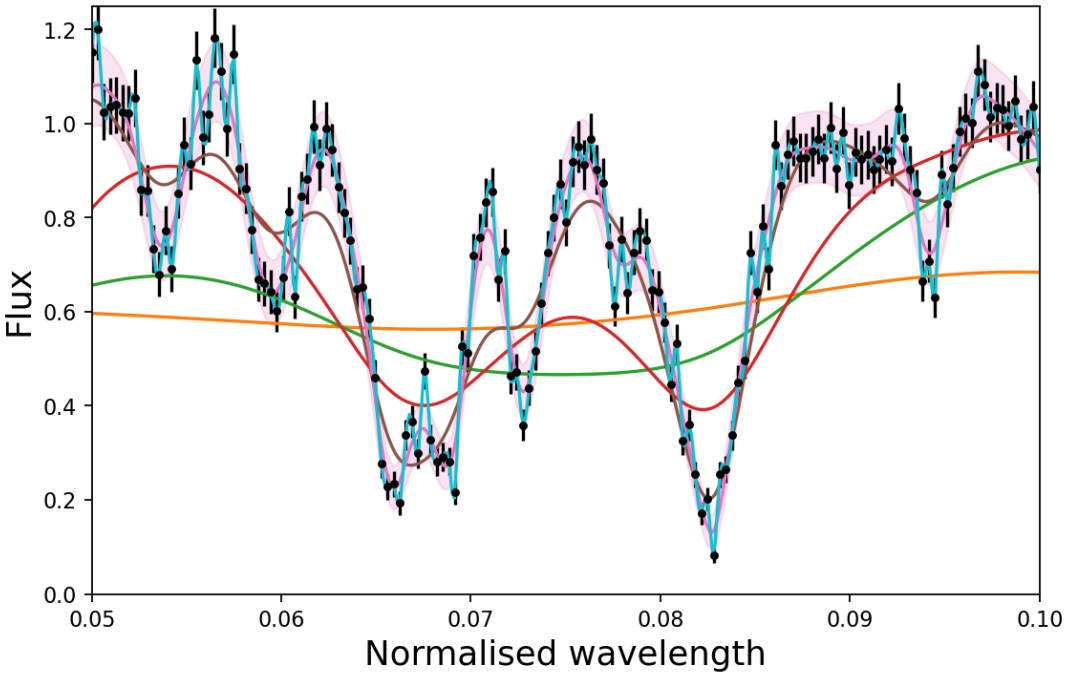

Figure 6.1: Sample GP Matérn 3/2 fit to simulated spectrum (R = 100 000, SNR = 30). GP fits are that are poor fits are shown in red, green and orange. Brown is a better fit but fails to fit closely spaced lines, whilst cyan is overfitting the data. The ideal fit is shown in pink with the uncertainties of the fit shown by the shaded area.

where x_j is the wavelength value with corresponding flux y_j, $\mathbf{x}$ and $\mathbf{y}$ are the vectors containing all the observations.

Having defined the Gaussian process g_i that models the observed spectrum $\mathcal{S}_i$, it is straightforward to evaluate (interpolate) it at any wavelength needed for cross-correlation, and the evaluated flux values will have principled errors - something that is hard to do with other interpolating tools. An important note to make is that it is more convenient to model each order from a spectrum separately. This is because, first, evaluating a GP is typically computationally expensive (in general because of the matrix inversion it scales as $\sim \mathcal{O}\left(M^3\right)$), and as such it is preferable to keep the number of data points small. Second, points that are very far apart are expected to have very little or no correlation (there is no reason to believe that spectral lines that are far apart are correlated). Lastly, because the spectral properties of lines change at different wavelengths (across échelle orders), it is sensible to allow for a different set of hyper-parameters. As such, let us adopt the following notation

for the GP posterior, $g_i^{(l)}(\lambda)$, for spectrum i and order l.

It is important to remember that in the case of spectroscopic observations, the measured fluxes are defined at the wavelength λ as measured on Earth. The true wavelengths at which they were emitted have shifted due to the radial velocity of the star and also because of Earth's motion. The shifts are described by the simplified[3] Doppler shift:

$$\lambda_{\text{obs}} = \lambda_{\text{em}}(1 + \frac{v}{c}) \tag{6.5}$$

where v is the radial velocity of the star.

Then, after correcting for the barycentric motion of Earth, we can say that the wavelength observations are dependent on this velocity v and I will note it as $\lambda(v)$ for the wavelengths. Assume that we have two separate observations, one will be at $\lambda(v_1)$ and the other will be at $\lambda(v_2)$, where $v_1 - v_2 = \delta = \text{RV}_{\text{star}}$. Then in order to obtain the relative RV between these two observed spectra, we need to find the best value of δ that maximises the overlap of the wavelengths. Let us use the notation $\boldsymbol{\alpha}_\delta$ for the combined dataset (in this case [$\lambda(v_1)$ and $\lambda(v_2)$]). Because we can consider δ to be a free parameter, we can incorporate it into our model f_i^l, and as such, we can determine it simultaneously with the GP hyper-parameters, by finding the parameter values that maximise the likelihood of the GP. Note that in the case where there are only 2 observations $\boldsymbol{\delta}$ is a scalar, but in the case of N observations it will be a vector that provides the $N-1$ relative shifts (shifting everything to the first observation, but in principle the reference could be any single observation). Because we perform the fitting for each order separately, the likelihood of a GP fitted to the combined observations, can be written as:

$$\begin{aligned} \ln \mathcal{L}(\boldsymbol{\theta}, \boldsymbol{\Phi}, \boldsymbol{\delta}) &= p(\alpha_\delta | \boldsymbol{\delta}, \boldsymbol{\theta}, \boldsymbol{\Phi}) \\ &= -\frac{1}{2}\left(M_\star \ln 2\pi + \ln |\mathbf{K}| + \mathbf{r}^\top \mathbf{K}^{-1} \mathbf{r}\right) \end{aligned} \tag{6.6}$$

where $M_\star$ is the number of combined data points (assuming that each spectrum has M data points in each order, then $M_\star = N \cdot M$, where N is the number observed spectra that we combined), $\mathbf{r} = \mathbf{y} - \boldsymbol{\mu}$ is the residual vector of the data $\mathbf{y}$ (fluxes)

[3]Not taking relativistic effects into consideration

and the mean function $\boldsymbol{\mu}$ (usually set to 1 as the fluxes are normalised). $|\mathbf{K}|$ is the determinant of the covariance matrix, and covariance matrix $\mathbf{K}$ is given by kernel function $\gamma(\lambda_i, \lambda_j)$ (note that i, j are between 1 and $M_\star$). As such our initial relative RV (or RVs if multiple observations were combined):

$$\mathbf{RV}^{(l)} = \arg\max_{|\boldsymbol{\delta}|<c} \mathcal{L}(\boldsymbol{\delta}) \tag{6.7}$$

where $\mathbf{RV}$ is composed of $N-1$ RVs, with RV_i being the relative shift of the i^{th} observation and $\boldsymbol{\delta}$ is the vector of shifts, composed of $N-1$ shifts, with δ_i representing the shift that best aligned observation i with the others.

In the case where we have N observations, our model will have $2+(N-1)$ free parameters (2 GP hyper-parameters and $N-1$ RV shifts). The final hyper-parameters and relative RVs together with their corresponding uncertainties are determined using an MCMC sampling method to explore the posterior[4].

Having shown how we can obtain the relative RVs for each spectrum at each order, it is necessary to discuss how we combine the different orders. Assuming we have L orders, this is done using inverse-variance weighting. As such the RV shift for observation i is given by:

$$\mathrm{RV}_i = \sum_{l=1}^{L} \frac{\mathrm{RV}_i^l}{(\sigma_i^l)^2} \tag{6.8}$$

where RV_i^l is the RV we obtained for observation i at order l, and σ_i^l is the corresponding error obtained from the MCMC (68% level). Similarly, the final error is given by:

$$\sigma_i = \frac{1}{\sqrt{\sum_{l=1}^{L}(\sigma_i^l)^2}} \tag{6.9}$$

As such, we would expect the errors to scale as $\sim 1/\sqrt{L}$. The dependence on N is very hard to quantify, but from simulations it is revealed that no additional information is gained after ~ 10 observations (noting that this number is dependent on the instrument resolution and SNR). The initial gain is because as we add

[4]The priors are all uninformative uniform priors.

more observations, the GP is able to better 'learn' the stellar spectrum and this can result in more accurate RVs.

It is important to note, that it is simpler and more robust to work in $\ln \lambda$ space, because $\Delta\lambda$ is wavelength dependent. If we perform the analysis in log-space, then shifting the spectra by RV δ, corresponds to simply adding δ to $\ln \lambda$. I adopt this formalism and the computations are all performed in log-space after which I transform them back to SI units.

6.3 BRaVe *Python* package

BRaVe is the *python* package that I developed to extract RVs directly from the observed spectra using Gaussian processes. It is available *open source* and it can be *pip installed*[5]. In addition to encoding the GP RV extraction method presented in the previous section, it has my own simplistic CCF implementation that uses theoretical stellar models as templates, various data reading routines for the common spectrographs, data plotting tools that can help quickly analyse the quality of the fit and identify sources of error, a blaze correction routine, various simple data manipulation tools (e.g. sigma clipping, normalisation, interpolating, convolution, etc.) and it is able to correct for the barycentric motion of the Earth[6].

6.3.1 Introduction and description

In this section I aim to describe the tools that are encoded in BRaVe and show how they all fit together. The package is fully automated and can be run from a setup file that specifies the parameters for the extraction process (theoretical template for the CCF, MCMC steps and burn-in, path to the data, instrument, etc.). The theoretical description of using GPs to model stellar spectra and extract RVs was presented in Section 6.2 and thus here I focus on the implementation side.

Let us start with an overview of the data reading processes. At the time of writing, BRaVe is able to read the 2-D spectral products (each échelle order

[5]At the time of writing it is on the test *PyPI* server.

[6]There are two implementations, one calling `astropy`, the other calling **barycorrpy** and **barycorr**.

separately) provided by the following instruments: CHIRON, Minerva, Expres, HARPS and HARPS-N (and the synthetic stellar spectrum that I generate). In the case of most instruments, the spectroscopic observations provided have been pre-processed by the instrument pipelines, and as such, they come wavelength calibrated, barycentre corrected, and telluric contamination corrected. The one exception is CHIRON, which doesn't provide barycentre corrected spectra. This motivated to incorporate a simple routine that calls `astropy` (Astropy Collaboration et al., 2018) or **barycorrpy** (Kanodia & Wright, 2018) to obtain the barycentric corrections[7] and apply them at the data reading step.

HARPS, HARPS-N and Expres provide the observer with the blaze correction that needs to be applied to the data, however CHIRON does not do this. As such I have implemented a simplistic approach to compute it. I fit the uncorrected flux with a function of the form $f = A(\frac{\sin(\mathbf{x})}{\mathbf{x}})^2 + a\mathbf{x}^2 + b\mathbf{x} + c$, where $\mathbf{x} = 1 - \frac{\boldsymbol{\lambda}}{\lambda_c}$ is the vector describing the wavelength axis, and λ_c is the central wavelength of that order[8]. A basic nightly binning function is available and can be called to help increase the SNR that simply co-adds all the observations from the same night, but I wouldn't recommend using it if the observations are not consecutive. Finally, I normalise the spectra to unity in case this hasn't been done. I note that we can ignore the continuum correction as each order usually spans a few nm and the Gaussian process can absorb this.

The sigma clipping algorithm implemented in BRAVE is a non-linear iterative filter with k-sigma clipping introduced by Aigrain & Irwin (2004). As such, it iteratively fits the spectrum with a rolling average looking for outliers (e.g. cosmic rays). This method then removes the outliers and replaces them with interpolated data.

[7] By default I call **barycorr** (Eastman et al., 2010; Wright & Eastman, 2014) via the python interface of **barycorrpy** . This is because **barycorr** has been shown to be highly reliable and provides accurate corrections to the 10s of $\mathrm{cm\,s^{-1}}$ level. Beyond this, it is necessary to include relativistic corrections.

[8] This is the sum of a sinc squared function, which is the expected functional form of the blaze function, and a low-order polynomial, which is intended to absorb small departures from this expected behaviour.

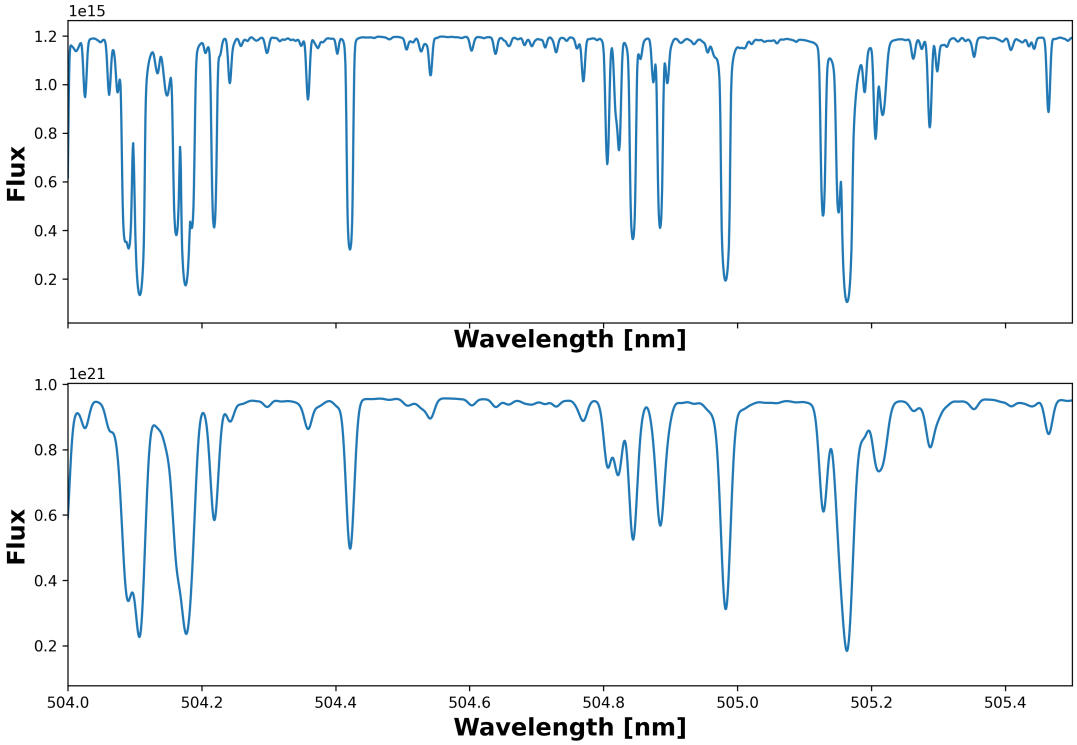

Figure 6.2: Figure showing a small chunk of a high resolution theoretical spectrum (top panel) and the convolved spectrum (bottom panel) with resolution reduced to 100 000.

I would like to mention that my code uses the following libraries: `astropy` library (Astropy Collaboration et al., 2018), `scipy` library (Virtanen et al., 2020), `numpy` library (Harris et al., 2020), and `matplotlib` library (Hunter, 2007) without which it would have been borderline impossible to build this framework.

6.3.2 CCF RV extraction

The motivation for including my own CCF RV extraction in BRAVE is both as a benchmark to compare the GP results against, as well as a method that can be used even when there are only one or two observations available.

The CCF implementation is simplistic and relies on the theoretical high resolution spectra provided by the Göttingen Spectral Library (Husser et al., 2013). BRAVE matches the best theoretical spectra to the observations and uses it to extract CCF RVs. This is performed in the following steps. First I read in the theoretical spectra over the desired spectral range and normalise it. Next, I convolve it with a

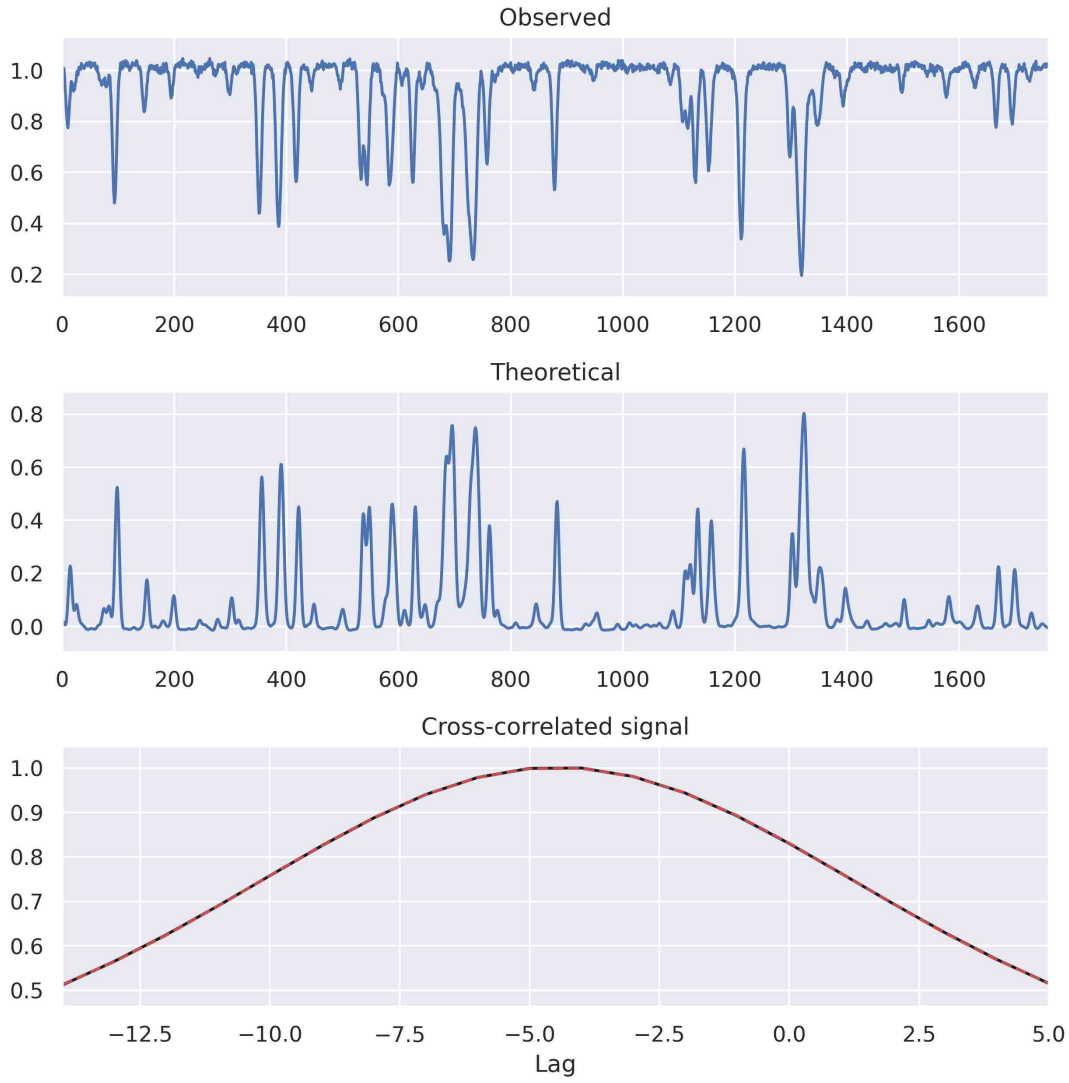

Figure 6.3: Figure showing the CCF of a simulated spectrum. The top panel shows the an order of the observed spectrum with SNR = 100, R = 100 000, that was shifted. The middle panel shows the theoretical spectrum used as a template for the cross-correlation (note this is the same spectrum that was used to create the synthetic spectra). The bottom panel shows the resulting CCF (black) as a function of lag, where each 'unit' of lag is the velocity step used in computing the CCF (750 $\mathrm{m\,s^{-1}}$), together with a Gaussian fit shown with a dasher red line.

Gaussian to reduce the resolution from 800 000 to match the spectral resolution of the instrument (see Figure 6.2 for an example, where the top panel shows the theoretical spectrum and the bottom panel shows it convolved to a resolution R = 100 000). In addition, I re-sample this template spectrum such that the pixel sampling is 4 times the spectral resolution (the typical sampling of modern spectrographs). This is followed by interpolating the theoretical noise-free spectra to the same grid as the observations and perform the cross-correlation using `scipy`'s signal routine (an example of this is shown in Figure 6.3). The resulting cross-correlation function is fitted with a Gaussian. In turn, the mean of the Gaussian is used to compute the best fit radial velocity, by multiplying with the velocity step of the CCF. I note that the results of the CCF extraction are not included in the thesis as there is a systematic offset of $\sim 200\,\mathrm{m\,s^{-1}}$ between the recovered radial velocities and injected shifts, for which I need to identify the source and correct. With the exception of this offset, the results are in line with expectations. The uncertainties decrease with increasing resolution and increasing SNR. This is part of my near-term goals.

6.3.3 Gaussian process RV extraction

For the Gaussian process functions I use the `celerite` package (Foreman-Mackey, 2018), because this implementation of the Matérn 3/2 kernel scales linearly ($\sim \mathcal{O}(M)$, where M is the number of data points). This kernel in `celerite` is defined as:

$$k(\tau) = \sigma^2 \left[(1 + 1/\epsilon)e^{-(1-\epsilon)\sqrt{3}\tau/\rho}(1 - 1/\epsilon)e^{-(1+\epsilon)\sqrt{3}\tau/\rho}\right] \tag{6.10}$$

where σ is the output scale hyper-parameter, ρ is the length scale hyper-parameter, and $\epsilon = 0.01$ controls the quality of the approximation (when $\epsilon \to 0$ we get the exact Matérm 3/2) that allows for the near linear scaling of the algorithm. This is crucial to this framework as we model a large number of data points together ($M \cdot N$ points). Note that in the remainder of this chapter, I adopt this notation for the hyper-parameters.

After fitting the GP to the combined dataset and obtaining maximum-likelihood (ML) values for the $N + 1$ free parameters of the model, I use the **emcee**

Markov-chain Monte Carlo package (Foreman-Mackey et al., 2013) to sample the posterior and obtain posterior distributions for each parameter (e.g. see Figure 6.5, showing the posteriors of an RV extraction on simulated data). I use the **corner** plotting tool (Foreman-Mackey, 2016) to create corner plots of these posteriors. Finally, I combine the RVs from each order as shown in equation 6.8 and compute the uncertainties on these using equation 6.9. It is important to note that as a sanity-check, I impose the constraint of only using RVs from orders, where the RV corresponding to that order is $\leq 5\sigma_{\rm RV}$ away from the mean of all RVs in the order. This means, that in cases where an order provides a poor fit, I discard that value and compute the RV only from the other orders. I note that in the current implementation I discard that order from all the RVs, this is not an efficient way of doing it as I discard potentially useful information. For example, consider that we have 5 observation and 10 orders. Let us assume that for observation 4, order 7 gives a poor fit compared to all the other orders. This doesn't mean that order 7 gives a bad estimate for all the other RVs and as such I discard it unnecessarily. It might just be that order 7 of observation 4 was contaminated. For all the other observations order 7 might give good results. This is something that I plan to correct in the next release of my package, improving the accuracy and precision of the extracted RVs when the SNR is low (this is mostly an issue for low SNR cases, $\leq\sim 10$).

6.3.4 Benchmarking

To test the feasibility of this GP based RV extraction method, I simulate synthetic observations of stellar spectra and try to recover the injected RV shift. I will present the results from one of these simulations, but in practice I have simulated multiple examples and tested the accuracy and precision of the GP based method. To simulate the synthetic observations I have used 3 high resolution theoretical spectra from the Göttingen Spectral Library (Husser et al., 2013), available here. Specifically, I have used a stellar spectrum with $T_{\rm eff} = 3700$K, $\log g = 4$, and solar metallicity; a spectrum with $T_{\rm eff} = 4500$K, $\log g = 4$, and solar metallicity; and a spectrum with $T_{\rm eff} = 6000$K, $\log g = 4$, and solar metallicity. For these 3 spectra,

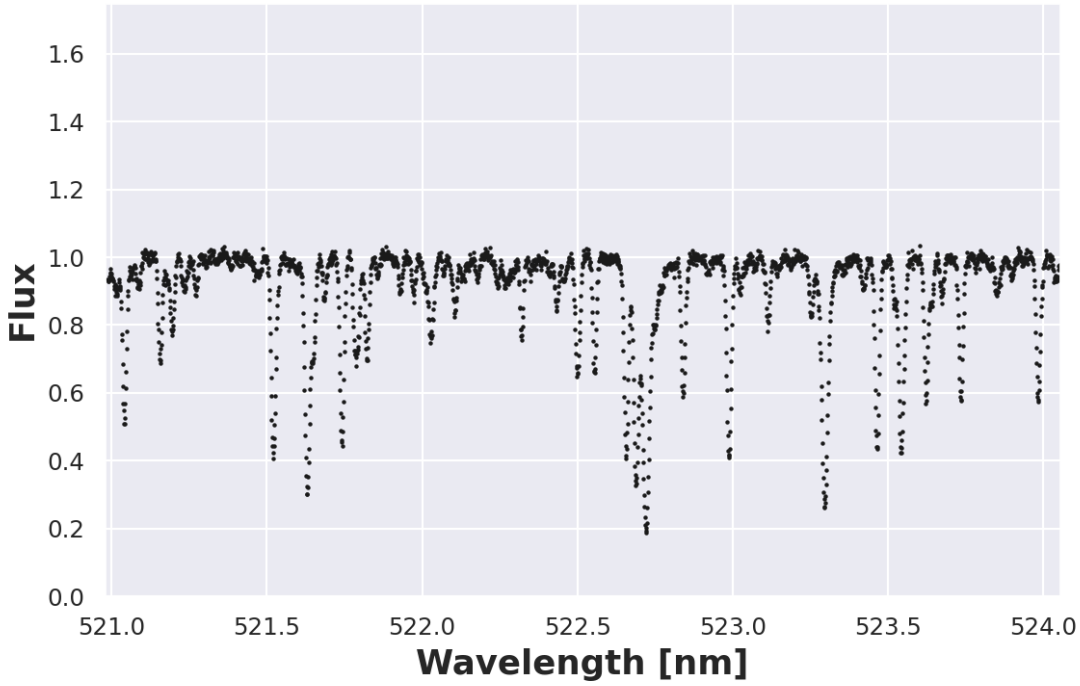

Figure 6.4: Figure showing order 7 for one of the simulated stellar spectrum at SNR = 100, and R = 100 000.

I selected the wavelength range between 500 and 800 nm. I then convolved each of these 1D theoretical spectra to the resolutions of R = [20 000, 50 000, 100 000], and resampled their pixel density such that it is 4 times the spectral resolution. Next, I split each of these 9 spectra $(3 \cdot 3)$ into 80 orders.

At each order for each spectrum I correct for the continuum by dividing with the average of the highest 500 flux values. This gives a good approximation for the continuum as the orders only span a few nm and as such a straight line gives a good fit. Noting that even if the continuum correction is not perfect the GP will be able to absorb this. As a result, we have 9 spectra each with 80 orders that have been renormalised to unity in flux. Afterwards I define a time grid in the range 0-45 days, and compute the expected radial velocity assuming an amplitude of 5000 $\mathrm{m\,s^{-1}}$ and a period of 27 days (I could have chosen any value as what we care about is the accuracy and precision compared to the truth). For each spectrum, I randomly draw 30 observations from this time-series that will represent our observation times and RVs. Then, I take each spectrum and shift it to accordingly to the RVs at each

Table 6.1: Table showing the uncertainties obtained from Brave for 10 simulated spectra, each containing 30 orders. I report the average uncertainty, but this is very similar to the median uncertainty as the distribution tends to be Gaussian. Note that in the case of R = 20 000 and SNR 10, the uncertainty is very large because only 5 orders were used to compute the final RVs. As detailed in the text, this is due to the way I discard outliers. Future versions will optimise this and improve the result.

Resolution	SNR	Average error $m\,s^{-1}$
20 000	10	812.9
20 000	30	122.3
20 000	100	35.1
50 000	10	74.4
50 000	30	23.1
50 000	100	6.9
100 000	10	22.6
100 000	30	7.4
100 000	100	2.2

of the 30 observation times (so I have 9 base spectra where each has been shifted to 30 different RVs). Next, I define 4 different values for the SNR $= 10, 30, 100, 500$. For each value of the SNR I take the 30 RV shifted spectra and add random white noise to the observations according to the SNR (a sample spectrum is shown in Figure 6.4). This means that we have 9 sets of spectra, at 4 SNR realisations and at 30 random observations (chosen to be split into 5 observations at a time, 10 observations and 30 all observations when trying to extract RVs).

To test the dependence of the uncertainty on the number of observations, for the $T_{\rm eff}$ = 6000K, R = 100 000, SNR = 100 case I have run the extraction on 5, 10, 18 and 30 observations. The results show that after about 7-8 observations there is no net gain in precision (this is expected as our RV_i doesn't depend on the number of observations), this number is slightly smaller for high SNR, as the GP can learn what the intrinsic stellar spectrum looks like.

For assessing the accuracy and precision of the method I will present the RV residuals for $T_{\rm eff}$ = 6000K, R = 100 000, SNR = 100, $N_{\rm order}$ = 30 and $N_{\rm obs}$ = 30. In addition, I show the scaling of the uncertainties as a function of SNR and resolution

in Table 6.1[9]. According to Lovis & Fischer (2010), the RV uncertainty σ scales as:

$$\sigma_{\mathrm{RV}} \sim \frac{\sqrt{\mathrm{FWHM}}}{C \cdot \mathrm{SNR}} \tag{6.11}$$

where FWHM is the width of the CCF (i.e. $v \sin i$ convolved with instrument resolution), C is the CCF contrast, SNR is the signal-to-noise ratio. This means that we expect a $\frac{1}{\mathrm{SNR}}$ dependence for the RV uncertainties. As it can be seen in Table 6.1, this is exactly the behaviour that we find. The average uncertainty for R = 100 000, decreases by a factor of 3 and ~ 3.3 when the SNR increases from 10 to 30, and 100 respectively.

An example for the parameter posterior distributions is shown in Figure 6.5, where there are 10 observations at R = 100 000 and SNR = 100. It can be seen in this plot that the posteriors for the 9 RV shifts are nicely Gaussian, with the two hyper-parameters being strongly correlated as expected.

The main results from testing and benchmarking the GP RV extraction method are summarised by Figure 6.6. In this plot I show the residuals of the GP RVs after subtracting the true RV shifts for each observation. It can be seen that residuals represent well the 'true' values, as only 6 observations out of 30 are more than 1σ away from a residual of 0 (perfect match). This is to be expected considering that $\sim 68\%$ of the observations should be within $1\sigma_{\mathrm{RV}}$ of the truth. The mean RV uncertainty is $\approx 2.2\ \mathrm{m\,s^{-1}}$ the same as in the case of 10 observations, as shown in Table 6.1. This is because the uncertainty doesn't have a direct dependence on the number of observations, only on the resolution, SNR and number of orders used. I note that in the case of very low SNR observations (10) the way I currently discard outliers is inefficient and leads to large uncertainties (unnecessarily one might argue).

The combined result from all these tests on simulated spectra demonstrates that the Gaussian process RV extraction is able to accurately retrieve radial velocities with realistic errors.

[9]Only 5 orders were used in the case of R = 20 000 and SNR = 10, hence the large uncertainty.

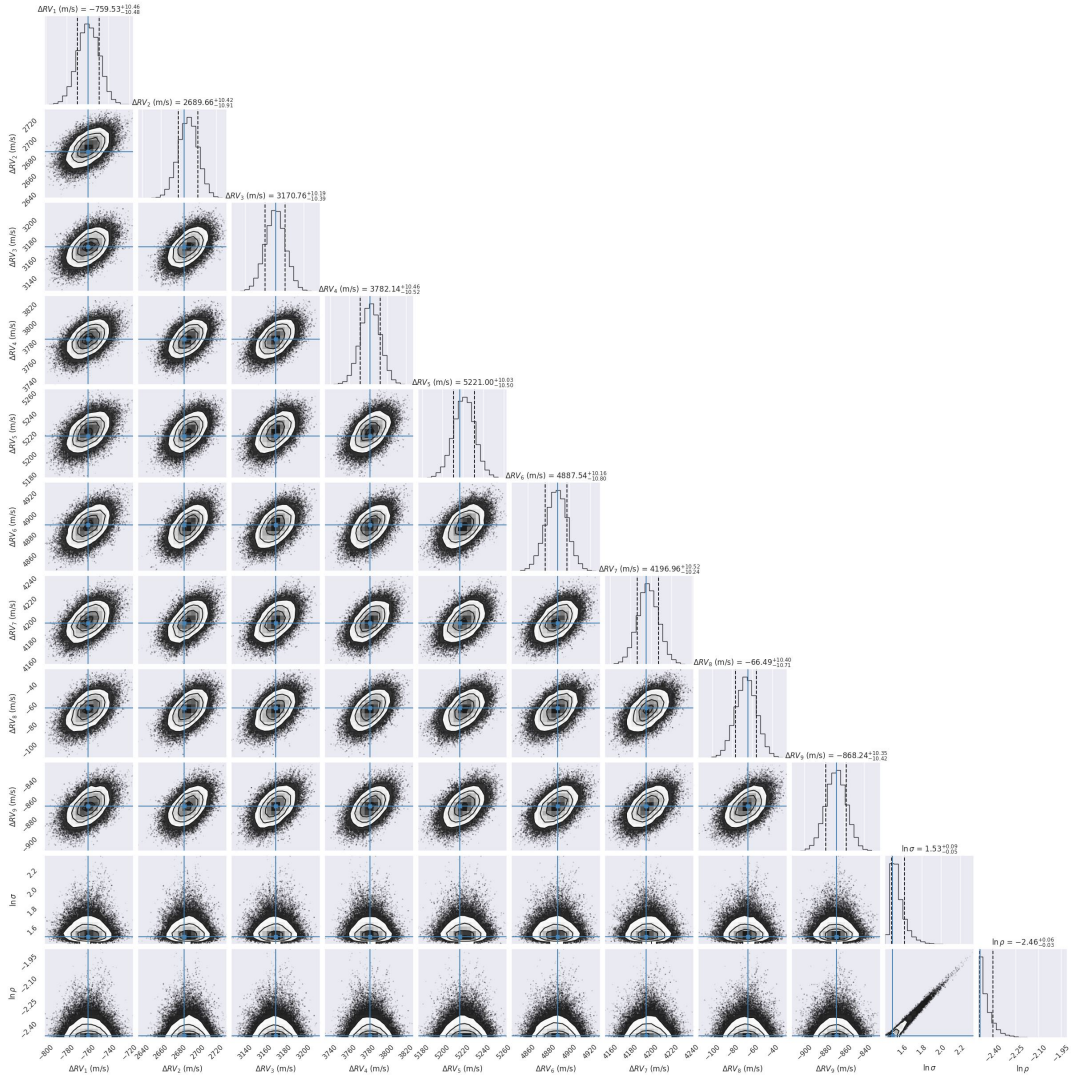

Figure 6.5: Posterior and correlation plots for the sampled parameters (MCMC corner plot) for the 9$^{\text{th}}$ order in the case of 10 simulated spectra with R = 100 000, and SNR = 100.

6.4 Applications

Having shown that the GP RV extraction method is able to accurately and precisely recover RV shifts on simulated data, I will present two cases of its application to real world datasets. The first application is on data obtained as part of the Monitor project (Irwin et al., 2006) using the FLAMES spectrograph (Pasquini et al., 2002), the second case presented is extracting radial velocities for TOI-813 (Eisner et al., 2020) (this was originally done to confirm its planetary nature) on spectra obtained with the CHIRON spectrograph (Tokovinin et al., 2013).

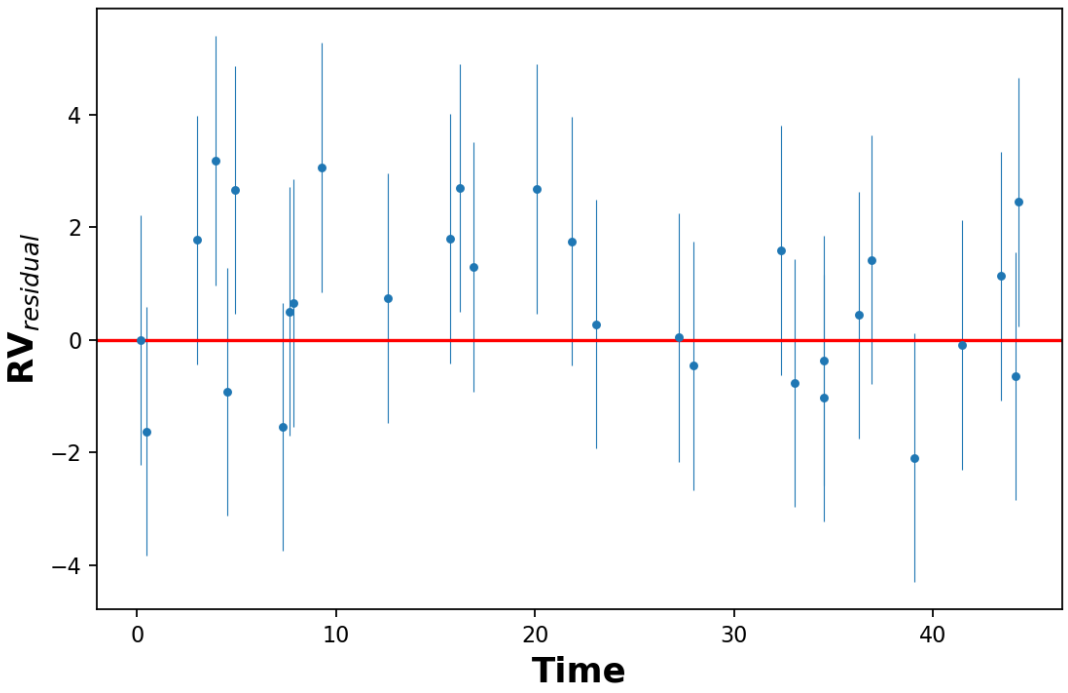

Figure 6.6: RV residuals plotted (blue dots with error bars) against observation time. These residuals were obtained from subtracting the true RV shifts from the RVs estimated by the GP method. A perfect fit would result in RV residuals of 0 shown with a red line. It can be seen that out of the 30 observations, only ~ 6 are more than $1\sigma_{\mathrm{RV}}$ away from the truth. This corresponds well to the theoretical expectation that 68% of the observations fall withing $1\sigma_{\mathrm{RV}}$.

6.4.1 M50

Messier 50 (NGC 2323) is a young open cluster in the Monoceros constellation. It is situated $\sim$ 3000 light-years from Earth (Kharchenko et al., 2005) with an estimated age of $\sim 140 \pm 20$ Myr (Frolov et al., 2012; Amin & Elsanhoury, 2017). The cluster was observed as part of the Monitor Project (2005-2009), which aimed to determine stellar rotation rates in nearby young open clusters and discover eclipsing and spectroscopic binaries (Irwin et al., 2006).

Introduction and context

The original photometric dataset was published by (Irwin et al., 2009) and reported measured rotation rates for 812 targets that were, at the time, believed to be cluster members based on a colour-magnitude cut. The photometric survey of M50

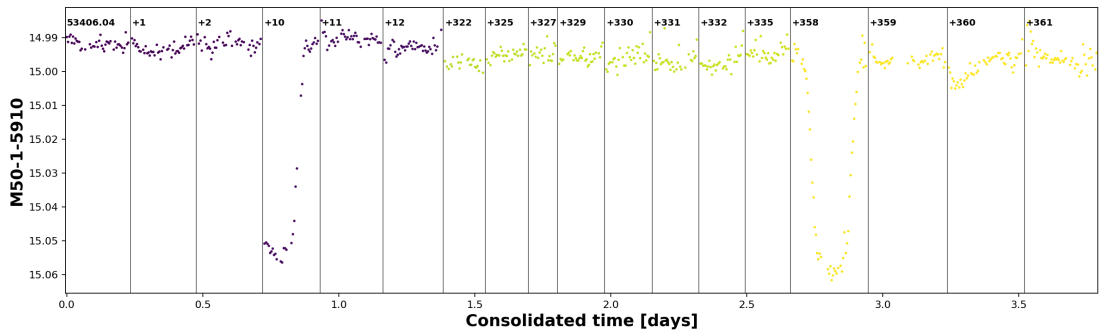

Figure 6.7: Light curve of M50-1-5910, showing two eclipses of the binary system.

was carried out using the Cerro Tololo Inter-American Observatory (CTIO) 4-m Blanco telescope and Mosaic-II detector. As there was data available from three observing runs separated by $\sim$ 10 and 1 month, they were able to observe evidence for evolution of the photometric amplitudes (spot patterns) over the 10 month gap.

The spectroscopic data that I worked on is an unpublished dataset that I have inherited from my supervisor who was involved in the Monitor project. This dataset contains 9 observations for 118 stars that were identified as interesting targets from the photometric survey, and were believed to be cluster members. The data was obtained using the FLAMES spectrograph (Pasquini et al., 2002) on the VLT. There are 9 epochs for each target spanning a period range of $\sim$ 20 days, with a typical SNR of $\sim 5 - 20$. The spectral resolution of the observations is $\sim$ 18000, and focuses on a $\sim$ 30 nm wavelength range around H_α.

The naming convention for the targets adopted in this section (and the original dataset) is 'cluster name - identifier', where the identifier is represented by the CCD and pixel number onto which the photometric observations fell (e.g. M50-2-5980, corresponds to CCD 2 and pixel number 5980). I will present in detail the analysis and results for M50-1-5910 which is an interesting target from this dataset, and discuss the overall results at the end of section 6.4.1.

The light curve of M50-1-5910 is shown in Figure 6.7. The x-axis is in consolidated time, where gaps in observations have been cut out, and the data is colour coded by the observation time. In total two eclipses were observed for this binary target, and as such spectroscopic follow-up observations were taken.

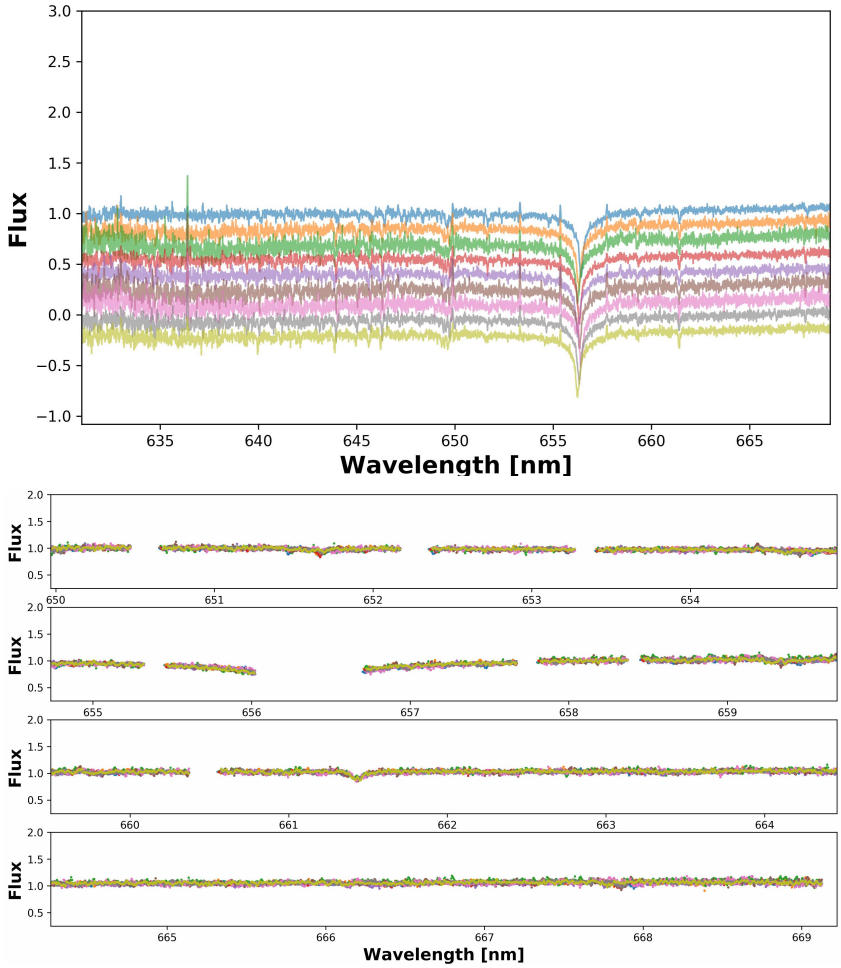

Figure 6.8: Top: Figure showing the observed spectra for M50-1-5910, offset from each other. It can be clearly seen that the spectral lines (e.g. H_α) are moving. Bottom: Figure showing the masked spectra for M50-1-5910 which were used to extract the radial velocities. The masked out regions were removed because of telluric contamination.

The spectroscopic observations are contaminated by telluric and sky emission lines and as such it was necessary to mask the contaminated regions out in an attempt to measure the radial velocity of the target stars(and not Earth's rotation). The full observed spectra are shown in the top panel of Figure 6.8, with the masked out spectra shown on the bottom.

Results

As this dataset only has a resolution of 18 000, spanning about 30 nm and there are only 9 epochs in total, the analysis has been performed on the whole spectrum, as opposed to different orders. Due to the telluric contamination, it was required to shift

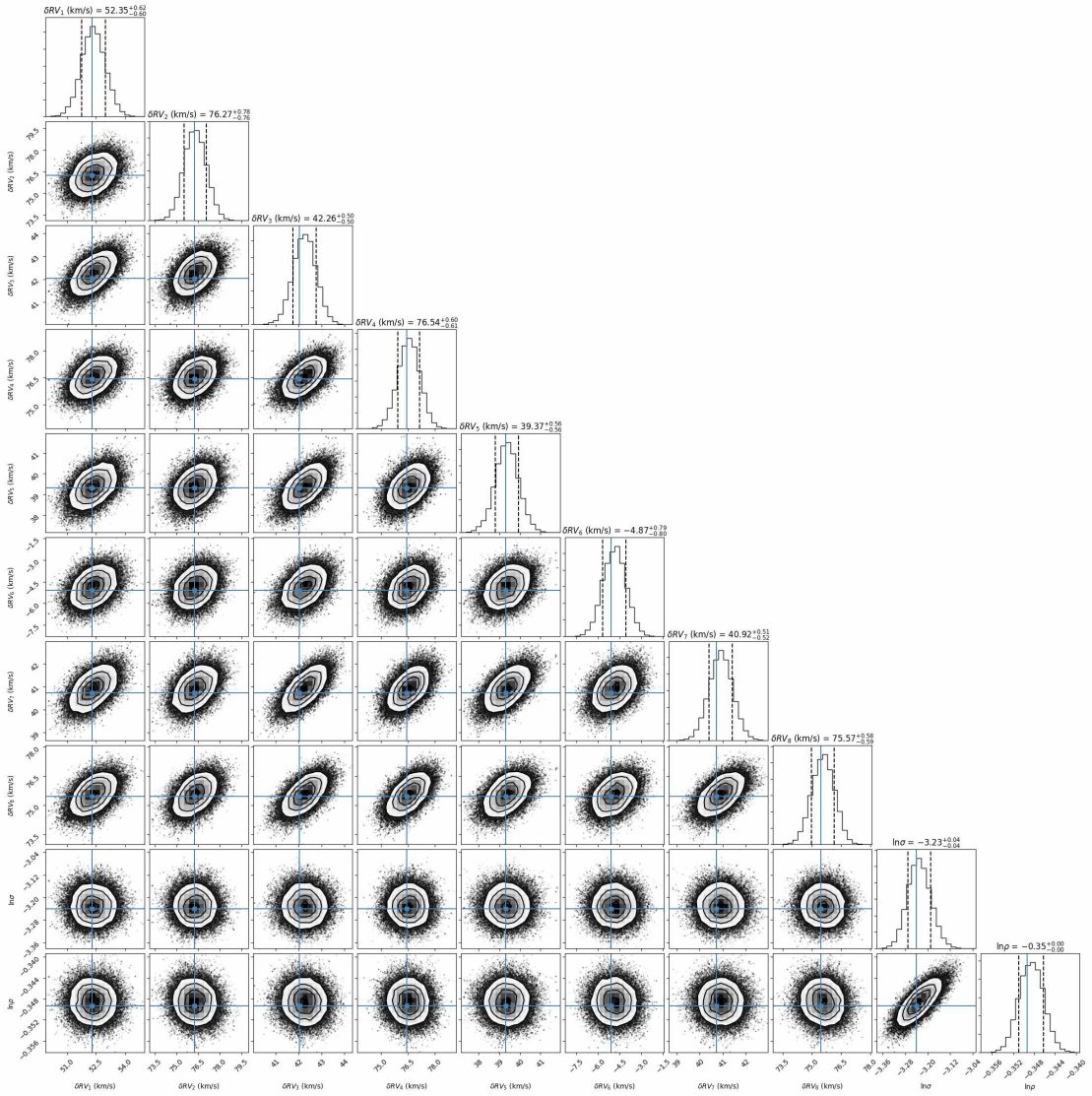

Figure 6.9: Posterior and correlation plots for the sampled parameters (MCMC corner plot) for M50-1-5910.

the observations to Earth's reference frame, identify contaminated regions and mask them out, before moving them back to the barycentric frame. Followed by applying the GP RV extraction method and obtaining posterior parameter distributions using the **emcee** MCMC sampler (corner plot showing the results in Figure 6.9).

The radial velocities obtained for this binary system are shown in Figure 6.10. It can be seen that this system is a binary in close orbit, with a period of 3.75 days. Some of the other interesting targets are presented in Figure 6.11.

Out of the 118 targets that have spectroscopic follow-up, I was able to extract

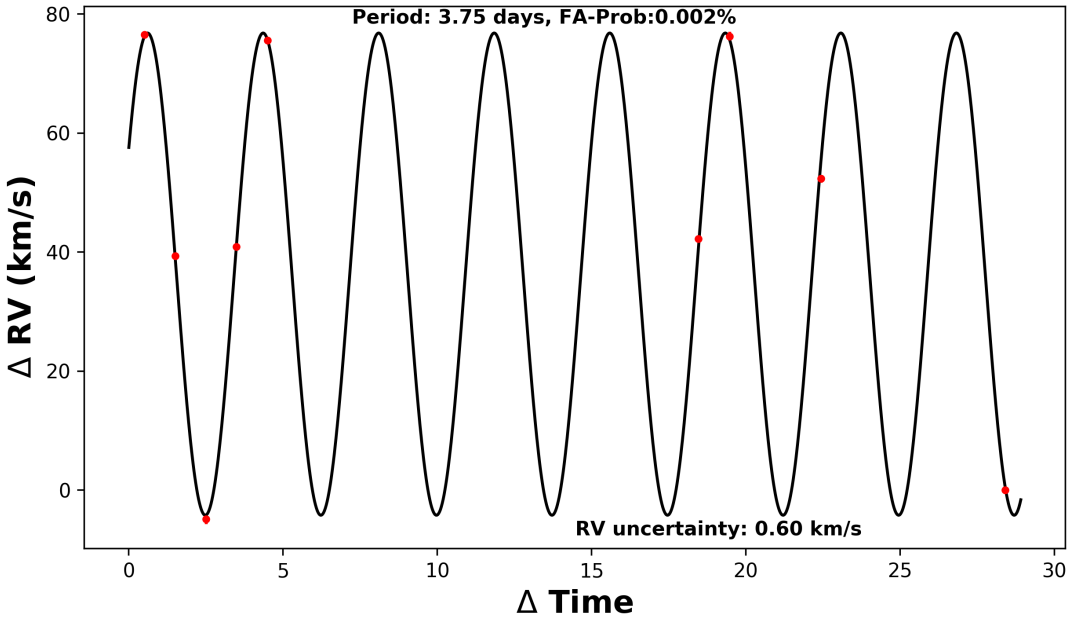

Figure 6.10: Extracted radial velocities for M50-1-5910, plotted with the best fit sinusoidal obtained from a periodogram. The errorbars are too small to be visible, with a typical uncertainty of $\sim 600\mathrm{m\,s^{-1}}$.

radial velocities for 112, with the caveat that in some cases I actually recover Earths rotation, so the RVs correspond to the barycentric motion. This is due to the strong telluric contamination even after trying to mask out the affected regions. The 6 targets where I was unable to extract any RVs had an SNR too small for my GP method to work (~ 3). In total I was able to recover good RVs (non-barycentre motion) for 51 targets, out of which only a handful (8-9) are interesting (show signs of being binaries). The large majority show a flat radial velocities or a small linear trend which is hard to quantify due to the low SNR and large uncertainties ($\chi^2 \leq 10$, or in the case of linear trends $\chi^2 \leq 15 - 30$). Out of the 118 targets with spectra, 101 had rotation periods published by Irwin et al. (2009).

Discussion - Cluster membership

The original photometric survey for M50 had ~ 63000 targets, out of these 4584 were selected as potential cluster members by Irwin et al. (2009) using a colour-magnitude diagram cute. In recent years a cluster membership catalogue was published by Cantat-Gaudin & Anders (2019), that utilises the astrometric data from Gaia's

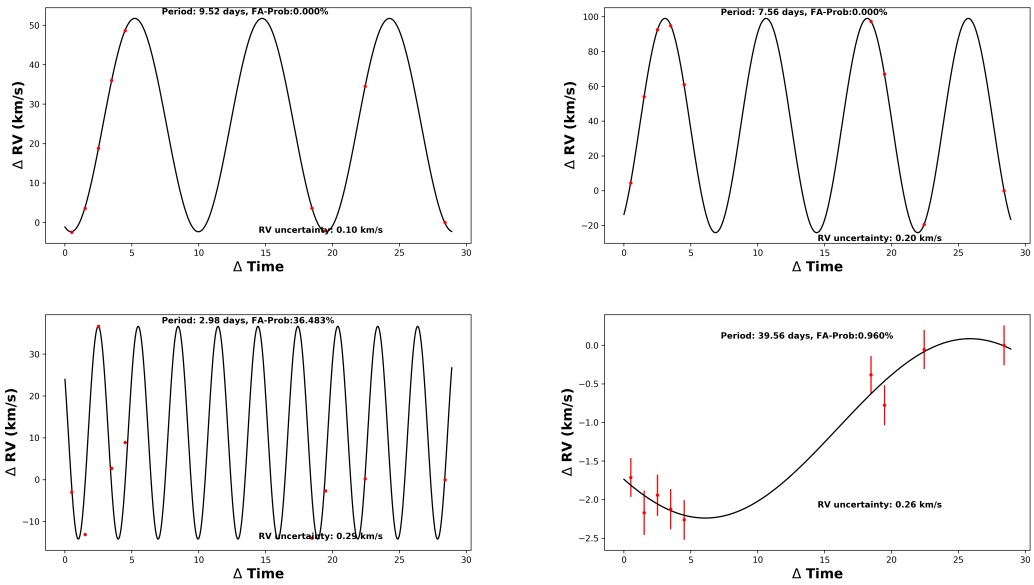

Figure 6.11: Figure showing the extracted RVs together with the best fit sinusoidal for 4 interesting targets from the M-50 dataset that are binaries. The top two panels show the results for M50-2-5980 (left) and M50-2-6314 (right), while the bottom two panels show the results for M50-2-7050 (left) and M50-7-690 (right).

data release 2 - DR2 (Gaia Collaboration et al., 2018) to determine membership probability. This catalogue published 1272 potential cluster members.

I compared the results for cluster membership published by Irwin et al. (2009) to the catalogue published by Cantat-Gaudin & Anders (2019). I found that out of the 4584 stars identified as potential members, 4249 were in the full Gaia catalogue with the remainder being too faint for Gaia. When I cross-match these with the ones published based on astrometry, I find that only 248 stars match, which is very interesting and will be examined as part of future work. When comparing the targets that had spectroscopic follow-up, out of the 112 targets I found that 110 were in the Gaia catalogue, and when cross-matched with the ones that are presumably cluster members I find an overlap of 33 targets. This number is smaller when I consider only the stars that have valid radial velocities extracted. I find that out of the 51 targets with successful RVs extracted, only 39 are in the Gaia catalogue, and only 26 are potential cluster members based on astrometry. Unfortunately, none of these show any signs of being binaries. As such, none of the results presented above are

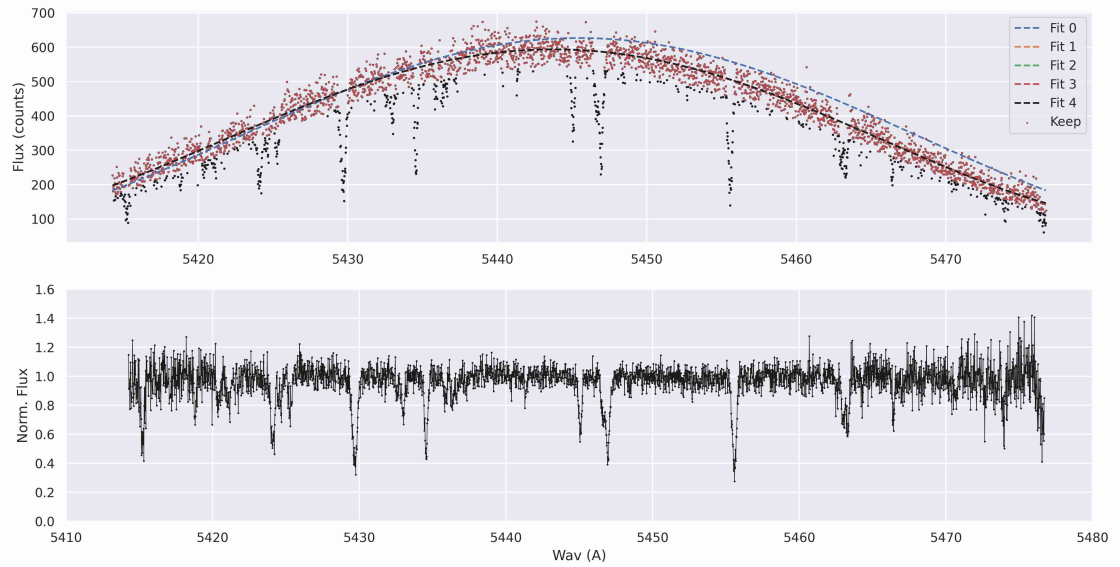

Figure 6.12: TOI-813: Figure showing the iterative blaze correction fit (top panel) for observation 1, order 19. The final blaze correction fit is shown with a solid black line in the top panel, the data points used to obtain this fit are shown in red. The blaze corrected normalised stellar spectrum is shown in the bottom panel.

expected to be members of M50, but nonetheless they are interesting binary-systems.

6.4.2 CHIRON

As part of the `Planet Hunters TESS` citizen science program, the Oxford group has identified 23 targets (Eisner et al., 2021) for which follow-up spectroscopic observations were taken with the CHIRON spectrograph (Tokovinin et al., 2013). As CHIRON doesn't provide radial velocities, I have used BRAVE to extract RVs for these targets, in order for us to be able to validate the planetary nature of the transiting objects.

I will present the analysis and results for TOI-813b (Eisner et al., 2020), which at the time didn't have radial velocities and we needed to validate it. The full table showing the number of observations for each of the 23 targets is shown in Appendix A.

TOI-813 and TOI-813b

The host star, TOI-813, is a subgiant (G0IV) that is located $\sim$ 858 light-years away. It has a mass of $M_\star = 1.32 \pm 0.06 M_\odot$, a radius of $R_\star = 1.94 \pm 0.1 R_\odot$, and an effective temperature of $5900 \pm 150 K$ (Eisner et al., 2020, and references therin).

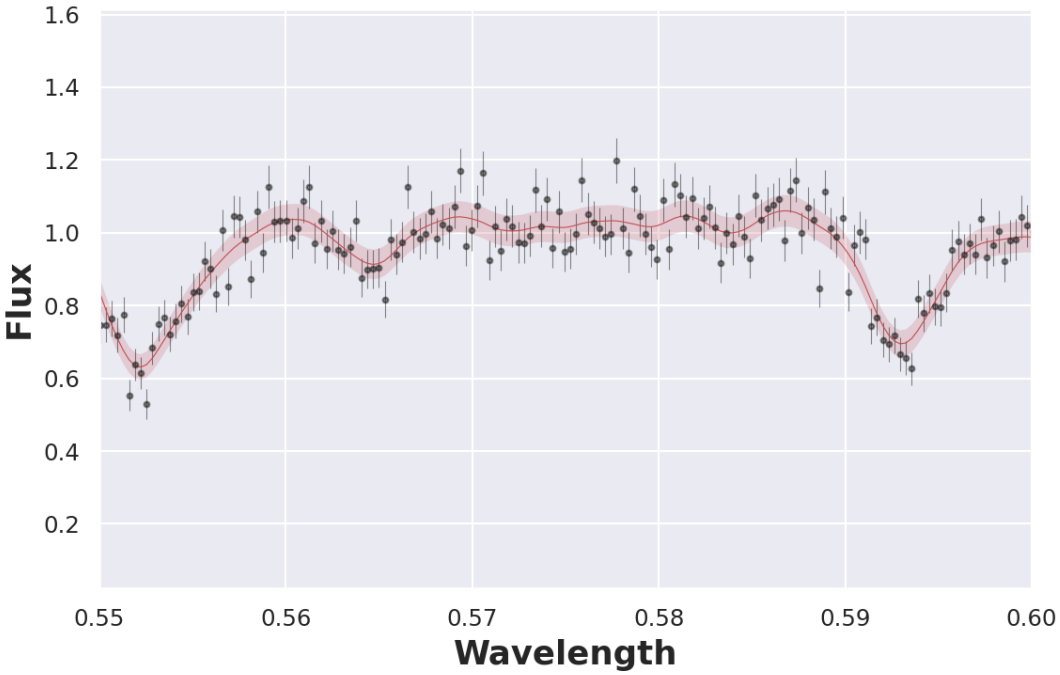

Figure 6.13: TOI-813: A sample plot of the GP fit for observation 3, order 17.

The citizen science discovered planet, TOI-813b, has a radius of $6.8 \pm 0.4 R_{\oplus}$ and an orbital period of P = 83.9days (Eisner et al., 2020).

Introduction and context

In total we obtained 8 CHIRON observations spanning a period of 2 months, with an average SNR of $\sim 15 - 20$ in the median order, and a spectral resolution of R = 80 000. I have used BRAVE to extract radial velocities for this target. As the CHIRON observations come only wavelength calibrated, I used **barycorrpy** to correct for the barycentric correction at the stage of reading in the data. Next, the observations need to be blaze corrected which is done using the algorithm described previously. A sample demonstration of this is shown in Figure 6.12, where I iteratively fit a function to obtain the best blaze correction. I mask the absorption lines using a sigma clipping in order for them to not effect the fitting process. The final fit, shown by the black line in the top figure is a good descriptor of the blaze correction and this is used to normalize the spectra shown in the bottom panel. The edges of each order tend to be very low signal-to-noise ratio ($\sim 3 - 4$).

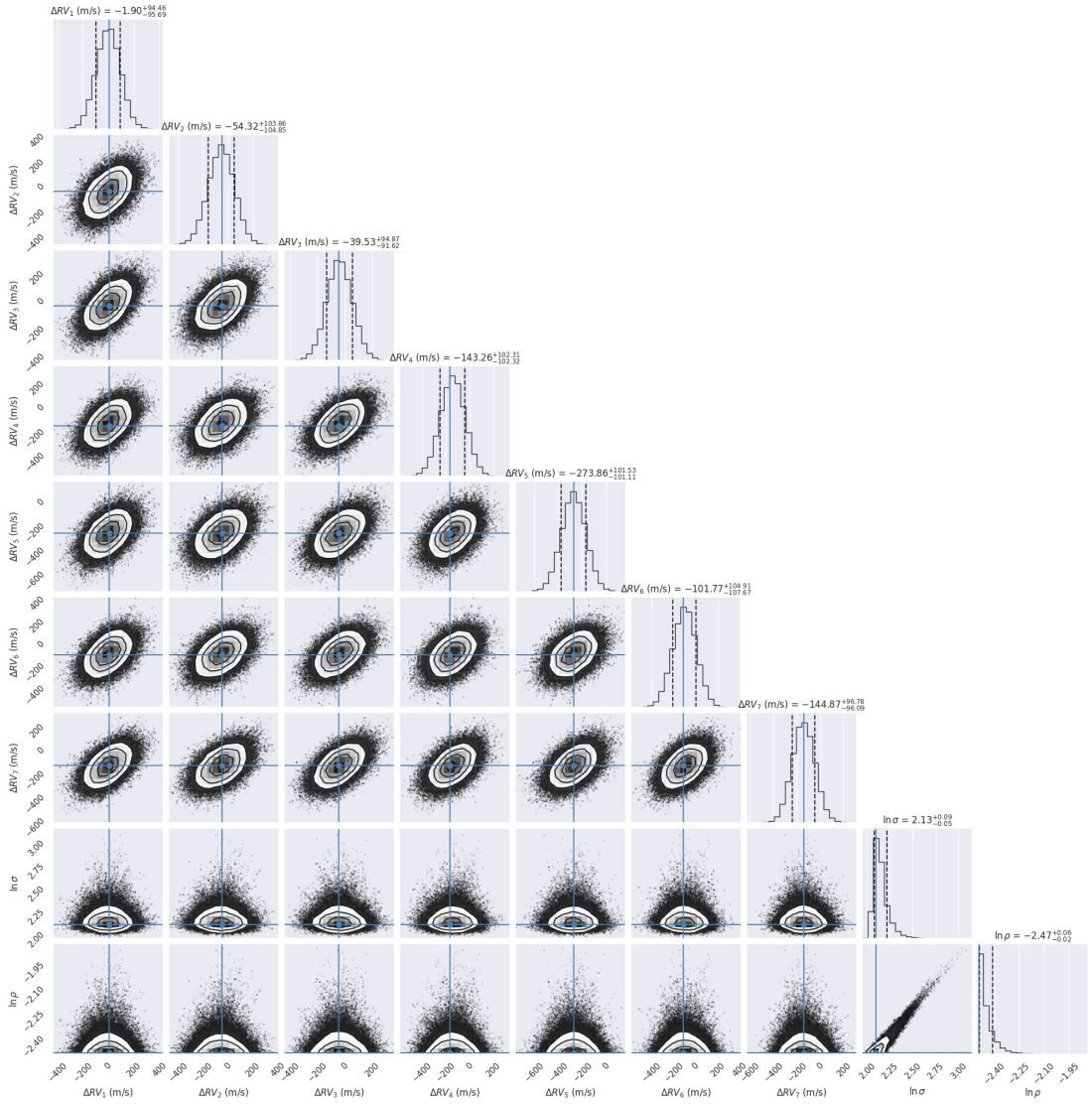

Figure 6.14: TOI-813 posterior and correlation plots for the sampled parameters (MCMC corner plot). These posteriors are for order 17.

After normalising the spectra, I fit the GP to them to obtain the maximum-likelihood parameters. An example of the GP fit is shown in Figure 6.13, for the 3rd observation at order 17. Note that the wavelengths have been transformed into log-space and normalised to fall between 0 and 1. It can be seen in this figure that the GP provides a good fit to the data, without overfitting.

Results

The results of the MCMC run are summarised in the corner plot shown in Figure 6.14. The RV shifts are Gaussian distributions and the GP hyper-parameters are strongly

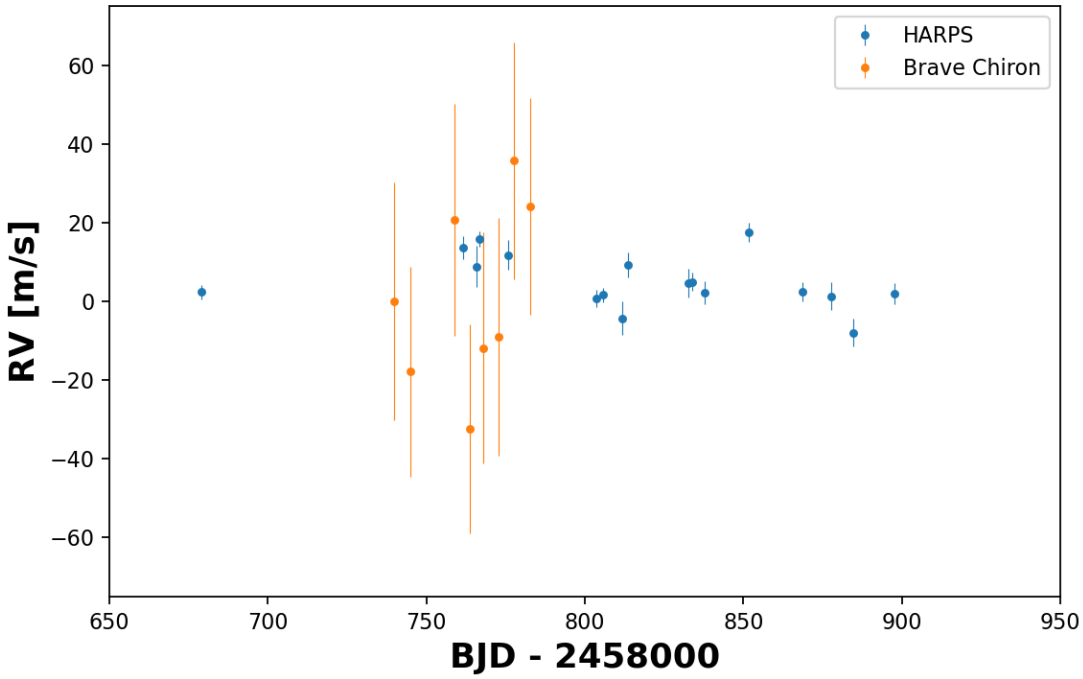

Figure 6.15: Figure showing the RVs extracted from the CHIRON observations using BRAVE in orange and HARPS DRS RVs in blue.

correlated as expected from the degeneracy. The bounds on the hyper-parameters stop the model from overfitting and allow us to fit for the RV shifts.

The final combined GP RVs for each observation are shown in orange in Figure 6.15, together with RVs extracted from HARPS observations using the HARPS DRS in blue. Taking the errorbars into consideration, the two pipelines provide results that are compatible with each other. Note that the CHIRON observations have significantly larger errorbars arising from the lower spectral resolution of the instrument and the much lower SNR of the observations. Future work will involve extracting radial velocities from the HARPS observations and comparing the results.

6.5 Discussion and conclusion

The GP RV extraction presented in this chapter is promising and could provide an alternative to classical methods, especially in cases where traditional CCF based methods show poor results. The simulations show that it is able to retrieve RVs

with high accuracy and precision. However, one big limitation is that it doesn't scale very well for large numbers of observations and it can be computationally expensive. It becomes extremely challenging to model more than 50 observations in the current setup, as it would take about 1-2 days when run on a cluster with 12 cores. Further improvements could provide better results and scaling as the current code doesn't fully leverage the power of parallel computing. In my opinion, the current biggest limitation is the posterior sampling, which if replaced with a more efficient method could make the method computationally feasible for any number of observations. I believe that it is an interesting avenue to explore, but there might be better ways to leverage the power of GPs in extracting radial velocities (e.g. pair-wise RVs - Rajpaul et al. 2020). The next step in the development and testing of this approach will be to compare it directly to the DRS, especially on M-dwarfs, where the CCF masks are not as optimised. In addition, an interesting test dataset will be the spectroscopic data from the *EXPRES Stellar-signals Project* (Zhao et al., 2020, 2022), allowing me to compare it directly to other modern methods that are currently in development.

In life, your dreams should aim for the stars ...
so you can hit the Moon.

— My father - Zsolt Zicher

7 Conclusions

Contents

7.1 Review and conclusions

In this thesis, I have measured the masses of 2 young transiting planets, developed an alternative method for extracting precise radial velocities, directly from stellar spectra, and further developed current techniques for exoplanet detection by introducing 2 extensions to the generalised Lomb-Scargle periodogram and use them to place detection constraints for AU Mic.

In Chapter 4, I present the results from our intensive monitoring campaign with HARPS for AU Mic. We measure the masses for the two extremely young transiting planets. This is the only system ($\sim$ 22Myr) younger than 500 Myr that has mass measurements for relatively low-mass planets ($11.7 \pm 5.0\ M_\oplus$ and $22.2 \pm 6.7\ M_\oplus$)[1]. The only other system with a similar age that has measured

[1]All the other systems that have similar masses are 600-800 Myr - see K2-100, TOI-1201, TOI-560.

masses is V1298 Tau ($\sim$ 20Myr), where the planets are 0.64M_{Jup} and 1.16 M_{Jup} (Suárez Mascareño et al., 2021). The RV signals of the two planets around AU Mic are around 50 times smaller than the activity signals. The mass measurements, combined with literature radius estimates, indicate that AU Mic b has a significant H/He envelope and may have an internal heat source. On the other hand, we find that AU Mic c is denser and compatible with either a rocky core surrounded by a $\sim$ 2% H/He envelope or a pure H_2O composition. These results are in tension with current core-accretion models, which predict that planet c, with a more massive core, should have the larger H/He envelope of the two. This system offers unprecedented testing opportunities for theoretical models.

In Chapter 5, I present two extensions to the generalised Lomb-Scargle periodogram, namely the linear activity-corrected periodogram (LACP) and Gaussian process based GdG periodogram. I demonstrate the effectiveness of these models in correcting for activity induced RV variations on simulated datasets. In addition, I presented the detection limits for long period planets ($>$ 20days) around AU Mic. The results from the injection-recovery test show that the probability of having any additional planets with amplitudes greater than 50 $m\,s^{-1}$ is very small.

In Chapter 6, I developed a Gaussian process based method for extracting precise radial velocities directly from the stellar spectra, offering an alternative to the traditionally used cross-correlation method. This GP RV extraction method is encoded in my publicly available *python* package called BRAVE , that I have presented in this chapter. I have benchmarked this method on simulated synthetic spectra, to show its capabilities and test its robustness, highlighting that it is able to accurately and precisely recover radial velocities for a variety of stars. In addition, I have presented two applications of this method. First, on the M50 open cluster, followed by CHIRON observations of TOI-813.

Perhaps the most important take-away from this thesis is the importance of accounting for stellar variability and the need for improved tools to model it. It is going to be crucial in the coming decade to increase our understanding of the underlying processes and improve on our ability to disentangle them from planetary

signals. In addition, characterising young planets will play a key role in refining current formation and evolution models. With only a handful of systems, it is still very difficult to distinguish between the different processes. We certainly need more of these young systems.

7.2 Future work

The work presented in the thesis naturally leads to future endeavours. Some of these are outlined below.

A possible extension involves optimising the GP RV extraction method, finding better ways for the posterior sampling, and improving the efficiency of the current model by utilising all the available information. I plan on comparing it to current pipelines to further test its performance and explore its full potential, as well as compare the results to my CCF extraction when the template used is a perfect match.

Secondly, I hope to release the periodogram extensions as part of a python package available to the larger astrophysics community. I hope that it would provide an easy to use and fast tool to analyse large datasets, and allow for extensive injection-recovery tests, without the computational overhead of more complex models.

Finally, I believe it is crucial that we measure the masses of more young planets considering their key role in refining theoretical models. I hope that over the coming years many more young systems are published with measured masses. I would like to improve on the mass measurement for AU Mic b as this would allow us to break the degeneracy between the internal entropy and envelope mass fraction, as well as measure the Rossiter-McLaughlin (RM) effect induced by AU Mic c.

7.3 Reflection

I believe that in the coming years I will find myself contemplating what I could have done differently, what could I have improved on more[2]. In full honesty, if I was to start my PhD today with my current knowledge and state of the field, I

[2]I will certainly regret not starting to write the thesis earlier.

probably would have done some of the things differently. But ... if you don't try, you will never know the answer, and so is the way of life.

I am very grateful for the opportunity to learn about such an interesting field and hopefully my contributions will aid future scientists in their discoveries, the same way the ones who came before me paved the way to where we are currently. After all, science is built on past knowledge and relies on collaboration to advance.

I am convinced that in the coming years numerous breakthroughs will take place in the field of exoplanetary science. With the increasing number of extreme precision spectrographs and extensive observing campaigns, the launch of James Webb Space Telescope, the continued observations from *TESS*, the upcoming Ariel and Plato missions (and many more that I probably forgot to mention), they will all have a deep impact on the science that is attainable. It is indubitable that we will discover more of these exotic far-away worlds, in such detail that is currently beyond our grasp. Our knowledge will grow swiftly, leading to new frontiers yet to be discovered.

Appendices

In a dark place we find ourselves,
and a little more knowledge lights our way.

— **Yoda**, from
Star Wars Episode III (2005)

A

Appendix - Chiron observations

Contents

A.1 CHIRON observations table

Table A.1 shows all the Chiron observations obtained for the 23 target stars.

Table A.1: Table showing the Target ID and the number of CHIRON observations.

Target ID	Number of observations
TOI-813	8
TIC-138126035	21
TIC-391903064	15
TIC-150299840	6
TIC-206361691	3
TIC-348835438	8
TIC-404518509	8
TIC-422914082	3
TIC-321978218	4
TIC-63698669	3
TIC-7422496	3
TIC-369779127	9
TIC-270371513	2
TIC-267608606	3
TIC-95768667	9
TIC-349576261	3
TIC-304339227	9
TIC-349095149	3
TIC-321978218	2
TIC-303317324	3
TIC-121636363	3

You cannot teach a man anything; you can only help him discover it himself.

— Galileo Galilei

B
Appendix - AU Mic

Contents

B.1 Time-series table

Table B.1 shows the full RV dataset as described in Section 4.2 and Table B.2 shows the activity time-series.

Table B.1: Radial velocity observations. Observations which were affected by flares or clouds are flagged in the 'Remarks' column.

Time	RV_{DRS} $m\,s^{-1}$	σ_{DRS} $m\,s^{-1}$	RV_{SERVAL} $m\,s^{-1}$	σ_{SERVAL} $m\,s^{-1}$	RV_{TERRA} $m\,s^{-1}$	σ_{TERRA} $m\,s^{-1}$	Remarks
7223.64	-4581.3	7.1	136.0	6.0	225.8	5.9	
7223.65	-4569.6	7.2	133.3	5.8	225.2	5.8	
7333.53	-4671.4	4.2	6.5	2.4	105.7	2.3	
7333.54	-4670.2	4.4	11.0	2.4	106.6	2.5	
7493.89	-4684.3	3.9	-0.4	4.0	105.9	4.8	
7493.9	-4683.2	3.7	-2.0	3.7	102.0	4.5	
7590.71	-4678.7	3.6	-13.5	2.2	82.2	2.6	
7590.72	-4675.9	3.8	-15.8	2.4	78.6	2.7	
7904.81	-4998.3	5.5	-378.9	6.5	-279.1	6.0	

Continued on next page

Table B.1 – continued from previous page

Time	RV_{DRS}	σ_{DRS}	RV_{SERVAL}	σ_{SERVAL}	RV_{TERRA}	σ_{TERRA}	Remarks
7904.82	-4996.9	5.6	-385.8	6.6	-283.5	5.5	
7917.89	-4618.4	5.6	77.0	4.1	172.3	4.1	
7917.9	-4614.5	5.3	71.9	4.1	168.6	4.2	
8035.52	-4774.3	4.2	-111.6	2.1	-11.0	2.6	
8035.53	-4774.2	4.3	-116.4	2.2	-17.0	2.4	
8037.49	-4818.4	6.7	-136.7	3.2	-34.2	3.9	
8037.5	-4810.1	7.0	-131.1	3.4	-28.4	4.3	
8206.87	-4804.6	3.9	-130.5	2.2	-31.8	2.6	
8206.88	-4802.0	3.9	-136.6	1.7	-33.5	2.0	
8207.89	-4761.9	4.8	-55.7	2.7	44.0	2.8	
8207.9	-4758.2	5.0	-54.7	2.8	49.1	2.8	
8208.88	-4662.1	3.4	4.3	2.5	94.1	2.8	
8208.89	-4668.8	3.4	1.4	2.4	90.8	2.8	
8591.91	-4662.9	4.0	26.1	3.6	126.1	2.9	
8591.92	-4661.2	4.0	34.0	3.1	135.3	2.8	
8593.9	-4628.0	5.4	38.2	3.4	132.3	4.1	
8593.91	-4612.7	5.4	38.0	3.8	129.4	4.3	
8594.9	-4753.1	6.7	-77.5	4.1	25.6	4.4	
8594.91	-4751.7	6.5	-73.5	3.2	30.5	4.3	
8602.92	-4769.2	4.9	-91.6	2.1	13.2	2.6	
8602.93	-4757.4	4.8	-78.0	2.7	26.7	2.8	
8605.91	-5056.7	5.2	-347.8	3.5	-241.1	3.3	
8605.92	-5051.4	5.1	-344.4	4.0	-236.1	3.6	
8786.53	-4833.2	6.3	-124.6	4.2	-21.2	5.2	
8787.5	-4827.2	5.1	-25.1	2.2	73.2	2.5	
8787.51	-4783.5	6.7	-32.4	2.0	67.6	2.3	
8789.51	-4699.6	4.4	-203.0	3.8	-109.3	5.0	
8789.52	-4716.2	4.1	-203.7	3.5	-111.3	3.7	
9168.6	-4622.2	6.7	58.7	4.4	154.5	4.7	New data
9170.58	-4785.9	8.9	-113.6	3.3	-13.0	6.2	
9171.54	-4668.9	7.0	26.9	4.4	127.2	4.5	
9172.54	-4928.0	4.8	-260.8	2.6	-158.0	3.2	
9175.51	-4770.9	5.3	-107.0	2.9	-5.0	3.0	
9175.56	-4773.2	6.3	-102.1	3.5	0.0	5.1	
9176.51	-4671.3	5.3	24.4	3.8	127.5	3.3	
9177.51	-4963.5	4.9	-288.1	3.2	-182.0	3.5	
9178.51	-4622.8	5.6	47.6	4.0	144.7	4.0	
9178.52	-4629.3	5.9	43.5	3.4	136.0	3.8	
9179.52	-4762.3	4.8	-172.4	4.2	-85.6	5.1	Flare
9180.54	-4749.4	5.2	-68.5	2.6	30.1	2.9	
9181.54	-4732.2	6.3	-24.7	4.7	85.5	4.5	
9182.54	-4922.7	4.9	-230.0	3.0	-124.2	3.4	
9183.54	-4656.8	4.4	1.4	3.0	92.7	3.2	
9184.54	-4812.7	4.4	-190.5	3.7	-93.6	3.5	
9185.54	-4727.5	7.2	-28.2	3.7	76.0	4.4	

Continued on next page

Table B.1 – continued from previous page

Time	RV_{DRS}	σ_{DRS}	RV_{SERVAL}	σ_{SERVAL}	RV_{TERRA}	σ_{TERRA}	Remarks
9188.55	-4715.8	5.5	-72.5	4.0	22.9	4.2	
9189.55	-4861.5	4.5	-222.8	4.5	-117.4	5.1	
9190.52	-4719.9	4.9	-9.7	3.6	94.1	3.6	
9191.52	-4834.0	4.3	-152.9	2.4	-49.2	2.5	
9192.52	-4807.6	4.0	-109.5	2.3	-0.8	3.3	
9358.8	-4559.7	3.9	140.0	4.8	238.3	3.8	
9359.76	-4791.5	4.4	-110.5	2.1	-9.4	2.4	
9359.87	-4714.3	4.2	-34.0	2.6	65.1	2.4	
9360.76	-4713.9	4.6	-38.5	2.4	59.4	2.6	
9360.88	-4756.4	5.4	-81.7	2.9	17.1	3.0	
9361.79	-4942.7	6.1	-257.6	3.1	-153.7	3.5	
9366.73	-4977.6	4.7	-299.3	2.9	-192.3	3.3	
9366.86	-4944.4	5.8	-286.1	3.8	-182.5	3.8	
9367.74	-4856.8	5.4	-166.4	3.4	-61.2	3.7	
9367.84	-4783.5	5.8	-96.8	3.9	10.1	3.6	
9368.81	-4711.0	4.8	-45.8	2.3	52.5	3.4	
9368.91	-4784.8	5.1	-130.9	3.0	-30.6	3.1	
9369.79	-4614.5	3.9	79.0	4.2	172.0	3.4	
9369.92	-4603.1	4.5	103.0	4.7	200.0	3.6	
9370.77	-4774.2	6.2	-110.5	2.8	-12.8	2.9	
9371.78	-4930.0	4.3	-276.4	2.8	-170.4	2.7	Flare
9371.91	-4921.3	4.8	-265.1	3.1	-159.4	3.2	
9372.75	-4777.5	5.6	-85.1	3.0	21.5	3.5	
9376.72	-4922.4	4.8	-257.2	2.4	-151.1	2.6	
9377.74	-4711.2	4.3	-8.6	3.0	97.9	3.5	
9378.79	-4859.0	4.6	-195.6	3.9	-98.1	3.4	
9379.86	-4651.6	5.9	46.6	4.3	146.7	4.0	
9405.78	-4968.4	4.3	-324.7	3.4	-218.0	2.8	
9406.71	-4814.8	7.0	-111.9	3.1	-8.1	3.8	
9408.91	-4611.2	8.0	63.5	4.2	156.2	7.8	
9409.71	-4777.7	6.5	-117.6	2.9	-22.3	3.3	
9410.71	-4961.9	5.5	-312.6	3.4	-205.9	3.7	
9410.79	-4930.6	5.7	-286.2	3.8	-179.4	4.0	
9411.74	-4697.1	4.2	13.6	2.8	114.6	3.6	
9412.62	-4696.5	5.3	-15.5	2.6	79.3	2.9	
9412.74	-4762.0	5.6	-97.0	2.2	-0.6	2.8	
9422.7	-4858.6	6.7	-191.8	3.5	-92.9	3.5	
9422.84	-4834.1	7.3	-185.7	3.0	-89.2	3.8	
9423.7	-4720.6	7.7	-31.2	4.5	61.6	8.2	Flare
9423.8	-4755.7	7.2	-58.3	3.8	41.2	5.5	Flare
9424.73	-4969.1	4.6	-296.0	2.9	-193.7	2.8	
9425.66	-4873.7	5.6	-208.0	3.3	-105.8	3.3	
9426.62	-4534.0	6.1	168.1	5.1	265.2	4.7	
9427.77	-4818.3	4.3	-162.6	2.3	-61.8	2.8	
9428.83	-4831.0	5.2	-92.1	4.5	12.7	6.4	Flare

Continued on next page

Table B.1 – continued from previous page

Time	RV_{DRS}	σ_{DRS}	RV_{SERVAL}	σ_{SERVAL}	RV_{TERRA}	σ_{TERRA}	Remarks
9429.76	-5033.5	5.8	-375.1	4.3	-270.4	4.0	
9430.72	-4821.2	11.8	-149.7	5.2	-51.2	7.1	
9432.66	-4822.1	5.7	-162.4	2.9	-61.5	3.1	
9433.71	-4748.3	5.4	-55.2	3.2	40.0	3.8	
9442.59	-4773.8	6.7	-116.5	3.4	-13.6	3.2	
9443.56	-4763.8	4.5	-83.2	2.0	12.3	3.8	
9443.77	-4821.7	4.5	-152.2	2.3	-55.5	4.7	
9444.57	-5005.0	4.1	-360.9	4.5	-257.4	3.5	
9444.67	-4955.8	4.0	-315.0	4.0	-213.1	3.5	
9444.79	-4899.6	4.2	-254.5	3.3	-153.9	3.5	
9449.54	-4963.8	5.9	-311.3	4.1	-208.1	4.3	Clouds
9449.65	-4888.5	7.9	-245.8	3.9	-143.4	4.4	Clouds
9449.79	-4909.5	12.2	-238.3	9.0	-140.5	13.4	Clouds
9460.65	-4555.9	4.0	145.0	3.7	240.8	3.8	
9461.56	-4823.3	4.6	-165.2	2.6	-62.5	2.7	
9462.73	-4716.7	5.9	-20.8	3.5	89.7	5.3	
9463.79	-5070.5	5.6	-411.9	6.0	-306.8	4.4	
9464.53	-4821.0	5.0	-132.5	3.3	-25.4	4.3	
9467.6	-4688.2	3.8	-0.5	2.2	97.9	2.4	
9470.61	-4463.7	5.5	242.8	5.9	337.9	5.7	
9471.56	-4792.2	3.8	-141.9	3.4	-48.2	3.6	
9472.58	-4784.8	4.6	-63.9	4.2	28.0	6.0	Flare
9476.49	-4838.7	4.7	-177.7	3.2	-75.8	2.9	
9477.52	-4753.1	7.5	-64.4	4.0	32.9	3.8	
9477.63	-4802.0	8.7	-114.6	3.9	-13.2	5.9	
9478.51	-5040.4	5.3	-403.4	5.1	-292.8	4.5	
9478.66	-4976.2	4.8	-322.8	3.6	-213.9	3.2	
9479.52	-4758.6	9.5	-75.6	4.6	17.0	4.6	
9479.72	-4769.8	6.2	-64.3	3.4	37.0	3.7	

Table B.2: Activity time-series observations.

Time	FWHM	Bis-span	DLW	σ_{DLW}	S_{HK}	σ_{SHK}	H_α	SNR
7223.64	10.7	-0.146	-12.26	5.53	7.85	0.02	-2.35	71.2
7223.65	10.69	-0.18	-3.28	4.85	7.8	0.02	-2.34	70.6
7333.53	10.58	-0.019	-40.27	4.71	7.82	0.02	-2.49	129.1
7333.54	10.58	-0.021	-41.63	4.84	7.72	0.02	-2.43	122.3
7493.89	10.82	-0.155	43.96	3.38	8.89	0.01	-3.09	136.9
7493.9	10.8	-0.139	79.8	5.41	8.23	0.01	-3.07	141.8
7590.71	10.78	-0.086	38.14	3.74	8.57	0.01	-2.74	146.9
7590.72	10.78	-0.083	35.38	4.58	8.59	0.01	-2.76	139.9
7904.81	10.76	0.134	25.02	3.37	7.78	0.02	-2.5	96.6

Continued on next page

Table B.2 – continued from previous page

Time	FWHM	Bis-span	DLW	σ_{DLW}	S_{HK}	σ_{SHK}	H_{α}	SNR
7904.82	10.75	0.12	21.39	4.15	7.84	0.02	-2.49	95.1
7917.89	10.79	-0.088	37.47	3.67	8.79	0.02	-2.94	96.4
7917.9	10.78	-0.065	33.08	4.4	8.84	0.02	-2.96	101.2
8035.52	10.84	0.011	53.37	4.97	8.95	0.02	-3.05	128.9
8035.53	10.83	0.0	49.51	4.53	8.75	0.02	-3.02	127.6
8037.49	10.63	0.041	-29.45	6.71	7.77	0.02	-2.26	78.6
8037.5	10.65	0.016	-40.8	7.67	7.39	0.02	-2.23	75.5
8206.87	10.62	0.002	-22.51	3.79	7.32	0.01	-2.14	129.1
8206.88	10.62	0.003	-30.74	3.53	7.37	0.01	-2.16	130.6
8207.89	10.57	0.002	-46.94	4.76	7.31	0.01	-2.15	104.3
8207.9	10.57	0.035	-49.83	4.44	7.34	0.02	-2.14	99.9
8208.88	10.71	-0.106	20.56	3.53	8.42	0.01	-2.74	147.2
8208.89	10.73	-0.088	21.51	3.58	8.32	0.01	-2.71	150.3
8591.91	10.58	-0.05	-53.72	3.73	8.3	0.01	-2.52	132.5
8591.93	10.59	-0.061	-44.22	4.73	8.22	0.01	-2.51	131.7
8593.9	10.74	-0.126	40.5	4.78	8.56	0.02	-2.67	99.1
8593.91	10.77	-0.139	51.92	5.19	8.61	0.02	-2.69	99.3
8594.9	10.76	-0.002	25.79	4.74	8.96	0.02	-2.83	79.0
8594.91	10.75	-0.006	36.2	5.61	9.11	0.02	-2.85	81.0
8602.92	10.6	0.043	-25.62	4.16	7.85	0.02	-2.43	105.7
8602.93	10.59	0.014	-23.22	3.27	8.0	0.02	-2.46	108.2
8605.91	10.54	0.267	-49.79	5.9	7.79	0.02	-2.48	99.8
8605.92	10.53	0.257	-48.17	5.14	7.79	0.02	-2.47	102.0
8786.53	10.78	-0.069	3.49	5.32	10.39	0.03	-3.25	80.9
8787.5	10.79	-0.066	19.44	3.64	7.8	0.02	-2.34	129.6
8787.51	10.51	0.096	25.63	3.4	7.81	0.02	-2.33	138.2
8789.51	10.77	-0.015	45.14	5.18	8.36	0.03	-2.69	90.1
8789.52	10.79	0.016	45.8	5.08	8.28	0.02	-2.7	112.3
9168.6	10.54	-0.156	-62.01	6.06	7.18	0.03	-2.11	75.1
9170.58	10.78	-0.016	-8.74	8.87	7.61	0.03	-2.44	59.2
9171.54	10.73	-0.028	-8.58	5.2	7.37	0.02	-2.34	73.2
9172.53	10.71	0.086	-27.37	3.98	7.41	0.02	-2.21	108.9
9175.51	10.76	-0.033	0.44	4.44	7.47	0.02	-2.43	101.4
9175.56	10.8	-0.054	8.78	5.3	7.66	0.02	-2.5	84.9
9176.51	10.77	-0.034	21.75	3.77	7.57	0.02	-2.46	99.4
9177.51	10.67	0.115	-43.06	3.36	7.57	0.02	-2.32	107.9
9178.51	10.67	-0.167	4.74	4.74	7.89	0.02	-2.51	93.0
9178.52	10.69	-0.147	-1.65	5.19	8.03	0.02	-2.51	88.2
9179.52	10.79	-0.066	42.91	4.61	9.91	0.02	-3.13	114.1
9180.54	10.81	-0.016	20.95	4.55	8.65	0.02	-2.78	107.1
9181.54	10.83	0.018	63.91	5.65	8.94	0.03	-2.95	86.0
9182.54	10.53	0.14	-72.15	4.96	7.52	0.02	-2.24	108.6
9183.54	10.77	-0.073	28.08	5.49	8.38	0.02	-2.71	123.3
9184.54	10.83	-0.004	19.73	3.13	8.03	0.02	-2.81	126.7
9185.54	10.78	0.006	5.69	5.13	7.8	0.03	-2.54	73.8

Continued on next page

Table B.2 – continued from previous page

Time	FWHM	Bis-span	DLW	σ_{DLW}	$S_{\rm HK}$	σ_{SHK}	H_α	SNR
9188.55	10.71	-0.017	11.73	4.06	7.38	0.02	-2.25	95.4
9189.55	10.81	0.072	49.87	4.12	8.92	0.02	-2.87	122.6
9190.52	10.79	0.074	26.87	4.14	8.5	0.02	-2.79	110.7
9191.52	10.81	0.1	45.16	4.65	8.01	0.02	-2.57	128.9
9192.52	10.41	0.032	-93.33	6.88	7.98	0.02	-2.46	128.5
9358.81	10.74	-0.179	16.1	2.97	7.82	0.01	-2.36	138.8
9359.76	10.52	0.018	-78.25	4.88	7.33	0.02	-2.34	120.3
9359.87	10.58	-0.064	-80.75	5.68	7.13	0.01	-2.27	122.8
9360.76	10.86	-0.015	42.34	4.81	7.38	0.02	-2.44	115.6
9360.88	10.84	0.04	36.15	5.5	7.63	0.02	-2.51	95.4
9361.79	10.71	0.134	-5.11	4.52	7.54	0.02	-2.43	84.8
9366.73	10.68	0.117	-22.8	3.21	7.57	0.02	-2.39	111.0
9366.86	10.64	0.069	-26.2	3.72	8.07	0.02	-2.52	86.2
9367.74	10.63	0.1	1.72	4.73	8.43	0.02	-2.54	97.9
9367.84	10.52	0.045	-48.55	6.45	8.53	0.02	-2.65	87.9
9368.81	10.99	-0.021	58.69	6.14	6.99	0.02	-2.1	110.8
9368.91	10.95	0.039	60.28	4.74	7.23	0.02	-2.22	107.5
9369.79	10.7	-0.128	-32.76	3.26	7.76	0.01	-2.43	131.8
9369.92	10.79	-0.097	-13.28	2.63	7.27	0.02	-2.32	120.4
9370.77	10.82	0.011	29.03	5.26	7.68	0.02	-2.56	83.5
9371.78	10.71	0.059	8.27	3.22	9.59	0.02	-3.29	124.1
9371.91	10.65	0.058	-24.42	3.55	8.16	0.02	-2.83	113.8
9372.75	10.48	0.048	-79.26	7.86	7.58	0.02	-2.29	92.7
9376.72	10.62	0.053	-32.54	3.27	8.12	0.02	-2.54	108.6
9377.74	10.44	0.005	-74.86	6.29	8.34	0.02	-2.55	120.9
9378.79	10.82	0.117	16.71	4.3	7.49	0.02	-2.2	115.3
9379.86	10.82	-0.081	53.04	4.91	8.09	0.02	-2.64	90.8
9405.78	10.56	0.081	-23.29	3.34	8.59	0.02	-2.75	122.2
9406.71	10.54	0.117	-77.37	7.95	7.46	0.02	-2.15	72.1
9408.91	10.79	-0.13	3.64	6.25	7.48	0.03	-2.36	66.2
9409.71	10.82	-0.046	39.76	4.8	8.44	0.02	-2.73	81.4
9410.71	10.6	0.05	-50.93	5.98	7.84	0.02	-2.39	93.6
9410.79	10.62	0.023	-38.76	4.49	8.53	0.02	-2.62	93.7
9411.74	10.45	0.017	-93.33	8.66	7.04	0.01	-2.1	121.3
9412.63	10.96	-0.012	82.11	6.33	7.83	0.02	-2.31	101.8
9412.74	10.9	0.048	61.12	5.77	7.77	0.02	-2.38	92.4
9422.7	10.71	0.083	16.75	4.22	8.75	0.02	-2.74	78.7
9422.84	10.63	0.033	-21.13	5.49	8.61	0.03	-2.88	72.3
9423.7	10.95	-0.023	143.19	9.34	11.95	0.03	-3.87	71.0
9423.8	10.9	0.053	88.61	7.22	10.92	0.03	-3.25	76.6
9424.73	10.92	0.123	54.11	4.66	8.23	0.02	-2.63	117.2
9425.66	10.67	0.011	-48.44	4.81	7.73	0.02	-2.3	92.9
9426.62	10.48	-0.111	-71.36	6.53	7.81	0.02	-2.31	80.8
9427.77	10.66	0.055	-41.27	3.54	7.22	0.02	-2.36	122.4
9428.83	10.78	0.133	76.49	5.68	10.88	0.02	-3.48	106.6

Continued on next page

Table B.2 – continued from previous page

Time	FWHM	Bis-span	DLW	σ_{DLW}	$S_{\rm HK}$	σ_{SHK}	H_α	SNR
9429.76	10.78	0.197	23.56	4.37	8.14	0.02	-2.48	90.0
9430.72	10.73	0.04	-39.24	8.12	8.27	0.04	-2.29	44.5
9432.66	10.64	0.031	-38.77	4.31	7.6	0.02	-2.43	88.6
9433.71	10.84	0.059	22.43	4.67	7.66	0.02	-2.38	97.3
9442.59	10.67	0.029	-3.6	5.09	8.91	0.02	-2.86	77.1
9443.56	10.81	0.049	34.39	3.88	8.4	0.02	-2.83	118.8
9443.77	10.84	-0.03	43.44	4.62	8.26	0.02	-2.71	123.7
9444.57	10.58	0.122	-47.14	4.92	8.48	0.02	-2.64	127.9
9444.67	10.54	0.062	-48.22	4.47	9.11	0.01	-2.81	128.1
9444.79	10.57	0.016	-65.14	5.41	8.52	0.02	-2.69	128.9
9449.54	10.53	0.058	-71.13	6.9	8.82	0.02	-2.9	87.2
9449.65	10.57	0.015	-71.15	9.22	8.28	0.03	-2.62	64.1
9449.79	10.67	-0.039	6.83	10.3	7.4	0.04	-2.64	44.3
9460.65	10.48	-0.096	-89.48	7.43	7.32	0.01	-2.15	131.4
9461.56	10.84	0.056	38.19	4.79	7.59	0.02	-2.3	113.4
9462.73	10.88	0.045	57.51	5.43	9.2	0.02	-2.99	92.7
9463.79	10.69	0.201	-7.17	3.54	8.07	0.02	-2.5	97.8
9464.53	10.71	-0.01	0.29	4.48	9.04	0.02	-2.81	106.7
9467.6	10.89	-0.003	26.94	3.39	7.42	0.01	-2.28	136.5
9470.61	10.63	-0.207	-35.81	4.9	7.09	0.02	-2.09	95.3
9471.56	10.64	0.027	4.88	2.92	8.44	0.01	-2.67	135.7
9472.57	10.82	0.031	151.85	10.98	8.55	0.01	-3.43	117.1
9476.49	10.63	0.049	-20.24	3.58	7.67	0.02	-2.53	108.9
9477.53	10.89	-0.01	63.19	6.48	7.55	0.02	-2.43	70.9
9477.63	10.92	-0.005	61.75	7.83	7.2	0.03	-2.35	62.0
9478.51	10.59	0.169	-55.44	6.16	8.03	0.02	-2.47	96.4
9478.66	10.57	0.101	-45.44	5.66	8.54	0.02	-2.6	110.9
9479.52	10.71	0.059	-0.56	7.43	7.81	0.03	-2.21	54.5
9479.72	10.53	0.083	-65.95	7.21	7.93	0.02	-2.45	85.8

B.2 Activity models

Table B.3 shows the priors and inferred parameters of the three models described in Section 4.3.3.

Table B.3: Priors and posteriors, median and confidence intervals, for the different models

Parameter	Prior[(a)]	Model 1 Posterior value[(b)]	Model 2 Posterior value[(b)]	Model 3 Posterior value[(b)]
AU Mic b's parameters				
Orbital period $P_{\rm orb}$ (days)	$\mathcal{N}[8.463, 0.000002]$	$8.4629998^{+2.1e-06}_{-2e-06}$	$8.463^{+2e-06}_{-2.1e-06}$	8.463000 ± 0.000002
Transit epoch T_0	$\mathcal{N}[8330.39051, 0.00015]$	$8330.39052^{+0.00015}_{-0.00016}$	$8330.39051^{+0.00016}_{-0.00015}$	8330.39051 ± 0.00015
Eccentricity e	$\mathcal{B}[1.52, 29]^{(c)}$	$0.042^{+0.05}_{-0.027}$	$0.042^{+0.044}_{-0.026}$	$0.04^{+0.045}_{-0.025}$
Angle of periastron ω (deg)	$\mathcal{U}[0, 360]$	$182.0^{+126.0}_{-126.0}$	$182.0^{+127.0}_{-129.0}$	179^{+128}_{-125}
Semi-amplitude K (m s^{-1})	$\mathcal{U}[0, 50]$	$5.89^{+2.98}_{-2.66}$	$5.1^{+2.32}_{-2.15}$	5.8 ± 2.5
AU Mic c's parameters				
Orbital period $P_{\rm orb}$ (days)	$\mathcal{N}[18.859019, 0.000016]$	$18.859019^{+1.5e-05}_{-1.6e-05}$	$18.85902^{+1.6e-05}_{-1.5e-05}$	18.859019 ± 0.0000016
Transit epoch T_0	$\mathcal{N}[8342.2223, 0.0005]$	$8342.22227^{+0.00048}_{-0.00046}$	$8342.2223^{+0.00051}_{-0.00051}$	8342.22231 ± 0.00050
Eccentricity e	$\mathcal{B}[1.52, 29]^{(c)}$	$0.039^{+0.045}_{-0.025}$	$0.04^{+0.047}_{-0.026}$	$0.041^{+0.047}_{-0.026}$
Angle of periastron ω (deg)	$\mathcal{U}[0, 360]$	$182.0^{+126.0}_{-126.0}$	$143.3^{+141.4}_{-95.8}$	153^{+124}_{-94}
Semi-amplitude K (m s^{-1})	$\mathcal{U}[0, 50]$	$6.7^{+3.09}_{-3.06}$	$8.86^{+2.42}_{-2.51}$	8.5 ± 2.5
Multidimensional GP parameters				
GP Period $P_{\rm GP}$ (days)	$\mathcal{U}[4.8, 4.9]$	$4.8604^{+0.0032}_{-0.0031}$	$4.8572^{+0.0037}_{-0.0025}$	$4.8571^{+0.0037}_{-0.0027}$
$\lambda_{\rm p}$	$\mathcal{U}[0.1, 2]$	$0.455^{+0.06}_{-0.048}$	$0.46^{+0.054}_{-0.045}$	$0.449^{+0.049}_{-0.043}$
$\lambda_{\rm e}$ (days)	$\mathcal{U}[10, 500]$	$142.7^{+35.1}_{-24.7}$	$111.7^{+17.3}_{-16.6}$	108 ± 15
$A_{\rm V}$ (m s^{-1})	$\mathcal{U}[0, 100]$	21^{+24}_{-14}	10^{+15}_{-07}	$7.5^{+10.9}_{-05.5}$
$B_{\rm V}$ (m s^{-1} d)	$\mathcal{U}[-1000, 1000]$	102^{+53}_{-26}	102^{+39}_{-23}	91^{+27}_{-18}
$A_{\rm DLW}$ (1000 m^2 s^{-2})	$\mathcal{U}[-1000, 1000]$	...	45^{+19}_{-10}	$38.7^{+12.3}_{-08.5}$
$A_{\rm FWHM}$ (km s^{-1})	$\mathcal{U}[-1, 1]$	$0.149^{+0.076}_{-0.039}$	...	...
$A_{\rm BIS}$ (km s^{-1})	$\mathcal{U}[-1, 1]$	$-0.0048^{+0.0097}_{-0.0119}$	$-0.003^{+0.008}_{-0.0093}$	...
$B_{\rm BIS}$ (km s^{-1} d)	$\mathcal{U}[-1, 1]$	$-0.06^{+0.016}_{-0.032}$	$-0.05^{+0.012}_{-0.02}$	...
Other parameters				
Offset RV (SERVAL, km s^{-1})	$\mathcal{U}[-1, 1]$	...	$-0.0972^{+0.0077}_{-0.005}$	$-0.0982^{+0.0047}_{-0.0043}$
Offset RV (DRS, km s^{-1})	$\mathcal{U}[-5, -3]$	$-4.775^{+0.01}_{-0.013}$	...	...
Offset FWHM (km s^{-1})	$\mathcal{U}[10, 12]$	$10.7^{+0.074}_{-0.085}$	...	...
Offset DLW (m^2 s^{-2})	$\mathcal{U}[-1, 1]$	...	$-0.001^{+0.024}_{-0.021}$	$-0.003^{+0.018}_{-0.019}$
Offset BIS (km s^{-1})	$\mathcal{U}[-1, 1]$	$0.0068^{+0.0076}_{-0.0073}$	$0.0072^{+0.0063}_{-0.007}$	...
Jitter term $\sigma_{\rm RV}$ (m s^{-1})	$\mathcal{J}[0, 1000]$	$13.14^{+2.26}_{-1.82}$	$10.32^{+1.68}_{-1.42}$	$10.3^{+1.6}_{-1.4}$
Jitter term $\sigma_{\rm FWHM}$ (m s^{-1})	$\mathcal{J}[0, 1000]$	$89.91^{+8.05}_{-7.0}$	...	...
Jitter term $\sigma_{\rm DLW}$ (1000 m^2 s^{-2})	$\mathcal{J}[0, 1000]$	...	$30.29^{+2.78}_{-2.39}$	$30.7^{+2.7}_{-2.4}$
Jitter term $\sigma_{\rm BIS}$ (m s^{-1})	$\mathcal{J}[0, 1000]$	$42.89^{+3.95}_{-3.52}$	$47.91^{+4.18}_{-3.73}$	...

Note – [(a)], [(b)] and [(c)] as defined in Table 4.3.

Bibliography

Addison B. C., et al., 2021, The Youngest Planet to Have a Spin-Orbit Alignment Measurement AU Mic b, AJ, 162, 137

Afram N., Berdyugina S. V., 2019, Complexity of magnetic fields on red dwarfs, A&A, 629, A83

Aigrain S., Irwin M., 2004, Practical planet prospecting, MNRAS, 350, 331

Aigrain S., Pont F., Zucker S., 2012, A simple method to estimate radial velocity variations due to stellar activity using photometry, MNRAS, 419, 3147

Ali-Dib M., Cumming A., Lin D. N. C., 2020, The imprint of the protoplanetary disc in the accretion of super-Earth envelopes, MNRAS, 494, 2440

Amin M. Y., Elsanhoury W. H., 2017, Astrometric and Photometric Study of the Open Cluster NGC 2323, Serbian Astronomical Journal, 194, 59

Anglada-Escudé G., Butler R. P., 2012, The HARPS-TERRA Project. I. Description of the Algorithms, Performance, and New Measurements on a Few Remarkable Stars Observed by HARPS, ApJS, 200, 15

Araujo-Hauck C., et al., 2007, Future Wavelength Calibration Standards at ESO: the Laser Frequency Comb, The Messenger, 129, 24

Armitage P. J., 2010, Astrophysics of Planet Formation

Astropy Collaboration et al., 2013, Astropy: A community Python package for astronomy, A&A, 558, A33

Astropy Collaboration et al., 2018, The Astropy Project: Building an Open-science Project and Status of the v2.0 Core Package, AJ, 156, 123

Baluev R. V., 2008, Assessing the statistical significance of periodogram peaks, MNRAS, 385, 1279

Baranne A., et al., 1996, ELODIE: A spectrograph for accurate radial velocity measurements., A&AS, 119, 373

Barning F. J. M., 1963, The numerical analysis of the light-curve of 12 Lacertae, Bull. Astron. Inst. Netherlands, 17, 22

Barragán O., Gandolfi D., Antoniciello G., 2019a, PYANETI: a fast and powerful software suite for multiplanet radial velocity and transit fitting, MNRAS, 482, 1017

Barragán O., et al., 2019b, Radial velocity confirmation of K2-100b: a young, highly irradiated, and low-density transiting hot Neptune, MNRAS, 490, 698

Barragán O., et al., 2021, The young HD 73583 (TOI-560) planetary system: Two 10-$M_\oplus$ mini-Neptunes transiting a 750-Myr-old, bright, and active K dwarf, arXiv e-prints, p. arXiv:2110.13069

Barragán O., Aigrain S., Rajpaul V. M., Zicher N., 2022, PYANETI - II. A multidimensional Gaussian process approach to analysing spectroscopic time-series, MNRAS, 509, 866

Baruteau C., Bai X., Mordasini C., Mollière P., 2016, Formation, Orbital and Internal Evolutions of Young Planetary Systems, Space Sci. Rev., 205, 77

Batalha N. E., Lewis T., Fortney J. J., Batalha N. M., Kempton E., Lewis N. K., Line M. R., 2019, The Precision of Mass Measurements Required for Robust Atmospheric Characterization of Transiting Exoplanets, ApJ, 885, L25

Bayes M., Price M., 1763, An Essay towards Solving a Problem in the Doctrine of Chances. By the Late Rev. Mr. Bayes, F. R. S. Communicated by Mr. Price, in a Letter to John Canton, A. M. F. R. S., Philosophical Transactions (1683-1775), 53, 370

Bean J. L., Raymond S. N., Owen J. E., 2021, The Nature and Origins of Sub-Neptune Size Planets, Journal of Geophysical Research (Planets), 126, e06639

Benedict G. F., et al., 2002, A Mass for the Extrasolar Planet Gliese 876b Determined from Hubble Space Telescope Fine Guidance Sensor 3 Astrometry and High-Precision Radial Velocities, ApJ, 581, L115

Beuzit J. L., et al., 2019, SPHERE: the exoplanet imager for the Very Large Telescope, A&A, 631, A155

Biersteker J. B., Schlichting H. E., 2019, Atmospheric mass-loss due to giant impacts: the importance of the thermal component for hydrogen-helium envelopes, MNRAS, 485, 4454

Bishop C. M., 2006, Pattern Recognition and Machine Learning

Boccaletti A., et al., 2015, Fast-moving features in the debris disk around AU Microscopii, Nature, 526, 230

Boccaletti A., et al., 2018, Observations of fast-moving features in the debris disk of AU Mic on a three-year timescale: Confirmation and new discoveries, A&A, 614, A52

Bolmont E., Mathis S., 2016, Effect of the rotation and tidal dissipation history of stars on the evolution of close-in planets, Celestial Mechanics and Dynamical Astronomy, 126, 275

Bond I. A., et al., 2004, OGLE 2003-BLG-235/MOA 2003-BLG-53: A Planetary Microlensing Event, ApJ, 606, L155

Bonfils X., et al., 2007, The HARPS search for southern extra-solar planets. X. A m sin i = 11 M_⊕ planet around the nearby spotted M dwarf <ASTROBJ>GJ 674</ASTROBJ>, A&A, 474, 293

Bonomo A. S., et al., 2019, A giant impact as the likely origin of different twins in the Kepler-107 exoplanet system, Nature Astronomy, 3, 416

Borgniet S., Meunier N., Lagrange A. M., 2015, Using the Sun to estimate Earth-like planets detection capabilities. V. Parameterizing the impact of solar activity components on radial velocities, A&A, 581, A133

Borucki W. J., et al., 2008, in A Decade of Extrasolar Planets around Normal Stars Proceedings of the Space Telescope Science Institute Symposium. pp 36–49

Bouchy F., Carrier F., 2001, P-mode observations on α Cen A, A&A, 374, L5

Bowler B. P., 2016, Imaging Extrasolar Giant Planets, PASP, 128, 102001

Buchner J., 2016, PyMultiNest: Python interface for MultiNest (ascl:1606.005)

Burrows A., Hubbard W. B., Lunine J. I., Marley M., Guillot T., Saumon D., Freedman R. S., 1997, in Soderblom D., ed., Astronomical Society of the Pacific Conference Series Vol. 119, Planets Beyond the Solar System and the Next Generation of Space Missions. p. 9 (arXiv:astro-ph/9705027)

Cale B., et al., 2021, Diving Beneath the Sea of Stellar Activity: Chromatic Radial Velocities of the Young AU Mic Planetary System, arXiv e-prints, p. arXiv:2109.13996

Cameron A. C., 2016, Extrasolar Planetary Transits. Springer International Publishing, doi:10.1007/978-3-319-27458-4_2, https://doi.org/10.1007/978-3-319-27458-4_2

Campbell B., Walker G. A. H., Yang S., 1988, A Search for Substellar Companions to Solar-type Stars, ApJ, 331, 902

Cantat-Gaudin T., Anders F., 2019, VizieR Online Data Catalog: Gaia DR2 open clusters in the Milky Way. II (Cantat-Gaudin+, 2020), VizieR Online Data Catalog, pp J/A+A/633/A99

Carroll B. W., Ostlie D. A., 2006, An introduction to modern astrophysics and cosmology

Cegla H., 2019, The Impact of Stellar Surface Magnetoconvection and Oscillations on the Detection of Temperate, Earth-Mass Planets Around Sun-Like Stars, Geosciences, 9, 114

Chambers J. E., 1999, A hybrid symplectic integrator that permits close encounters between massive bodies, MNRAS, 304, 793

Charbonneau D., Brown T. M., Latham D. W., Mayor M., 2000, Detection of Planetary Transits Across a Sun-like Star, ApJ, 529, L45

Chen Y.-X., Li Y.-P., Li H., Lin D. N. C., 2020, The Preservation of Super-Earths and the Emergence of Gas Giants after Their Progenitor Cores Have Entered the Pebble-isolation Phase, ApJ, 896, 135

Christensen-Dalsgaard J., 2002, Helioseismology, Reviews of Modern Physics, 74, 1073

Claret A., 2018, A new method to compute limb-darkening coefficients for stellar atmosphere models with spherical symmetry: the space missions TESS, Kepler, CoRoT, and MOST, A&A, 618, A20

Collier Cameron A., et al., 2019, Three years of Sun-as-a-star radial-velocity observations on the approach to solar minimum, MNRAS, 487, 1082

Collier Cameron A., et al., 2020, Separating planetary reflex Doppler shifts from stellar variability in the wavelength domain, arXiv e-prints, p. arXiv:2011.00018

Copernicus N., 1543, De revolutionibus orbium coelestium

Cumming A., Marcy G. W., Butler R. P., 1999, The Lick Planet Search: Detectability and Mass Thresholds, ApJ, 526, 890

David T. J., et al., 2016a, New Pleiades Eclipsing Binaries and a Hyades Transiting System Identified by K2, AJ, 151, 112

David T. J., et al., 2016b, A Neptune-sized transiting planet closely orbiting a 5-10-million-year-old star, Nature, 534, 658

David T. J., et al., 2019a, A Warm Jupiter-sized Planet Transiting the Pre-main-sequence Star V1298 Tau, AJ, 158, 79

David T. J., Petigura E. A., Luger R., Foreman-Mackey D., Livingston J. H., Mamajek E. E., Hillenbrand L. A., 2019b, Four Newborn Planets Transiting the Young Solar Analog V1298 Tau, ApJ, 885, L12

Davies R. B., 1987, Hypothesis Testing when a Nuisance Parameter is Present Only Under the Alternatives, Biometrika, 74, 33

Deck K. M., Agol E., Holman M. J., Nesvorný D., 2014, TTVFast: An efficient and accurate code for transit timing inversion problems, The Astrophysical Journal, 787, 132

Delisle J. B., Hara N., Ségransan D., 2020a, Efficient modeling of correlated noise. I. Statistical significance of periodogram peaks, A&A, 635, A83

Delisle J. B., Hara N., Ségransan D., 2020b, Efficient modeling of correlated noise. II. A flexible noise model with fast and scalable methods, A&A, 638, A95

Donati J. F., et al., 2016, A hot Jupiter orbiting a 2-million-year-old solar-mass T Tauri star, Nature, 534, 662

Donati J. F., et al., 2020, SPIRou: NIR velocimetry and spectropolarimetry at the CFHT, MNRAS, 498, 5684

Duane S., Kennedy A. D., Pendleton B. J., Roweth D., 1987, Hybrid Monte Carlo, Physics Letters B, 195, 216

Dumusque X., 2018, Measuring precise radial velocities on individual spectral lines. I. Validation of the method and application to mitigate stellar activity, A&A, 620, A47

Dumusque X., Udry S., Lovis C., Santos N. C., Monteiro M. J. P. F. G., 2011, Planetary detection limits taking into account stellar noise. I. Observational strategies to reduce stellar oscillation and granulation effects, A&A, 525, A140

Dumusque X., et al., 2012, An Earth-mass planet orbiting α Centauri B, Nature, 491, 207

Dumusque X., Boisse I., Santos N. C., 2015, SOAP 2.0: Spot Oscillation And Planet 2.0 (ascl:1504.021)

Dumusque X., et al., 2021, Three years of HARPS-N high-resolution spectroscopy and precise radial velocity data for the Sun, A&A, 648, A103

Eastman J., Siverd R., Gaudi B. S., 2010, Achieving Better Than 1 Minute Accuracy in the Heliocentric and Barycentric Julian Dates, PASP, 122, 935

Eaton M. L., 1983, Multivariate Statistics: A Vector Space Approach

Eisner N. L., et al., 2020, Planet Hunters TESS I: TOI 813, a subgiant hosting a transiting Saturn-sized planet on an 84-day orbit, MNRAS, 494, 750

Eisner N. L., et al., 2021, Planet Hunters TESS II: findings from the first two years of TESS, MNRAS, 501, 4669

Fellgett P., 1955, A Proposal for a Radial Velocity Photometer, Optica Acta, 2, 9

Feroz F., Hobson M. P., Bridges M., 2009, MULTINEST: an efficient and robust Bayesian inference tool for cosmology and particle physics, MNRAS, 398, 1601

Foreman-Mackey D., 2016, corner.py: Scatterplot matrices in Python, The Journal of Open Source Software, 1, 24

Foreman-Mackey D., 2018, Scalable Backpropagation for Gaussian Processes using Celerite, Research Notes of the American Astronomical Society, 2, 31

Foreman-Mackey D., Hogg D. W., Lang D., Goodman J., 2013, emcee: The MCMC Hammer, PASP, 125, 306

Frolov V. N., Ananjevskaja Y. K., Polyakov E. V., 2012, Investigation of the open star cluster NGC 2323 (M50) based on the proper motions and photometry of its constituent stars, Astronomy Letters, 38, 74

Gaia Collaboration et al., 2018, Gaia Data Release 2. Summary of the contents and survey properties, A&A, 616, A1

Gaia Collaboration et al., 2021, Gaia Early Data Release 3. Summary of the contents and survey properties, A&A, 649, A1

Gaidos E., et al., 2017, Zodiacal exoplanets in time (ZEIT) - II. A 'super-Earth' orbiting a young K dwarf in the Pleiades Neighbourhood, MNRAS, 464, 850

Gelman A., Rubin D. B., 1992, Inference from Iterative Simulation Using Multiple Sequences, Statistical Science, 7, 457

Gelman A., Carlin J. B., Stern H. S., Rubin D. B., 2004, Bayesian Data Analysis, 2nd ed. edn. Chapman and Hall/CRC

Gilbert E. A., et al., 2021, Flares, Rotation, and Planets of the AU Mic System from TESS Observations, arXiv e-prints, p. arXiv:2109.03924

Gilbertson C., Ford E. B., Jones D. E., Stenning D. C., 2020, Towards Extremely Precise Radial Velocities: II. A Tool For Using Multivariate Gaussian Processes to Model Stellar Activity, arXiv e-prints, p. arXiv:2009.01085

Ginzburg S., Schlichting H. E., Sari R., 2016, Super-Earth Atmospheres: Self-consistent Gas Accretion and Retention, ApJ, 825, 29

Gomes da Silva J., Santos N. C., Bonfils X., Delfosse X., Forveille T., Udry S., 2011, Long-term magnetic activity of a sample of M-dwarf stars from the HARPS program. I. Comparison of activity indices, A&A, 534, A30

Goodman J., Weare J., 2010, Ensemble samplers with affine invariance, Commun Appl Math Comput Sci, 5, 65

Grandjean A., et al., 2020, A HARPS RV search for planets around young nearby stars, A&A, 633, A44

Grandjean A., et al., 2021, A SOPHIE RV search for giant planets around young nearby stars (YNS). A combination with the HARPS YNS survey, A&A, 650, A39

Gregory P. C., 2005, A Bayesian Analysis of Extrasolar Planet Data for HD 73526, ApJ, 631, 1198

Gullberg D., Lindegren L., 2002, Determination of accurate stellar radial-velocity measures, A&A, 390, 383

Hale G. E., 1908, On the Probable Existence of a Magnetic Field in Sun-Spots, ApJ, 28, 315

Hall R. D., Thompson S. J., Handley W., Queloz D., 2018, On the Feasibility of Intense Radial Velocity Surveys for Earth-Twin Discoveries, MNRAS, 479, 2968

Halverson S., et al., 2016, in Evans C. J., Simard L., Takami H., eds, Society of Photo-Optical Instrumentation Engineers (SPIE) Conference Series Vol. 9908, Ground-based and Airborne Instrumentation for Astronomy VI. p. 99086P (arXiv:1607.05634), doi:10.1117/12.2232761

Handley W. J., Hobson M. P., Lasenby A. N., 2015, PolyChord: Nested sampling for cosmology (ascl:1502.011)

Hara N. C., 2021, in Siebert A., et al., eds, SF2A-2021: Proceedings of the Annual meeting of the French Society of Astronomy and Astrophysics. Eds.: A. Siebert. pp 51–54

Hara N. C., Mari A. R., 2021, l1p: Python implementation of the l1 periodogram (ascl:2112.024)

Hara N. C., Boué G., Laskar J., Correia A. C. M., 2017, Radial velocity data analysis with compressed sensing techniques, MNRAS, 464, 1220

Harris C. R., et al., 2020, Array programming with NumPy, Nature, 585, 357

Hastings W. K., 1970, Monte carlo sampling methods using Markov chains and their applications, Biometrika, 57, 97

Hatzes A. P., 1996, Simulations of Stellar Radial Velocity and Spectral Line Bisector Variations: I. Nonradial Pulsations, PASP, 108, 839

Haywood R. D., 2015, Hide and Seek: Radial-Velocity Searches for Planets around Active Stars, PhD thesis, University of St Andrews

Haywood R. D., et al., 2014, Planets and stellar activity: hide and seek in the CoRoT-7 system, MNRAS, 443, 2517

Hebb L., Petro L., Ford H. C., Ardila D. R., Toledo I., Minniti D., Golimowski D. A., Clampin M., 2007, A search for planets transiting the M-dwarf debris disc host, AU Microscopii, MNRAS, 379, 63

Heng K., 2017, Exoplanetary Atmospheres: Theoretical Concepts and Foundations

Henry G. W., Marcy G., Butler R. P., Vogt S. S., 1999, HD 209458, IAU Circ., 7307

Hirano T., et al., 2020, Limits on the Spin-Orbit Angle and Atmospheric Escape for the 22 Myr Old Planet AU Mic b, ApJ, 899, L13

Hogg D. W., Bovy J., Lang D., 2010, Data analysis recipes: Fitting a model to data, arXiv e-prints, p. arXiv:1008.4686

Howell S. B., et al., 2014, The K2 Mission: Characterization and Early Results, PASP, 126, 398

Hunter J. D., 2007, Matplotlib: A 2D graphics environment, Computing in Science & Engineering, 9, 90

Husser T. O., Wende-von Berg S., Dreizler S., Homeier D., Reiners A., Barman T., Hauschildt P. H., 2013, A new extensive library of PHOENIX stellar atmospheres and synthetic spectra, A&A, 553, A6

Ikoma M., Hori Y., 2012, In Situ Accretion of Hydrogen-rich Atmospheres on Short-period Super-Earths: Implications for the Kepler-11 Planets, ApJ, 753, 66

Inamdar N. K., Schlichting H. E., 2016, Stealing the Gas: Giant Impacts and the Large Diversity in Exoplanet Densities, ApJ, 817, L13

Irwin A. W., Campbell B., Morbey C. L., Walker G. A. H., Yang S., 1989, Long-Period Radial-Velocity Variations of Arcturus, PASP, 101, 147

Irwin J., Aigrain S., Hodgkin S., Irwin M., Bouvier J., Clarke C., Hebb L., Moraux E., 2006, The Monitor project: rotation of low-mass stars in the open cluster M34, MNRAS, 370, 954

Irwin J., Aigrain S., Bouvier J., Hebb L., Hodgkin S., Irwin M., Moraux E., 2009, The Monitor project: rotation periods of low-mass stars in M50, MNRAS, 392, 1456

Jacob W. S., 1855, On certain Anomalies presented by the Binary Star 70 Ophiuchi, MNRAS, 15, 228

Jankovic M. R., Owen J. E., Mohanty S., 2019, Close-in Super-Earths: The first and the last stages of planet formation in an MRI-accreting disc, MNRAS, 484, 2296

Jeffreys H., 1939, The Theory of Probability

Jones D. E., Stenning D. C., Ford E. B., Wolpert R. L., Loredo T. J., Gilbertson C., Dumusque X., 2017, Improving Exoplanet Detection Power: Multivariate Gaussian Process Models for Stellar Activity, arXiv e-prints, p. arXiv:1711.01318

Jurgenson C., Fischer D., McCracken T., Sawyer D., Szymkowiak A., Davis A., Muller G., Santoro F., 2016, in Evans C. J., Simard L., Takami H., eds, Society of Photo-Optical Instrumentation Engineers (SPIE) Conference Series Vol. 9908, Ground-based and Airborne Instrumentation for Astronomy VI. p. 99086T (arXiv:1606.04413), doi:10.1117/12.2233002

Kalas P., Liu M. C., Matthews B. C., 2004, Discovery of a Large Dust Disk Around the Nearby Star AU Microscopii, Science, 303, 1990

Kanodia S., Wright J., 2018, Python Leap Second Management and Implementation of Precise Barycentric Correction (barycorrpy), Research Notes of the American Astronomical Society, 2, 4

Kharchenko N. V., Piskunov A. E., Röser S., Schilbach E., Scholz R. D., 2005, Astrophysical parameters of Galactic open clusters, A&A, 438, 1163

Klein B., et al., 2021, Investigating the young AU Mic system with SPIRou: large-scale stellar magnetic field and close-in planet mass, MNRAS, 502, 188

Kossakowski D., et al., 2021, TOI-1201 b: A mini-Neptune transiting a bright and moderately young M dwarf, arXiv e-prints, p. arXiv:2109.09346

Lagrange A. M., et al., 2009, A probable giant planet imaged in the β Pictoris disk. VLT/NaCo deep L'-band imaging, A&A, 493, L21

Lagrange A. M., Desort M., Meunier N., 2010, Using the Sun to estimate Earth-like planets detection capabilities . I. Impact of cold spots, A&A, 512, A38

Lannier J., et al., 2017, Combining direct imaging and radial velocity data towards a full exploration of the giant planet population. I. Method and first results, A&A, 603, A54

Latham D. W., Stefanik R. P., Mazeh T., Torres G., 1989, in Bulletin of the American Astronomical Society. p. 1224

Lee E. J., Chiang E., 2015, To Cool is to Accrete: Analytic Scalings for Nebular Accretion of Planetary Atmospheres, ApJ, 811, 41

Lee E. J., Chiang E., 2016, Breeding Super-Earths and Birthing Super-puffs in Transitional Disks, ApJ, 817, 90

Lee E. J., Chiang E., Ormel C. W., 2014, Make Super-Earths, Not Jupiters: Accreting Nebular Gas onto Solid Cores at 0.1 AU and Beyond, ApJ, 797, 95

Lindegren L., Dravins D., 2003, The fundamental definition of "radial velocity", A&A, 401, 1185

Liu S.-F., Hori Y., Lin D. N. C., Asphaug E., 2015, Giant Impact: An Efficient Mechanism for the Devolatilization of Super-Earths, ApJ, 812, 164

Lo Curto G., et al., 2015, HARPS Gets New Fibres After 12 Years of Operations, The Messenger, 162, 9

Lomb N. R., 1976, Least-Squares Frequency Analysis of Unequally Spaced Data, Ap&SS, 39, 447

Lopez E. D., Fortney J. J., 2013, The Role of Core Mass in Controlling Evaporation: The Kepler Radius Distribution and the Kepler-36 Density Dichotomy, ApJ, 776, 2

Lovis C., Fischer D., 2010, in Seager S., ed., , Exoplanets. pp 27–53

Maldonado J., Martínez-Arnáiz R. M., Eiroa C., Montes D., Montesinos B., 2010, A spectroscopy study of nearby late-type stars, possible members of stellar kinematic groups, A&A, 521, A12

Mamajek E. E., Bell C. P. M., 2014, On the age of the Beta Pictoris moving group, MNRAS, 445, 2169

Mann A. W., et al., 2016a, Zodiacal Exoplanets in Time (ZEIT). III. A Short-period Planet Orbiting a Pre-main-sequence Star in the Upper Scorpius OB Association, AJ, 152, 61

Mann A. W., et al., 2016b, Zodiacal Exoplanets in Time (ZEIT). I. A Neptune-sized Planet Orbiting an M4.5 Dwarf in the Hyades Star Cluster, ApJ, 818, 46

Mann A. W., et al., 2017, Zodiacal Exoplanets in Time (ZEIT). IV. Seven Transiting Planets in the Praesepe Cluster, AJ, 153, 64

Mann A. W., et al., 2018, Zodiacal Exoplanets in Time (ZEIT). VI. A Three-planet System in the Hyades Cluster Including an Earth-sized Planet, AJ, 155, 4

Mann A. W., et al., 2020, TESS Hunt for Young and Maturing Exoplanets (THYME). III. A Two-planet System in the 400 Myr Ursa Major Group, AJ, 160, 179

Mann A. W., et al., 2021, TESS Hunt for Young and Maturing Exoplanets (THYME) VI: an 11 Myr giant planet transiting a very low-mass star in Lower Centaurus Crux, arXiv e-prints, p. arXiv:2110.09531

Marcy G. W., Butler R. P., 1992, Precision Radial Velocities with an Iodine Absorption cell, PASP, 104, 270

Marois C., Macintosh B., Barman T., Zuckerman B., Song I., Patience J., Lafrenière D., Doyon R., 2008, Direct Imaging of Multiple Planets Orbiting the Star HR 8799, Science, 322, 1348

Marsh T. R., Horne K., 1988, Images of accretion discs - II. Doppler tomography., MNRAS, 235, 269

Martioli E., et al., 2020, Spin-orbit alignment and magnetic activity in the young planetary system AU Mic, A&A, 641, L1

Martioli E., Hébrard G., Correia A. C. M., Laskar J., Lecavelier des Etangs A., 2021, New constraints on the planetary system around the young active star AU Mic. Two transiting warm Neptunes near mean-motion resonance, A&A, 649, A177

Mayor M., Queloz D., 1995, A Jupiter-mass companion to a solar-type star, Nature, 378, 355

Mayor M., et al., 2003, Setting New Standards with HARPS, The Messenger, 114, 20

Mestel L., 1968, Magnetic braking by a stellar wind-I, MNRAS, 138, 359

Metropolis N., Rosenbluth A. W., Rosenbluth M. N., Teller A. H., Teller E., 1953, Equation of State Calculations by Fast Computing Machines, J. Chem. Phys., 21, 1087

Meunier N., Lagrange A. M., 2013, Using the Sun to estimate Earth-like planets detection capabilities. IV. Correcting for the convective component, A&A, 551, A101

Meunier N., Lagrange A. M., De Bondt K., 2012, Comparison of different exoplanet mass detection limit methods using a sample of main-sequence intermediate-type stars, A&A, 545, A87

Meunier N., Lagrange A. M., Borgniet S., Rieutord M., 2015, Using the Sun to estimate Earth-like planet detection capabilities. VI. Simulation of granulation and supergranulation radial velocity and photometric time series, A&A, 583, A118

Michel E., et al., 2008, CoRoT Measures Solar-Like Oscillations and Granulation in Stars Hotter Than the Sun, Science, 322, 558

Millholland S. C., Winn J. N., 2021, Split Peas in a Pod: Intra-system Uniformity of Super-Earths and Sub-Neptunes, ApJ, 920, L34

Millholland S., Wang S., Laughlin G., 2017, Kepler Multi-planet Systems Exhibit Unexpected Intra-system Uniformity in Mass and Radius, ApJ, 849, L33

Mortier A., Collier Cameron A., 2017, Stacked Bayesian general Lomb-Scargle periodogram: Identifying stellar activity signals, A&A, 601, A110

Mortier A., Faria J. P., Correia C. M., Santerne A., Santos N. C., 2015, BGLS: A Bayesian formalism for the generalised Lomb-Scargle periodogram, A&A, 573, A101

Motalebi F., et al., 2015, The HARPS-N Rocky Planet Search. I. HD 219134 b: A transiting rocky planet in a multi-planet system at 6.5 pc from the Sun, A&A, 584, A72

Murphy M. T., Tzanavaris P., Webb J. K., Lovis C., 2007, Selection of ThAr lines for wavelength calibration of echelle spectra and implications for variations in the fine-structure constant, MNRAS, 378, 221

Murray C. D., Dermott S. F., 2000, Solar System Dynamics

Newton E. R., et al., 2019, TESS Hunt for Young and Maturing Exoplanets (THYME): A Planet in the 45 Myr Tucana-Horologium Association, ApJ, 880, L17

Newton E. R., et al., 2021, TESS Hunt for Young and Maturing Exoplanets (THYME). IV. Three Small Planets Orbiting a 120 Myr Old Star in the Pisces-Eridanus Stream, AJ, 161, 65

Ormel C. W., Shi J.-M., Kuiper R., 2015, Hydrodynamics of embedded planets' first atmospheres - II. A rapid recycling of atmospheric gas, MNRAS, 447, 3512

Osborne M. A., 2010, Bayesian Gaussian Processes for Sequential Prediction, Optimisation and Quadrature, PhD thesis, University of Oxford, United Kingdom

Owen J. E., 2019, Atmospheric Escape and the Evolution of Close-In Exoplanets, Annual Review of Earth and Planetary Sciences, 47, 67

Owen J. E., 2020, Constraining the entropy of formation from young transiting planet, MNRAS, 498, 5030

Owen J. E., Wu Y., 2013, Kepler Planets: A Tale of Evaporation, ApJ, 775, 105

Owen J. E., Wu Y., 2016, Atmospheres of Low-mass Planets: The "Boil-off", ApJ, 817, 107

Owen J. E., Wu Y., 2017, The Evaporation Valley in the Kepler Planets, ApJ, 847, 29

Pasquini L., et al., 2002, Installation and commissioning of FLAMES, the VLT Multifibre Facility, The Messenger, 110, 1

Pepe F., Mayor M., Galland F., Naef D., Queloz D., Santos N. C., Udry S., Burnet M., 2002, The CORALIE survey for southern extra-solar planets VII. Two short-period Saturnian companions to HD 108147 and HD 168746, A&A, 388, 632

Pepe F. A., et al., 2010, in Ground-based and Airborne Instrumentation for Astronomy III. p. 77350F, doi:10.1117/12.857122

Pepe F., et al., 2011, The HARPS search for Earth-like planets in the habitable zone. I. Very low-mass planets around HD 20794, HD 85512, and HD 192310, A&A, 534, A58

Pepe F., et al., 2021, ESPRESSO at VLT. On-sky performance and first results, A&A, 645, A96

Pepper J., et al., 2017, A Low-mass Exoplanet Candidate Detected by K2 Transiting the Praesepe M Dwarf JS 183, AJ, 153, 177

Perryman M., 2018, The Exoplanet Handbook

Piso A.-M. A., Youdin A. N., 2014, On the Minimum Core Mass for Giant Planet Formation at Wide Separations, ApJ, 786, 21

Plavchan P., Werner M. W., Chen C. H., Stapelfeldt K. R., Su K. Y. L., Stauffer J. R., Song I., 2009, New Debris Disks Around Young, Low-Mass Stars Discovered with the Spitzer Space Telescope, ApJ, 698, 1068

Plavchan P., et al., 2020, A planet within the debris disk around the pre-main-sequence star AU Microscopii, Nature, 582, 497

Pollack J. B., Hubickyj O., Bodenheimer P., Lissauer J. J., Podolak M., Greenzweig Y., 1996, Formation of the Giant Planets by Concurrent Accretion of Solids and Gas, Icarus, 124, 62

Poon S. T. S., Nelson R. P., Jacobson S. A., Morbidelli A., 2020, Formation of compact systems of super-Earths via dynamical instabilities and giant impacts, MNRAS, 491, 5595

Press W. H., 2007, Numerical Recipes: The Art of Scientific Computing

Prša A., et al., 2016, Nominal Values for Selected Solar and Planetary Quantities: IAU 2015 Resolution B3, AJ, 152, 41

Queloz D., et al., 2001, No planet for HD 166435, A&A, 379, 279

Quinn S. N., et al., 2012, Two “b”s in the Beehive: The Discovery of the First Hot Jupiters in an Open Cluster, ApJ, 756, L33

Quirrenbach A., et al., 2014, in Ramsay S. K., McLean I. S., Takami H., eds, Society of Photo-Optical Instrumentation Engineers (SPIE) Conference Series Vol. 9147, Ground-based and Airborne Instrumentation for Astronomy V. p. 91471F, doi:10.1117/12.2056453

Rackham B. V., et al., 2022, Final Report for SAG 21: The Effect of Stellar Contamination on Space-based Transmission Spectroscopy, arXiv e-prints, p. arXiv:2201.09905

Rafikov R. R., 2006, Atmospheres of Protoplanetary Cores: Critical Mass for Nucleated Instability, ApJ, 648, 666

Rajpaul V. M., 2017, Gaussian process tools for modelling stellar signals and studying exoplanets, PhD thesis, University of Oxford, United Kingdom

Rajpaul V., Aigrain S., Osborne M. A., Reece S., Roberts S., 2015, A Gaussian process framework for modelling stellar activity signals in radial velocity data, MNRAS, 452, 2269

Rajpaul V., Aigrain S., Roberts S., 2016, Ghost in the time series: no planet for Alpha Cen B, MNRAS, 456, L6

Rajpaul V. M., Aigrain S., Buchhave L. A., 2020, A robust, template-free approach to precise radial velocity extraction, MNRAS, 492, 3960

Rasmussen C. E., Williams C. K. I., 2006, Gaussian Processes for Machine Learning

Rauer H., et al., 2014, The PLATO 2.0 mission, Experimental Astronomy, 38, 249

Raymond S. N., 2015, Runaway Gas Accretion. Springer Berlin Heidelberg, doi:10.1007/978-3-662-44185-5_1396, https://doi.org/10.1007/978-3-662-44185-5_1396

Ricker G. R., et al., 2015, Transiting Exoplanet Survey Satellite (TESS), Journal of Astronomical Telescopes, Instruments, and Systems, 1, 014003

Rizzuto A. C., Vanderburg A., Mann A. W., Kraus A. L., Dressing C. D., Agüeros M. A., Douglas S. T., Krolikowski D. M., 2018, Zodiacal Exoplanets in Time (ZEIT). VIII. A Two-planet System in Praesepe from K2 Campaign 16, AJ, 156, 195

Rizzuto A. C., et al., 2020, TESS Hunt for Young and Maturing Exoplanets (THYME). II. A 17 Myr Old Transiting Hot Jupiter in the Sco-Cen Association, AJ, 160, 33

Rogers J. G., Owen J. E., 2021, Unveiling the planet population at birth, MNRAS, 503, 1526

Santos N. C., et al., 2014, The HARPS search for southern extra-solar planets. XXXV. The interesting case of HD 41248: stellar activity, no planets?, A&A, 566, A35

Scargle J. D., 1982, Studies in astronomical time series analysis. II. Statistical aspects of spectral analysis of unevenly spaced data., ApJ, 263, 835

Schrijver C. J., Zwaan C., 2000, Solar and Stellar Magnetic Activity

Schuster A., 1898, On the investigation of hidden periodicities with application to a supposed 26 day period of meteorological phenomena, Terrestrial Magnetism (Journal of Geophysical Research), 3, 13

Seager S., 2010, Exoplanets

See T. J. J., 1895, Perturbations in the motion of the double star 70 Ophiuchi = T, 2272, AJ, 15, 180

Sharma S., 2017, Markov Chain Monte Carlo Methods for Bayesian Data Analysis in Astronomy, ARA&A, 55, 213

Shevchenko I. I., 2017, The Lidov-Kozai Effect - Applications in Exoplanet Research and Dynamical Astronomy, doi:10.1007/978-3-319-43522-0.

Skilling J., 2006, Nested sampling for general Bayesian computation, Bayesian Analysis, 1, 833

Southworth J., Wheatley P. J., Sams G., 2007, A method for the direct determination of the surface gravities of transiting extrasolar planets, MNRAS, 379, L11

Spiegel D. S., Burrows A., 2012, Spectral and Photometric Diagnostics of Giant Planet Formation Scenarios, ApJ, 745, 174

Stein M. L., 1999, Interpolation of Spatial Data: Some Theory for Kriging

Struve O., 1952, Proposal for a project of high-precision stellar radial velocity work, The Observatory, 72, 199

Suárez Mascareño A., et al., 2021, Rapid contraction of giant planets orbiting the 20-million-year-old star V1298 Tau, Nature Astronomy,

Szabó G. M., et al., 2021, The changing face of AU Mic b: stellar spots, spin-orbit commensurability, and Transit Timing Variations as seen by CHEOPS and TESS, arXiv e-prints, p. arXiv:2108.02149

Terquem C., 2014, On the formation of the Kepler-10 planetary system, MNRAS, 444, 1738

Thompson S. J., et al., 2016, in Evans C. J., Simard L., Takami H., eds, Society of Photo-Optical Instrumentation Engineers (SPIE) Conference Series Vol. 9908, Ground-based and Airborne Instrumentation for Astronomy VI. p. 99086F (arXiv:1608.04611), doi:10.1117/12.2232111

Tokovinin A., Fischer D. A., Bonati M., Giguere M. J., Moore P., Schwab C., Spronck J. F. P., Szymkowiak A., 2013, CHIRON—A Fiber Fed Spectrometer for Precise Radial Velocities, PASP, 125, 1336

Toner C. G., Gray D. F., 1988, The Star Patch on the G8 Dwarf chi Bootis A, ApJ, 334, 1008

Torres C. A. O., Quast G. R., da Silva L., de La Reza R., Melo C. H. F., Sterzik M., 2006, Search for associations containing young stars (SACY). I. Sample and searching method, A&A, 460, 695

Traub W. A., Oppenheimer B. R., 2010, in Seager S., ed., , Exoplanets. pp 111–156

Trotta R., 2008, Bayes in the sky: Bayesian inference and model selection in cosmology, Contemporary Physics, 49, 71

Udalski A., et al., 2002, The Optical Gravitational Lensing Experiment. Search for Planetary and Low-Luminosity Object Transits in the Galactic Disk. Results of 2001 Campaign, Acta Astron., 52, 1

Van Eylen V., et al., 2019, The Orbital Eccentricity of Small Planet Systems, AJ, 157, 61

VanderPlas J. T., 2018, Understanding the Lomb-Scargle Periodogram, ApJS, 236, 16

Vanderburg A., et al., 2018, Zodiacal Exoplanets in Time (ZEIT). VII. A Temperate Candidate Super-Earth in the Hyades Cluster, AJ, 156, 46

Virtanen P., et al., 2020, SciPy 1.0: Fundamental Algorithms for Scientific Computing in Python, Nature Methods, 17, 261

Weiss L. M., et al., 2018, The California-Kepler Survey. V. Peas in a Pod: Planets in a Kepler Multi-planet System Are Similar in Size and Regularly Spaced, AJ, 155, 48

White R., Schaefer G., Boyajian T., von Braun K., ten Brummelaar T., Bieryla A., Dupuy T., Latham D. W., 2019, in American Astronomical Society Meeting Abstracts #233. p. 259.41

Wolszczan A., Frail D. A., 1992, A planetary system around the millisecond pulsar PSR1257 + 12, Nature, 355, 145

Wright J. T., 2018, in Deeg H. J., Belmonte J. A., eds, , Handbook of Exoplanets. p. 4, doi:10.1007/978-3-319-55333-7_4

Wright J. T., Eastman J. D., 2014, Barycentric Corrections at 1 cm s^{-1} for Precise Doppler Velocities, PASP, 126, 838

Yu L., et al., 2017, A hot Jupiter around the very active weak-line T Tauri star TAP 26, MNRAS, 467, 1342

Zechmeister M., Kürster M., 2009, The generalised Lomb-Scargle periodogram. A new formalism for the floating-mean and Keplerian periodograms, A&A, 496, 577

Zechmeister M., et al., 2018, Spectrum radial velocity analyser (SERVAL). High-precision radial velocities and two alternative spectral indicators, A&A, 609, A12

Zeng L., Sasselov D. D., Jacobsen S. B., 2016, Mass-Radius Relation for Rocky Planets Based on PREM, ApJ, 819, 127

Zeng L., et al., 2019, Growth model interpretation of planet size distribution, Proceedings of the National Academy of Science, 116, 9723

Zhao L., Fischer D. A., Ford E. B., Henry G. W., Roettenbacher R. M., Brewer J. M., 2020, The EXPRES Stellar-signals Project. I. Description of Data, Research Notes of the American Astronomical Society, 4, 156

Zhao L. L., et al., 2022, The EXPRES Stellar Signals Project II. State of the Field in Disentangling Photospheric Velocities, arXiv e-prints, p. arXiv:2201.10639

Zicher N., et al., 2022, One year of AU Mic with HARPS - I. Measuring the masses of the two transiting planets, MNRAS, 512, 3060